

AD-A078 520

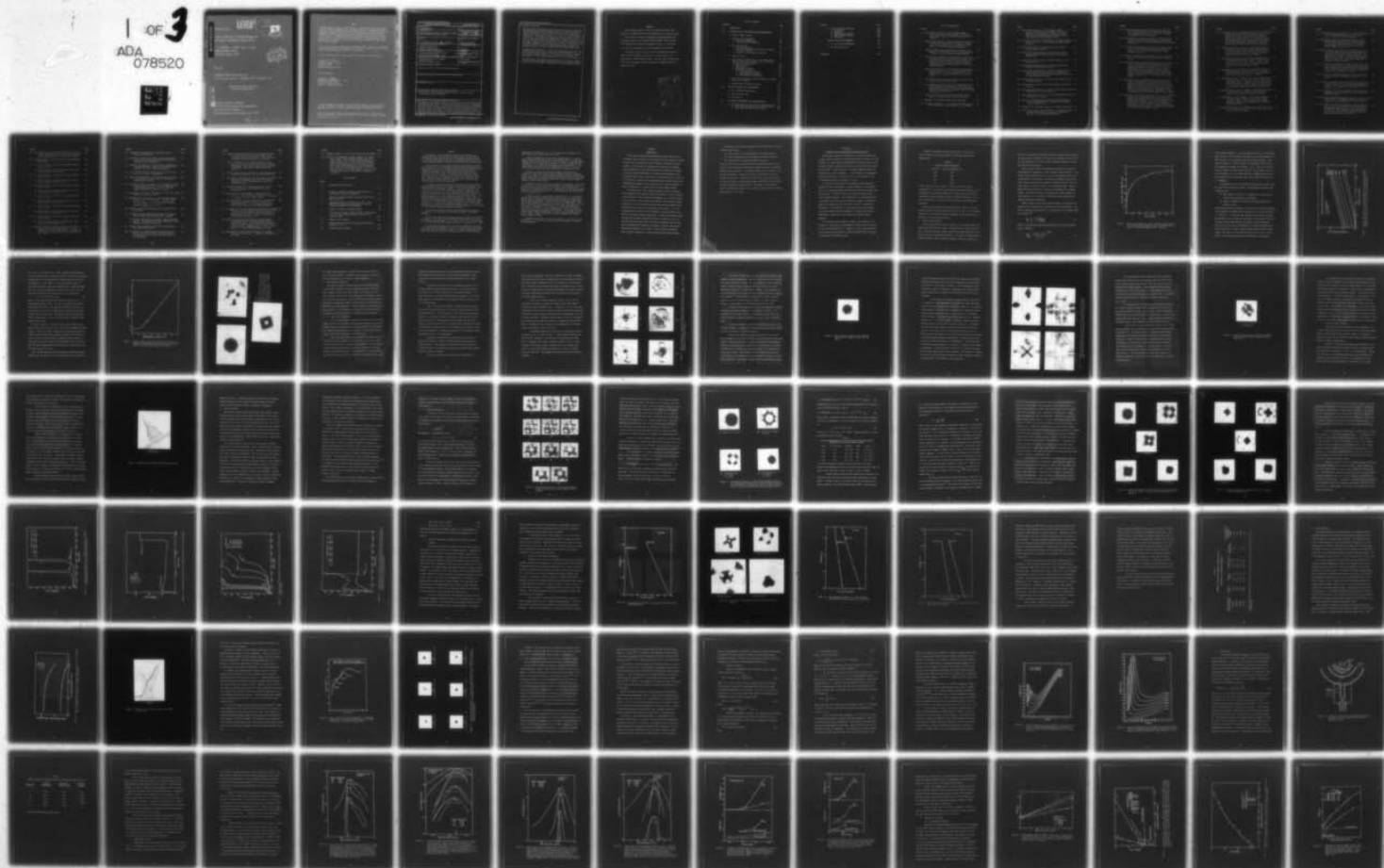
OREGON GRADUATE CENTER BEAVERTON DEPT OF APPLIED PHY--ETC F/G 20/12  
FIELD ELECTRON AND ION SOURCE RESEARCH FOR HIGH DENSITY INFORMAT--ETC(U)  
MAY 79 L W SWANSON , J ORLOFF , A E BELL F33615-76-C-1327

UNCLASSIFIED

AFAL-TR-79-1133

NL

1 OF 3  
ADA  
078520



ADA 078520

LEVEL *TLA*

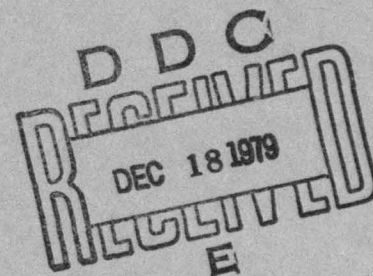
*2*

AFAL-TR-79-1133

FIELD ELECTRON AND ION SOURCE RESEARCH FOR  
HIGH DENSITY INFORMATION STORAGE SYSTEM

L. W. SWANSON, J. ORLOFF, AND A. E. BELL  
OREGON GRADUATE CENTER  
BEAVERTON, OREGON 97005

A072541



MAY 1979

TECHNICAL REPORT AFAL-TR-79-1133

FINAL TECHNICAL REPORT - SEPTEMBER 1977 TO DECEMBER 1978

APPROVED FOR PUBLIC RELEASE;  
DISTRIBUTION UNLIMITED

DDC FILE COPY

DDC

AIR FORCE AVIONICS LABORATORY  
AIR FORCE WRIGHT AERONAUTICAL LABORATORIES  
AIR FORCE SYSTEMS COMMAND  
WRIGHT-PATTERSON AIR FORCE BASE, OHIO 45433

79 12 18 117

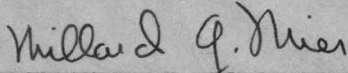


NOTICE

When Government drawings, specifications, or other data are used for any purpose other than in connection with a definitely related Government procurement operation, the United States Government thereby incurs no responsibility nor any obligation whatsoever; and the fact that the government may have formulated, furnished, or in any way supplied the said drawings, specifications, or other data, is not to be regarded by implication or otherwise as in any manner licensing the holder or any other person or corporation, or conveying any rights or permission to manufacture, use, or sell any patented invention that may in any way be related thereto.

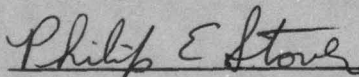
This report has been reviewed by the Information Office (OI) and is releasable to the National Technical Information Service (NTIS). At NTIS, it will be available to the general public, including foreign nations.

This technical report has been reviewed and is approved for publication.



MILLARD G. MIER  
Project Engineer  
Electronic Research Branch

FOR THE COMMANDER



PHILIP E. STOVER, Chief  
Electronic Research Branch  
Electronic Technology Division

"If your address has changed, if you wish to be removed from our mailing list, or if the addressee is no longer employed by your organization please notify AFAL/DHR, W-PAFB, OH 45433 to help us maintain a current mailing list".

Copies of this report should not be returned unless return is required by security considerations, contractual obligations, or notice on a specific document.

SECURITY CLASSIFICATION OF THIS PAGE (When Data Entered)

19 REPORT DOCUMENTATION PAGE		READ INSTRUCTIONS BEFORE COMPLETING FORM
1. REPORT NUMBER AFAL-TR-79-1133	2. GOVT ACCESSION NO.	3. RECIPIENT'S CATALOG NUMBER
4. TITLE (and Subtitle) FIELD ELECTRON AND ION SOURCE RESEARCH FOR HIGH DENSITY INFORMATION STORAGE SYSTEM,		5. TYPE OF REPORT & PERIOD COVERED Final Technical Report. September 77-Dec 78
7. AUTHOR(s) L. W. Swanson, J. Orloff and A. E. Bell		6. PERFORMING ORG. REPORT NUMBER
9. PERFORMING ORGANIZATION NAME AND ADDRESS Oregon Graduate Center 19600 N.W. Walker Road Beaverton, Oregon 97005		8. CONTRACT OR GRANT NUMBER(s) F33615-76-C-1327
11. CONTROLLING OFFICE NAME AND ADDRESS Air Force Avionics Laboratory (DHR) Air Force Systems Command Wright-Patterson AFB, Ohio 45433		10. PROGRAM ELEMENT, PROJECT, TASK AREA & WORK UNIT NUMBERS 3164-01-01
14. MONITORING AGENCY NAME & ADDRESS (if different from Controlling Office) Advanced Research Projects Agency 1400 Wilson Blvd. Arlington, Virginia 22209		12. REPORT DATE May 1979
		13. NUMBER OF PAGES 104
		15. SECURITY CLASS. (of this report) Unclassified
		15a. DECLASSIFICATION/DOWNGRADING SCHEDULE
16. DISTRIBUTION STATEMENT (of this Report) Approved for public release; distribution unlimited		
17. DISTRIBUTION STATEMENT (of the abstract entered in Block 20, if different from Report) 61101F		
18. SUPPLEMENTARY NOTES		
19. KEY WORDS (Continue on reverse side if necessary and identify by block number) Field electron, field ionization, electron source, ion source, thermal field emission, energy distribution		
20. ABSTRACT (Continue on reverse side if necessary and identify by block number) The purpose of this research program is the evaluation and characterization of high brightness field electron and ion sources suitable for use in high density information storage systems. In addition, preliminary evaluation of focussing optics suitable for forming submicron beams of both ions and electrons has been performed. Several new field electron source materials including Mo, LaB <sub>6</sub> , SmB <sub>6</sub> and HfC have been examined. In addition, a complete characterization and comparison between the Zr/W(100) and built-up W(100) emitters operating in the thermal-field (TF) mode is reported. Such source parameters as angular		

DD FORM 1 JAN 73 1473 EDITION OF 1 NOV 65 IS OBSOLETE

SECURITY CLASSIFICATION OF THIS PAGE (When Data Entered)

407 883

mt



## 20. ABSTRACT (continued)

intensity, energy distribution, beam noise spectrum, and source life have been measured. Both emitters exhibit long life ( $\sim 1500$  hrs and  $5000$  hrs for the W(100) built up and Zr/W(100) sources respectively) operating at angular intensities  $I'$  of  $10^{-4}$  to  $10^{-3}$  A sr $^{-1}$  in  $\sim 1 \times 10^{-8}$  torr pressure of residual gas. An anomalous broadening (1 to 2 eV) of the total energy distribution  $I' > 10^{-4}$  A sr $^{-1}$  was observed and studied in detail for both TF sources. The energy broadening, believed due to coulomb interactions between the emitted electrons, can be reduced by increasing the emitter radius. The primary advantage of the Zr/W(100) over the built up W(100) emitter was the smaller amplitude of current fluctuations ( $\sim 0.22\%$ ). A simple magnetically focussed electron gun using the Zr/W(100) TF source gave a focussed beam spot of  $0.1 \mu\text{m}$  and a current density of  $1000 \text{ A/cm}^2$  at  $12 \text{ kV}$ .

A maximum angular intensity of  $1 \mu\text{A sr}^{-1}$  was achieved with the  $\text{H}_2^+$ /Ir field ionization (FI) source at  $77 \text{ K}$ . Preliminary life tests showed steady current operating times in excess of  $385 \text{ hrs}$  for the Ir FI emitter. Preliminary studies of focussed beams from a gas phase FI source suggests the possibility of  $1 \text{ A cm}^{-2}$  target current of  $\text{H}_2^+$  or  $\text{Ar}^+$  in a  $0.1 \mu\text{m}$  beam size.

A detailed study of the emission characteristics of a liquid film gallium ion source was also performed. Results showed that at an angular intensity of  $20 \mu\text{A sr}^{-1}$  the full width half maximum of the energy spread was  $4.5 \text{ eV}$ .



# FOREWORD

This technical report covers the research performed under Contract No. F33615-76-C-1327 from September 1977 to December 1978.

This contract is with the Department of Applied Physics and Electronic Science of the Oregon Graduate Center, with Professor L. W. Swanson as principal investigator, and Drs. J. Orloff and A. E. Bell as contributors to various aspects of the program.

The primary thrust of the work was the development and evaluation of high brightness electron and ion sources for use in high density archival memory systems. Work was under the direction of Mr. John Blasingame, Avionics Laboratory, Wright-Patterson Air Force Base, Ohio.

Accession For	
NTIS GCR&I	<input checked="checked" type="checkbox"/>
DDC TAB	<input type="checkbox"/>
Unannounced	
Justification	
By _____	
Distribution/	
Availability Codes	
Dist	Avail and/or special
A	

# TABLE OF CONTENTS

SECTION	PAGE
I. INTRODUCTION	1
II. ELECTRON SOURCE DEVELOPMENT AND CHARACTERIZATION	3
A. Emitter Radius Control	4
B. Binary Emitter Materials	12
1. Rare Earth Hexaborides	12
2. Refractory Metal Carbides	22
C. Built-up Emitters	25
1. Build-up Mechanism	27
2. Specific Processing and Operating Procedures for W(100) Build-up	41
3. Build-up of Other Emitter Materials	42
D. Coated Emitters	50
E. Total Energy Distributions of Field Emitter Electrons at High Current Density For the Zr/W(100) and Built-up W(100) Cathodes	56
1. Method of Approach	58
2. Experimental	63
3. Experimental Results	66
4. Discussion of Results	74
4.1 Low Temperature Results	74
4.2 High Temperature Results	84
4.3 External Beam Interactions	87
F. Noise Study Comparison Between Zr/W(100) and W(100) Built-up TF Cathodes	90
G. Thermal-Field Cathode Life Studies	103
III. FOCUSED ELECTRON BEAM MEASUREMENTS	122
A. Gun and System Configuration	122
B. Gun Performance Data	125
C. Conclusions	128
IV. ION SOURCE DEVELOPMENT AND CHARACTERIZATION	134
A. Gas Phase Field Ionization Source Characterization	134
1. Source Materials and Emission Characteristics	134
2. Field Ionization Emitter Life Study	140



SECTION	PAGE
B. Liquid Gallium Ion Emission	142
1. Introduction	142
2. Mechanism	145
3. Experimental Procedure	149
4. Results and Discussion	151
5. Conclusions	162
V. FOCUSED ION BEAM MEASUREMENTS	163
A. Gun and System Configuration	163
B. Gun Performance Data	172
REFERENCES	179



# LIST OF ILLUSTRATIONS

FIGURE		PAGE
1.	Emitter apex radius of a <100> oriented tungsten emitter as a function of the number of 10 V, 100 msec etching pulses in 2N NaOH following emitter formation.	6
2.	Emitter apex radius of a tungsten emitter as a function of emitter heating time at the indicated temperatures calculated from Eq.(2). Emitter cone half angle $\alpha = 0.1$ rad for these measurements.	8
3.	Tungsten emitter apex radius (based on FN plots) as a function of three minute field evaporation periods at 2500 K at the indicated processing voltages.	10
4.	Field electron patterns of a W(100) emitter after (a) a one minute 2500 K heating period; (b) after a three minute field evaporation at 9 kV and 2500 K; (c) pattern (b) after one minute heating at 2500 K. Indicated are the voltages required to obtain the emission pattern.	11
5.	Pattern sequence for a LaB <sub>6</sub> field emitter thermally processed as follows: (a) 4 hours at 1665 K; (b) 24 hours at 1665; (c) 34 hours at 1665 K; (d) 1 hour at 1890 K; (e) 4 hours at 1890 K; (f) 5 hours at 1890 K.	15
6.	Field emission pattern of LaB <sub>6</sub> typically observed after heating between 1600 and 1700 K.	17
7.	(a) Hydrogen field ion pattern of an LaB <sub>6</sub> emitter after field evaporation in hydrogen at 30 kV; (b) field electron image of (a) at 4 kV; (c) pattern (a) after heating for five minutes at 1300 K; (d) field electron pattern of (c) at 4 kV.	19
8.	Field electron pattern of SmB <sub>6</sub> after heating several minutes at 1800 K; pattern voltage 1050 volts.	21
9.	SEM photo of HfC emitter and mounting structure.	24
10.	FE pattern sequence of a <110> oriented tungsten emitter heated at 1800 K in the presence of a dc voltage.	28

FIGURE	PAGE
11. Various FE patterns of a $\langle 100 \rangle$ oriented tungsten emitter; (a) thermally clean emitter; (b) during heating for several hours at 1630 K; (c) after (310) build-up during heating at 1750 K; (d) after (100) build-up during heating at 1600 K.	30
12. FE pattern sequence of (100) build-up for a clean tungsten emitter at 1745 K. Current/time relationship given in Fig. 15.	34
13. FE pattern sequence of (100) build-up for a slightly oxidized tungsten emitter.	35
14. Current/time characteristics of (100) build-up from a slightly oxidized W(100) emitter at two different temperatures.	37
15. Current/time characteristics of W(100) build-up from a clean emitter.	38
16. Current/time characteristics of W(100) build-up from a slightly oxidized W(100) emitter.	39
17. Current/time characteristics for (100) build-up with (1) and without (2) a load resistor. A slightly oxidized emitter was used and the build-up carried out in high background pressure.	40
18. Room temperature FN plot of an unbuilt and (100) built-up molybdenum emitter.	43
19. FE patterns of unbuilt and built-up iridium and tantalum emitters.	44
20. Room temperature FN plot of a $\langle 100 \rangle$ oriented iridium emitter before and after (110) build-up.	45
21. Room temperature FN plot of a $\langle 111 \rangle$ oriented emitter before and after (111) build-up.	46
22. Plot of the indicated Auger spectrum peak height ratios from a co-adsorbed layer of oxygen and zirconium on a W(100) crystal face.	51
23. SEM photo of a zirconium coating on a W(100) field emitter.	52
24. Plot of the current emitted through a 7.5 mrad half angle aperture vs oxygen pressure using a Zr/W(100) TF emitter at the indicated temperatures.	54



FIGURE	PAGE
25. Pattern pictures through a 86 mrad half angle aperture for a Zr/W(100) TF emitter operating at 1770 K and in an oxygen pressure of $2 \times 10^{-7}$ torr. The time and current levels are indicated.	55
26. Plot of theoretical values of FWHM for the energy distribution of field-emitted electrons as a function of electric field F at various temperatures; work function is 2.5 eV.	61
27. Plot of theoretical values of FWHM for the energy distribution of field-emitted electrons as a function of electric field F at various temperatures; work function is 4.5 eV.	62
28. Diagram of the electrode configuration for the non-cross-over retarding electron energy analyzer. Dimensions in mm.	64
29. Solid lines are the experimental TED curves for a W(100) built-up emitter taken at the indicated electric fields and temperature; dashed lines are the corresponding theoretical curves using $\phi = 4.5$ eV and normalized to the peak heights and Fermi level $E_f$ of the respective experimental curves. Horizontal dashed lines indicate the experimental FWHM values. Crossover analyzer with $\Omega = 0.14$ mSr used for these results.	68
30. Solid lines are the experimental TED curves for a W(100) built-up emitter taken at the indicated electric fields and temperature; dashed lines are the corresponding theoretical curves using $\phi = 4.5$ eV and normalized to the peak heights and Fermi level $E_f$ of the respective experimental curves. Horizontal dashed lines indicate the experimental FWHM values. Crossover analyzer with $\Omega = 0.14$ mSr used for these results.	69
31. Solid lines are the experimental TED curves for a Zr/W(100) emitter taken at the indicated electric fields and temperature; dashed lines are the corresponding theoretical curves using $\phi = 2.5$ eV and normalized to the peak heights and Fermi level $E_f$ of the respective experimental curves. Horizontal dashed lines indicate the experimental FWHM values. Crossover analyzer with $\Omega = 0.14$ mSr used for these results.	70



32. Solid lines are the experimental TED curves for a Zr/W(100) emitter taken at the indicated electric fields and temperature; dashed lines are the corresponding theoretical curves using  $\phi = 2.5$  eV and normalized to the peak heights and Fermi level  $E_f$  of the respective experimental curves. Horizontal dashed lines indicate the experimental FWHM values. Crossover analyzer with  $\Omega = 0.14$  mSr used for these results. 71
33. Solid and dot-dashed lines are the experimental values of transmitted current (upper figure) and FWHM values vs. electric field (lower figure). Results correspond to Fig. 29 and 30 data. Dashed lines (lower figure) are theoretical values of FWHM. 72
34. Solid and dot-dashed lines are the experimental values of transmitted current (upper figure) and FWHM values vs. electric field (lower figure). Results correspond to Fig. 31 and 32 data. Dashed lines (lower figure) are theoretical values of FWHM. 73
35. Experimental values of FWHM vs. beam angular intensity for three W(100) built-up emitters with the indicated values of emitter field factor  $\beta$ . Data obtained from the crossover analyzer with  $\Omega = 0.54$  mSr. 75
36. Experimental values of FWHM vs. beam angular intensity for the W(100) built-up emitter at various values of beam acceptance angle  $\Omega$ . Values for  $\Omega = .97$  mSr are obtained from the non-crossover analyzer; other values of  $\Omega$  are taken from crossover analyzer. Dashed lines are theoretical curves for the 84 and 1685 K data. 76
37. Experimental values of the FWHM vs. beam angular intensity for a W(100) built-up emitter at the indicated temperatures using the non-crossover analyzer. 77
38. Experimental values of FWHM vs. beam angular intensity for the Zr/W(100) emitter at two values of beam acceptance angle  $\Omega$ . Data obtained from crossover analyzer. Dashed lines are theoretical curves for 84 and 1600 K data. 78
39. Experimental values of the FWHM vs. the field factor  $\beta$  for  $\Omega = 0.54$  mSr; upper curve for  $I/\Omega = 1$  mA/Sr and lower curve for  $I/\Omega = 0.5$  mA/Sr. 79

FIGURE	PAGE
40. Curves show the current density $J$ vs. angular intensity for the indicated emitters at $T = 84$ K where $\beta \approx 1.1 \times 10^4 \text{ cm}^{-1}$ for both emitters.	81
41. Experimental values and indicated theoretical curves (dashed lines) of $J(\epsilon)2d/J_0$ vs. current density for the W(100) built-up emitter at $T = 84$ K and the indicated values of $\epsilon$ using the crossover analyzer where $\Omega = 0.14 \text{ mSr}$ .	86
42. Upper curves show the variation of relative noise level of a W(100) built up emitter with temperature at 3 frequency intervals and a 320 Hz band width. The probe current through a 13 mrad aperture was held constant at $I_p = 10 \text{ nA}$ . The lower curve shows the relative variation in voltage with temperature to maintain a constant current.	92
43. Plot of the rms noise level vs emitter temperature using the current through a 13 mrad. aperture from a Zr/W field cathode. Lower curves show the corresponding plots of the transmitted current $I_p/I_t$ and relative voltage $V/V_0$ to maintain $I_p = 10 \text{ nA}$ .	93
44. Curves (a) are obtained from Fig. 43. Curves (b) show the same plot at a background pressure of $3 \times 10^{-8}$ torr.	94
45. Plot of the rms noise level vs beam deflection angle from the emitter axis. A 13 mrad. aperture angle was employed. Lower curve shows plot of the relative voltage for $I_p = 55 \text{ nA}$ , $P = 5 \times 10^{-10}$ torr.	95
46. The variation of the spectral density function $W(f)$ with frequency at two temperatures is given for a built up W(100) emitter.	96
47. Plot of the spectral density function $W(f)$ vs $f$ for a Zr/W field cathode. Measurements obtained from current through a 13 mrad. aperture, $P = 5 \times 10^{-10}$ torr.	97
48. The variation of the spectral density function $W(f)$ with probe current $I_p$ is given for the built up and zirconium coated W(100) emitters at $f = 2000 \text{ Hz}$ and $\Delta f \approx 300 \text{ Hz}$ . The $\beta$ values for these emitters were 2.0 and $1.23 \times 10^4 \text{ cm}^{-1}$ for the built-up and zirconium coated emitters respectively.	99



FIGURE	PAGE
49. The variation of the spectral density function $W(f)$ for the Zr/W(100) with $\beta = 0.1 \times 10^4 \text{ cm}^{-1}$ . Data taken from a focussed beam in an electron gun column.	102
50. Detailed drawing of an electron gun using the Zr/W(100) TFE cathode.	105
51. (a) Total current vs. time data; operating conditions given in Table 7.	108
(b) Percent current fluctuation averaged over 8 hour time intervals for data in (a).	109
52. (a) Total current vs. time data; operating conditions given in Table 7.	110
(b) Percent current fluctuation averaged over 8 hour time intervals for data in (a).	111
53. (a) Total current vs. time data; operating conditions given in Table 7.	112
(b) Percent current fluctuation averaged over 8 hour time intervals for data in (a).	113
54. (a) Total current vs. time data; operating conditions given in Table 7.	114
(b) Percent current fluctuation averaged over 8 hour time intervals for data in (a).	115
55. (a) Total current vs. time data; operating conditions given in Table 7.	116
(b) Percent current fluctuation averaged over 8 hour time intervals for data in (a).	117
56. (a) Total current vs. time data; operating conditions given in Table 7.	118
(b) Percent current fluctuation averaged over 8 hour time intervals for data in (a).	119
57. Total ( $I_t$ ) and transmitted ( $I_p$ ) current at the indicated applied emitter voltage and pressure vs. time using the Fig. 50 gun configuration. At 90 hrs the half angle of the beam aperture was decreased from 86 to 5 mrad.	120



FIGURE	PAGE
58. Diagram of the magnetically focussed TFE gun and detector configuration.	123
59. Total ( $I_T$ ) and beam ( $I_P$ ) current vs voltage characteristics for a high voltage Zr/W(100) TFE emitter in the Fig. 50 gun configuration.	129
60. Total ( $I_T$ ) and beam ( $I_P$ ) current vs emitter temperature characteristics for a high voltage Zr/W(100) TFE emitter in the Fig. 50 gun configuration.	130
61. Total and beam current vs suppressor electrode voltage for the Fig. 50 gun configuration.	131
62. Typical SEM photographs at the indicated magnifications of a mesh with 5 $\mu$ m wide wires (a) and (b) and radiolarian (c) and (d).	132
63. Field ion microscope patterns of a <110> oriented iridium emitter taken at $3 \times 10^{-3}$ torr of hydrogen and 77 K. (a) After field build-up, $V = 20$ kV. (b) After thermal annealing at $\sim 2000$ K, $V = 28$ kV.	136
64. Same emitter as in Fig. 63(b) taken at $1 \times 10^{-6}$ torr argon pressure, 77 K and $V = 20$ kV.	137
65. Hydrogen field ion patterns of a <100> oriented tungsten emitter, $P_{H_2} = 1.3 \times 10^{-3}$ torr. (a) After (100) build-up, $I_{TOTAL} = 1 \times 10^{-9}$ A; (b) after thermal annealing, $I_{TOTAL} = 3.6 \times 10^{-9}$ A.	139
66. Schematic diagram of multiemitter field ionization life test device.	141
67. (a) SEM photographs (backscattered mode) of a tungsten emitter wetted with a thick coating of gallium; (b) A similar photograph of a poorly or nearly exhausted emitter. The light and dark areas correspond to bare tungsten and gallium respectively.	148
68. Typical total and probe current-voltage characteristics for a gallium LMI source.	153
69. Ion patterns of an operational gallium LMI source at various total current levels. The dark region in the central portion of the 20 $\mu$ A photo is due to ion beam damage.	154

FIGURE	PAGE
70. Angular intensity distribution for a gallium LMI source at various values of total current using a probe with the indicated solid angle $\Omega$ . Upper curve gives the FWHM of the lower curves vs total current.	155
71. Values of FWHM for the total energy distribution of a gallium LMI source vs total current at the indicated temperatures. Upper curve shows a typical relationship between source angular intensity and total current.	157
72. Typical energy distribution curves at the indicated total currents and temperature for the gallium LMI source.	158
73. Curves show the variation of the total energy distribution FWHM and corresponding probe current with emitter temperature at the indicated total current for a gallium LMI source.	159
74. Schematic diagram of the SIM optical system, with FI source at the top. Typical values for $f_o$ are 5-9 mm and $R = 5-9$ .	163
75. Scale drawing of the asymmetric, three-element lens. $D = S = t = 3$ mm, $t' = 1$ mm, $D' = 18$ mm. $V_1 = V_{\text{initial}}$ , $V_3 = V_{\text{final}}$ , $V_2$ is the control voltage.	168
76. The properties of the three-element lens in the infinite magnification mode as a function of the control voltage when $V_3/V_1 = 2$ . $F$ is the position of the focal point to the left of the first electrode.	169
77. A comparison of the three-element lens with the two-element Munro lens at low voltage ratios and for $\Delta E = 2$ eV as a function of lens entrance aperture half angle, $\alpha$ . In cases C and D, $V_2/V_1 = 6.5$ and 11, respectively. Field emission voltage $E = 5$ kV.	171
78. Curves show the predicted variation of beam current in the focussed spot for hydrogen gas phase FI and gallium LMI sources. The three-element electrostatic lens, has a beam voltage of 36 kV, a central lens voltage of 55 kV, a magnification of 3.65, $C_s = 68.2$ mm, $C_c = 7.9$ mm and working distance of 25 mm.	173
79. Micrograph of a dc dropoff W field emitter. Diameter at widest point is 130 $\mu$ m. Imaged with hydrogen ions at 15 kV.	175



FIGURE	PAGE
80. Schematic diagram of the FI source used in this experiment.	176
81. A plot of the experimental angular intensity vs. voltage for an iridium (110) oriented hydrogen field ionization source. Curve (a) was a source which had no prior processing; (b) a source that was field evaporated at room temperature; (c) the same as (b) but with further field evaporation. The hydrogen pressure at the emitter was approximately $1 \times 10^{-2}$ torr. Data was taken in an ion beam optical column with the indicated beam aperture solid angle $\Omega$ subtended at the emitter.	177

#### LIST OF TABLES

TABLE		
1	Metalloid Emitter Materials	4
2		31
3	Summary of Emission Parameters Comparing Built Up and Unbuilt up Emission Parameters	49
4	Spherical Retarding Analyzer Electrode Specification Based on Eq.(19)	65
5	Experimental Values of $J(\epsilon)2d/J_0$ for the $T = 84$ K Results are Compared with Predictions of the Two Theoretical Models of TED Broadening	84
6	Summary of Current Fluctuation Results	98
7	Life Test Data Summary; Nominal Pressure During Tests: $\sim 8 \times 10^{-9}$ Torr Voltage Changes Occurred at the Indicated Times	104
8	Magnetic Lens Parameters	126
9	Experimental and Predicted Gun Operating Parameters; Values of $d$ in $\mu\text{m}$	126
10	Iridium Life Test Summary	143

## SUMMARY

The purpose of this research program is the evaluation and characterization of high brightness field emission sources of both ions and electrons suitable for use in information storage systems. In addition, preliminary evaluation of focussing optics suitable for forming submicron beams of both ions and electrons has been performed.

Three classes of field electron (FE) sources have been examined which include (1) a clean tungsten W(100) oriented emitter which has been field built-up so as to confine emission along the (100) crystallographic direction; (2) a W(100) emitter that has an adsorbed zirconium/oxygen (ZrO) layer which specifically lowers the work function of the (100) plane; (3) metalloid emitters which include  $\text{LaB}_6$ ,  $\text{SmB}_6$  and  $\text{HfC}$ . Included in the class of (1) above are iridium (Ir), tantalum (Ta) and molybdenum (Mo) which form field built up end forms that confine emission along the (110), (111) and (100) crystallographic directions respectively.

At present the built-up W(100) and Zr/W(100) emitters operated in the thermal-field (TF) mode appear to be the most promising. Both emitters exhibit long life ( $\sim 1500$  hrs for the built up W(100) and  $\sim 5000$  hrs for the Zr/W(100)) operating at angular intensities  $I'$  of  $10^{-4}$  to  $10^{-3}$   $\text{A sr}^{-1}$  in  $\sim 1 \times 10^{-8}$  torr pressure of residual gas. An anomalous broadening of the energy distribution of these emitters, which occurs for  $I' > 2 \times 10^{-4}$   $\text{A sr}^{-1}$  has been studied in detail. This energy broadening will cause chromatic aberration to be the most dominant aberration for low voltage guns and must be taken into careful consideration when designing a microprobe gun. In general, higher voltage (i.e., larger radii) emitters provided a smaller beam energy spread (i.e., 1 to 2 eV) for an angular intensity of  $\sim 1 \times 10^{-3}$   $\text{A sr}^{-1}$ . A simple in situ method of altering the emitter radius over a wide range of corresponding operating voltages is described.

The built-up Ta and Mo emitters exhibited useful emitting characteristics, but not superior to the built-up W(100) or Zr/W(100) emitters.

Careful noise measurement investigations showed that the Zr/W(100) is superior to the built up W(100) emitter when operated at 1800 K in the angular intensity range 1 to  $10 \times 10^{-4}$   $\text{A sr}^{-1}$ . Over the band width of 1 to 5 kHz the Zr/W(100) emitter exhibited a noise level of  $\sim 0.22\%$ .

A simple double magnetic lens electron gun column was constructed and tested with the Zr/W(100) TF source. By using the electron gun as a scanning electron microscope beam size vs current measurements were made. The results showed that a current density of  $\sim 1000$   $\text{A/cm}^2$  was



achievable at a beam size of 0.1  $\mu\text{m}$ . During these measurements the beam throw from the final lens was 3.14 cm.

Further investigation of the source characteristics of the gas phase field ionization (FI) source was performed using Ir, W and  $\text{LaB}_6$  emitter materials with  $\text{H}_2^+$  and  $\text{He}^+$  as the ion species. A maximum angular intensity of 1  $\mu\text{A}/\text{sr}$  has been achieved at 77 K with the  $\text{H}_2^+/\text{Ir}$  source combination using a differentially pumped source configuration. Life test studies for the  $\text{H}_2/\text{Ir}$  source operating at 300 K and  $1.5 \times 10^{-2}$  torr  $\text{H}_2$  showed steady total current operation in excess of 385 hrs.

A variety of emitter processing procedures including field evaporation, field build up and thermal annealing have been evaluated in order to provide an optimum emission intensity along the emitter axis. Results have shown that a field evaporated Ir(110) emitter provides high angular intensity and maximum stability with respect to field induced chemical erosion of the emitter.

Preliminary studies with an electrostatic focussing ion column have shown that up to 0.5 nA of  $\text{H}_2^+$  and  $\text{H}^+$  current can be focussed into a 0.65  $\mu\text{m}$  beam size while 20 pA of  $\text{Ar}^+$  current can be focussed into 0.2  $\mu\text{m}$  beam size. An improved electrostatic focussing column has been designed which provides the possibility of  $\sim 1 \text{ A}/\text{cm}^2$  target current of  $\text{H}_2^+$  or  $\text{Ar}^+$  in a 0.1  $\mu\text{m}$  beam size.

A detailed study of the emission characteristics of a liquid film gallium (Ga) ion source emission characteristics such as energy distribution, angular intensity distribution, noise current and temperature effects have been measured. The full width half maximum value of the energy distribution at low current ( $I_T \approx 1 \mu\text{A}$ ) and temperature ( $\sim 300 \text{ K}$ ) was 4.5 eV and increased monotonically with current and temperature. Beam angular intensity at  $I_T \approx 1 \mu\text{A}$  was  $\sim 20 \mu\text{A}/\text{sr}$  and increased to  $\sim 40 \mu\text{A}/\text{sr}$  at  $I_T \approx 25 \mu\text{A}$ . As  $I_T$  increased from 1 to 20  $\mu\text{A}$  a large increase in beam angular divergence was observed. An unusually low noise current almost entirely accounted for by shot noise was exhibited by the ion source. These results point toward a strongly space charge limited emission process.

Calculations show that a  $\text{Ga}^+$  current density of  $\sim 40 \text{ A}/\text{cm}^2$  can be obtained in a 0.1  $\mu\text{m}$  beam size using a recently designed electrostatic lens configuration.

## SECTION I

### INTRODUCTION

This report describes progress made during the second year of a research program aimed at the development of high brightness charged particle sources suitable for use in archival information storage systems. In particular the charged particle source and focussing system envisioned for this application must be capable of providing a particle beam with sufficient flux density and smallness of size to address and/or read at less than  $0.1 \mu\text{m}$  resolution and at a rate of  $\sim 10^7$  bits/sec. Because such requirements place a severe limit on the brightness requirements of the particle source, very few sources remain in contention as a viable option for such a memory system.

The primary aim of this research program has been to evaluate high brightness field emission sources with respect to their potential for satisfying the above mentioned requirements for a particle source. In view of the fact that present high density archival memory schemes include both ion and electron beams this research has examined field ionization (FI) as well as field electron (FE) sources. It is now established that FE and FI are the brightest sources presently available for electrons and ions respectively. Although considerable understanding and knowledge concerning the basic processes of FI and FE have been developed since their theoretical formulation some 50 years ago by Oppenheimer<sup>1</sup> and Fowler and Nordheim,<sup>2</sup> and their experimental embodiment pioneered by E. W. Müller,<sup>3</sup> many questions concerning their ultimate suitability as stable and long lived emitters remain.



Specifically this research program has been divided into the three following major tasks:

- (1) Field Electron Source Development and Characterization
- (2) Field Ionization Source Development and Characterization
- (3) Electron and Ion Focussing Systems Evaluation

In each of the first two tasks new source materials and modes of operation have been developed coupled with detailed evaluation of emission characteristic properties. In addition, effort was also devoted to the further development of existing FE sources. Preliminary results of focussed beam studies using both FE and FI sources have been carried out and show promise of meeting the design requirements of high density archival information storage systems. The method of approach and specific measurements carried out are given in greater detail in following sections of this report.

## SECTION II

### ELECTRON SOURCE DEVELOPMENT AND CHARACTERIZATION

The physical properties desirable for an emitter material are

1) high tensile strength to withstand electrostatic stresses, 2) high resistance to sputtering and contamination and 3) high melting point to permit thermal cleaning and survival after transient high temperature episodes. Possible materials possessing these properties can be divided into three categories: 1) pure metals, 2) heterogeneous cathodes consisting of a surface layer on a solid substrate, and 3) homogeneous metalloid compounds or alloys.

Of the pure metal materials investigated in the past which satisfy the above requirements, tungsten operated at room temperature or in the thermal-field (TF) mode has proved to be a most suitable material. TF mode operation has worked successfully with  $\langle 100 \rangle$  oriented tungsten,  $\langle 110 \rangle$  iridium and  $\langle 111 \rangle$  tantalum emitters by allowing electrostatic induced geometric change to reshape the emitter to a particular end form that is stable at elevated temperatures.<sup>4,5</sup> The mobility of the surface atoms at high temperature causes cathode sputtering damage to instantly heal thereby maintaining a smooth and clean surface that exhibits stable emission.

The zirconium coated tungsten cathode, also operated in the TF mode, is an example of a heterogeneous cathode that has proved to be a practical emitter.<sup>4-7</sup> Resupply of the zirconium sputtered from the emitter apex occurs by surface diffusion from a reservoir of zirconium on the emitter shank.



Examples of homogeneous metalloid compounds of interest as emitter materials are given in Table 1 along with their melting temperatures.

TABLE 1

METALLOID EMITTER MATERIALS

Material	Melting Temperature (C)
LaB <sub>6</sub>	2715
SmB <sub>6</sub>	2580
TaC	3825
HfC	3830

Of the materials listed in Table 1 only LaB<sub>6</sub> and HfC evaporate congruently (i.e., the vapor and solid have the same composition). For noncongruently evaporating compounds one cannot control the surface stoichiometry during thermal cleaning or subsequent heating. Thus, we have concentrated our attention on LaB<sub>6</sub> and HfC as advanced emitter materials.

Methods of fabricating the various emitters referred to in this section has been discussed previously<sup>6</sup> except for HfC. In the following sections we provide further results regarding the fabrication and processing of various emitter materials.

A. Emitter Radius Control

As will be discussed in later sections it is becoming evident that large radii emitters have a number of advantages over smaller diameter ones. There are two ways in which emitters have been historically fabricated to form a specified apex radius: (1) during the electrochemical etching procedures used in emitter formation, additional etching can

be used in a reasonably controlled fashion to increase emitter radius;  
 (2) after emitter formation the emitter can be heated in vacuum so as to cause dulling due to surface tension motivated diffusion of atoms away from the emitter apex.

Emitter radius control for tungsten using method (1) above has been moderately successful for (100) oriented tungsten emitters. After initial emitter formation by the ac or dc electrochemical process described earlier,<sup>6</sup> the emitter is immersed in 2N NaOH and given additional material removal which results in uniform dulling of the originally sharp (i.e. emitter radius  $\sim 0.1 \mu\text{m}$ ) emitter apex. Figure 1 shows the emitter radius as a function of the number of dc etching pulses. From this we are able to conclude that emitter radius control between 0.1 to 1.2  $\mu\text{m}$  with  $\pm 10\%$  accuracy can be realized for tungsten using these procedures.

Emitter radius control using thermal dulling is less attractive because of the rapid decrease in dulling rate  $dr/dt$  with radius. The rate of change of emitter radius  $r$  in the presence of an applied field  $F_o$  is given by<sup>8,9</sup>

$$\frac{dr}{dt} = \left(1 - \frac{r F_o^2}{8 \pi \gamma}\right) \left(\frac{dr}{dt}\right)_o \quad (1)$$

where  $\gamma$  is the surface tension and  $(dr/dt)_o$ , the zero field dulling rate, is given by

$$\left(\frac{dr}{dt}\right)_o = \frac{\gamma \Omega_o D_o \alpha 1.25 e^{-E_d/dT}}{A_o k T r^3} \quad (2)$$



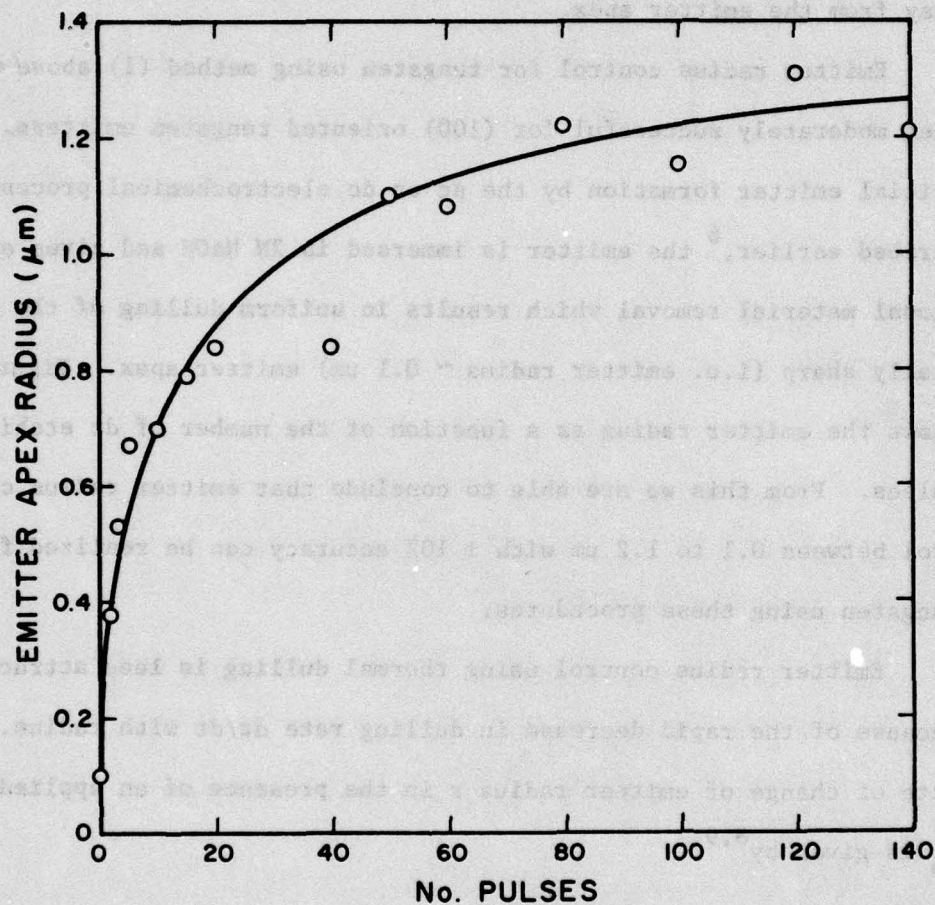


Figure 1. Emitter apex radius of a <100> oriented tungsten emitter as a function of the number of 10 V, 100 msec etching pulses in 2N NaOH following emitter formation.

In the above expression  $\Omega_0$  is the volume per atom,  $A_0$  is the surface area per atom,  $\alpha$  is the emitter cone angle,  $D_0$  is the diffusivity constant and  $E_d$  is the activation energy for surface diffusion. Fig. 2 shows the change in  $r$  with  $t$  based on the integrated form of Eq.(2) and appropriate constants for tungsten. If  $F_0 > (8\pi \gamma/r)^{1/2}$  the dulling is reversed and field build up occurs. It is clear from Fig. 2 that achievement of a 1  $\mu\text{m}$  radius emitter by thermal dulling will require prohibitively long heating times even at 2400 K because of the  $r^{-3}$  dependence.

A third method of "in situ" emitter radius control involves thermal field (TF) processing in vacuum. This procedure consists of the following steps:

- (1) Heat emitter to 2500 K for 3 minutes with a positive processing voltage applied to the emitter
- (2) Anneal the emitter at 2500 K for one minute without processing voltage

During step (1) material transport to the emitter via surface diffusion is motivated by the applied field according to Eq.(1) where initially  $F_0 > (8\pi \gamma/r)^{1/2}$ . At the same time material removal occurs via small protuberances that are formed on the emitter apex from which high ion currents of the emitter material are drawn via field evaporation.

During step (2) the small protuberances are removed via surface diffusion resulting in a smooth emitter surface with an overall larger radius. The radius of the emitter after steps (1) and (2) is determined by the processing voltage used during step one as shown in



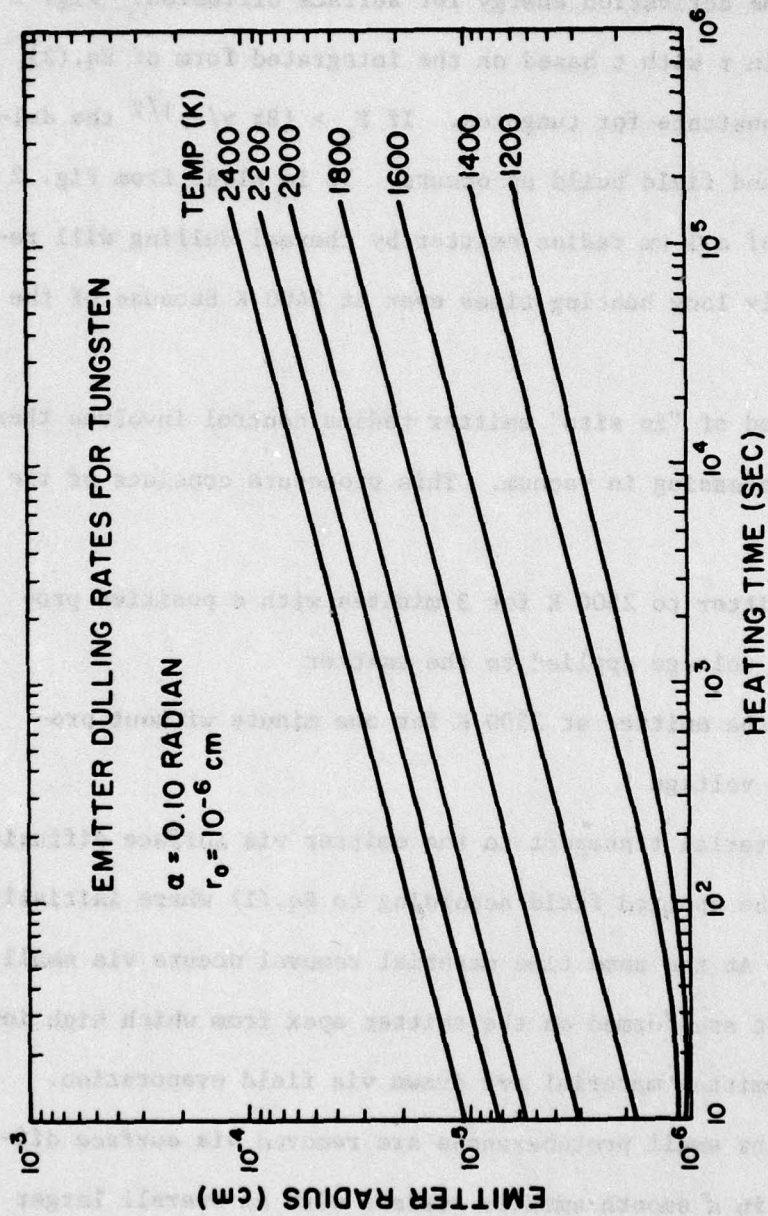


Figure 2. Emitter apex radius of a tungsten emitter as a function of emitter heating time at the indicated temperatures calculated from Eq.(2). Emitter cone half angle  $\alpha = 0.1$  rad for these measurements.

Fig. 3 for a run carried out on a  $\langle 100 \rangle$  oriented tungsten emitter. It can be observed that increasing the value of the field evaporating voltage leads to an increasing emitter radius such that a processing voltage of  $\sim 12$  kV leads to a  $1 \mu\text{m}$  radius emitter apex. In this study the emitter radii were determined from a Fowler-Nordheim (FN) plot of the room temperature  $I(V)$  data (i.e.  $\ln I/V^2$  vs  $1/V$ ). The slope  $m$  of the FN plot is related to  $\beta = F/V$  according to

$$\beta = 2.81 \times 10^7 \phi^{3/2}/m \text{ (cm}^{-1}\text{)} \quad (3)$$

where  $\phi$  is the average emitter work function in units of eV. A relationship between  $\beta = f(r, \alpha, R)$  can be obtained from a sphere-on-orthogonal cone model of the emitter described in reference 6. The parameters  $\alpha$  and  $R$  are the emitter cone half angle and emitter-to-anode spacing respectively. The emitter radii so obtained were found to agree within  $\sim \pm 15\%$  of the actual radii obtained by high resolution microscopy.

A typical sequence of emission patterns and the emitter operating voltages after steps (1) and (2) of the TF processing are shown in Fig. 4. Photo (a) of Fig. 4 shows the field electron pattern of a W(100) oriented emitter after heating at 2500 K for one minute in vacuum. Photo (b) shows the small protuberances which appear at a low emitter voltage after step (1) TF processing at 9 kV. Photo (c) shows the high voltage emitter pattern after the protuberances have been removed by step (2) above.

Thus, we have shown that by electrochemical etching procedures during emitter fabrication or by TF processing after the emitter is



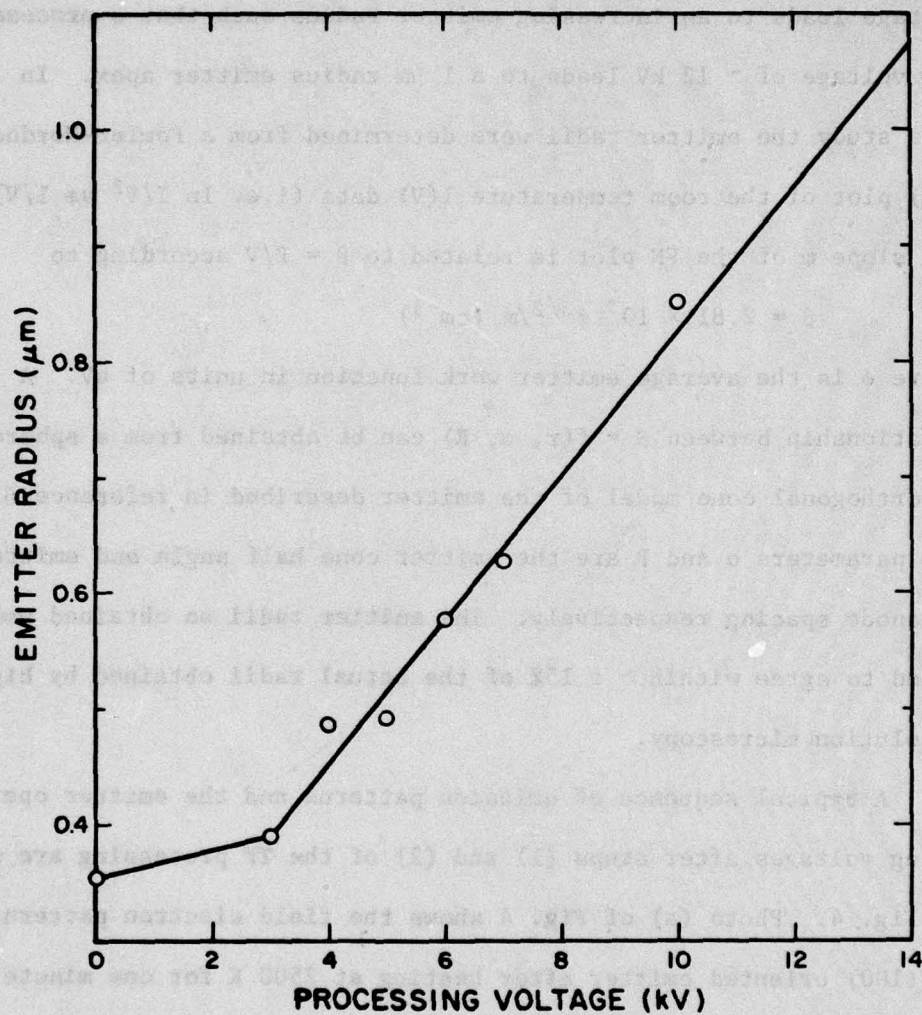
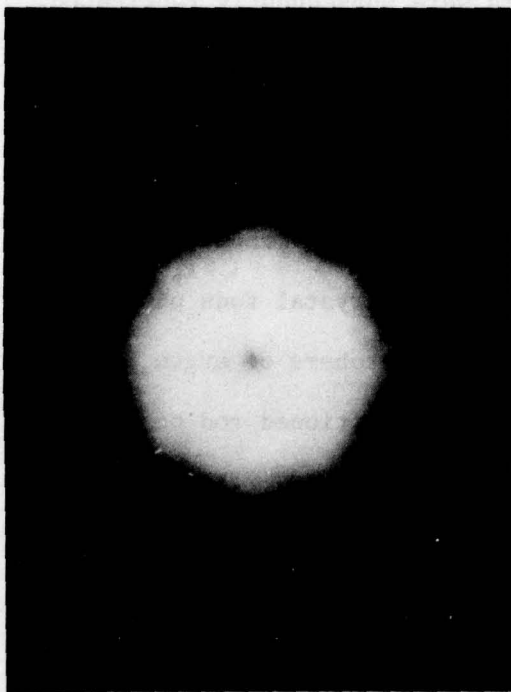


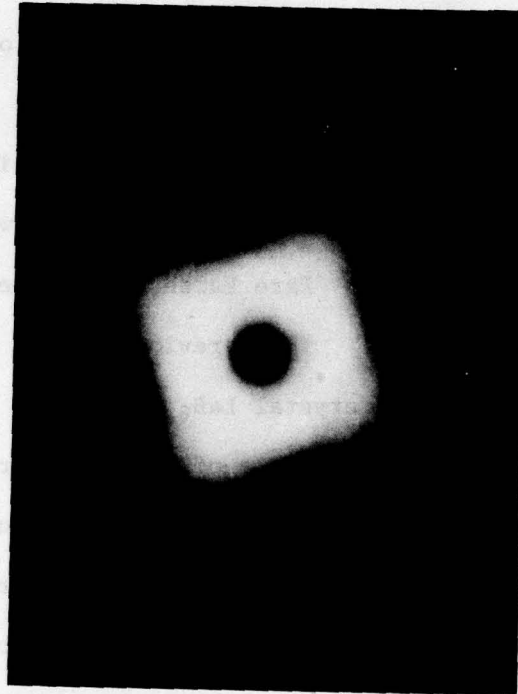
Figure 3. Tungsten emitter apex radius (based on FN plots) as a function of three minute field evaporation periods at 2500 K at the indicated processing voltages.



(a)  
V = 4 kV



(b)  
V = 2.5 kV



(c)  
V = 8 kV  
Figure 4

Figure 4.

Field electron patterns of a W(100) emitter after (a) a one minute 2500 K heating period; (b) after a three minute field evaporation at 9kV and 2500 K; (c) pattern (b) after one minute heating at 2500 K. Indicated are the voltages required to obtain the emission pattern.



in a high vacuum environment a specific emitter radius between 0.1 and 1  $\mu\text{m}$  can be obtained. Presumably these procedures with appropriate modification can be applied to other materials.

#### B. Binary Emitter Materials

Two classes of binary compounds which have been investigated as potentially promising new emitter materials include refractory metal carbides and rare earth hexaborides. The former are of interest because of their very high melting points (see Table 1) while the latter have been known to exhibit low work functions and unusual resistance to sputtering. Before emitters can be fabricated and investigated from such compounds a number of materials related problems must be solved. In the following sections a few of these problems are given consideration along with preliminary emission studies.

##### 1. Rare Earth Hexaborides

In a previous report procedures were described for producing single crystal  $\text{LaB}_6$  from which emitters were subsequently fabricated.<sup>6</sup> Further studies of materials preparation procedures have shown that a zone refining process allows one to produce  $\sim 1$  mm diameter single crystal rods from which emitters can be fabricated.

The zone melting procedure described by Verhoeven, et al.,<sup>10</sup> has been successfully employed to make single crystal rods of  $\text{LaB}_6$ . In this procedure an arc is struck in one atmosphere of argon between a pointed tantalum electrode and a vertical positioned rod of high density, polycrystalline  $\text{LaB}_6$  ( $\sim 1$  mm separation). Sufficient power is provided to the arc so that a molten zone is formed which is moved

vertically along the  $\text{LaB}_6$  rod by moving the pointed tantalum electrode. Three passes of the molten zone not only forms a homogeneous single crystal, but also significantly lowers the impurity level to below 100 ppm.

The degree of success of the zone melting procedure for fabricating single crystal  $\text{LaB}_6$  rods was found to be directly related to the reduction of volatile impurities in the original material. If a high concentration of volatile impurities were contained in the initial  $\text{LaB}_6$  material it was heated in vacuum slightly below the melting point for several minutes.

Thus, we now have two methods of fabricating  $\text{LaB}_6$  crystals: (1) the zone melting method and (2) the molten aluminum solvent method described earlier.<sup>6</sup> At this juncture we favor the zone melting method because of the ability to reduce the impurity level and the ability to orient a specified crystallographic direction along the wire axis by fusing the polycrystalline rod to an appropriately oriented seed crystal. Both fabrication methods suffer from an inability to accurately control the B/La stoichiometry, although the importance of the latter on emitter performance has yet to be established.

Preliminary emission characteristics reported earlier for  $\text{LaB}_6$  were promising as coherent emission patterns were obtained by thermal heating.<sup>6</sup> Unfortunately we, along with others<sup>11</sup> have noted a great difficulty in obtaining a predictable and reproducible emission pattern by thermal processing.

Three  $\text{LaB}_6$  cathodes have recently been investigated in a



field electron microscope. The first, referred to as LaB<sub>6</sub>-1 was made from a single crystal grown by precipitation from the molten Al solvent. The second cathode, designated LaB<sub>6</sub>-2, and formed from a zone melted crystal obtained from Iowa State University, was operated over a period of about six weeks before the supporting filament was accidentally melted. The third cathode LaB<sub>6</sub>-3 was made from a zone melted crystal grown at the Oregon Graduate Center.

Early in the thermal treatment of LaB<sub>6</sub>-1, the tip was inadvertently subjected to a high over voltage in the field electron emission mode which presumably led to a vacuum arc. In any case, when the emission pattern was next viewed the central portion was completely dark and the viewing voltage had increased from approximately 700 volts to around 4000 volts. Emission from the central portion of the pattern was restored after heating the cathode at a temperature between 1600-1700 K. Following 34 hours heating at this temperature, the viewing voltage was reduced to about 1700 volts.

Photographs depicting the evolution of the emission patterns following the arc, are shown in Fig. 5. These emission patterns were observed after heating for the times and at the temperatures indicated. Although a well defined, symmetric pattern, such as is characteristic of metals, was never observed, there is a definite indication of the four-fold symmetry expected for a LaB<sub>6</sub> tip oriented along the (100) axis. This symmetry persisted with continued heating at 1650 K.

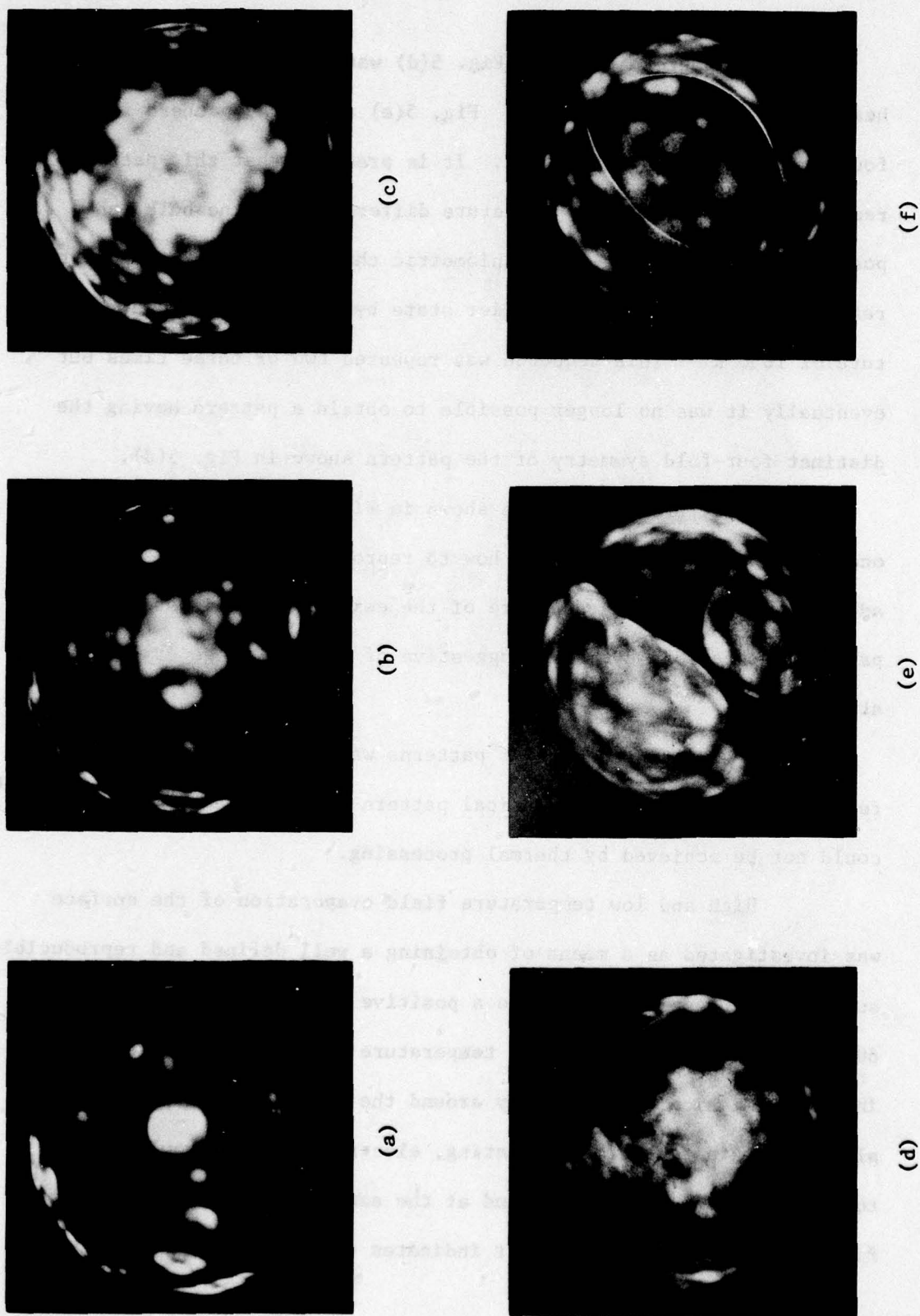


Figure 5. Pattern sequence for a  $\text{LaB}_6$  field emitter thermally processed as follows: (a) 4 hours at 1665 K; (b) 24 hours at 1665 K; (c) 34 hours at 1665 K; (d) 1 hour at 1890 K; (e) 4 hours at 1890 K; (f) 5 hours at 1890 K.



The pattern shown in Fig. 5(d) was found to be unstable when heating to higher temperatures. Fig. 5(e) shows the pattern following four hours of heating at 1900 K. It is presumed that this pattern represents a surface having a structure different from the bulk  $\text{LaB}_6$ , possibly as a result of a stoichiometric change. It was possible to restore the pattern to its earlier state by heating at a lower temperature of 1650 K. This sequence was repeated two or three times but eventually it was no longer possible to obtain a pattern having the distinct four-fold symmetry of the pattern shown in Fig. 5(d).

A pattern of the type shown in Fig. 6 was observed on several occasions but we never learned how to reproduce it at will. In addition to the localized nature of the emission in this state, the pattern indicated a symmetry suggestive of a short range crystalline state.

A similar sequence of patterns was observed for  $\text{LaB}_6$ -2, and for  $\text{LaB}_6$ -3 samples. A symmetrical pattern of the type reported earlier<sup>6</sup> could not be achieved by thermal processing.

High and low temperature field evaporation of the surface was investigated as a means of obtaining a well defined and reproducible surface. Subjecting the tip to a positive potential of approximately 6000 volts for one minute at a temperature of 1400 K led to a pattern in which emission occurred only around the edges of an otherwise completely dark pattern. Upon heating, electron emission would return to the center of the pattern and at the same emitter voltage as before field evaporation. This result indicates that no significant increase



**Figure 6. Field emission pattern of LaB<sub>6</sub> typically observed after heating between 1600 and 1700 K.**

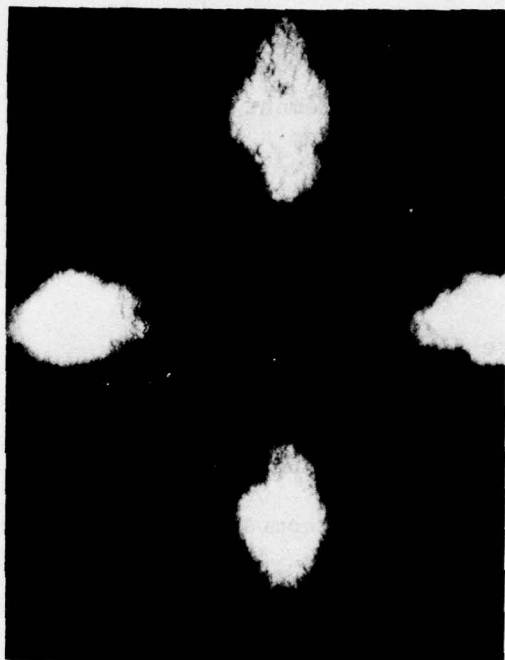


in emitter radius had occurred and that the changes in the electron emission pattern were due to the field evaporation of only the surface layer or a few layers of material. It is presumed that field evaporation leads to a depletion of lanthanum on the surface since other studies show an increase in work function as the B/La ratio increases.

A brief study of the electron emission pattern obtained by low temperature field evaporation in hydrogen and helium using both field ion and field electron microscopy was carried out. A  $\text{LaB}_6(100)$  oriented emitter fabricated from a needle crystal obtained from the molten aluminum method was used. In Fig. 7 photo (a) a hydrogen field ion image of the surface after field evaporation in a hydrogen pressure of  $1 \times 10^{-4}$  torr is shown. An electron emission pattern of the same emitter in high vacuum is shown in photo (b). The bright (or highly emitting) regions in photo (b) are due to the  $[110]$  directions. This result was very reproducible and shows that a coherent pattern with emission from the  $[110]$  directions can be obtained from  $\text{LaB}_6$  by field evaporation in hydrogen. A similar electron pattern was obtained with helium as the imaging gas. Field evaporation in hydrogen occurred rapidly at a voltage of 1.5 times the best image voltage (BIV). In helium the BIV occurred at  $\sim 2$  times the hydrogen BIV and field evaporation in helium required  $\sim 10\%$  increase in voltage. We thus conclude that hydrogen promotes the field evaporation probably by forming  $\text{LaH}^+$  or  $\text{BH}^+$  which are field evaporated.



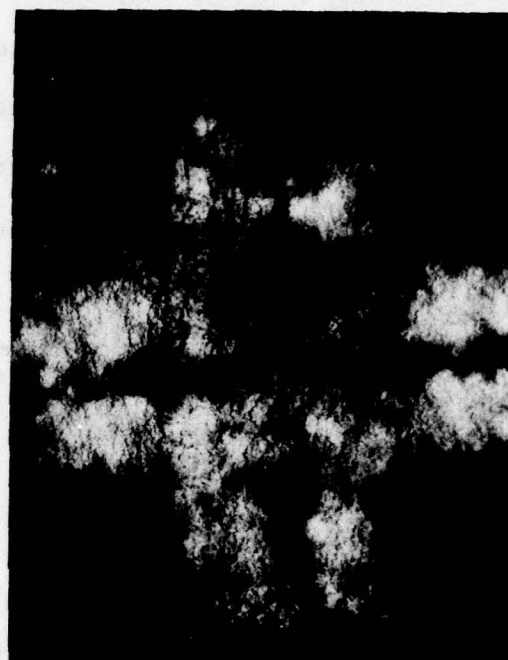
(a)  $V = 19 \text{ kV}$



(b)  $V = 4 \text{ kV}$



(c)  $V = 22 \text{ kV}$



(d)  $V = 4 \text{ kV}$

Figure 7. (a) Hydrogen field ion pattern of an  $\text{LaB}_6$  emitter after field evaporation in hydrogen at 30 kV; (b) field electron image of (a) at 4 kV; (c) pattern (a) after heating for five minutes at 1300 K; (d) field electron pattern of (c) at 4 kV.  $P_{\text{H}_2} = 1 \times 10^{-4} \text{ torr}$ .



The low temperature field evaporation electron emission patterns when compared with the previously reported<sup>6</sup> coherent thermally annealed patterns show that the (110) plane work function is reduced by the former process. A comparison of the hydrogen ion pattern of Fig. 7(a), which reflects the field enhancement distribution, with the corresponding electron pattern in Fig. 7(b), which reflects the work function  $\phi$  distribution, clearly shows that  $\phi_{110} < \phi_{100}$ .

On annealing the low temperature field evaporated surface at  $\sim 1300$  K a dramatic change occurs in both the ion and electron pattern distribution (see Fig. 7(c) and 7(d)). Electron emission patterns show that the (110) planes have become dark compared to the central (100) plane and  $\phi_{110} > \phi_{100}$ . Higher temperature annealing ultimately leads to the incoherent patterns described in Fig. 5.

A brief study of electrode emission patterns from an  $\text{SmB}_6$  emitter obtained from a crystal grown by the molten aluminum method<sup>6</sup> was carried out. The emitter point was formed by electrochemical etching using the identical procedures employed for  $\text{LaB}_6$  emitter fabrication. Thermally annealed emitter patterns which have been investigated at this juncture, show exactly the same incoherent pattern distribution as observed for the  $\text{LaB}_6$  emitter. A typical  $\text{SmB}_6$  field electron pattern obtained after heating at 1800 K is shown in Fig. 8. The  $\text{SmB}_6$  emitter, like the  $\text{LaB}_6$ , proved to be extremely resistant to dulling but only on occasion was a coherent pattern obtained.



V = 1050 volts

**Figure 8. Field electron pattern of  $\text{SmB}_6$  after heating several minutes at 1800 K; pattern voltage 1050 volts.**



In conclusion we note that both  $\text{LaB}_6$ ,  $\text{SmB}_6$  and presumably other rare earth hexaborides, such as  $\text{CeB}_6$ , undergo geometric reconstruction of the surface at elevated temperatures so as to cause the field electron emission distribution to have little correlation with the underlying bulk crystallographic symmetry. On the other hand, low temperature ( $\sim 77$  K) field evaporation in a low pressure ( $\sim 10^{-5}$  torr) of hydrogen provides a reproducible and symmetric electron emission distribution in which the (110) planes exhibit the lowest work function. These results were independent of the various single crystal growth methods used and seem to be intrinsic with this class of materials. Thus, a  $\langle 110 \rangle$  oriented  $\text{RB}_6$  emitter processed by field evaporation in hydrogen with subsequent heating not exceeding  $\sim 1300$  K can be used to provide a high emission current along the emitter axis.

## 2. Refractory Metal Carbides

Two refractory metal carbides have been considered as potentially interesting emitter materials because of their high melting point. A high melting emitter material leads to an increased resistance to failure due to melting of the emitter by emission heating during a transient voltage pulse.

Earlier,<sup>6</sup> a TaC emitter was fabricated according to a procedure outlined by Eckstein and Forman<sup>12</sup> whereby a tantalum emitter was carburized by heating in  $5 \times 10^{-3}$  torr of benzonitrile. Because of little success in obtaining reproducible electron emission patterns from this fabrication procedure, we attempted an arc-zone melting procedure in argon similar to that carried out for  $\text{LaB}_6$ .

Unfortunately when  $T > 2500$  K the reaction  $TaC \rightarrow Ta_2C + C$  takes place with subsequent evaporation of carbon. This leads to an inability to control stoichiometry of the surface.

It was decided to investigate HfC since it evaporates congruently at its melting point (like  $LaB_6$ ) and thus would be amenable to single crystal fabrication via the arc-zone melting method in one atmosphere argon pressure. Such a procedure was carried out using a high density 1 mm diameter rod of HfC obtained from CERAC Inc., Milwaukee, Wisconsin. From a small section of the 1 mm diameter rod an emitter was fabricated electrochemically using a solution of 3 parts nitric and 1 part hydrochloric acid and 6 to 10 VAC.

Figure 9 shows an SEM photo of the HfC emitter and mount. From the faceted nature of the emitter we conclude that the emitter is not single crystal, but contains several large crystal grains. The mounting was accomplished by brazing the emitter in a rhenium sleeve using a  $Ta_2Co/TaC$  brazing compound. The rhenium sleeve was spot welded to 0.20 mm diameter rhenium support leads which were used to resistively heat the emitter. Unfortunately the emitter support leads melted before emission photographs could be obtained. However, preliminary results were encouraging showing that  $\sim 1$  mA of dc emitted current could be obtained. The emission patterns showed that the (111) plane was dark (i.e. high work function) and the (113) crystallographic regions exhibited high emission density.

These preliminary results show that single crystals of HfC can be fabricated by arc-zone melting techniques and formed into field





1000  $\mu\text{m}$

**Figure 9. SEM photo of HfC emitter and mounting structure.**

emitter structures. Preliminary emission results show that coherent emission patterns can be obtained by thermal cleaning of the HfC emitter and that relatively large dc currents are obtainable.

### C. Built-up Emitters

Upon heating a field cathode above 1000 K while drawing a field emission current, surface tension forces, which tend to cause local surface smoothing and overall dulling of a sharp emitter, are counter-balanced by field stress forces as described in Sec. IIA. The latter forces do not work against the tendency to smooth microscopic roughness caused by ion bombardment; however, they do overcome and reverse the macroscopic dulling forces and cause faceting of certain crystal faces exposed at the hemispherical, single crystal emitter tip. This process is called "field build up."<sup>13</sup>

It has been known for some time that two important corrective processes occur during TF operation. First, the adsorption of residual gases on the emitter surface which cause undesirable current reduction and flicker noise can be eliminated. This is due to the rapid thermal desorption of adsorbed gas layers so that the equilibrium coverage is negligible. These effects combine to provide complete current stability with respect to gas adsorption at high ambient pressures. The second corrective measure in TF emission has to do with smoothing of microscopic surface roughness caused by positive ion bombardment. Surface roughness due to ion bombardment not only leads to current increase and instability, but does so in a regenerative fashion leading to rapid emitter destruction. The rate of formation of surface roughness



increases with ambient pressure and current. It is also influenced by the fraction of the total current intercepted by the anode structure through electron induced desorption of gas layers from the anode surface. Thus, angular confinement of the electron beam at the source is highly desirable since it increases transmission for a given angular aperture. By operating a tungsten field cathode at an elevated temperature (e.g., ~ 1000 to 1800 K) these microroughness sites caused by ion bombardment are immediately smoothed.

Now let us examine the main difficulties in reducing a TF cathode to a practical device. Upon applying a high electrical field to a heated field cathode, geometric modification due to field build up occurs. If the field stress exceeds a critical value these geometric changes continue to occur with time thereby leading to a generally unstable current. Moreover, because of geometric alterations the emission distribution can be markedly changed. This can be a serious deterrent to applications where a small solid angle of emission is being utilized from one of the more brightly emitting portions of the emitter. Because field build up can lead to several different end forms each with different emission distribution configurations,<sup>4,13</sup> TF cathodes have only recently been considered practical. It has generally been assumed that no field built up end form could be expected to reach a state of equilibrium with respect to further geometric alteration.

With these factors in mind we have examined several emitters which, after undergoing field build up, operate with varying degrees of

stability in a TF mode. We will examine in detail the results with a W(100) oriented emitter since the general mechanism is similar for other emitters.

### 1. Build-up Mechanism

According to Eqs.(1) and (2) the condition that the applied electrostatic field stress just balance the thermodynamic dulling force (a condition not attainable for the total emitter surface) is given by the following:

$$F_o = \left( \frac{8 \pi \gamma}{r} \right)^{1/2} \quad (4)$$

For tungsten  $\gamma = 2900$  dyne/cm, thus,

$$F_o = 8.1 \times 10^4 r^{-1/2} \text{ (V/cm)} \quad (5)$$

For a typical emitter radius value of  $1600 \text{ \AA}$ , the value of  $F_o$  is  $2 \times 10^7 \text{ V/cm}$ ; however, for a clean tungsten emitter ( $\phi = 4.52 \text{ eV}$ ) the useful range of current densities ( $J = 10^4$  to  $10^8 \text{ A/cm}^2$ ) corresponds to apex fields  $F_o = 4$  to  $8 \times 10^7 \text{ V/cm}$ . Thus, according to Eq. (5) TF cathodes with  $r > 800 \text{ \AA}$  would be inherently unstable with respect to field build up.

The basic mechanism which controls the mode of field build up is the relative surface free energy of the various exposed crystal faces on the hemispherical emitter. The low index planes of the tungsten bcc crystal structure possess the lowest surface free energy and, thus, form facets that grow at the expense of neighboring high index planes. Faceting occurs through self surface migration and requires temperatures in excess of  $\sim 1300 \text{ K}$ . Figure 10 shows a typical sequence of



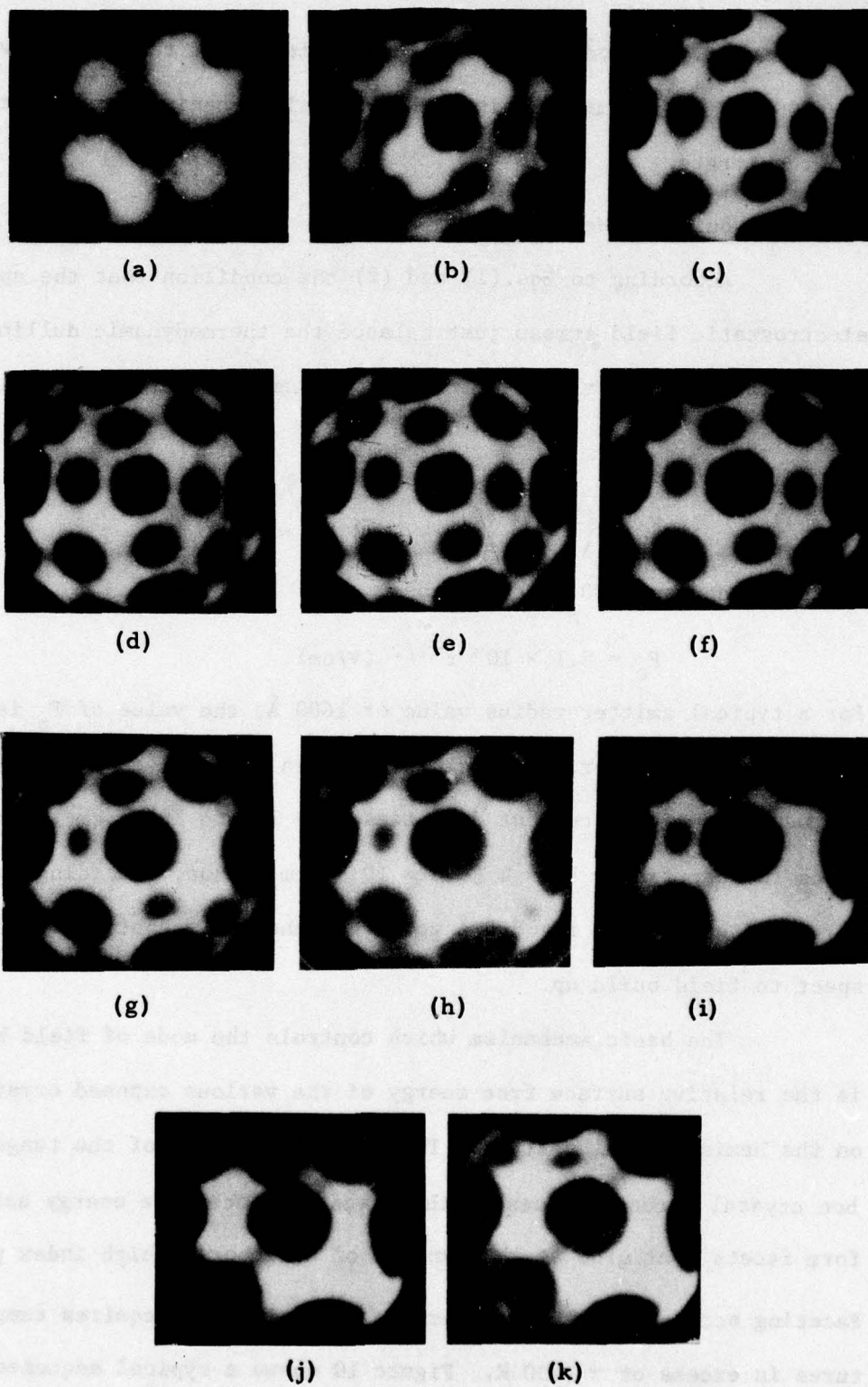


Figure 10. FE pattern sequence of a  $\langle 110 \rangle$  oriented tungsten emitter heated at 1800 K in the presence of a dc voltage.

patterns observed during field build up of a  $\langle 110 \rangle$  oriented tungsten emitter in which the central (110) plane, the surrounding (112) and (100) planes form larger facets. The final end form, however, is one in which the (112) planes ultimately become ridges (or protrusions) due to the expanding (110) plane facets. This end form is known as (112) build up. Two other end forms of field build up have been observed and are shown in Fig. 11. Faceting of the (110), (112) and (100) planes lead to (310) build up (pattern c), while faceting of the (110) and (112) planes lead to (100) build up (pattern d). It is this later built-up end form which leads to a stable TF emission mode and is of central interest for tungsten and molybdenum emitters.

By use of a  $\langle 100 \rangle$  oriented field cathode one may dramatically confine the emission to a small solid angle about the emitter axis provided that (100) build up can be obtained. Until recently it has not been possible to predictably obtain a particular built up end form.<sup>4,13</sup>

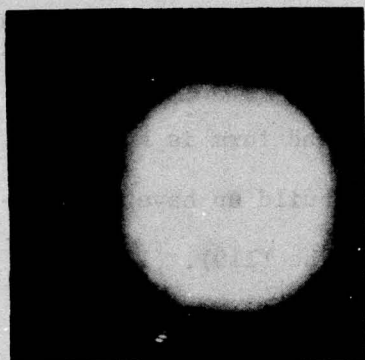
It is instructive to derive an expression relating the maximum current  $I_m$  and emitter radius  $r$  for the balance condition given by Eq.(4). The Fowler-Nordheim equation is given by

$$J = \frac{1.54 \times 10^{-6} F^2}{\phi t(y)} \exp [-6.83 \times 10^7 \phi^{3/2} v(y)/F] \text{ (A/cm}^2\text{)} \quad (6)$$

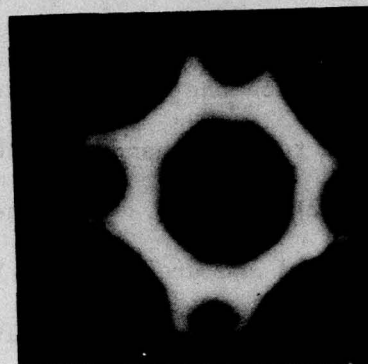
where  $J$  and  $\phi$  are the current density and work function (in eV) respectively. The applied field  $F$  is in volts/cm. Noting that the image potential correction terms  $t(y) \approx 1$  and  $v(y) \approx 0.943 -$

$1.525 \times 10^{-7} F/\phi^2$  in the  $F$  and  $\phi$  range of interest, Eq.(6) becomes

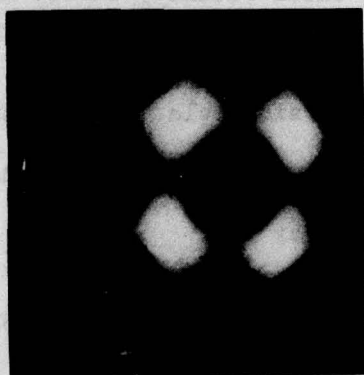




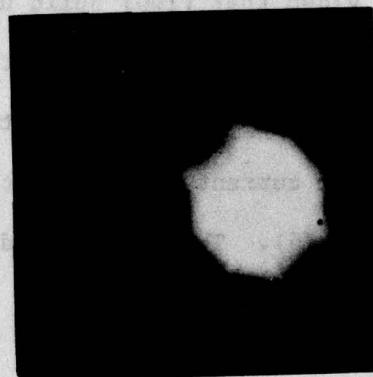
(a) Clean W  $I = 3.6 \mu\text{A}$



(b) Carbon/W;  $T = 1630 \text{ K}$   
 $I = 36 \mu\text{A}$



(c) (310) Build up;  
 $T = 1750 \text{ K}$   
 $I = 78 \mu\text{A}$



(d) (100) Build up  
 $T = 1600 \text{ K}$   
 $I = 21 \mu\text{A}$

Figure 11. Various FE patterns of a  $\langle 100 \rangle$  oriented tungsten emitter; (a) thermally clean emitter; (b) during heating for several hours at  $1630 \text{ K}$ ; (c) after (310) build-up during heating at  $1750 \text{ K}$ ; (d) after (100) build-up during heating at  $1600 \text{ K}$ .

$$J = \frac{1.54 \times 10^{-6} F^2}{\phi} 10^{4.53/\phi^{1/2}} 10^{-2.8 \times 10^7 \phi^{3/2}/F} \text{ (A/cm}^2\text{)} \quad (7)$$

Combining Eqs.(5) and (7) and letting the emitting area be  $\pi r^2$  we obtain the relation between I and r:

$$I = \frac{3.16 \times 10^4 r}{\phi} 10^{4.53/\phi^{1/2}} 10^{-3.45 \times 10^2 \phi^{3/2} r^{1/2}} \text{ (A)} \quad (8)$$

Eq.(8) gives the maximum current available when the balance condition in Eq.(4) is maintained. It is easily shown that Eq.(8) has a maximum at

$$r_m = 3.36 \times 10^{-5}/\phi^3 \text{ (cm)} \quad (9)$$

thus, for  $\phi = 4.5 \text{ eV}$ ,  $r_m = 37 \text{ \AA}$ . Table 2 gives values of J, r, and I obtained from Eqs.(7) and (8).

TABLE 2

EMISSION CHARACTERISTICS AT THE CONDITION OF BALANCE BETWEEN  
ELECTROSTATIC AND SURFACE TENSION FORCES

$\phi$ (eV)	$F(\times 10^7 \text{ V/cm})$	$J(\text{A/cm}^2)$	$r(\text{\AA})$	$I(\text{A})$
4.50	4.0	$6.8 \times 10^4$	410	$3.6 \times 10^{-7}$
4.50	5.0	$2.0 \times 10^6$	266	$4.4 \times 10^{-6}$
4.50	6.0	$2.6 \times 10^7$	182	$2.7 \times 10^{-5}$
4.50	13.3	$8.3 \times 10^9$	37	$3.6 \times 10^{-3}$

It is only through the pyramidal structure formed on the (100) plane by the expanding (110) and (112) facets that such small radii and large current densities as given in Table 2 can be realized.

Current density values for the W(100) built up cathode in the  $10^8$  to  $10^9 \text{ A/cm}^2$  range have been measured while operating in a stable mode.<sup>14</sup> The basic limit to the current drawn from the emitter is resistive heating of the conical shaped emitter shank. Using the model



of a truncated cone whose radius at the point of truncation is  $r$  and interior cone half angle is  $\alpha$ , one obtains the following solution for the temperature difference  $\Delta T$  between the cone base and point of truncation:<sup>15</sup>

$$\Delta T = \frac{\rho}{2K\pi^2} \left( \frac{I}{\alpha r} \right)^2 \quad (10)$$

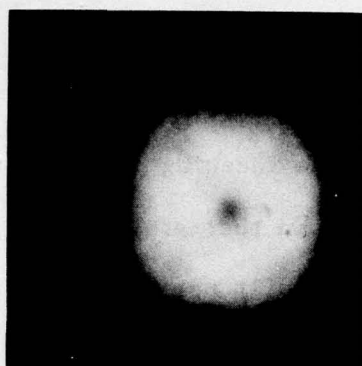
where  $\rho$  and  $K$  are the resistivity and thermal conductivity of the emitter. This equation suggests that as  $r$  decreases at a constant  $I$  both the current density  $J = I/\pi r^2$  and emitter temperature  $\Delta T$  increase. In the truncated cone model the decrease in  $r$  is obtained by increasing the length of the truncated cone at constant  $\alpha$ . In contrast, the built up W(100) emitter increases  $J$  at a constant  $I$  not by decreasing  $r$  on a macroscopic scale, but rather by confining the emitting area on a microscopic scale through a local geometric change in both  $r$  and  $\alpha$  so that  $(I/\alpha r)$  remains roughly unchanged. In other words, the gross dimensions of the emitter which control the heat flow and, hence,  $\Delta T$  are not altered by the act of build up. From FN plots it has been determined that the emitting area of a built up W(100) emitter is reduced by a factor of  $\sim 0.005$ ; if we assume that the above analysis is correct, then  $J_{\max}$  for the built up emitter is increased by a factor of 200 or  $J_{\max} \approx 10^8$  to  $10^9$  A/cm<sup>2</sup> for W(100) built up.

The basic mechanism which controls the mode of field build up is the relative surface free energy of the various exposed crystal faces on the hemispherical emitter.<sup>16</sup> The surface free energy of the various crystal planes is affected by the presence of adsorbed layers. Figures

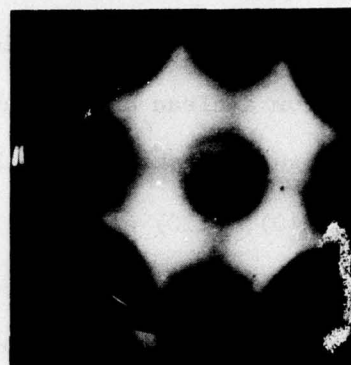
12 and 13 show the emission pattern sequence during (100) build up from a clean and slightly oxidized tungsten surface respectively. Figure 12 shows that the initial stage involves the faceting of the (110), (112) and (100) planes. Experience has shown that a slight amount of carbon will cause the undesirable (310) built up end form shown in pattern (c) of Fig. 11. A truly clean tungsten surface may revert to a (112) built up end form shown in the Fig. 10 sequence. In contrast, Fig. 13 shows that starting with an oxide surface inhibits the central (100) plane from faceting at any stage and promotes faceting of the (112) and (310) planes. In all cases starting with a slightly oxidized surface leads to (100) build up. Clearly, the oxide layer increases the surface free energy of the (100) plane. The final built up end form appears to consist of a pyramid with four (110) sides intersecting near the apex with a small radius of curvature that confines the emission solid angle and reduces the voltage required to draw a specific current by approximately 50%.

Another important role played by the oxide layer is that of removing carbon impurities by forming the stable molecule carbon monoxide which desorbs from the surface at 1400 K. The undesirable role of carbon is illustrated in Fig. 11 pattern (b) which shows a large facet on the (100) plane. Apparently carbon lowers the surface free energy of the (100) plane. Such a surface is resistant to any form of build up unless it is treated with a partial pressure of oxygen at 1400 K to remove carbon as carbon monoxide.

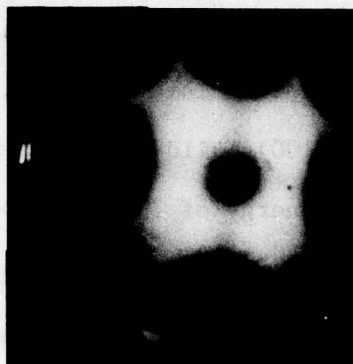




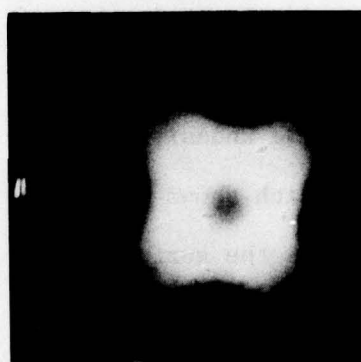
t = 0 sec



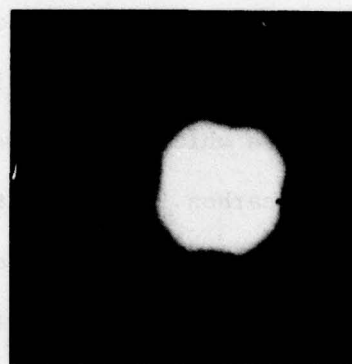
t = 110 sec



t = 2100 sec

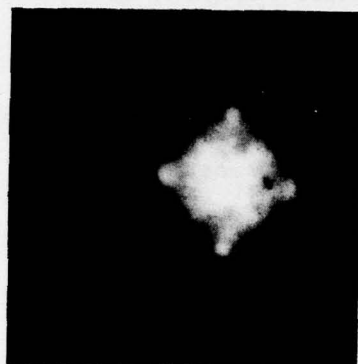


t = 2170 sec

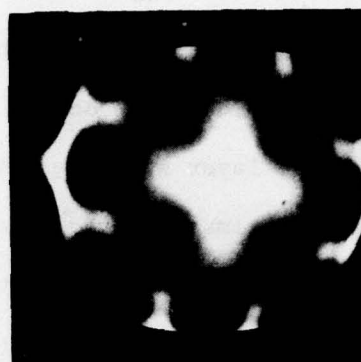


t = 2200 sec

Figure 12. FE pattern sequence of (100) build-up for a clean tungsten emitter at 1745 K. Current/time relationship given in Figure 15.



$t = 0 \text{ sec}$



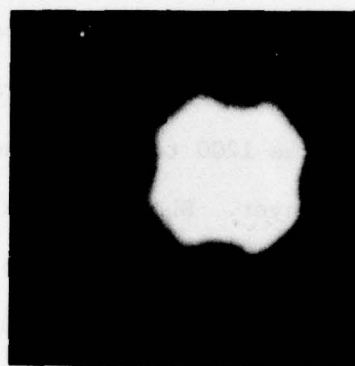
$t = 30 \text{ sec}$



$t = 510 \text{ sec}$



$t = 1015 \text{ sec}$



$t = 1340 \text{ sec}$

Figure 13. FE pattern sequence of (100) build-up for a slightly oxidized tungsten emitter.



Figures 14 and 15 illustrate the dramatic change in the time/temperature relationship for build up caused by oxygen. As observed, (100) build up occurs with a large increase in current. With the oxide layer starting point Fig. 14 shows that at the same temperature the time required to attain (100) build up is reduced by a factor of 27. Figure 16 shows the temperature dependence of the current time relationship of (100) build-up from an oxide surface starting point.

We have observed that (100) build up can take place in a pressure as high as  $2 \times 10^{-7}$  torr as shown in Fig. 17. A comparison with the Fig. 14 results shows that the build up time is 100 seconds at  $T = 1745^\circ \text{K}$  both at  $P = 1 \times 10^{-9}$  torr and  $P = 2 \times 10^{-7}$  torr. However, in order to experience long lived and relatively noise free cathode operation one should operate in the  $10^{-8}$  torr pressure range. The presence of a load resistor (indicated by  $R_L$ ) in the anode circuit of the field emission diode has the effect of slowing down the build-up process and limiting the maximum current.

It should be pointed out that the thermal removal of the oxide layer requires temperatures in excess of 1900 K. Thus, operation in the 1200 to 1700 K range will allow nearly infinite life of the oxide layer. Should the oxide layer become removed it can be readily restored by heating at 1200 to 1600 K in a pressure range of oxygen of  $10^{-6}$  to  $10^{-7}$  torr for a few minutes. Frequently, water vapor and carbon dioxide are more common residual gas components than oxygen. Both  $\text{CO}_2$  and  $\text{H}_2\text{O}$  can be sources of replenishment of the oxide layer through dissociative adsorption as follows:

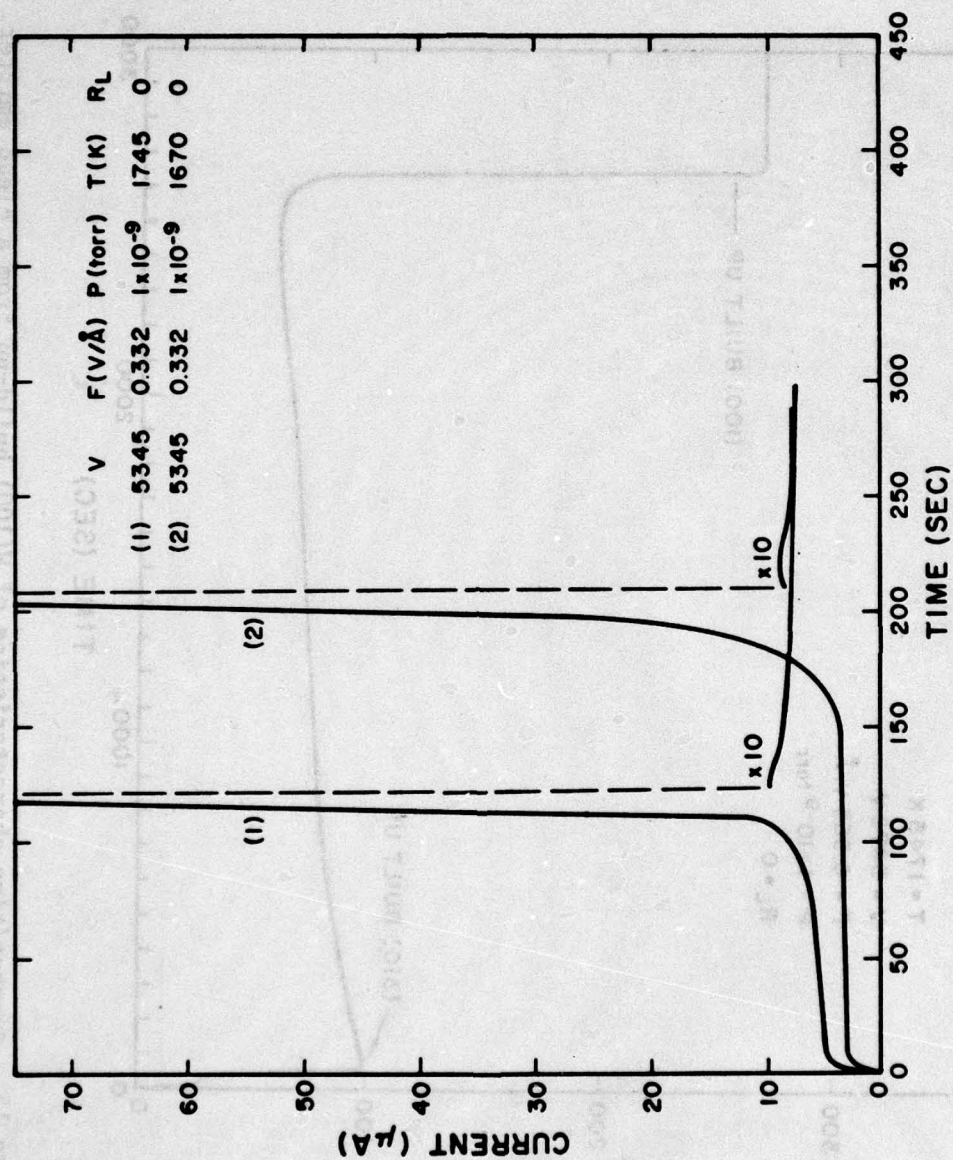


Figure 14. Current/time characteristics of (100) build-up from a slightly oxidized W(100) emitter at two different temperatures.



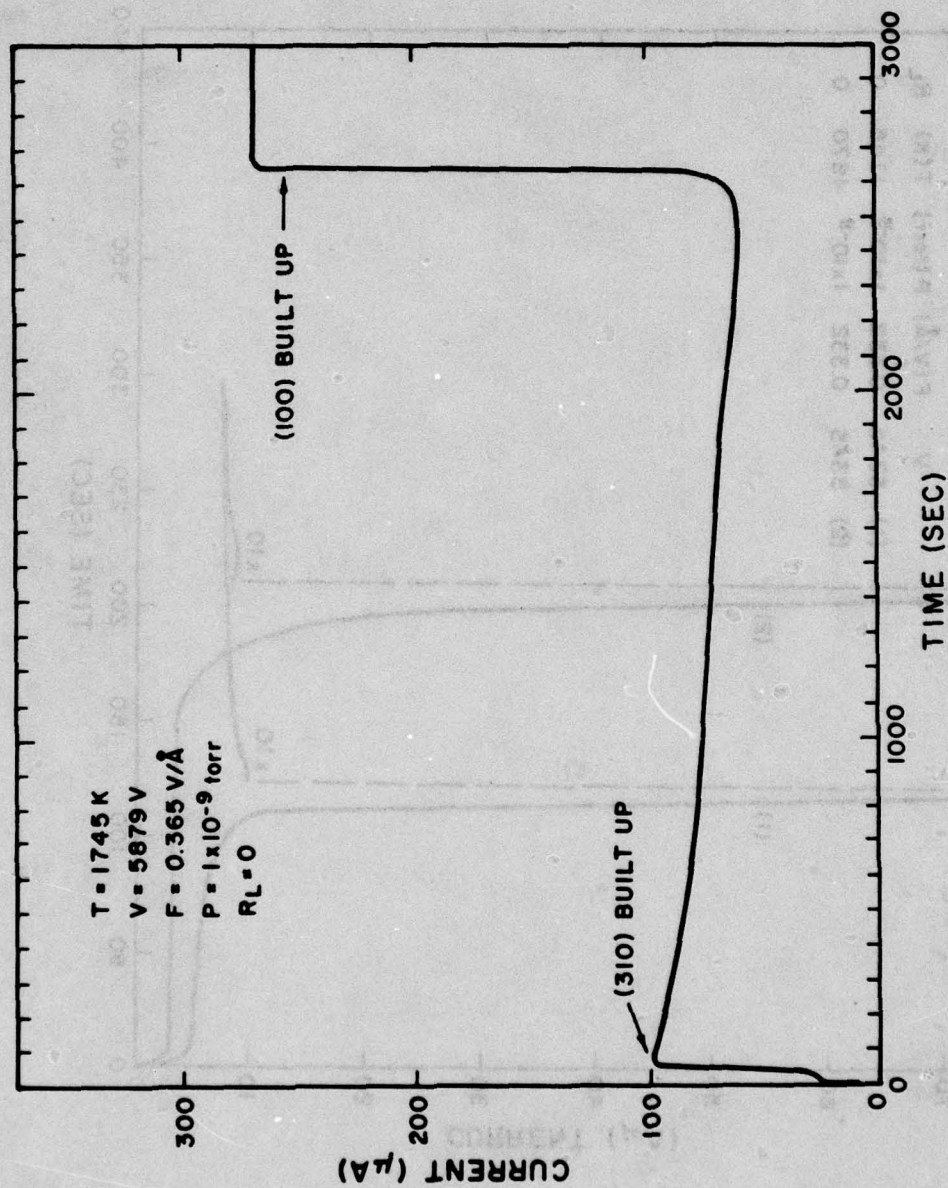


Figure 15. Current/time characteristics of W(100) build-up from a clean emitter.

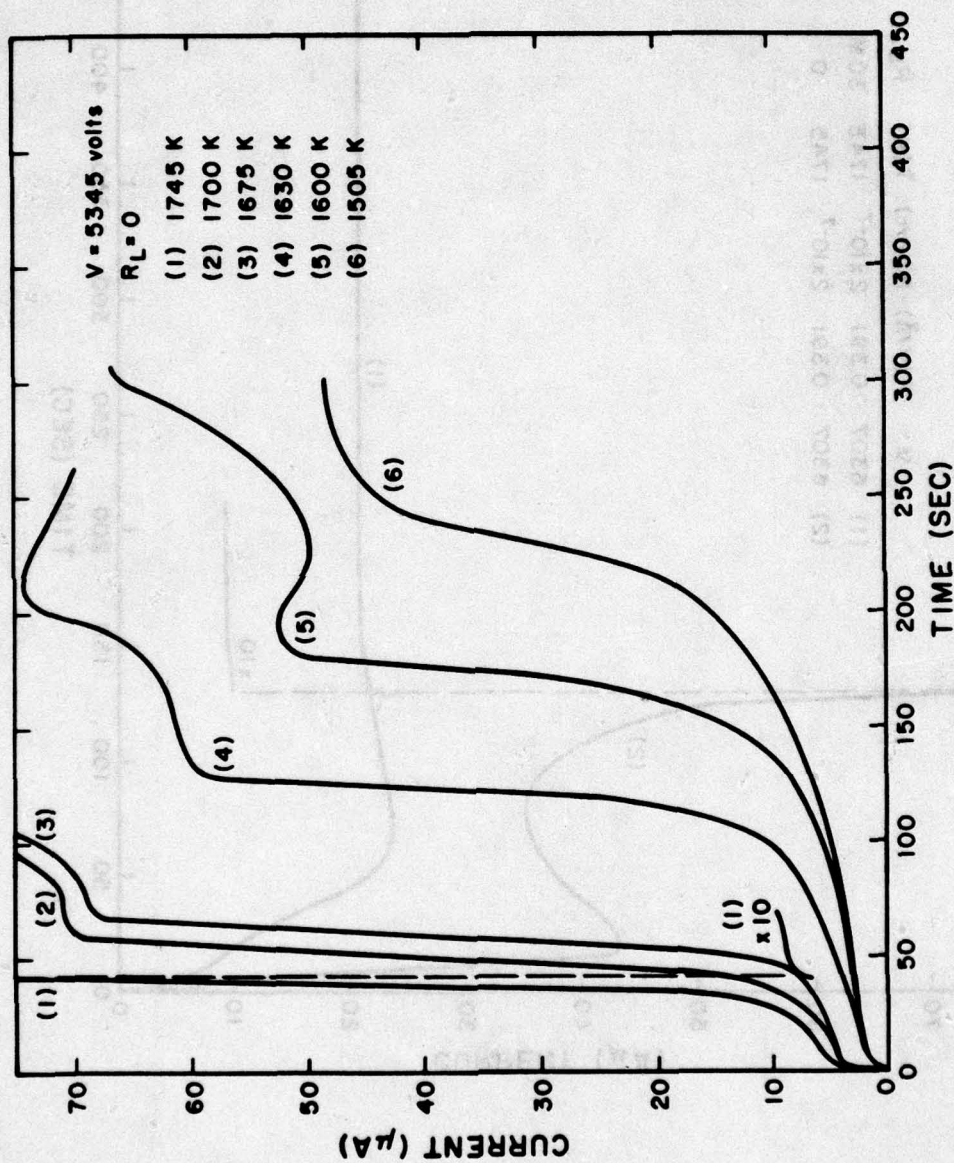


Figure 16. Current/time characteristics of W(100) build-up from a slightly oxidized W(100) emitter.



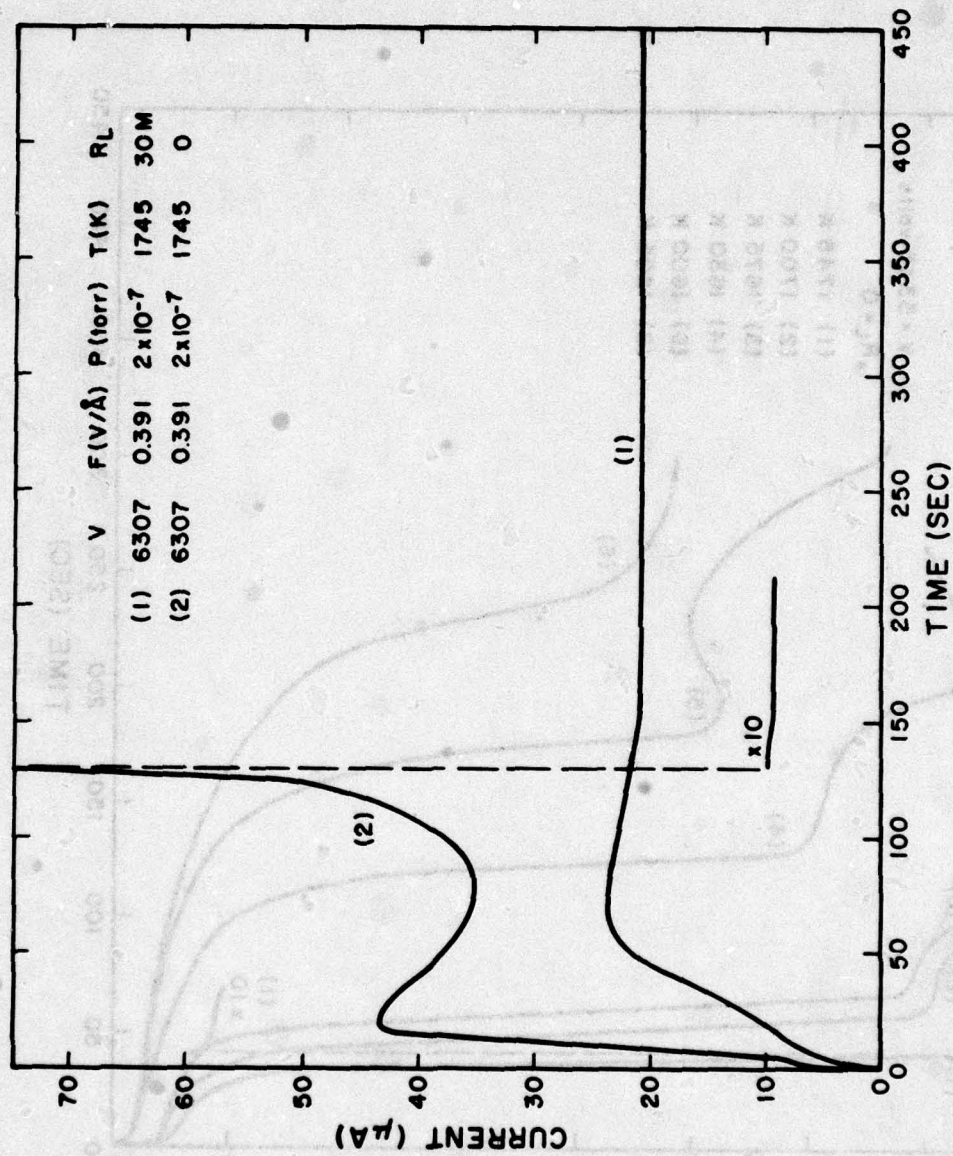


Figure 17. Current/time characteristics for (100) build-up with (1) and without (2) a load resistor. A slightly oxidized emitter was used and the build-up carried out in high background pressure.



Hydrocarbon gases such as methane, ethane, etc. are undesirable in that they adsorbed dissociatively leaving carbon impurities at the surface.

## 2. Specific Processing and Operating Procedures for W(100)

### Build-up

The specific ingredient necessary to assure <100> build up is the presence of an oxide layer on the tungsten surface. Fortunately an oxide layer occurs naturally during initial thermal processing of a freshly formed field emitter. Specifically, <100> build up can be obtained with nearly complete reliability by heating in the range 1200 to 1800 K and slowly increasing the field such that a current of 1 to 20  $\mu\text{A}$  is obtained. The higher forming temperature results in a higher voltage cathode. The transition to the <100> build up mode occurs rapidly with a sudden increase in current and shift in emission distribution as noted in Figs. 14-16. After build up the temperature can be adjusted to a desired value between 1200 and 1900 K; however, for most stable long term operation an operating temperature of 1850 K is most desirable. If the pressure is in the  $10^{-9}$  torr range the cathode can be operated for short periods at room temperature with little risk.

In order to retain the build up configuration after turn off, the cathode temperature should be reduced a few seconds prior to turning off the high voltage. On turning on the field cathode current the voltage and temperature should be turned on simultaneously. The emitter



can be unbuilt by reducing the field while the temperature remains on. Generally, it can be built up again and this cycle can be repeated at will provided the surface oxide layer is retained.

In most applications a total pressure of 1 to  $5 \times 10^{-8}$  torr will possess a sufficiently high partial pressure of oxygen that <100> build up can be expected. Operation above 1900 K will remove the oxide layer and can lead to non- <100> build up. Therefore carbonaceous gases such as methane and other hydrocarbon gases should not be allowed to exceed  $10^{-9}$  torr range in the tip region.

### 3. Build-up of Other Emitter Materials

Field build up of one sort or another will occur with all emitter materials provided the temperature is sufficiently high to cause mobility. As mentioned previously certain bulk impurities (e.g. carbon in tungsten) are able to inhibit surface mobility and, hence, build-up (see reference 16). As a rule the bcc metals molybdenum and tungsten undergo (100) build-up in the absence of carbon and with a slightly oxidized surface. Tungsten, because of its higher melting point and tensile strength appears to be the more durable emitter of the two. Figure 18 shows a FN plot of the  $I(V)$  characteristics of a molybdenum emitter before and after (100) build-up. The emission patterns and build up mechanism is nearly identical with that of tungsten.

Figure 19 shows the before and after built-up patterns for a <100> oriented iridium and <111> oriented tantalum emitter. Figures 20 and 21 show the before and after FN plots of the iridium and tantalum emitters. In the case of tantalum it was observed the carbon or oxygen

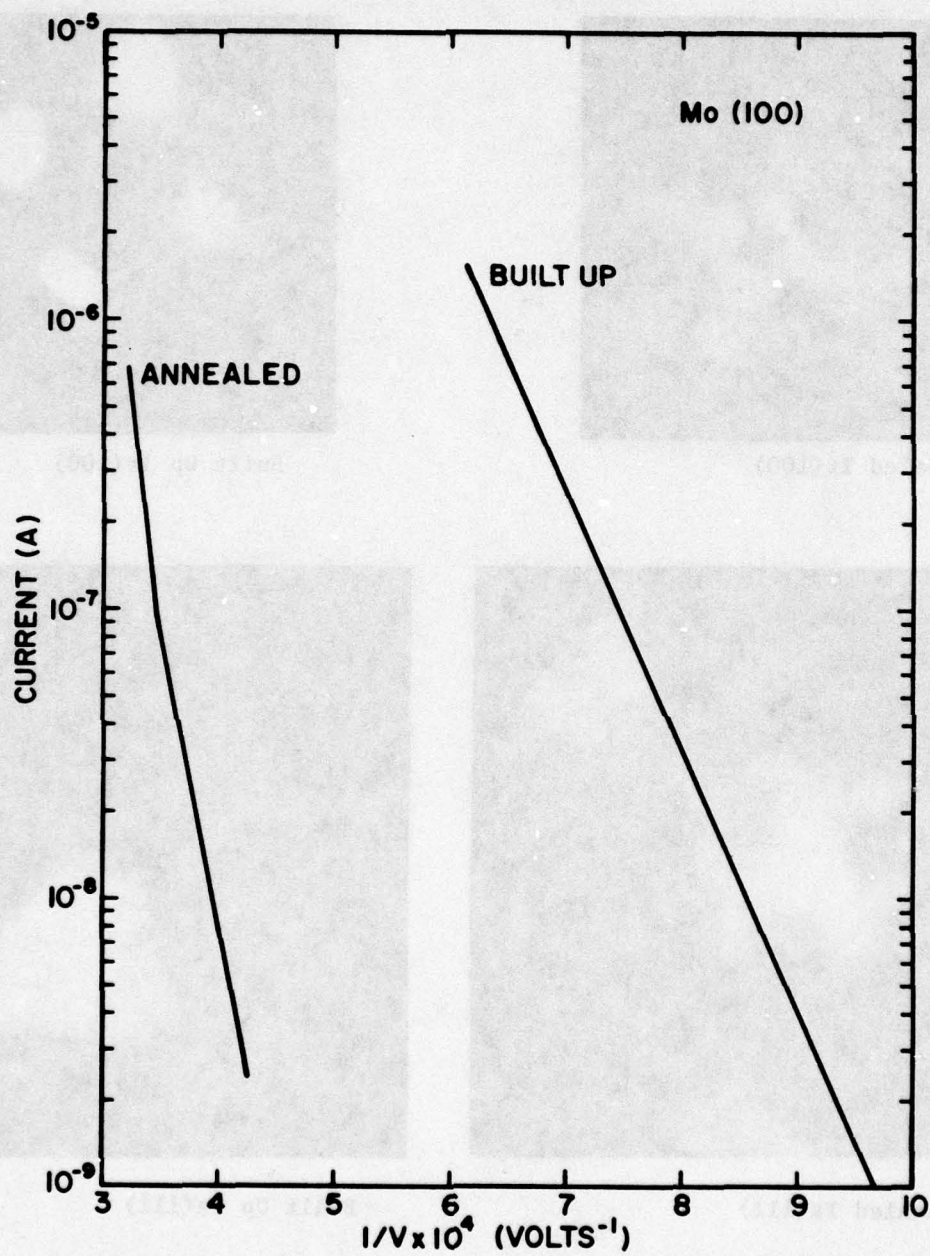
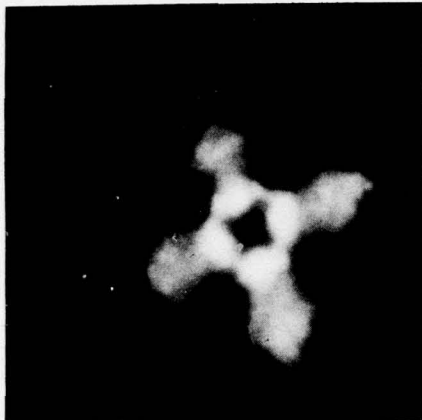
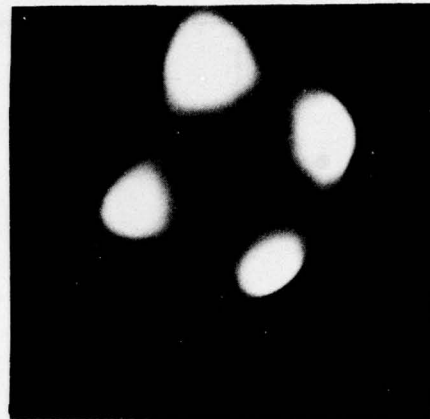


Figure 18. Room temperature FN plot of an unbuilt and (100) built-up molybdenum emitter.

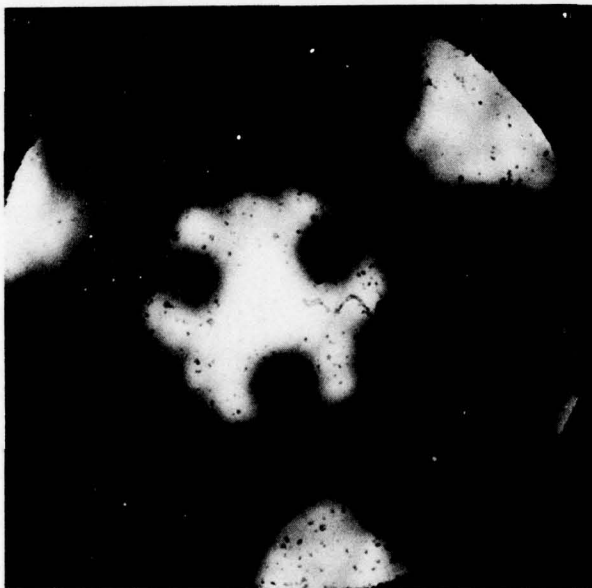




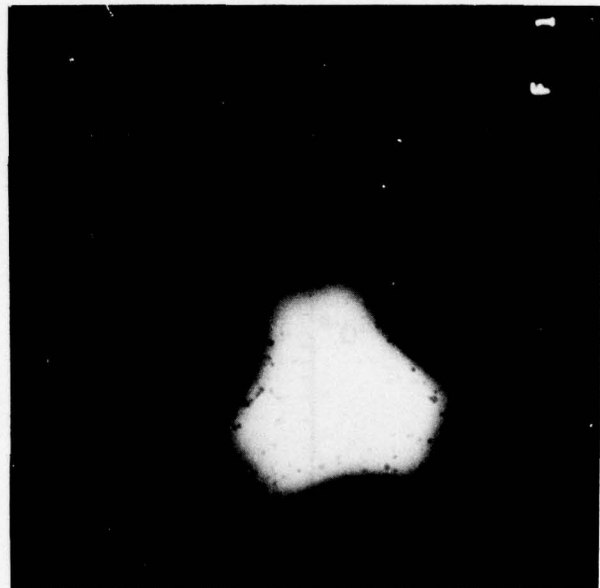
Annealed Ir(100)



Built Up Ir(100)



Annealed Ta(111)



Built Up Ta(111)

Figure 19. FE patterns of unbuilt and built-up iridium and tantalum emitters.

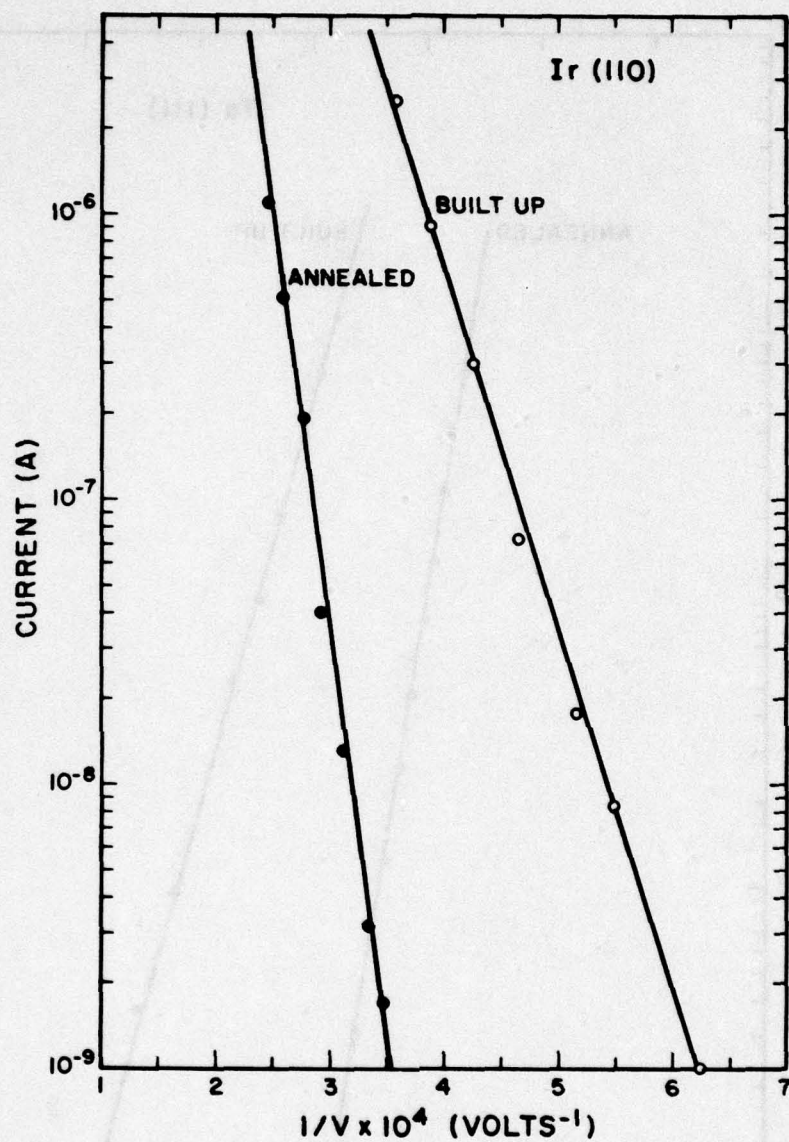


Figure 20. Room temperature FN plot of a <100> oriented iridium emitter before and after (110) build-up.



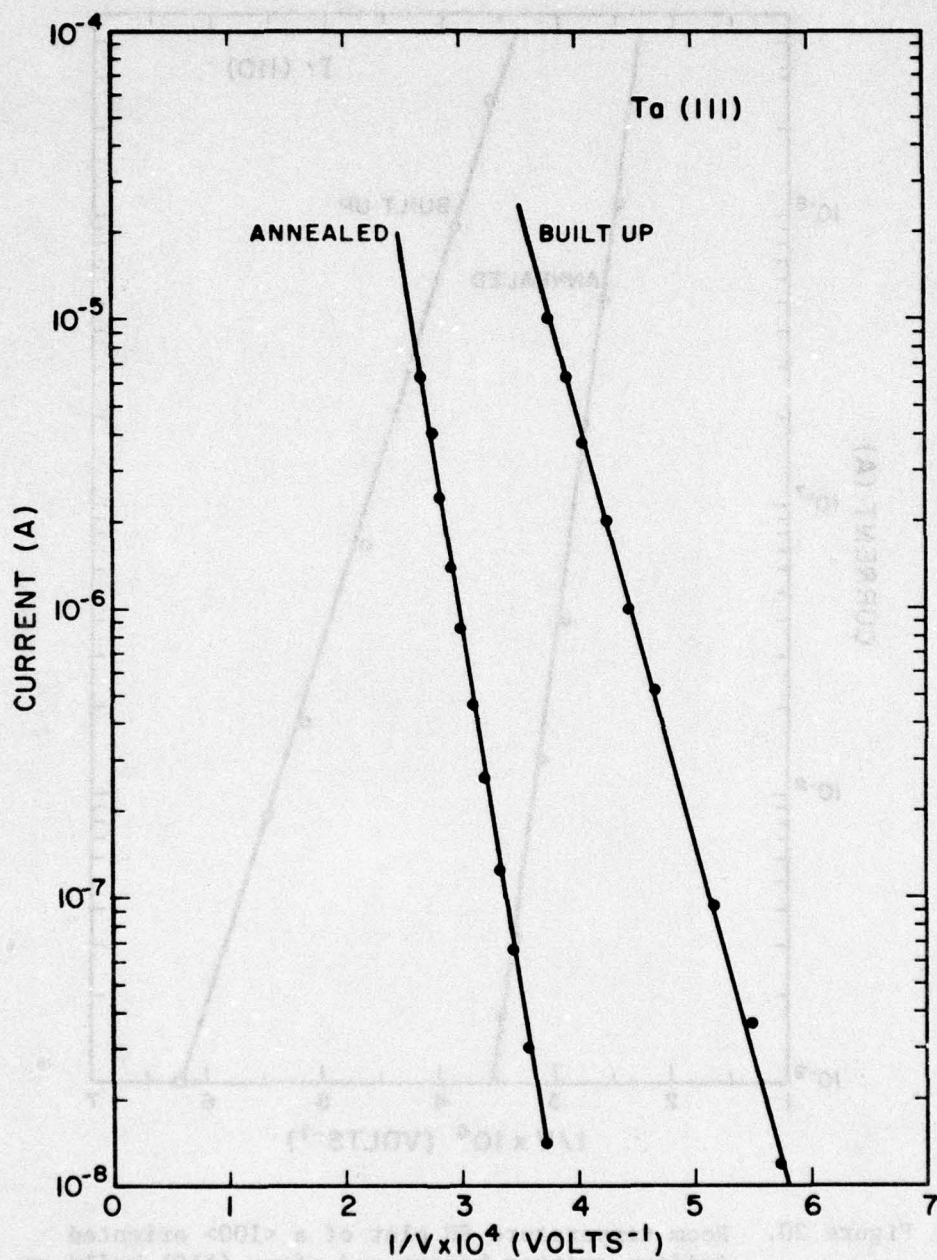


Figure 21. Room temperature FN plot of a  $\langle 111 \rangle$  oriented emitter before and after (111) build-up.

impurities caused the (100) plane to build up much like tungsten; however with a clean tantalum surface the (111) plane builds up in the temperature range 1400-1750 as shown in Fig. 19. Apparently the (112) and (100) planes facet so as to cause a protrusion to occur along the  $\langle 111 \rangle$  direction. The three symmetrical bright emission regions on the edge of the annealed tantalum emission pattern are the (100) planes. Because of the high melting point of tantalum the (111) built-up emitter operated in the TF mode has proven to be a durable emitter. Life studies carried out for this emitter are discussed in a later section of this report.

The build up process of the fcc metal iridium was also investigated. In this case the build-up occurs on the (110) plane in the temperature range 1300 to 1500 K due to facet formation on the (100) and (111) planes. The ring around central (100) plane in the annealed iridium pattern of Fig. 19 is due to impurities which are suspected to be carbon. It was found that when build-up would not occur properly, heating in  $10^{-7}$  torr oxygen at  $\sim 1200$ -1400 K frequently led to successful (110) build-up. Obviously, one would require a  $\langle 110 \rangle$  oriented iridium emitter in order to place the high emission direction on the emitter axis. The built-up iridium emitter will be discussed later in connection with use as a field ion source. At present it appears to offer no advantage over tungsten as a built-up TF source.

Table 3 gives a summary of some of the relevant parameters comparing the built-up with the unbuilt (annealed) end forms. In



terms of angular confinement of the various end forms, the (100) build-up end form of tungsten and molybdenum are superior. This results from the largest angular separation between the built up direction and the nearest crystallographic direction with the same set of Miller indices. The built-up iridium emitter, if it were oriented along the  $\langle 110 \rangle$  direction, may also build up along the 101, 011,  $0\bar{1}\bar{1}$  or  $10\bar{1}$  directions since the field  $60^\circ$  from the emitter apex may be sufficiently high to cause partial build-up of the latter planes. Such would not be the case for W(100), Mo(100) and probably Ta(111) build-up. In addition, the (100) built-up emitters exhibit the largest FN slope and voltage ratios in Table 3 which is indicative of the greater localization of the emission after build-up.

The last column of Table 3 gives the activation energies calculated from the variation of build-up times with temperature for each material. The order of the activation energy reflects the order of the gross surface diffusion rates involved in mass transport as the build-up occurs.

TABLE 3

SUMMARY OF EMISSION PARAMETERS COMPARING BUILT UP  
AND UNBUILT UP EMISSION PARAMETERS

Emitter Material and Orientation	Build-up Mode	FN Slope Ratio*	Voltage Ratio* (I = 1 $\mu$ A)	Activation Energy (eV)	Ang. Separation of Built-Up Directions (deg)
W(100)	(100)	0.40 $\pm$ .05	0.52 $\pm$ .05	2.1	90
Mo(100)	(100)	0.45 $\pm$ .05	0.48 $\pm$ .05	-	90
Ta(111)	(111)	0.60 $\pm$ .05	0.70 $\pm$ .05	1.8	70.5
Ir(110)	(100)	0.50 $\pm$ .05	0.65 $\pm$ .05	2.3	60

\*ratio of built-up/unbuilt-up end slopes form and voltages to draw 1  $\mu$ A of current at room temperature



#### D. Coated Emitters

The primary emphasis on coated emitters (i.e., emitters with an adsorbed monolayer film) during this investigation has been the zirconium coated  $\langle 100 \rangle$  oriented tungsten emitter. The desirable properties of this emitter are (1) the confinement of emission to the  $\langle 100 \rangle$  direction due to selective work function lowering; (2) the high degree of thermal stability of the coating; (3) the ability to use large radii emitters without concomitant increase in emitter operating voltage. The latter property is due to the low ( $\sim 2.6$  eV) work function of the coating.

In a recent investigation<sup>17</sup> of the basic surface physics of zirconium and oxygen coadsorbed on W(100) it was learned that the low work function surface consisted of a ZrO entity absorbed in the bulk and adsorbed at the W(100) surface. Increasing the ambient oxygen pressure above the heated Zr/O/W(100) surface leads to a decrease in both oxygen and tungsten as measured by Auger electron spectroscopy (AES). This result is shown in Fig. 22 where the Zr and O AES peaks relative to W decrease with increasing oxygen pressure. The work function also increased with increasing oxygen pressure. Interestingly, this process is reversible, i.e., decreasing the oxygen pressure leads to a restoration of the ZrO complex at the surface and a reduction in work function. Apparently the oxygen partial pressure controls the partitioning of the ZrO complex between the adsorbed and absorbed state.

Various methods of applying zirconium to the field emitter were discussed earlier.<sup>6</sup> Figure 23 shows an SEM photograph of a W(100) emitter with a reservoir of zirconium located along the emitter shaft. When

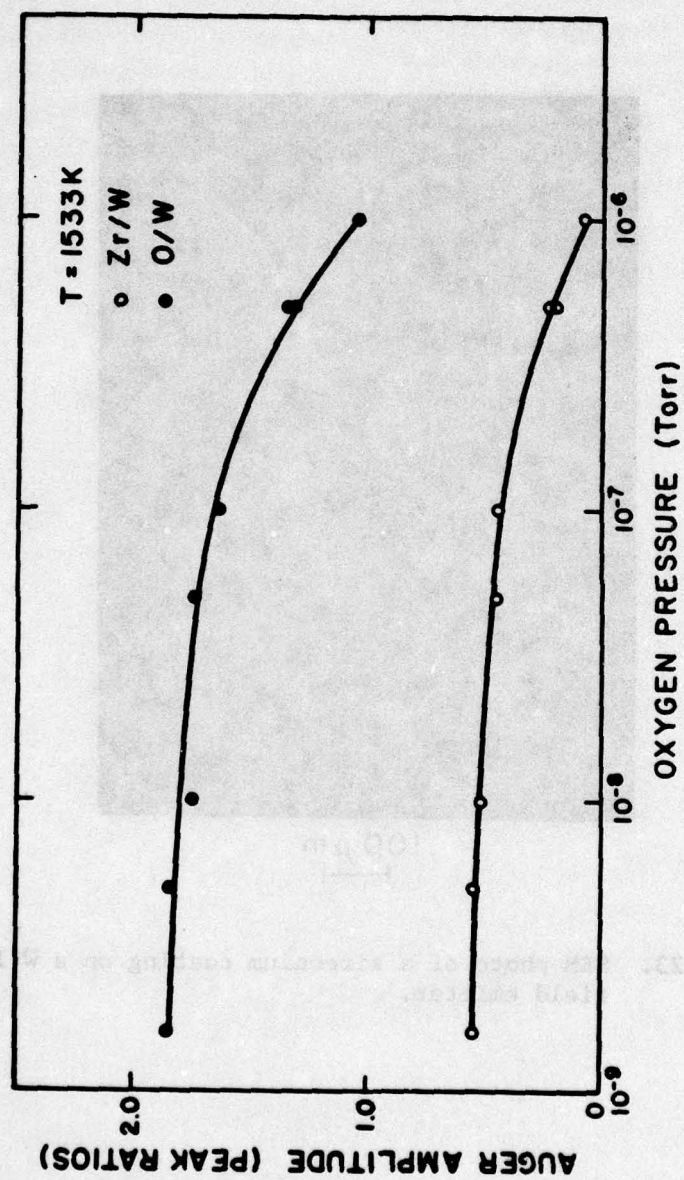


Figure 22. Plot of the indicated Auger spectrum peak height ratios from a co-adsorbed layer of oxygen and zirconium on a W(100) crystal face.





100  $\mu\text{m}$

Figure 23. SEM photo of a zirconium coating on a W(100) field emitter.

operated at  $\sim 1800$  K the zirconium reservoir supplies the emitter tip via surface and bulk diffusion.

The effect of oxygen on the TF emission properties of the Fig. 23 Zr/O/W(100) field emitter has been investigated. Figure 24 shows the effect of oxygen pressure on the TF emitted current at various emitter operating temperatures. The beam current being measured in Fig. 24 through a 7.5 mrad half angle aperture exhibits a maximum value at various oxygen partial pressures depending on the emitter temperature.

In addition, the emission pattern, which consists of a central bright spot surrounded by one or two concentric rings of emission, undergoes a cyclic variation shown in Fig. 25. A beam acceptance half angle of 86 mrad partly obscures the ring of emission which surrounds the central bright spot (see Fig. 25 (b)). However, it can be seen in the sequence of pattern pictures that the central bright spot and concentric ring collapse toward the center with time while operating at elevated temperature and oxygen pressure. With increasing emitter temperature and oxygen pressure the rate of the cyclic pattern and current change increases.

In view of the Figs. 22 and 24 results and other studies,<sup>17</sup> a possible explanation of the cause of the Fig. 25 results is an oxygen induced diffusion of excess zirconium into the bulk. This results in a dynamic equilibrium between supply by surface diffusion and removal by bulk diffusion of the ZrO overlayer. The shifting of the equilibrium ZrO coverage by oxygen pressure will also alter the surface work function which, in turn, governs the emission current variations as shown in Fig. 24.



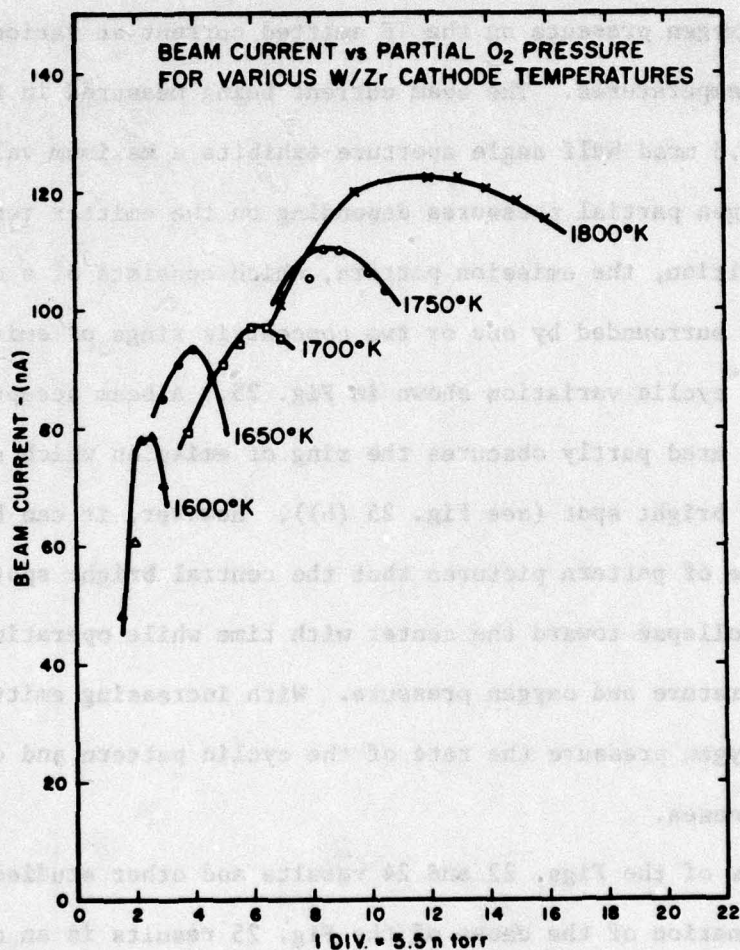


Figure 24. Plot of the current emitted through a 7.5 mrad half angle aperture vs oxygen pressure using a Zr/W(100) TF emitter at the indicated temperatures.

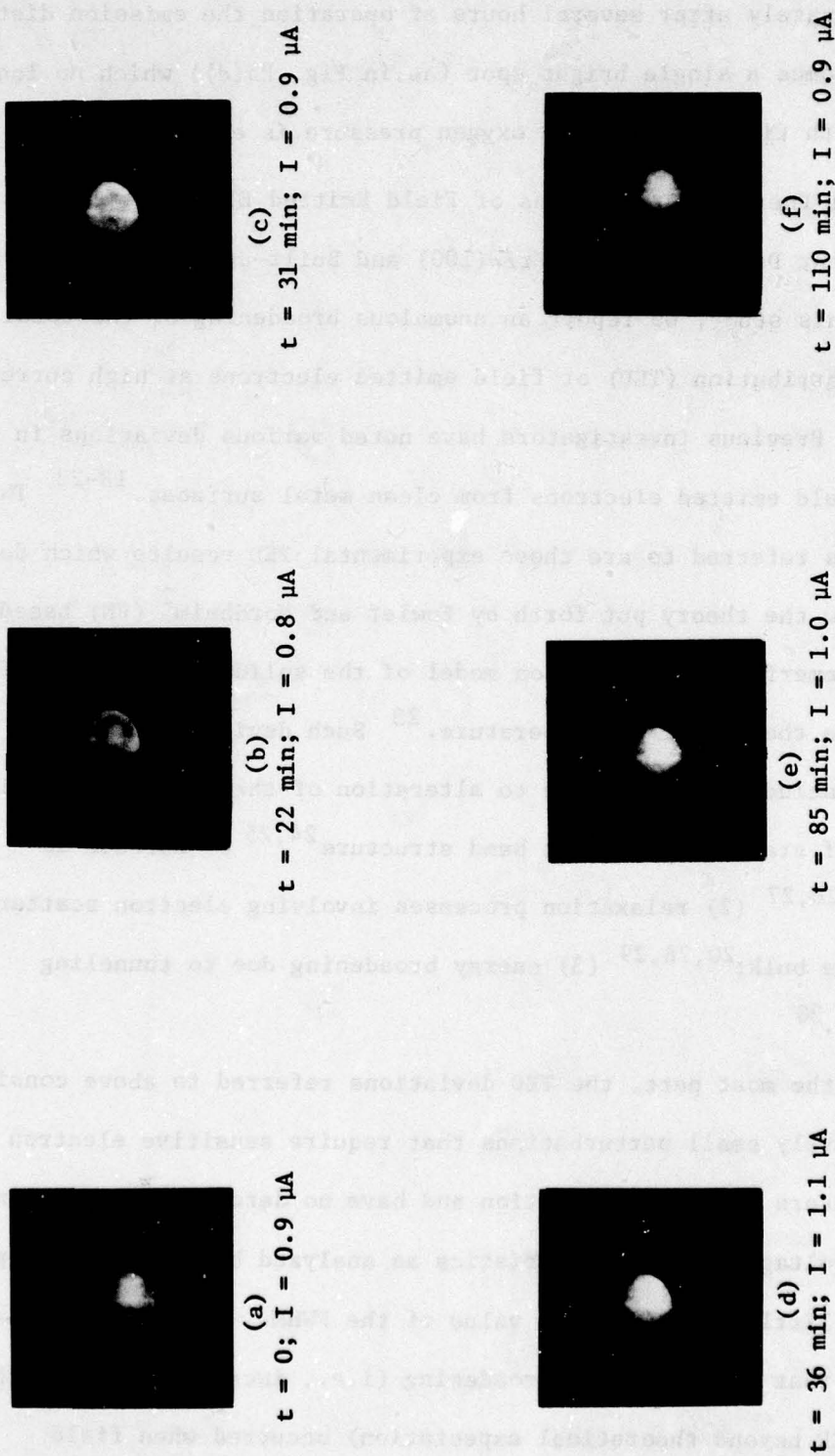


Figure 25. Pattern pictures through a 86 mrad half angle aperture for a Zr/W(100) TF emitter operating at 1770 K and in an oxygen pressure of  $2 \times 10^{-7}$  torr. The time and current levels are indicated.



Fortunately after several hours of operation the emission distribution becomes a single bright spot (as in Fig. 25(d)) which no longer changes with time provided the oxygen pressure is eliminated.

E. Total Energy Distributions of Field Emitted Electrons at High Current Density For the Zr/W(100) and Built-up W(100) Cathodes

In this study, we report an anomalous broadening of the total energy distribution (TED) of field emitted electrons at high current density. Previous investigators have noted various deviations in the TED of field emitted electrons from clean metal surfaces.<sup>18-22</sup> The deviations referred to are those experimental TED results which do not follow the theory put forth by Fowler and Nordheim<sup>2</sup> (FN) based on the Sommerfeld free electron model of the solid and later modified to include the effect of temperature.<sup>23</sup> Such deviations observed in the TED include (1) those due to alteration of the substrate local density of states due to bulk band structure<sup>24,25</sup> or surface adsorption;<sup>26,27</sup> (2) relaxation processes involving electron scattering in the bulk;<sup>20,28,29</sup> (3) energy broadening due to tunneling lifetimes.<sup>30</sup>

For the most part, the TED deviations referred to above consist of relatively small perturbations that require sensitive electron spectrometers for their detection and have no detectable effect on the current-voltage  $I(V)$  characteristics as analyzed by so-called FN plots and have little effect on the value of the FWHM. Recently, it was reported that a significant broadening (i.e., increase in the FWHM of the TED beyond theoretical expectation) occurred when field

emitters were operated in the thermal field (TF) mode at high current density  $J > 10^6 \text{ A/cm}^2$ .<sup>14</sup> In addition, this anomalous increase in FWHM of the TED was accompanied by deviations in the FN plot, which had been observed earlier,<sup>31</sup> and an unusual reduction in the  $1/f$  noise amplitude.

The purpose of this investigation was to study the effect of such parameters as emitter size, current density, temperature, work function and beam acceptance angle on the FWHM of TED measurements taken at large values of  $J$ . The FE sources used in this study were low work function zirconium coated Zr/W(100)<sup>4,7,14</sup> and the high work function W(100) built up<sup>4,14,32</sup> emitter. These emitters are capable of high  $J$  operation over the temperature range 78 to 1900 K and confine the emission to an  $8^\circ$  half angle.

Besides the general interest in characterizing and understanding the TED broadening phenomenon, there is further interest regarding its effect on the use of FE sources in a growing number of microprobe applications. Both of the FE sources investigated here are capable of long lived dc operation at angular intensities in excess of  $1 \text{ mA/sr}$ . However, the enhanced broadening of the TED will cause chromatic aberration to become a dominant factor limiting the spot size of a focussed beam.

In Section 1, the FE sources and method of measurement are described in further detail. Sections 2 and 3 describe the experimental techniques and results. In Section 4, a discussion of the results and possible mechanisms explaining the enhanced TED are presented. We conclude that a possible mechanism is that involving collective coulomb interaction between the emitted electrons similar to that proposed by



Loeffler,<sup>33</sup> Zimmerman<sup>34</sup> and others<sup>35</sup> to explain the TED broadening noted by Boersch<sup>36</sup> at beam crossovers. However, certain electron energy broadening mechanisms occurring in the bulk cannot be ruled out as contributing to the anomalous TED broadening reported here.

#### 1. Method of Approach

Based on the Sommerfeld model of metals, the TED of field emitted electrons is given by

$$J(\epsilon) = (4\pi me/h^3) f(\epsilon) \int_0^{E_f + \epsilon} D(W) dW \quad (13)$$

where  $\epsilon = E - E_f$  is the total electron energy relative to the Fermi level  $E_f$  and  $W$  is the kinetic energy associated with the component of momentum perpendicular to the surface. The term  $f(\epsilon)$  is the Fermi function,  $f(\epsilon) = 1/[1 + \exp(\epsilon/kT)]$ , while  $D(W)$  is the one-dimensional transmission function which is obtained from<sup>37</sup>

$$D(W) = [1 + \exp A(W)]^{-1} \quad (14)$$

where

$$A(W) = \frac{4}{3} \left( \frac{2m}{\hbar^2} \right)^{1/2} \frac{(E_f + \phi - W)^{3/2}}{E_f} v(y) .$$

When TED measurements are made at low temperatures and examined in an energy range extending no more than a few tenths of an eV on either side of the Fermi level, then it may be adequately represented by the simple expression:

$$J(\epsilon) = (J_0/d) f(\epsilon) \exp(\epsilon/d) \quad (15)$$

where

$$d = \hbar eF/2(2m\phi)^{1/2} t(y) \quad (16)$$

and  $J_0$  is the 0 K FN relation

$$J_0 = \frac{e^3 F^2}{8\pi \hbar \phi t^2(y)} \exp [-4(2m\phi^3)^{1/2} v(y)/3\hbar eF] \quad (17)$$

where  $v(y)$  and  $t(y)$  are tabulated correction terms due to the image potential and are explained in detail elsewhere.<sup>23</sup>

The approximate expression for  $J(\epsilon)$  given in Eq.(15) is accurate for  $p = kT/d < 0.7$ . However, for  $p > 0.7$  the approximations used in deriving Eq.(15) break down and the TED must be evaluated by numerically integrating Eq.(13). El-Kareh, Wolfe and Wolfe<sup>38</sup> have carried out the numerical integration of Eq.(13) over the complete temperature field and work function range; in addition, they along with others<sup>39</sup> performed the integration

$$J(T, F) = \int_0^{\infty} J(\epsilon) d\epsilon \quad (18)$$

which gives the current density over the complete range of the variables  $T$ ,  $F$  and  $\phi$ . Eq.(17) is the result of performing the integration of Eq.(18) at  $T = 0$ .

Eqs.(13) and (18) were evaluated at  $\phi = 2.5$  and  $4.5$  eV using the numerical integration techniques described elsewhere.<sup>38</sup> These are the work function values appropriate for the Zr/W(100) and W(100) built-up emitters investigated in this study. Figures 26 and 27 give the relationship between the FWHM and  $F$ . The arrows on the ordinate indicate the electric field range applicable to the respective emitters. The



origin of the maxima in the FWHM is as follows: at high fields, emission is dominated by emission from the vicinity of the Fermi level, whereas at low fields, it is confined to the top of the work function barrier. On the other hand, at intermediate fields, comparable emission occurs in the region of the Fermi level and the top of the work function barrier leading to the maxima in the Figs. 26 and 27 curves. The maxima in the Figs. 26 and 27 curves are largest for the high work function emitter; however, except for  $T > 1800$  K, they lie outside the field range of interest.

We thus conclude that in the field and temperature range of interest for the two emitters investigated in this study, the FWHM should not exceed  $\sim 1$  eV. Previous studies by Gadzuk and Plummer<sup>40</sup> and others<sup>18,20</sup> have shown that for low field strengths and a temperature range extending from 78 to 1500 K a tungsten emitter gave TED results in agreement with theoretical expectations except for the well known structure in the W(100) TED that occurs at  $\epsilon = -0.35$  and  $-0.70$  eV.

The two emitters chosen for this study, besides their capability of being operated at temperatures up to 1900 K, can also be operated at very high values of current density. The thrust of this study was to measure the FWHM of the TED curves obtained from these two emitters and compare the results with Fig. 26 and 27 predictions. In particular, we measured the TED curves obtained from these two emitters for higher values of  $J$  than have heretofore been examined.

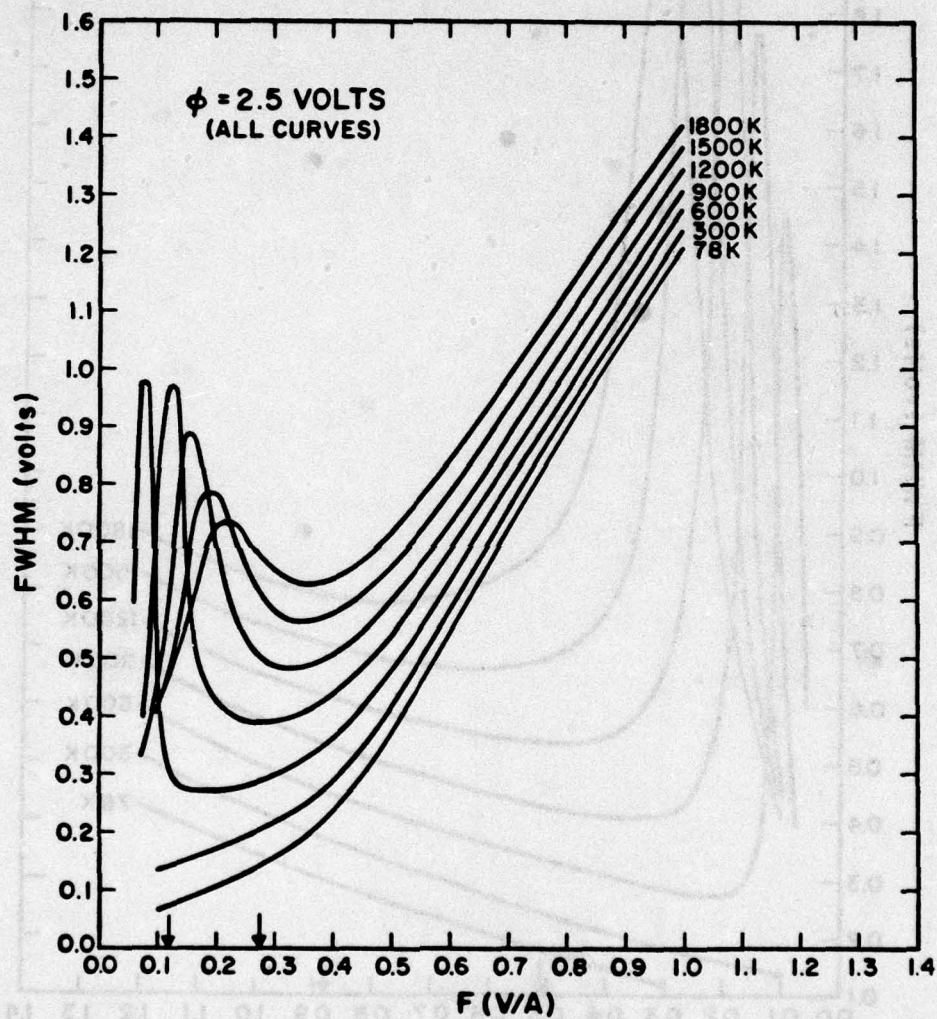


Figure 26. Plot of theoretical values of FWHM for the energy distribution of field-emitted electrons as a function of electric field  $F$  at various temperatures; work function is 2.5 eV.



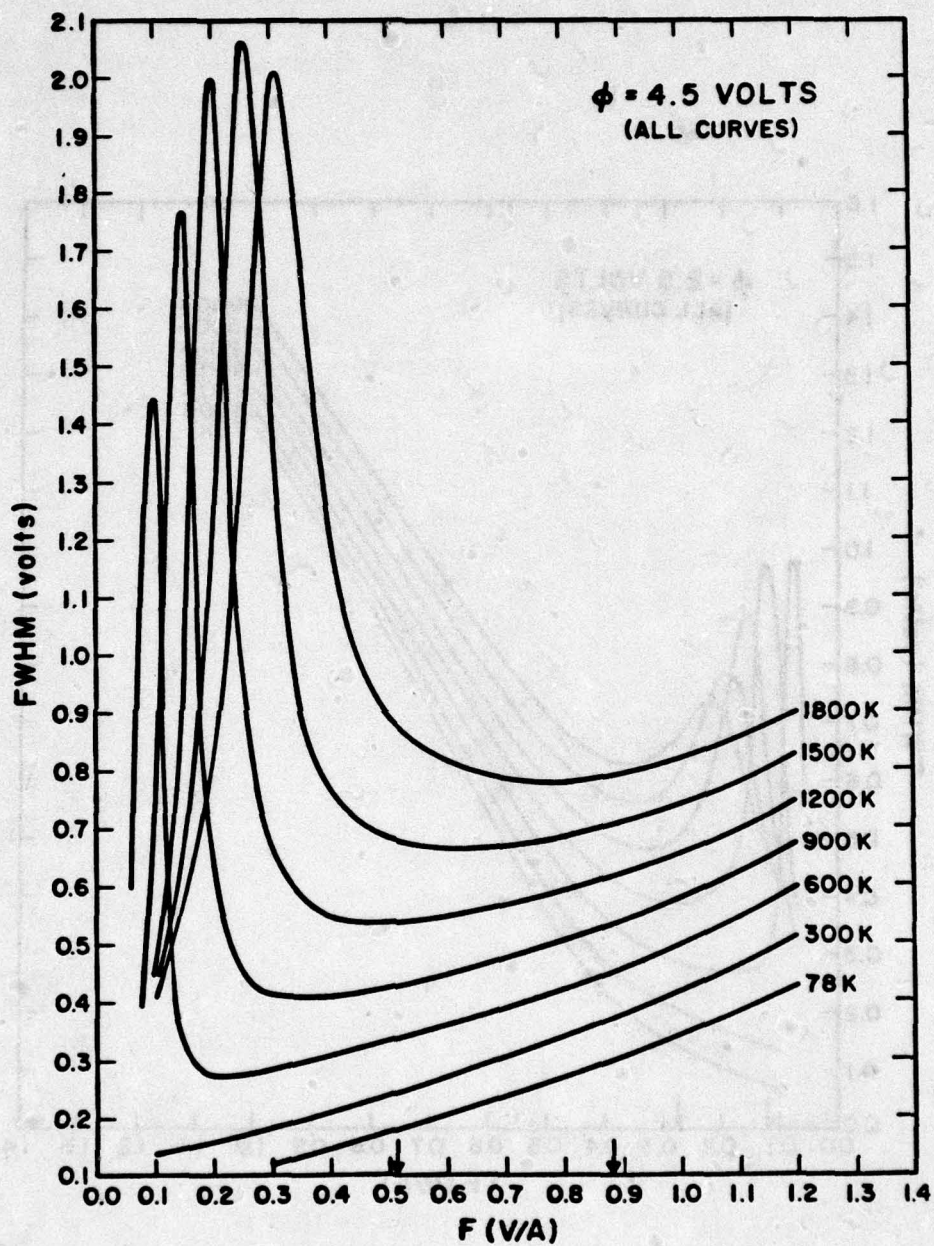


Figure 27. Plot of theoretical values of FWHM for the energy distribution of field-emitted electrons as a function of electric field  $F$  at various temperatures; work function is 4.5 eV.

## 2. Experimental

Two retarding potential analyzers were used in this study, one of which has been described earlier<sup>18</sup> and involves focussing the emitted electrons to a crossover at the center of a retarding hemisphere; the other analyzer employed was a non-crossover retarding analyzer in which the electrons are retarded along radial paths by concentrically-arranged spherical electrodes. A cross section of the latter analyzer is depicted in Fig. 28 and Table 4 gives the radii and relative operating potentials of the electrodes. Electrode potentials were determined according to

$$V(r)/V(r_0) = 1 - \frac{R}{R - r_0} \left( 1 - \frac{r_0}{r} \right) \quad (19)$$

where  $r_0$  is the inner sphere radius and  $R$  is the outer sphere radius. In practice, the best resolution was obtained if the potential of electrode D was  $.03 V(r_0)$  and electrode E was operated at 3V. A negative sweep potential was applied to the emitter in order to display the retarding current-voltage characteristics. The selecting electrode (E) contained a 1000 line/in. platinum-coated copper mesh through which electrons were transmitted into the Faraday collector (F). The emitter was mounted on a glass bellows arrangement in order to align it with the spherical electrodes. For best resolution, the emitter was positioned .56 mm behind the center of symmetry of the hemispherical electrodes. A fluorescent screen on electrode (B) was provided for pattern observation. The resolution of this analyzer was



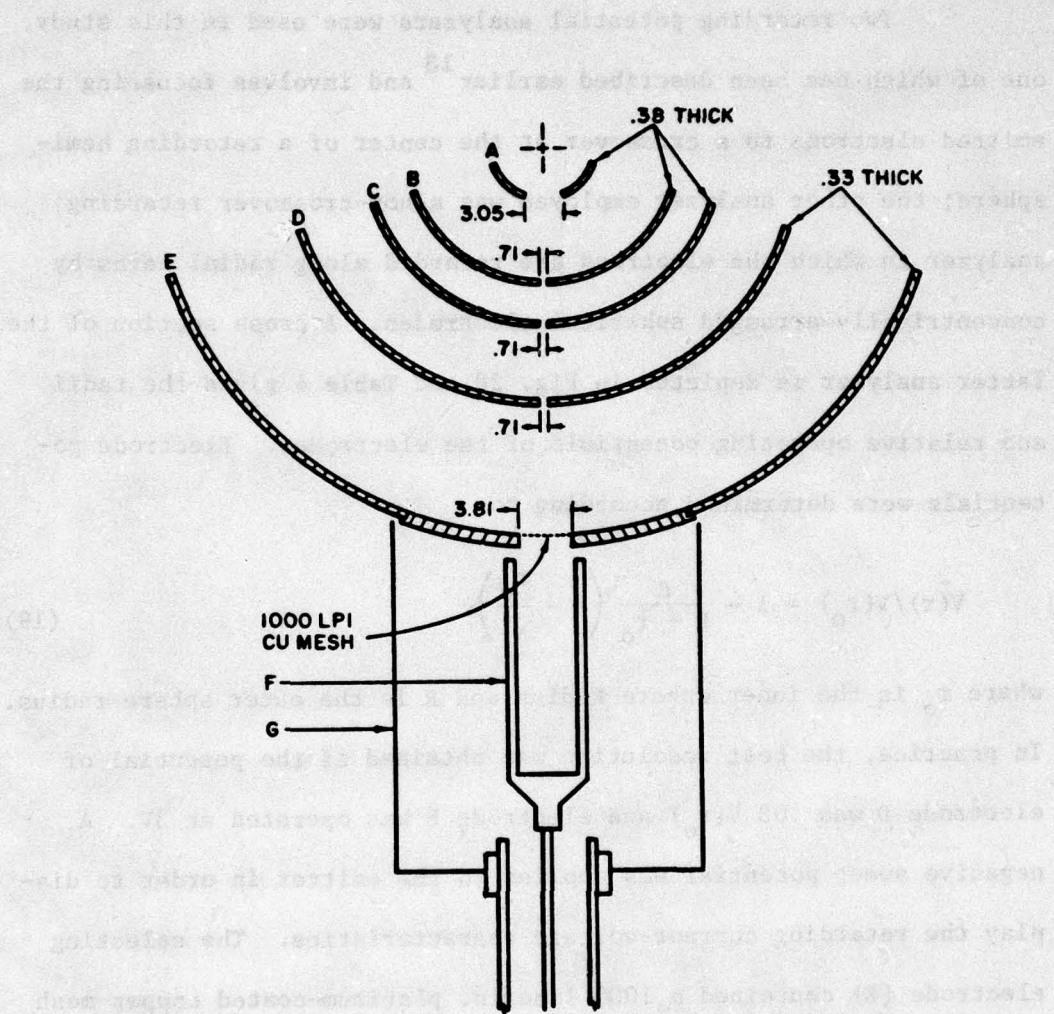


Figure 28. Diagram of the electrode configuration for the non-crossover retarding electron energy analyzer. Dimensions in mm.

TABLE 4  
SPHERICAL RETARDING ANALYZER ELECTRODE SPECIFICATION BASED ON EQ.(19)

<u>Electrode</u>	<u>Inner Radius (mm)</u>	<u>Aperture Diameter (mm)</u>	<u>Relative Voltage</u>
A	3.96	3.05	1.0
B	10.54	0.71	0.264
C	14.10	0.71	0.164
D	20.27	0.71	0.060
E	30.38	3.81*	0

\* covered by 1000 lines/in. copper mesh



$\sim 50$  meV as determined from the leading edge of the TED taken at an emitter temperature of 78 K.

Both electron energy analyzers yielded directly the integral of the FE current with respect to the electron energy; this was differentiated electronically to provide the TED. At elevated temperature, the extent to which the TED measurements could be carried out along the low energy tail was limited by beam noise. Temperature control of the emitter was accomplished by the well known 4 lead emitter assembly where two small diameter ( $\sim 0.1$  mm) leads sample the emitter filament resistance. Temperature calibration for  $T > 1000$  K was performed using an optical pyrometer, while temperature calibration for  $T < 1000$  K was accomplished by using the resistivity-temperature dependence relationship for pure tungsten.

The two electron energy analyzers were mounted on bakable, high-vacuum systems capable of attaining a pressure  $< 8 \times 10^{-10}$  torr. Because of the high total electron current levels used in this study, electron-stimulated desorption of absorbed gases on the anode limited the effective pressure at the emitter. This problem could be reduced to a tolerable level by operating the emitter for several hours at high current level prior to taking TED measurements.

### 3. Experimental Results

Measurements of the TED curves were carried out as a function of  $T$ ,  $F$ ,  $\beta$  and beam aperture angle. The field factor  $\beta = F/V$  was determined in the usual way from the slope of the low temperature FN plot

(i.e.  $\ln I/V^2$  vs  $1/V$ ) by assuming the previously stated  $\phi$  values. The beam acceptance angle was the solid angle ( $\Omega$ ) subtended at the emitter by the beam defining aperture. The "crossover" analyzer was operated with two different apertures giving  $\Omega = 0.14$  and  $0.54$  msr, while the non-crossover analyzer was operated with one aperture size giving  $\Omega = 0.97$  msr.

Figures 29 to 32 show the experimental TED curves obtained from the crossover energy analyzer for the W(100) built up and Zr/W(100) emitters at various values of  $F$  and two extreme values of  $T$ . A few of the theoretical curves normalized to the respective experimental curve peak heights are given for comparison purposes. Figures 33 and 34 give the comparison between the experimental and theoretical values of FWHM for the Figs. 29 to 32 data. A large discrepancy can be seen between experiment and theory at large values of  $F$  for both high and low temperatures.

Figure 35 shows the high temperature FWHM values for the W(100) built up emitter taken in the crossover analyzer with a larger beam acceptance angle ( $\Omega = 0.54$  mSr) and at various values of emitter radii. The FWHM values are given in terms of the beam angular intensity in order to show its dependence on the latter parameter. Figure 36 gives similar results for a W(100) built up emitter with approximately the same emitter radius  $r$  (i.e. similar values of  $\beta$ , where  $\beta \propto 1/r$ ) but at various beam acceptance angles. The values for  $\Omega = 0.97$  mSr in Fig. 36 were obtained from the non-crossover analyzer as were the Fig. 37 results which were taken with a smaller  $\beta$  value emitter at several



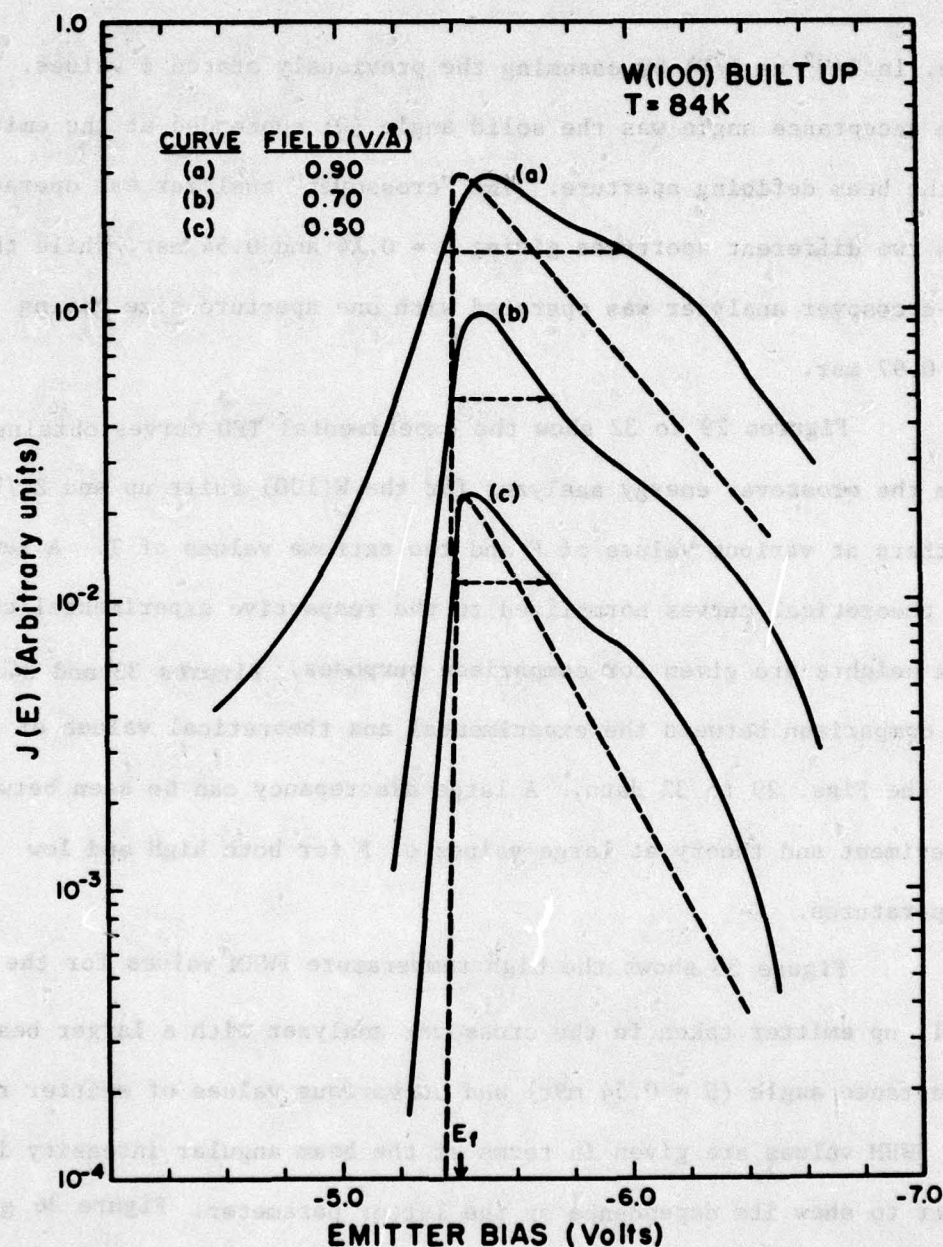


Figure 29. Solid lines are the experimental TED curves for a W(100) built-up emitter taken at the indicated electric fields and temperature; dashed lines are the corresponding theoretical curves using  $\phi = 4.5$  eV and normalized to the peak heights and Fermi level  $E_f$  of the respective experimental curves. Horizontal dashed lines indicate the experimental FWHM values. Crossover analyzer with  $\Omega = 0.14$  mSr used for these results.

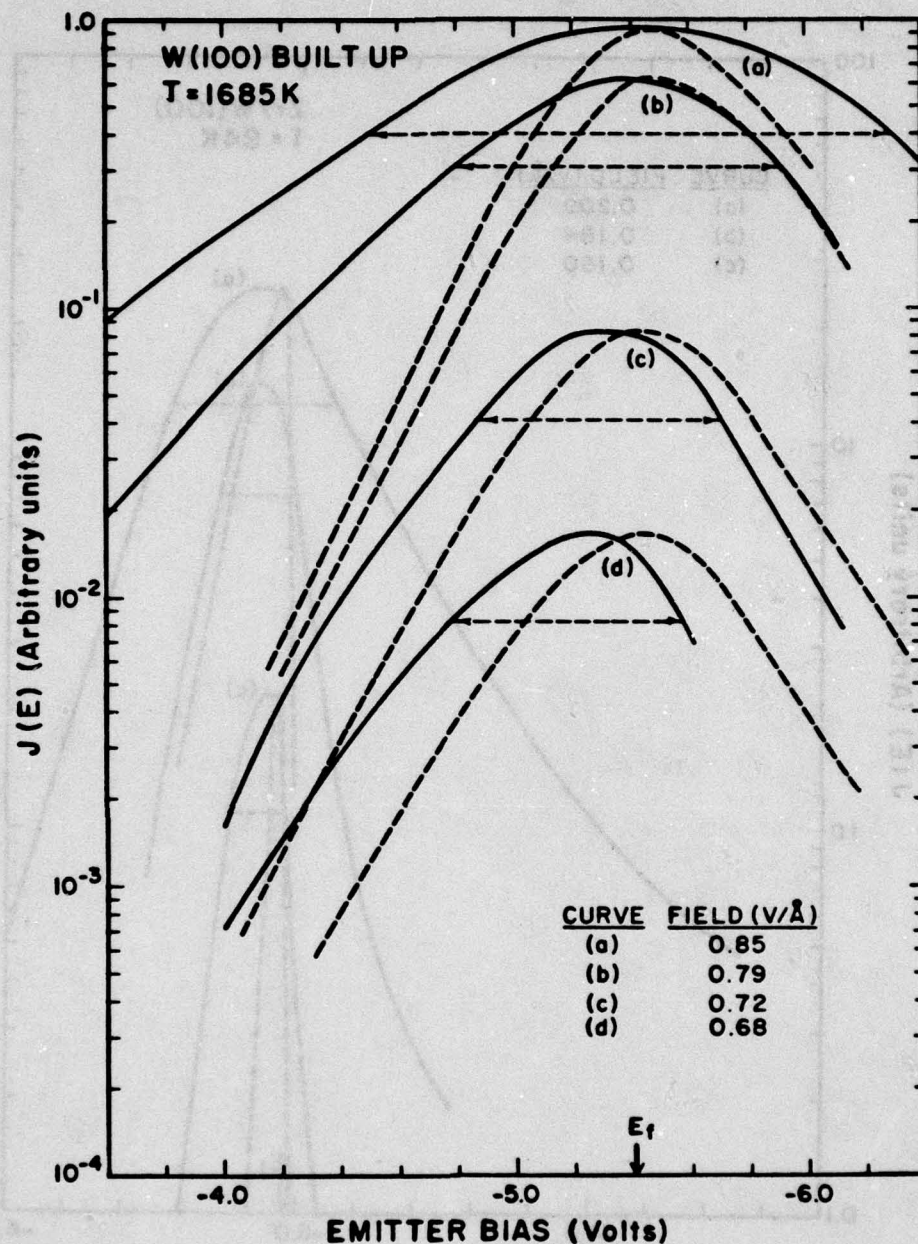


Figure 30. Solid lines are the experimental TED curves for a W(100) built-up emitter taken at the indicated electric fields and temperature; dashed lines are the corresponding theoretical curves using  $\phi = 4.5$  eV and normalized to the peak heights and Fermi level  $E_f$  of the respective experimental curves. Horizontal dashed lines indicate the experimental FWHM values. Crossover analyzer with  $\Omega = 0.14$  mSr used for these results.



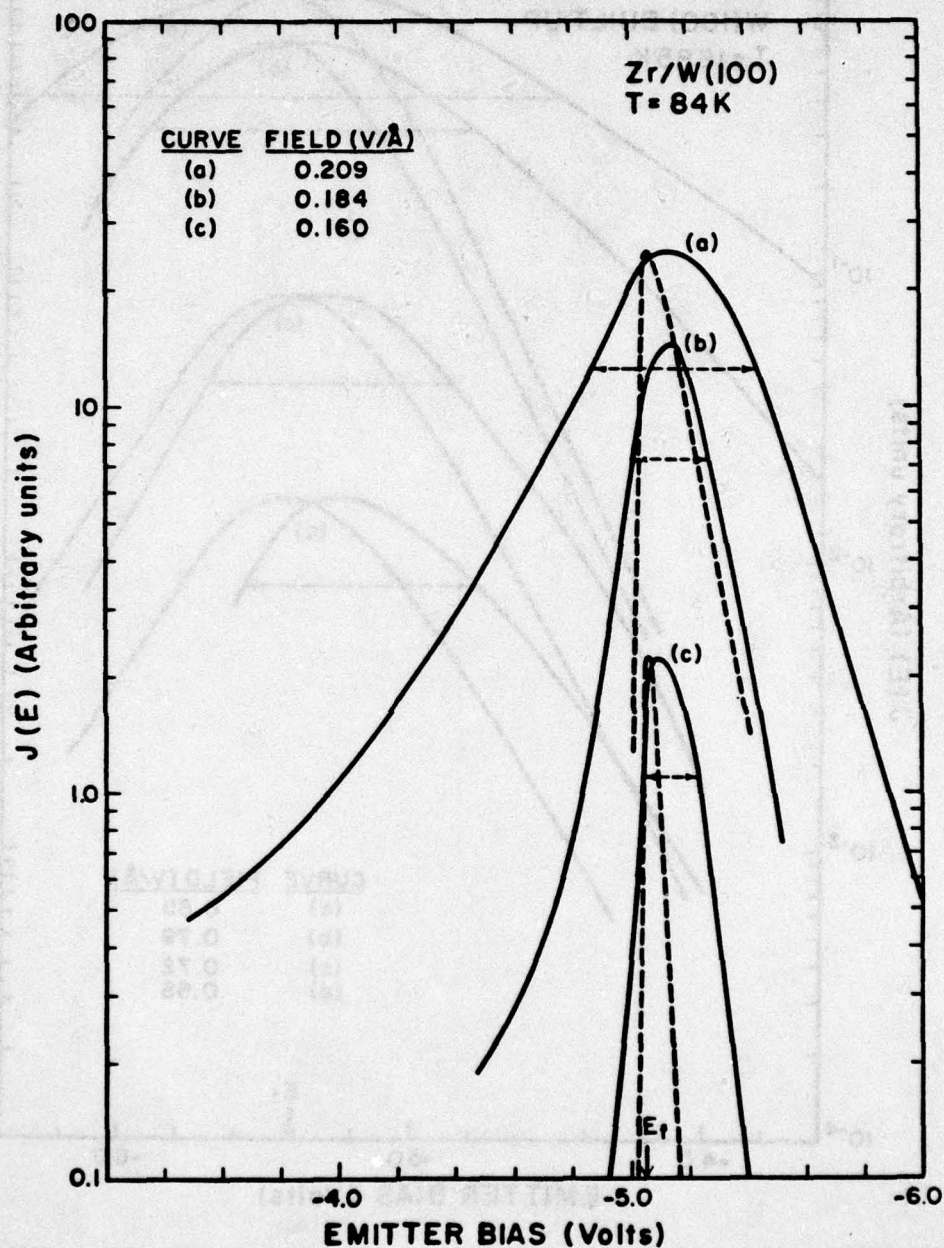


Figure 31. Solid lines are the experimental TED curves for a Zr/W(100) emitter taken at the indicated electric fields and temperature; dashed lines are the corresponding theoretical curves using  $\phi = 2.5$  eV and normalized to the peak heights and Fermi level  $E_f$  of the respective experimental curves. Horizontal dashed lines indicate the experimental FWHM values. Crossover analyzer with  $\Omega = 0.14$  mSr used for these results.

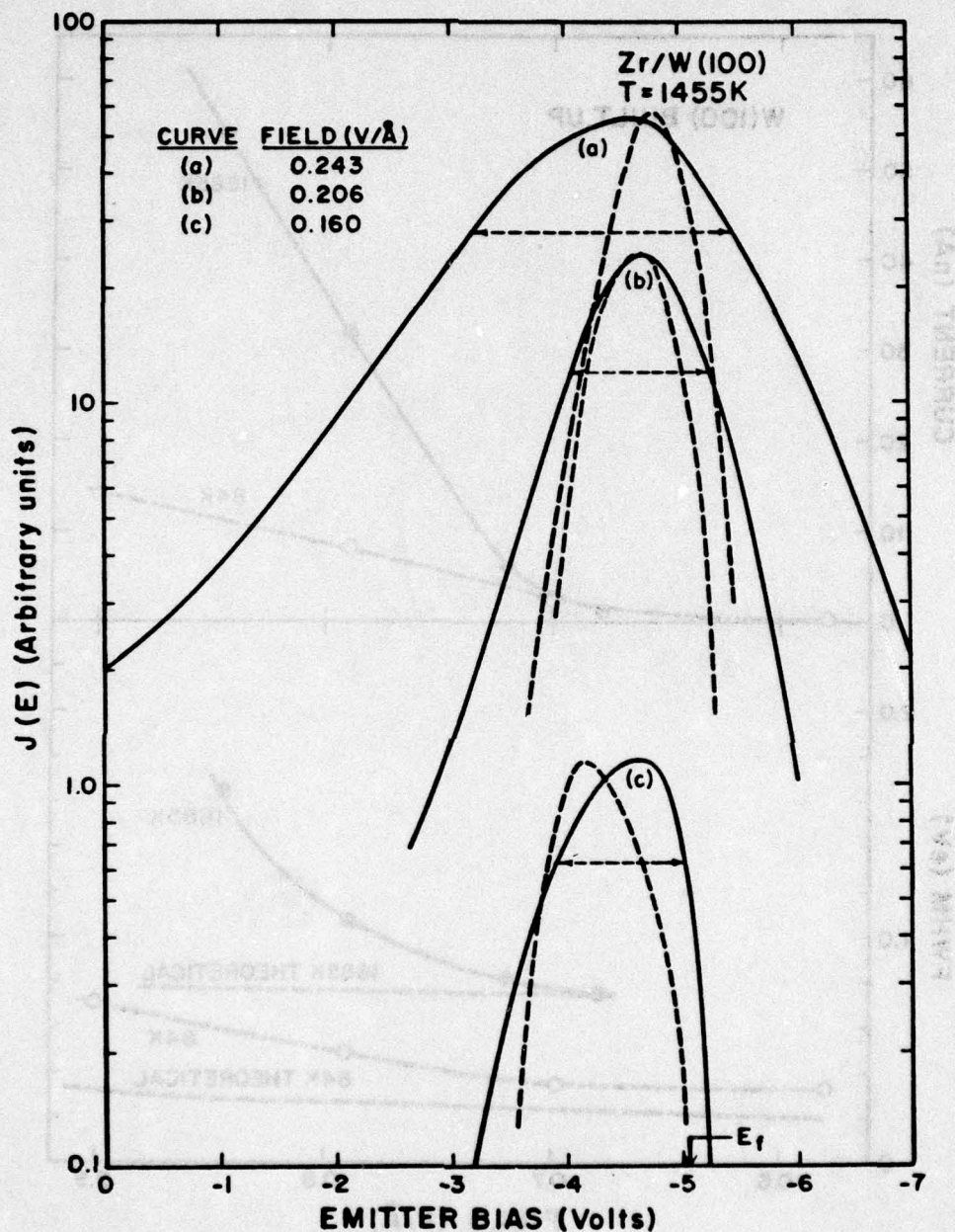


Figure 32. Solid lines are the experimental TED curves for a Zr/W(100) emitter taken at the indicated electric fields and temperature; dashed lines are the corresponding theoretical curves using  $\phi = 2.5$  eV and normalized to the peak heights and Fermi level  $E_f$  of the respective experimental curves. Horizontal dashed lines indicate the experimental FWHM values. Crossover analyzer with  $\Omega = 0.14$  mSr used for these results.



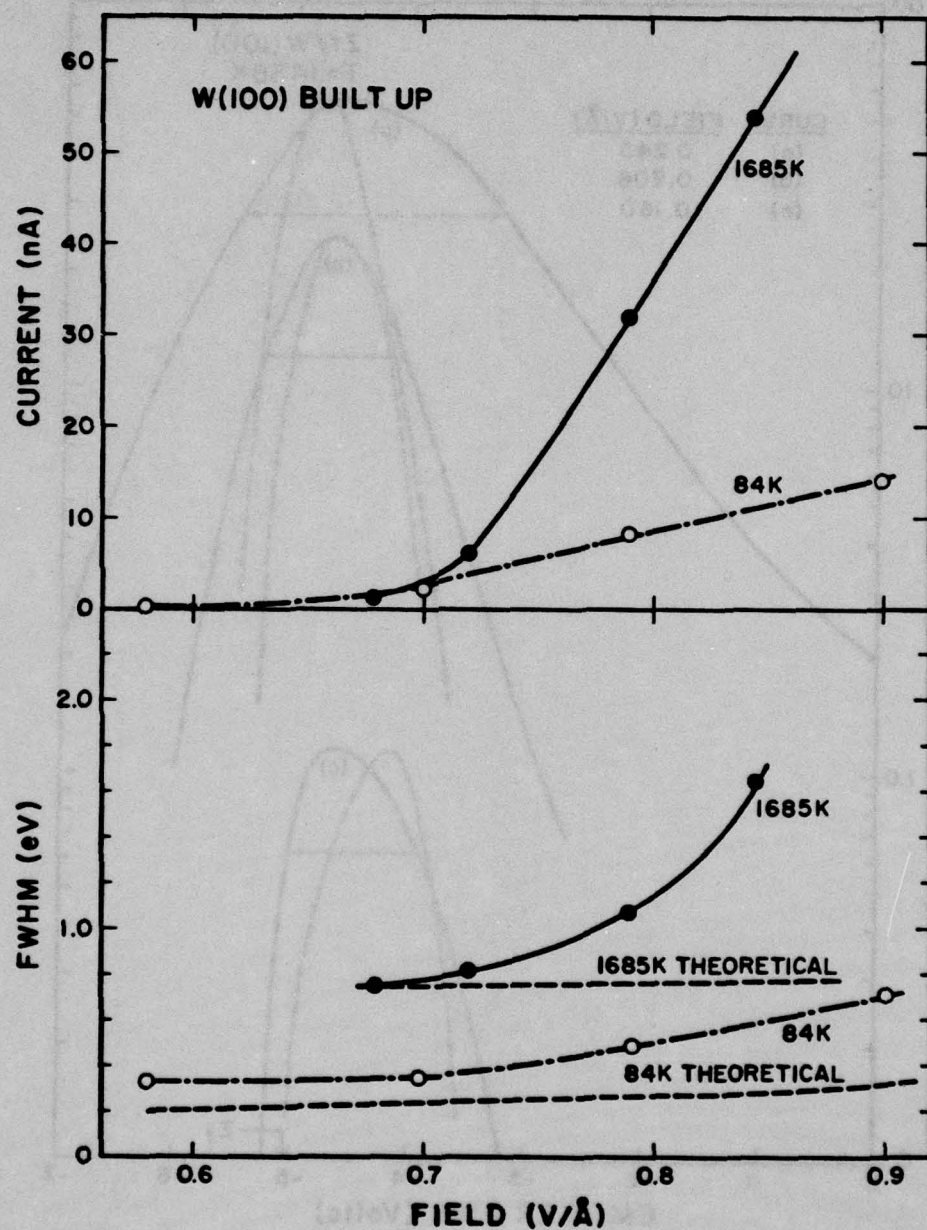


Figure 33. Solid and dot-dashed lines are the experimental values of transmitted current (upper figure) and FWHM values vs. electric field (lower figure). Results correspond to Fig. 29 and 30 data. Dashed lines (lower figure) are theoretical values of FWHM.

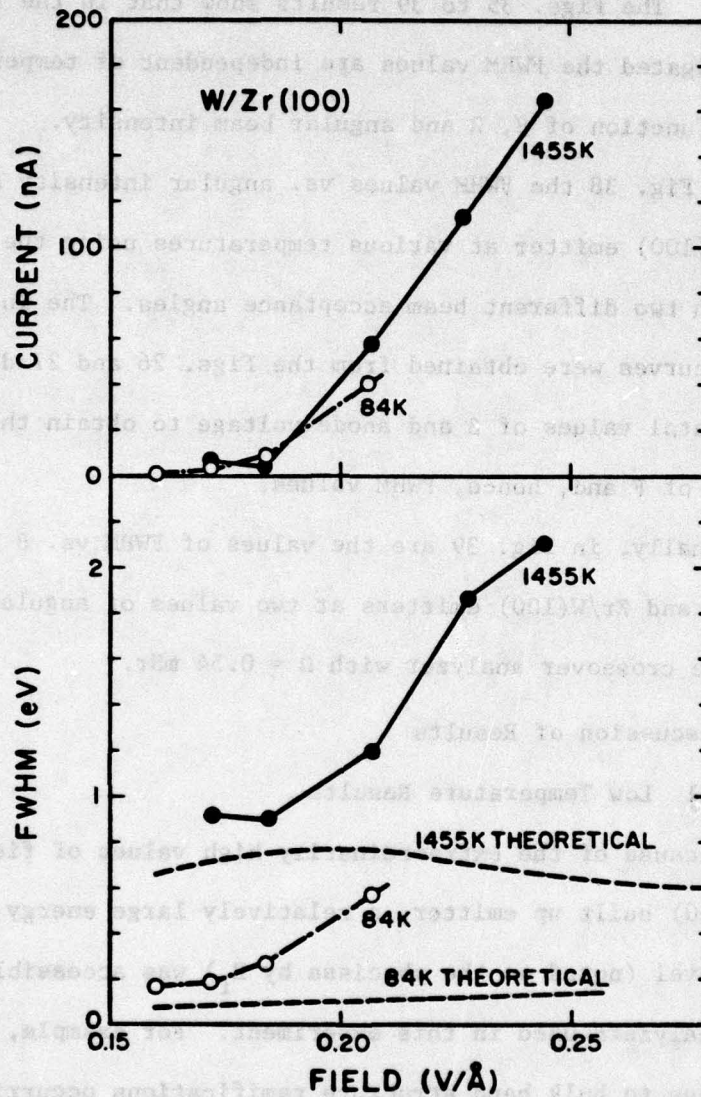


Figure 34. Solid and dot-dashed lines are the experimental values of transmitted current (upper figure) and FWHM values vs. electric field (lower figure). Results correspond to Fig. 31 and 32 data. Dashed lines (lower figure) are theoretical values of FWHM.



temperatures. The Figs. 35 to 39 results show that in the temperature range investigated the FWHM values are independent of temperature and primarily a function of  $\beta$ ,  $\Omega$  and angular beam intensity.

In Fig. 38 the FWHM values vs. angular intensity are given for the Zr/W(100) emitter at various temperatures using the crossover analyzer with two different beam acceptance angles. The indicated theoretical curves were obtained from the Figs. 26 and 27 data using the experimental values of  $\beta$  and anode voltage to obtain the appropriate value of  $F$  and, hence, FWHM values.

Finally, in Fig. 39 are the values of FWHM vs.  $\beta$  for both the built up and Zr/W(100) emitters at two values of angular intensity and using the crossover analyzer with  $\Omega = 0.54$  mSr.

#### 4. Discussion of Results

##### 4.1 Low Temperature Results

Because of the extraordinarily high values of field attainable for the W(100) built up emitter, a relatively large energy range below the Fermi level (noted on the abscissa by  $E_f$ ) was accessible to the retarding analyzers used in this experiment. For example, the bulge in the TED due to bulk band structure ramifications occurring at  $\epsilon \approx -0.8$  eV, observed previously by Plummer and Gadzuk<sup>21</sup> for emission from the W(100) plane of a thermally-annealed W emitter, is also observed in these studies as shown in Fig. 29. It should be emphasized, however, that in the present case, the (100) crystal plane contains a pyramidal structure<sup>4</sup> with a very small (less than  $20 \text{ \AA}$ ) (100) crystal plane at the tip of the pyramid. Apparently, for the latter reason,

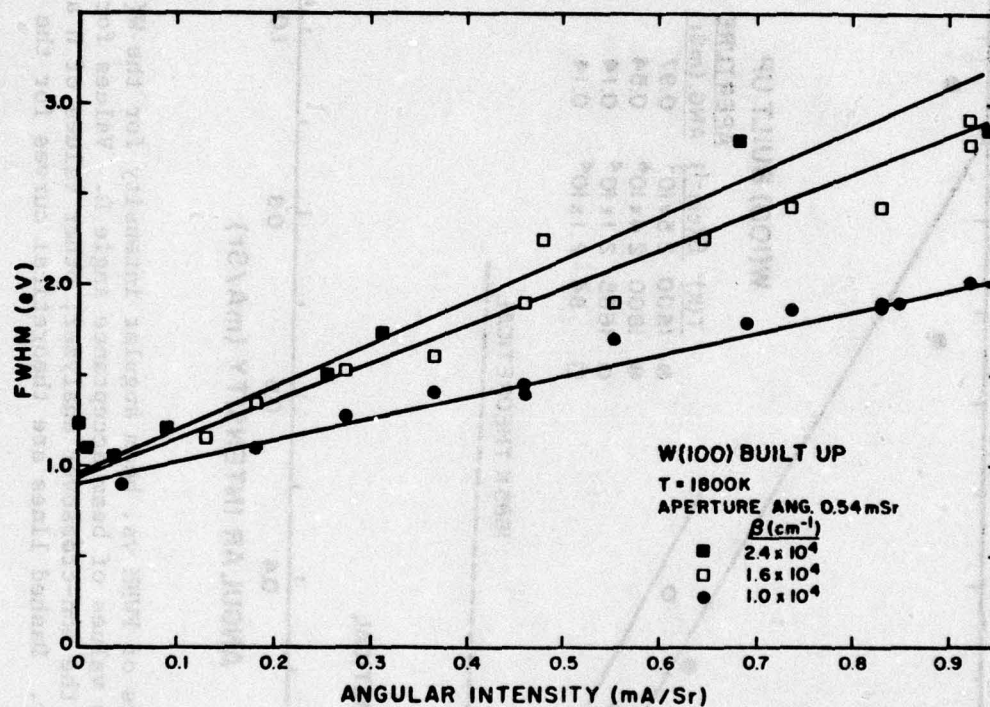


Figure 35. Experimental values of FWHM vs. beam angular intensity for three W(100) built-up emitters with the indicated values of emitter field factor  $\beta$ . Data obtained from the crossover analyzer with  $\Omega = 0.54$  mSr.



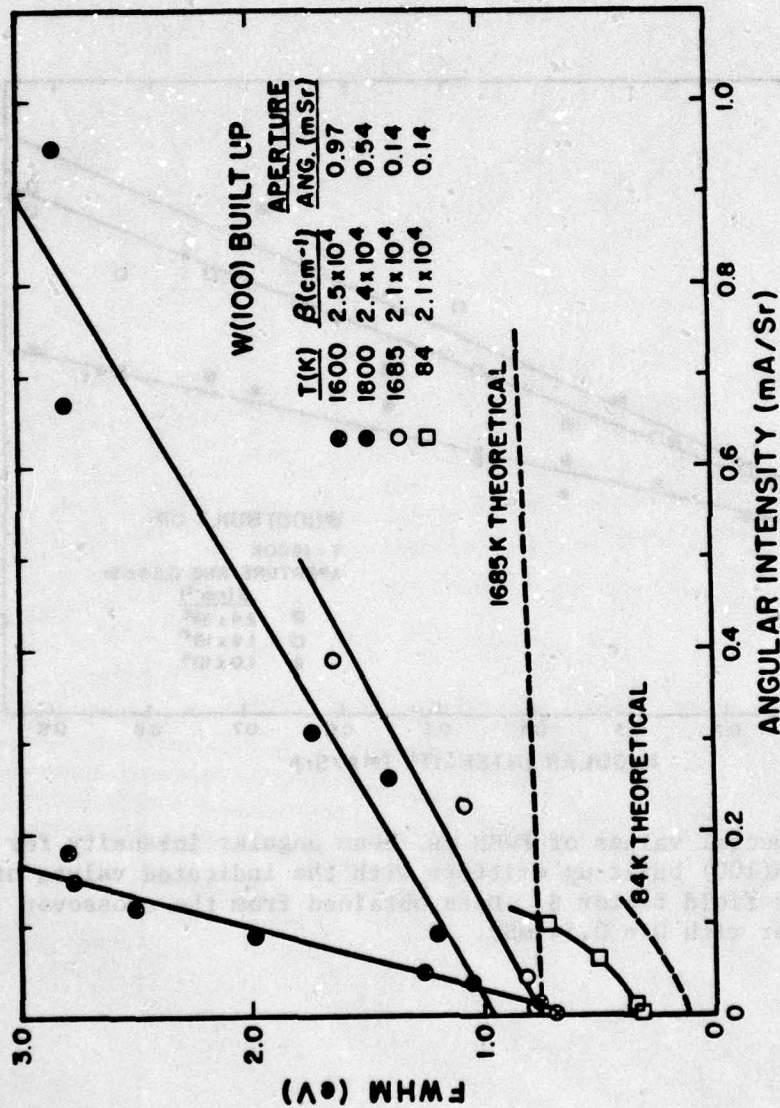


Figure 36. Experimental values of FWHM vs. beam angular intensity for the W(100) built-up emitter at various values of beam acceptance angle  $\Omega$ . Values for  $\Omega = .97$  mSr are obtained from the non-crossover analyzer; other values of  $\Omega$  are taken from crossover analyzer. Dashed lines are theoretical curves for the 84 and 1685 K data.

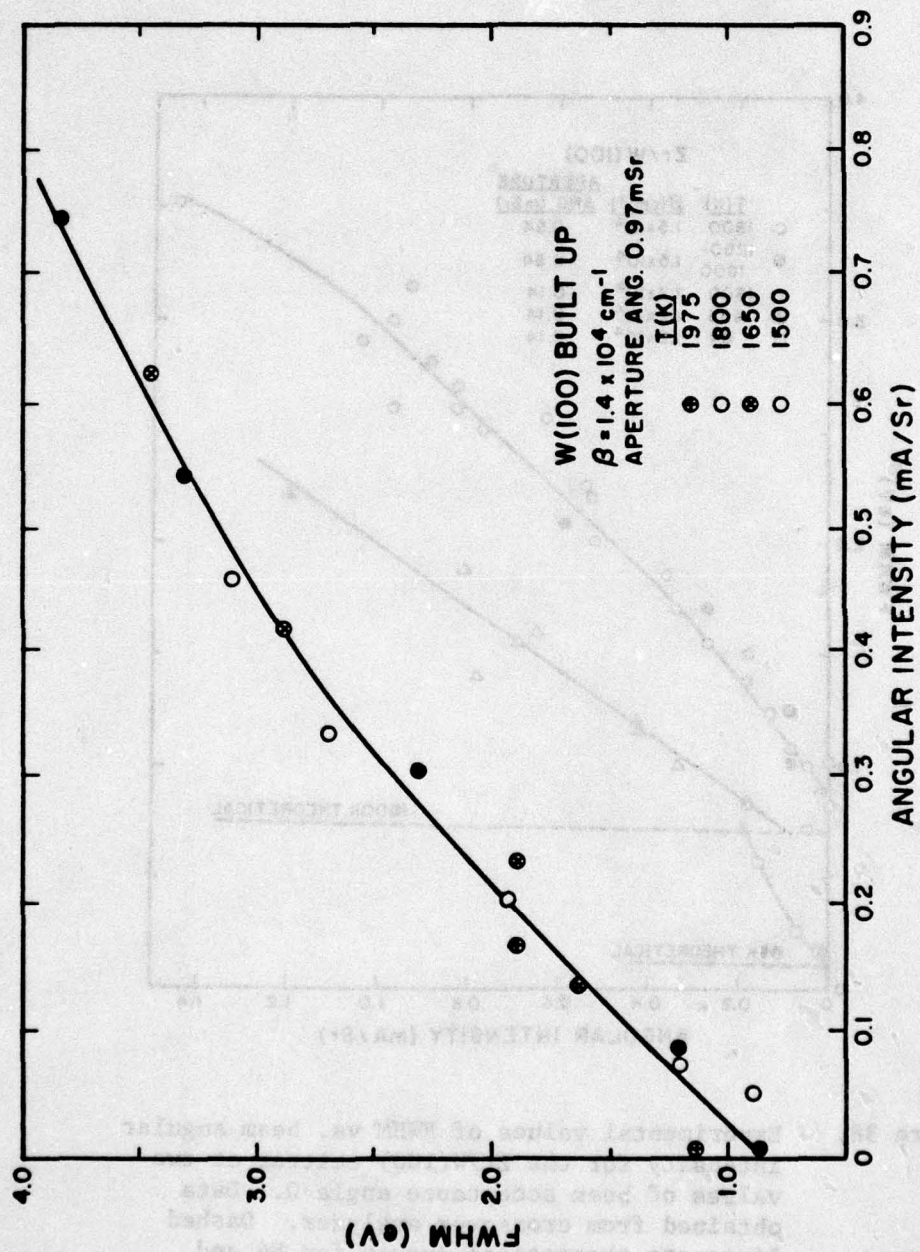


Figure 37. Experimental values of the FWHM vs. beam angular intensity for a W(100) built-up emitter at the indicated temperatures using the non-crossover analyzer.



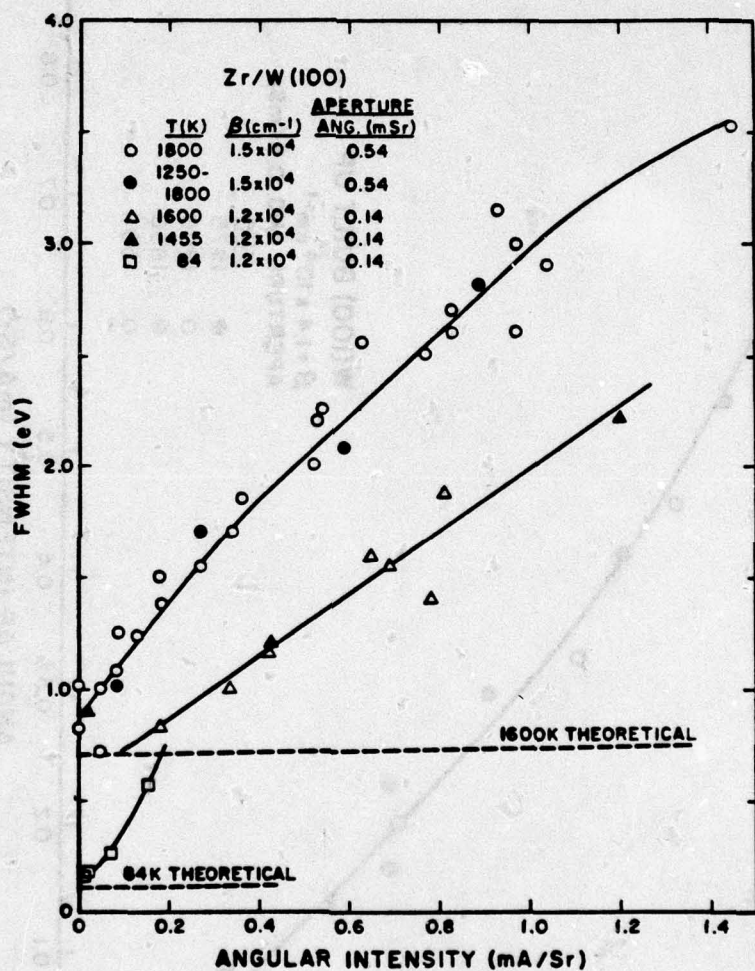


Figure 38. Experimental values of FWHM vs. beam angular intensity for the Zr/W(100) emitter at two values of beam acceptance angle  $\Omega$ . Data obtained from crossover analyzer. Dashed lines are theoretical curves for 84 and 1600 K data.

AD-A078 520

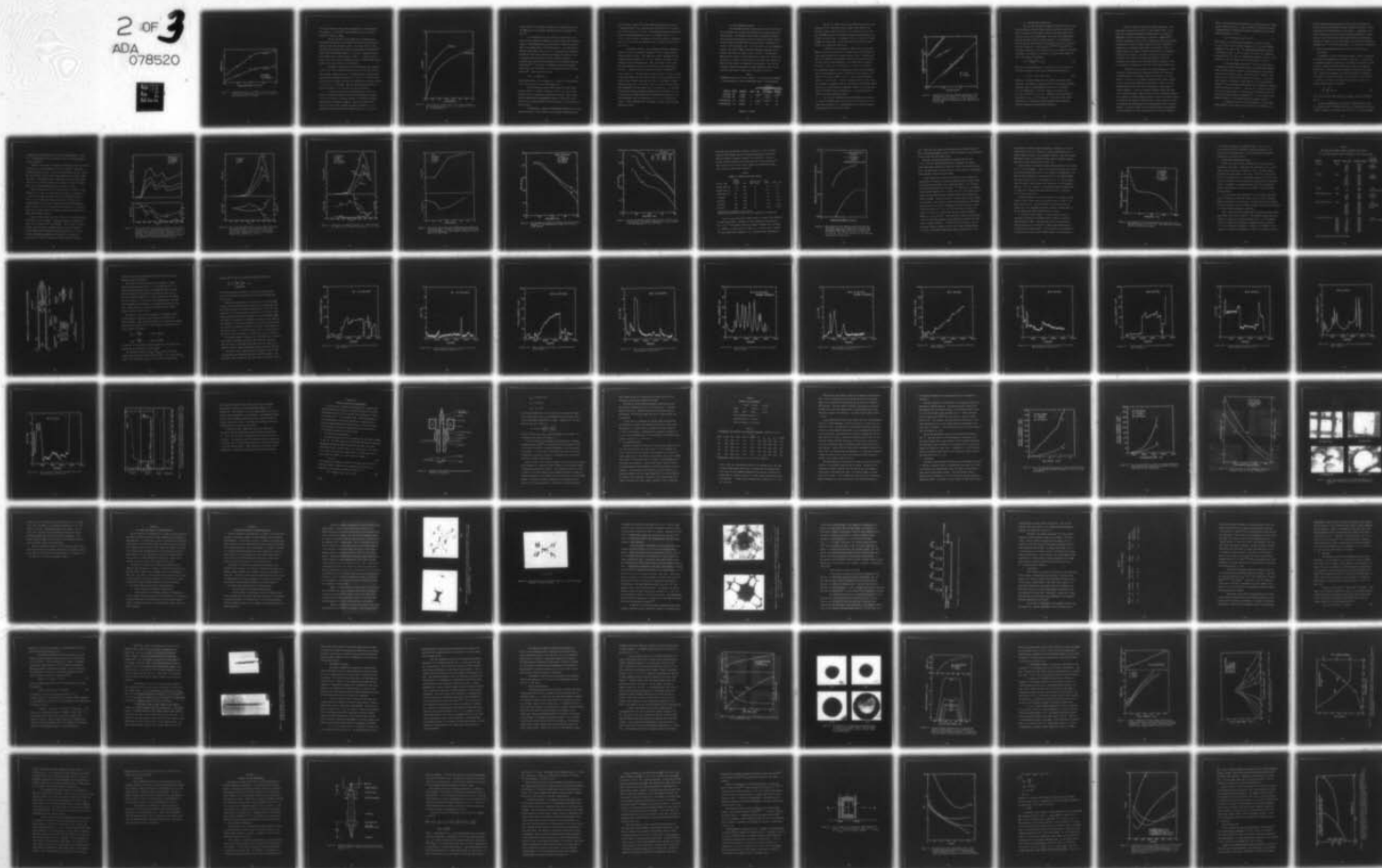
OREGON GRADUATE CENTER BEAVERTON DEPT OF APPLIED PHY--ETC F/G 20/12  
FIELD ELECTRON AND ION SOURCE RESEARCH FOR HIGH DENSITY INFORMA--ETC(U)  
MAY 79 L W SWANSON , J ORLOFF , A E BELL F33615-76-C-1327

UNCLASSIFIED

AFAL-TR-79-1133

NL

2 OF 3  
ADA  
078520





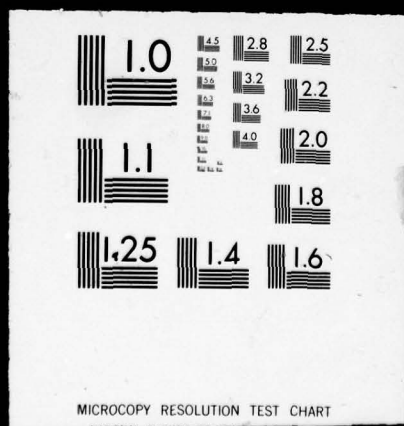
2

OF

3

ADA

078520



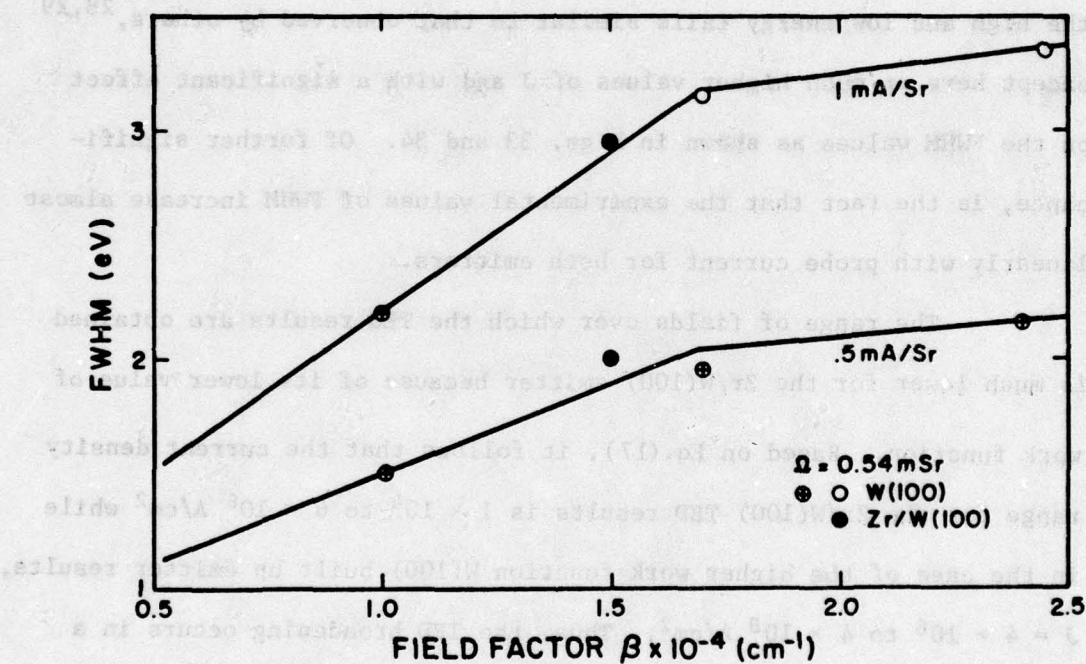


Figure 39. Experimental values of the FWHM vs. the field factor  $\beta$  for  $\Omega = 0.54 \text{ mSr}$ ; upper curve for  $I/\Omega = 1 \text{ mA/Sr}$  and lower curve for  $I/\Omega = 0.5 \text{ mA/Sr}$ .



the surface sensitive peak in the trailing edge of the TED normally occurring at  $\epsilon = -0.35$  eV<sup>18,21</sup> and believed to be due to surface states,<sup>21,41</sup> does not appear.

The Fig. 29 and 31 results show that both emitters give experimental TED curves at 84 K whose deviation from the theoretical curves increase with increasing field. An increase occurs in both the high and low energy tails similar to that observed by others,<sup>28,29</sup> except here at much higher values of  $J$  and with a significant effect on the FWHM values as shown in Figs. 33 and 34. Of further significance, is the fact that the experimental values of FWHM increase almost linearly with probe current for both emitters.

The range of fields over which the TED results are obtained is much lower for the Zr/W(100) emitter because of its lower value of work function. Based on Eq.(17), it follows that the current density range for the Zr/W(100) TED results is  $1 \times 10^4$  to  $6 \times 10^6$  A/cm<sup>2</sup> while in the case of the higher work function W(100) built up emitter results,  $J = 4 \times 10^6$  to  $4 \times 10^8$  A/cm<sup>2</sup>. Thus, the TED broadening occurs in a much lower range of  $J$  for the lower work function emitter.

In terms of the practical considerations as an electron source, it should be pointed out that for a given angular intensity (i.e.  $I/\Omega$ ), the built up emitter, because of its inherently smaller emitting area, operates at a higher  $J$  than the Zr/W(100) emitter. This can be seen in Fig. 40 where the angular intensity vs.  $J$  is compared for the two emitters with similar values of  $\beta$ . Thus, for

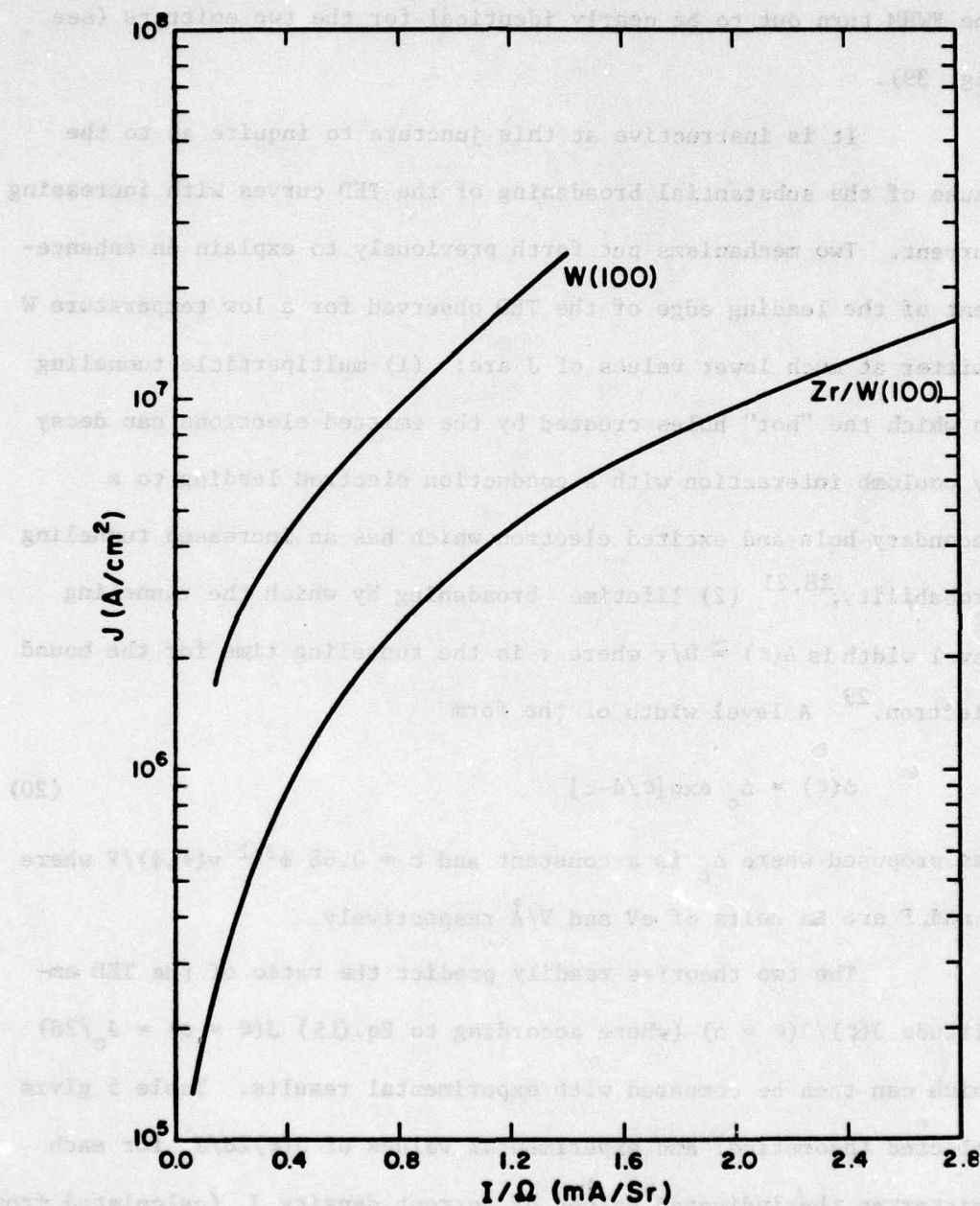


Figure 40. Curves show the current density  $J$  vs. angular intensity for the indicated emitters at  $T = 84$  K where  $\beta \approx 1.1 \times 10^4$  cm<sup>-1</sup> for both emitters.



similar values of  $\beta$  and angular intensity, the respective values of the FWHM turn out to be nearly identical for the two emitters (see Fig. 39).

It is instructive at this juncture to inquire as to the cause of the substantial broadening of the TED curves with increasing current. Two mechanisms put forth previously to explain an enhancement of the leading edge of the TED observed for a low temperature W emitter at much lower values of  $J$  are: (1) multiparticle tunneling in which the "hot" holes created by the emitted electrons can decay by coulomb interaction with a conduction electron leading to a secondary hole and excited electron which has an increased tunneling probability;<sup>28,21</sup> (2) lifetime broadening by which the tunneling level width is  $\Delta(\epsilon) \approx \hbar/\tau$  where  $\tau$  is the tunneling time for the bound electron.<sup>29</sup> A level width of the form

$$\Delta(\epsilon) = \Delta_0 \exp[\epsilon/d-c] \quad (20)$$

was proposed where  $\Delta_0$  is a constant and  $c = 0.68 \phi^{3/2} v(F, \phi)/F$  where  $\phi$  and  $F$  are in units of eV and  $V/\text{\AA}$  respectively.

The two theories readily predict the ratio of the TED amplitude  $J(\epsilon)/J(\epsilon = 0)$  (where according to Eq.(15)  $J(\epsilon = 0) = J_0/2d$ ) which can then be compared with experimental results. Table 5 gives selected theoretical and experimental values of  $J(\epsilon)2d/J_0$  for each emitter at the indicated values of current density  $J_0$  (calculated from Eq.(17)) and  $\epsilon$ .

In attempting to compare the experimental results with the two theoretical models, it was found that the lifetime broadening theory,

while failing to agree with the Zr/W(100) emitter TED results using a reasonable value of  $\Delta_0$ , does agree with the W(100) built up results at  $\epsilon = 0.2$  eV using  $\Delta_0 = 0.35$  eV. The agreement between experiment and theory as shown graphically in Fig. 41 is somewhat poorer at  $\epsilon = 1$  if  $\Delta_0 = 0.35$  eV is used. According to Eq. (20) one obtains a reasonable  $\Delta(\epsilon = 1) = 0.27$  eV for the indicated value of  $\Delta_0$  when  $F = 0.79$  V/Å and  $\phi = 4.5$  eV.

According to Table 5, the cascading multiparticle tunneling model, which has no adjustable parameters,<sup>29</sup> fails to agree with the built-up emitter results. This model does exhibit agreement with the Zr/W(100) emitter results at  $\epsilon = 0.2$  eV. However, this model is inadequate for the following reason: Figs. 29 through 32 show clearly that TED broadening occurs on both the high and low-energy sides of the TED. A similar result was obtained by Gadzuk and Plummer<sup>29</sup> at lower values of  $J$ . The multiparticle tunneling model involves a coulomb interaction between the "hot" holes formed by electron emission and conduction state electrons such that the latter are scattered to higher-momentum states prior to tunneling. Thus, this model fails to predict the broadening of the low-energy side of the TED curves. We therefore conclude that another broadening mechanism must be operative in order to explain the Zr/W(100) results and the discrepancy between the lifetime broadening theory and experiment at  $J(\epsilon = 1)$  for the built-up emitter. Before examining other mechanisms, we shall review the high-temperature results.



## 4.2 High Temperature Results

The high temperature TED results given in Figs. 30 and 32 for the two emitters show a much larger deviation of the high energy tail from FN theory. The Zr/W(100) results show a substantial deviation from theoretical expectations on both the high and low-energy sides of the TED, whereas the W(100) built-up emitter shows a predominant deviation on the high-energy side. As in the case of the low temperature results, the value of FWHM at elevated temperature increases almost linearly with current as shown in Figs. 33 and 34. The increase of FWHM with beam current is shown dramatically in Figs. 35 to 38 for the two emitters. Figures 37 and 38 show that the near-linear increase of FWHM with beam current is independent of temperature. Even the low temperature FWHM values approach the high temperature values at sufficiently high values of beam current (see Figs. 36 and 37).

TABLE 5

EXPERIMENTAL VALUES OF  $J(\epsilon)2d/J_0$  FOR THE  $T = 84$  K RESULTS ARE COMPARED WITH PREDICTIONS OF THE TWO THEORETICAL MODELS OF TED BROADENING

Emitter	F(V/A)	J(A/cm <sup>2</sup> )	$\epsilon$ (eV)	J( $\epsilon$ )2d/J <sub>0</sub>		
				EXP	Lifetime Broadening*	Electron Cascade
Zr/W(100)	.207	3.2x10 <sup>5</sup>	1	5.9x10 <sup>-2</sup>	2.9x10 <sup>-5</sup>	1.0x10 <sup>-3</sup>
Zr/W(100)	.207	3.2x10 <sup>5</sup>	.2	.55	7.7x10 <sup>-4</sup>	.34
W(100)Buildup	.79	8.0x10 <sup>7</sup>	1	6.7x10 <sup>-3</sup>	9.4x10 <sup>-4</sup>	.19
W(100)Buildup	.79	8.0x10 <sup>7</sup>	.2	.16	.13	50

\*Using  $\Delta_0 = 0.35$ eV

The Fig. 35 results show that the FWHM values decrease with decreasing  $\beta$  for a specified value of angular beam intensity  $I/\Omega$ . Curiously, Figs. 36 and 38 show that, for a constant value of  $\beta$  and  $I/\Omega$ , the FWHM values for both emitters increase with increasing value of beam acceptance angle. For example, in Fig. 37 where  $\Omega = 0.97$  mSr, a FWHM value approaching 4 eV was measured at 0.9 mA/Sr-more than 3 eV above the theoretical expectation!

In addition to the variation of FWHM with  $\Omega$ , we note that FWHM values for the W(100) built-up emitter shown in Fig. 39 also decrease significantly with increasing emitter radius. Although only one value of FWHM for the Zr/W(100) emitter was obtained in Fig. 39, its value agrees closely with that of the W(100) built-up emitter. According to Fig. 40 at a given value of  $\beta$  and  $I/\Omega$ , the value of  $J$  is considerably larger for the higher work function built-up emitter. Thus, the near-identical values of FWHM for the two emitters, as observed in Fig. 39 at a given  $\beta$  and  $I/\Omega$ , occur at widely-differing values of  $J$  as well as  $F$ . It may be concluded that for a given angular intensity, the higher values of  $J$  obtained for the built-up emitter do not lead to higher values of FWHM when compared to the lower work function Zr/W(100) emitter presumably due to a compensating factor such as the increased electric field.

The fact that the built-up emitter exhibits lower values of  $I/\Omega$  than the Zr/W(100) emitter for the same  $J$  is probably due to the larger beam divergence (i.e. high magnification) from the pyramidal-shaped structure of the built-up emitter.



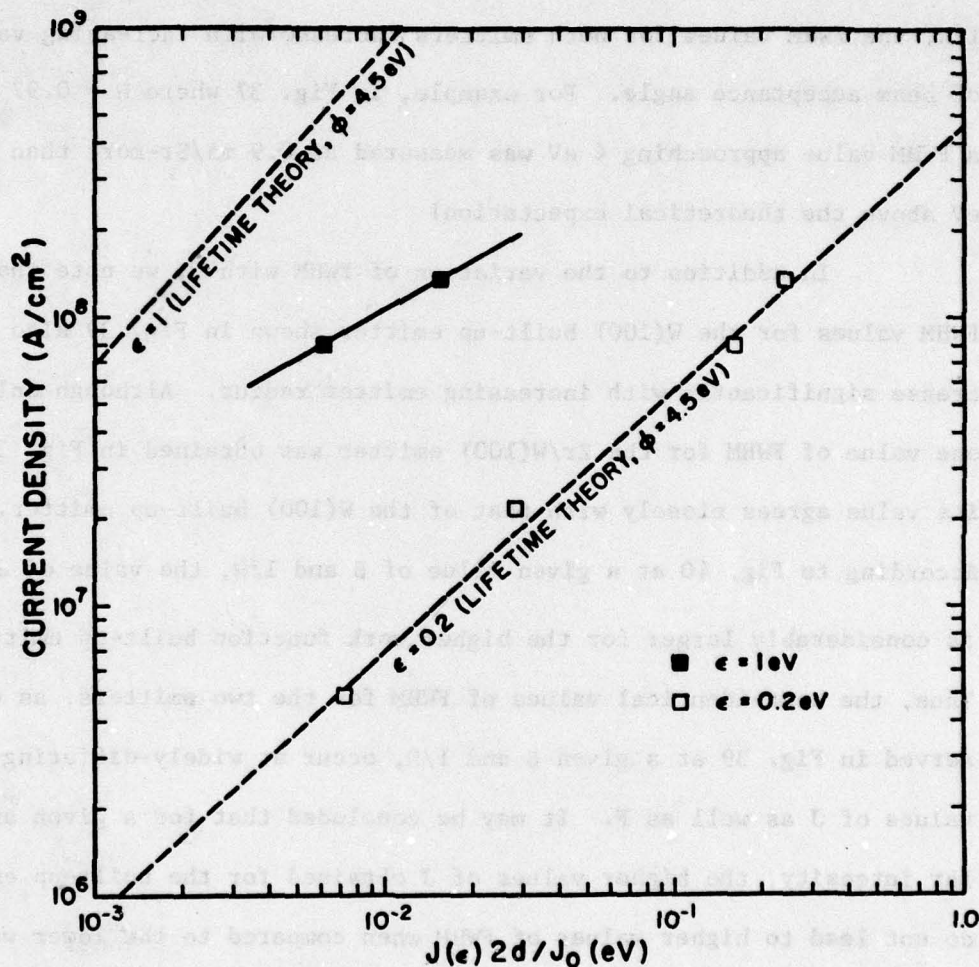


Figure 41. Experimental values and indicated theoretical curves (dashed lines) of  $J(\epsilon)2d/J_0$  vs. current density for the W(100) built-up emitter at  $T = 84$  K and the indicated values of  $\epsilon$  using the crossover analyzer where  $\Omega = 0.14$  mSr.

### 4.3 External Beam Interactions

The fact that anomalous broadening of the TED occurs in data from two different kinds of energy analyzer, one with a high-current density crossover and one without, tends to eliminate analyzer artifacts as a source of the broadening. Since most of the experimental data was obtained from the crossover analyzer, it is worthwhile to estimate the well known energy broadening which occurs in an electron beam drift region or at a beam crossover.<sup>33-36,42</sup> Loeffler<sup>33</sup> has calculated a quantity  $\Omega_0$  as a function of  $\lambda r_0$  and presented the results in graphical form where  $\Omega_0$  is related to the beam energy spread  $\Delta E$  due to the crossover according to

$$\Delta E = \frac{1.44 \times 10^{-7}}{\alpha_0 r_0} \Omega_0 \text{ (eV)} \quad (21)$$

where  $\alpha_0$  is the beam half-angle in radians, and  $r_0$  is the radius in cm of the crossover;  $\lambda$  is the axial electron density given by:

$$\lambda = 1.053 \times 10^{11} I/V_0^{1/2} \text{ (cm}^{-1}\text{)} \quad (22)$$

where  $V_0$  is the beam voltage and  $I$  the current in amperes at the crossover. Calculation of lens properties of the crossover analyzer indicates that  $V_0$  is approximately 0.2 volts at the crossover  $\alpha_0 \sim 0.1$  radian; and  $r_0 \sim 10^{-4}$  cm. Hence,  $\Delta E \sim 0.014 \Omega_0$  and  $\lambda = 2.35 \times 10^4 \text{ cm}^{-1}$  so  $\lambda r_0 = 2.35$ . Loeffler's curves show that at this value of  $\lambda r_0$ ,  $\Omega_0 \sim 15$  so that  $\Delta E \sim 0.21$  volts, which, while significant, is still below the experimental values observed in both the crossover and non-crossover analyzers.



While the previously mentioned internal mechanisms of TED broadening can account for a portion of the observed effect, we conclude that an additional mechanism involving electron interaction immediately in front of the emitter is operative. Zimmerman<sup>34</sup> describes a mechanism by which a beam of charged particles, whose initial distribution of velocity between transverse and axial components is changed due to acceleration when viewed in the center of mass coordinate system, can undergo collective interactions at a subsequent crossover or drift space. The latter interaction, which tends to "thermalize" or restore the initial equi-partition of velocity components, when viewed in the laboratory frame of reference, leads to a substantial broadening of the initial total energy distribution.

Loeffler<sup>33</sup> has calculated this energy broadening at a beam crossover, as discussed above, and points out that the "electrons contributing most to the energy spread are those that stay closely behind or in front of the reference electron and move almost parallel to it or on only slowly-diverging trajectories"; clearly, the field emission source itself falls into this category at high values of angular intensity. In his calculations of energy spread, discussed above, Loeffler assumes a beam crossover with electrons moving through the crossover at constant energy  $V_0$  whereas at the field emission source, the electrons are rapidly accelerated from a virtual crossover so that acceleration and thermalization occur simultaneously near the emitter. However, it has been found<sup>43</sup> that the same functional relationship derived by Loeffler for a beam crossover holds for the more realistic

model of an electron beam accelerated from a spherical source of radius  $r'_0$  by a distant anode at  $V_0$ . Thus, according to Loeffler, the energy broadening  $\Delta E$  due to external interactions expressed in terms of beam angular intensity  $I' = I/\Omega$  is

$$\Delta E = \pi^{1/2} k(\lambda r'_0) (I'/r'_0)^{1/2} V_0^{-1/4} \quad (23)$$

where  $k(\lambda r'_0)$  is a slowly-varying logarithmic function of  $\lambda$  and  $r'_0$ .

We can see that  $\Delta E$  is only weakly dependent on  $V_0$ , but more strongly dependent on the ratio  $I'/r'_0$ . The experimental dependence of  $\Delta E$  on  $I'$ , according to Figs. 37 and 38, supports the square root dependence predicted by Eq.(21); also, the experimental dependence of  $\Delta E$  on  $\beta \propto 1/r'_0$  according to Fig. 39 conforms with the expectations of Eq.(23).

At constant angular intensity  $I'$  Eq.(23) does not predict an increase in  $\Delta E$  with beam aperture angle as observed experimentally. Such an effect could be a result of the non-homogeneous space charge potential that decreases with  $\alpha_0$ , thereby imparting a greater transverse velocity to those electrons emitted at larger  $\alpha_0$ . Since transverse velocity is converted to axial velocity for the field emitter geometry,<sup>18</sup> the total energy distribution will be broadened by accepting electrons emitted with larger  $\alpha_0$ . The fact that a space charge effect occurs at the high values of  $J$  employed here is confirmed both by the deviations observed from the FN equation<sup>4,6,31</sup> and an increase in the angular divergence of the electron beam with applied voltage.<sup>4,7</sup>

In conclusion, we note that the broadening of the TED FWHM values measured in this study can be explained by a combination of an



internal lifetime broadening mechanism and collective coulomb interactions involving transformation between transverse and radial velocity components in the region exterior to the emitter. A knowledge of the exact contributions of the two energy-broadening mechanisms at various values of current density must await further theoretical development, although the results of this study indicate that the external mechanism dominates for  $J > 10^6$  and  $10^8$  A/cm<sup>2</sup> where  $\phi = 2.5$  and  $4.5$  eV respectively.

#### F. Noise Study Comparison Between Zr/W(100) and W(100) Built-up TF Cathodes

A comparison of current fluctuations between a built up W(100) and zirconium coated tungsten field cathode is given here. In all cases the acceptance aperture solid angle at the emitter was between 0.11 and 0.14 msr. Current fluctuations were made by using a well-shielded Faraday cup to collect the current transmitted through the beam aperture. Quan-Tech and Tektronix 1L5 spectrum analyzers were employed to measure the frequency dependence of the rms noise current  $\overline{\Delta I}$  from 1 to  $10^5$  Hz. The data is, in some cases, reported in terms of the spectral density function  $W(f)$  where

$$\overline{\Delta I^2} = \int_{f_1}^{f_2} W(f) df \quad (24)$$

and  $f_1$  and  $f_2$  are the lower and upper frequency range of the measurement.

The noise measurements as a function of temperature were taken at a constant value of transmitted current  $I_p$  by adjusting the emitter-to-anode voltage  $V$ . The emitter field factors  $\beta = F/V$  were determined

according to Eq.(3) from FN plots of the  $I(V)$  characteristics. Since  $\beta \propto r^{-1}$ , the relative size of the emitter radius  $r$  can be established from the  $\beta$  factors.

Figures 42 and 43 show the temperature dependence of the rms current fluctuation in a narrow bandwidth for the two cathodes. The current fluctuation maxima occur at  $\sim 700$  K for the W(100) built up and  $\sim 1300$  K for the Zr/W(100) with the former maximum exhibiting a value of 3 times the latter. The reproducibility of the sharp decrease in noise above 1600 K for the Zr/W(100) cathode was not always as dramatic as shown here, but a definite maximum seems to be a general result.

Figure 44 shows the effect of pressure on the 2 kHz  $\overline{\Delta I}/I_p$  vs temperature curve of Fig. 43. These results show that a CO pressure of  $3 \times 10^{-8}$  torr actually decreases the current fluctuation amplitude. Fig. 45, on the other hand, shows the variation of  $\overline{\Delta I}/I_p$  for the Zr/W(100) emitter as the beam is deflected across the beam defining aperture using a set of electrostatic deflection plates. The results show that the central portion of the beam is the least noisy for this particular Zr/W(100) cathode.

Figures 46 and 47 show a fall off in the spectral density function  $W(f)$  with  $f$  for both cathodes. Interesting structure is observed in these curves, especially for the Zr/W(100). Table 6 gives the values of  $\overline{\Delta I}/I_p$  over the complete frequency range for the two cathodes at various temperatures and angular current intensity (i.e.  $I/\Omega$ , where  $\Omega$  is the solid angle subtended at the emitter by the aperture). We note that the built up cathode has a larger current fluctuation



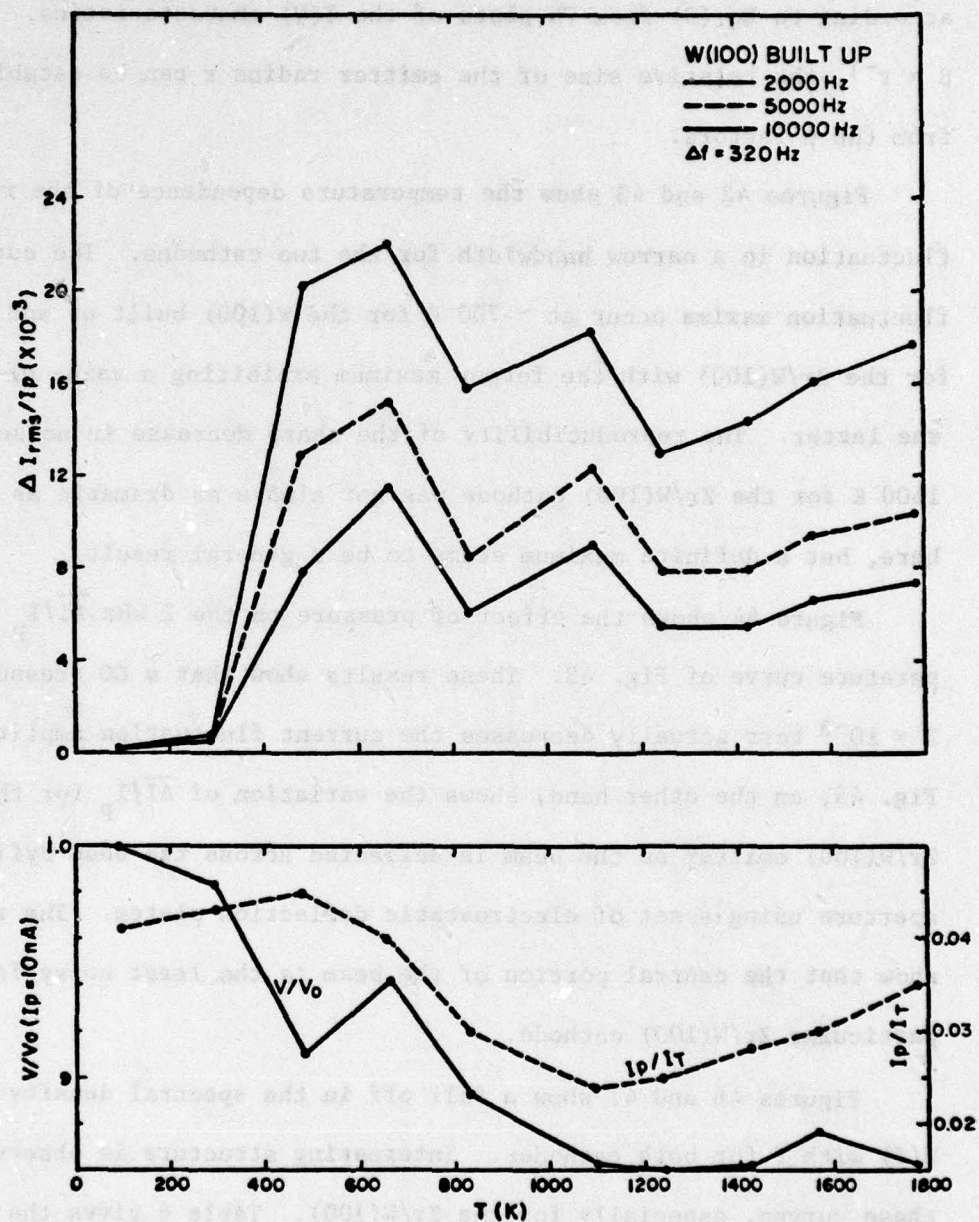


Figure 42. Upper curves show the variation of relative noise level of a W(100) built up emitter with temperature at 3 frequency intervals and a 320 Hz band width. The probe current through a 10 mrad aperture was held constant at  $I_p = 10$  nA. The lower curve shows the relative variation in voltage with temperature to maintain a constant current.

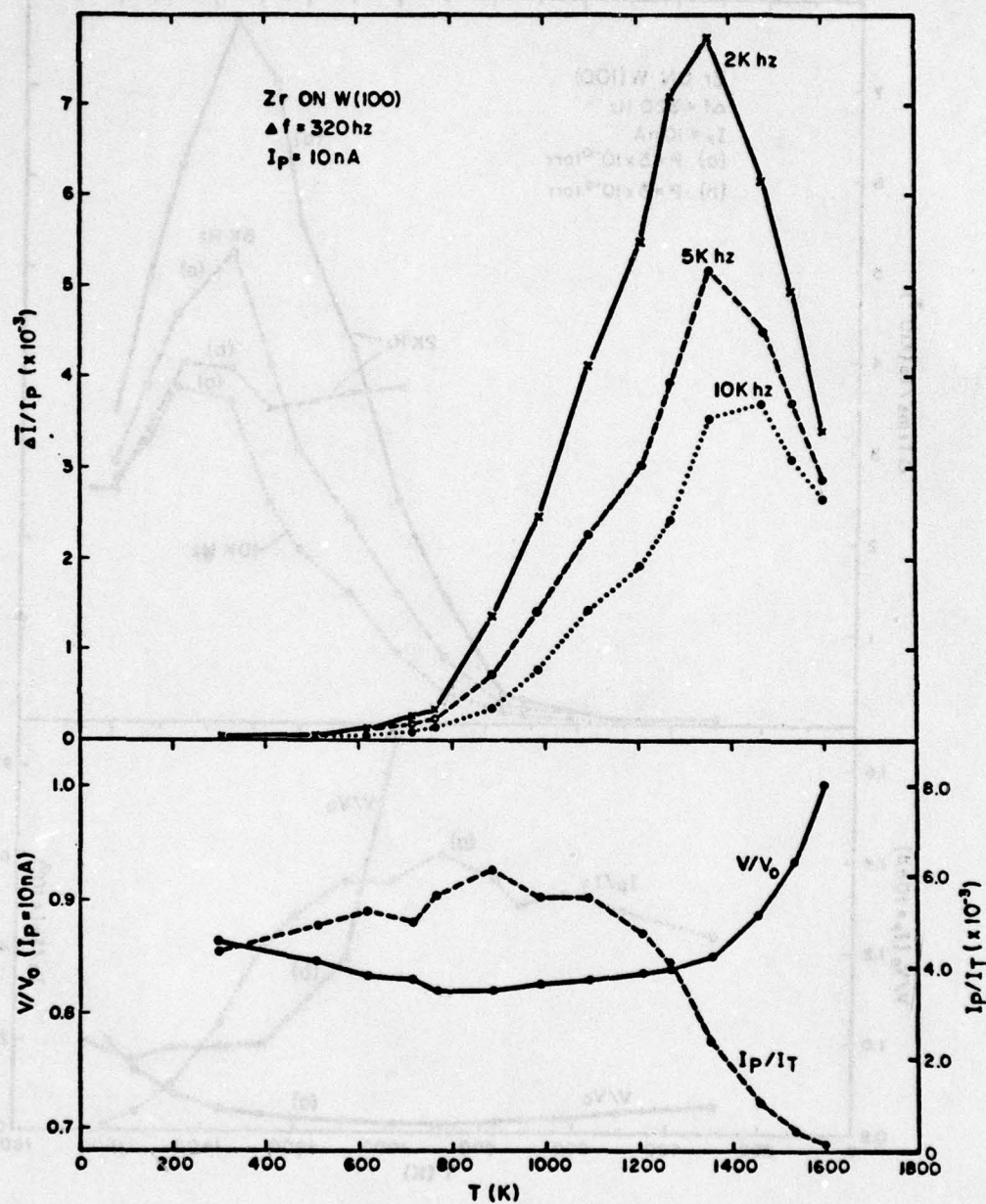


Figure 43. Plot of the rms noise level vs emitter temperature using the current through a 13 mrad. aperture from a Zr/W field cathode. Lower curves show the corresponding plots of the transmitted current  $I_p/I_T$  and relative voltage  $V/V_0$  to maintain  $I_p = 10$  nA.



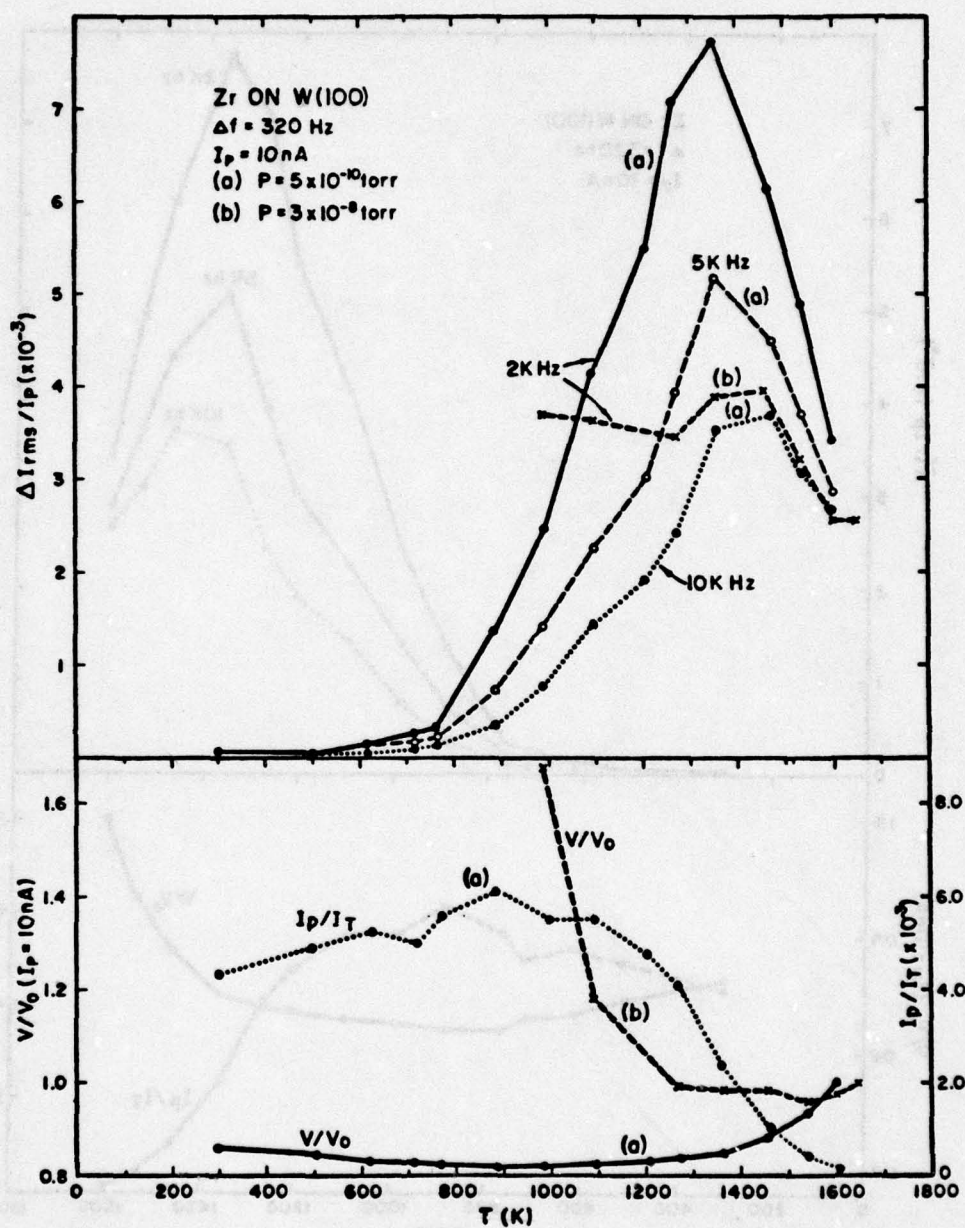


Figure 44. Curves (a) are obtained from Fig. 43. Curves (b) show the same plot at a background pressure of  $3 \times 10^{-8}$  torr.

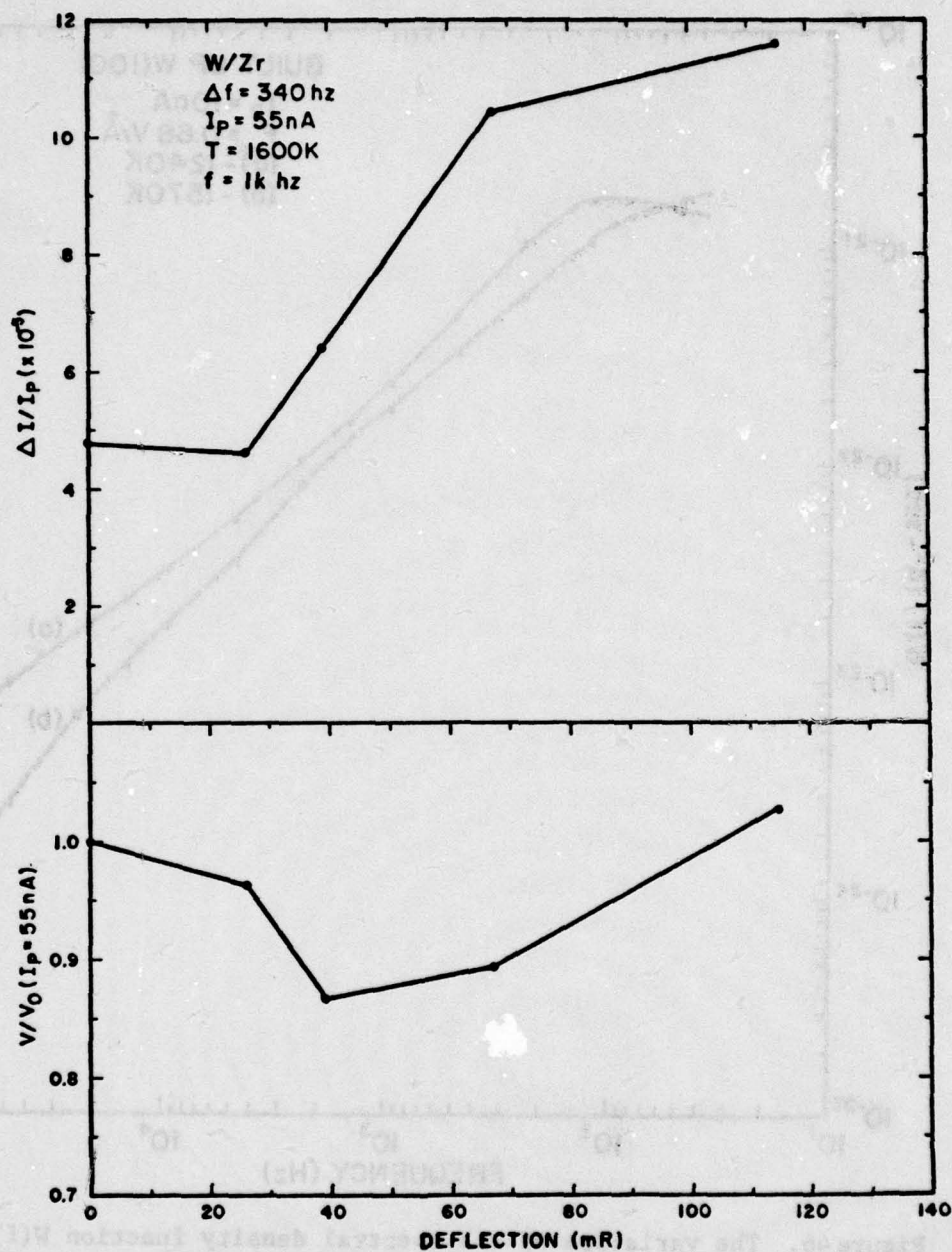


Figure 45. Plot of the rms noise level vs beam deflection angle from the emitter axis. A 10 mrad. aperture angle was employed. Lower curve shows plot of the relative voltage for  $I_p = 55 \text{ nA}$ ,  $P = 5 \times 10^{-10} \text{ torr}$ .



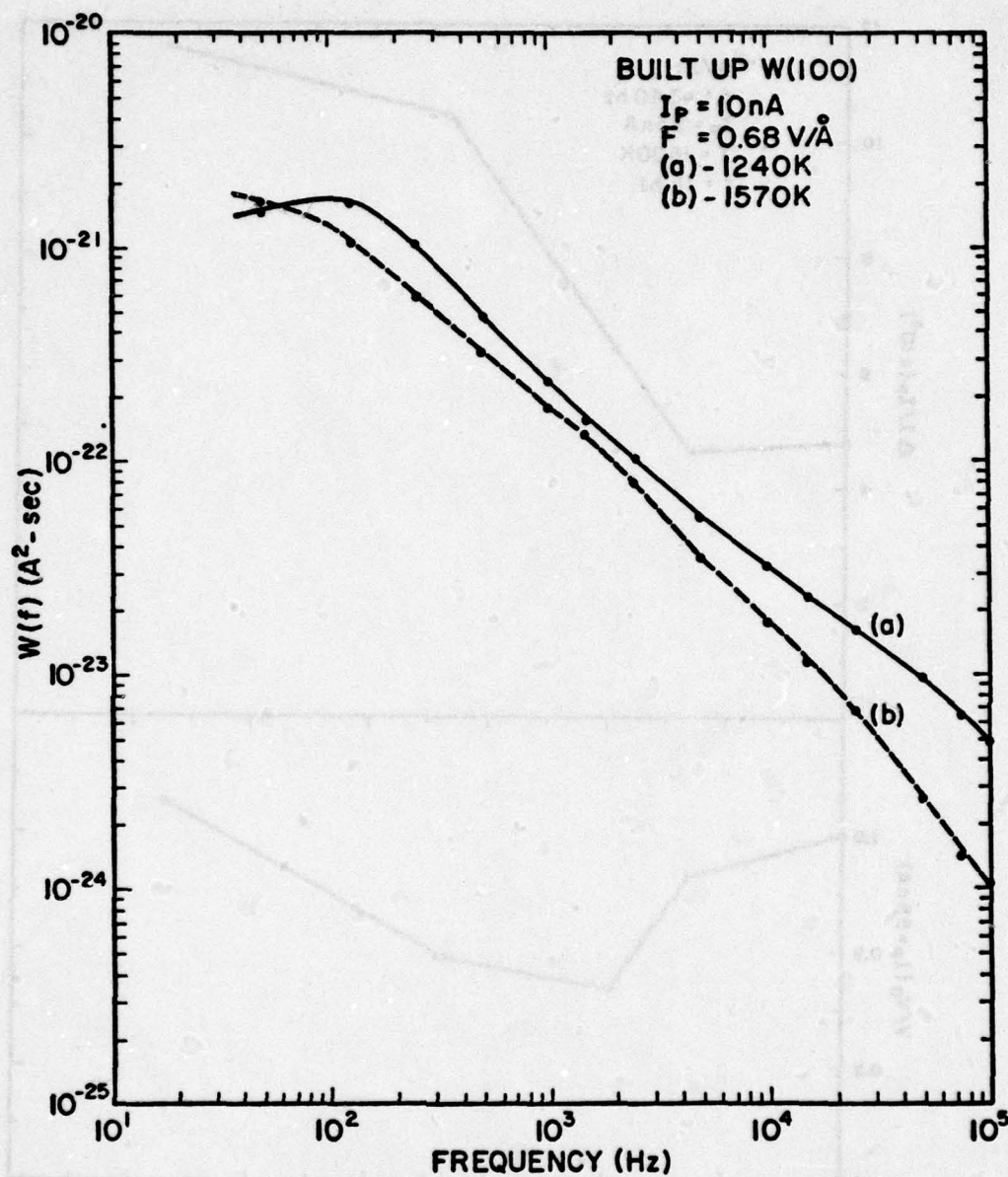


Figure 46. The variation of the spectral density function  $W(f)$  with frequency at two temperatures is given for a built up  $W(100)$  emitter.

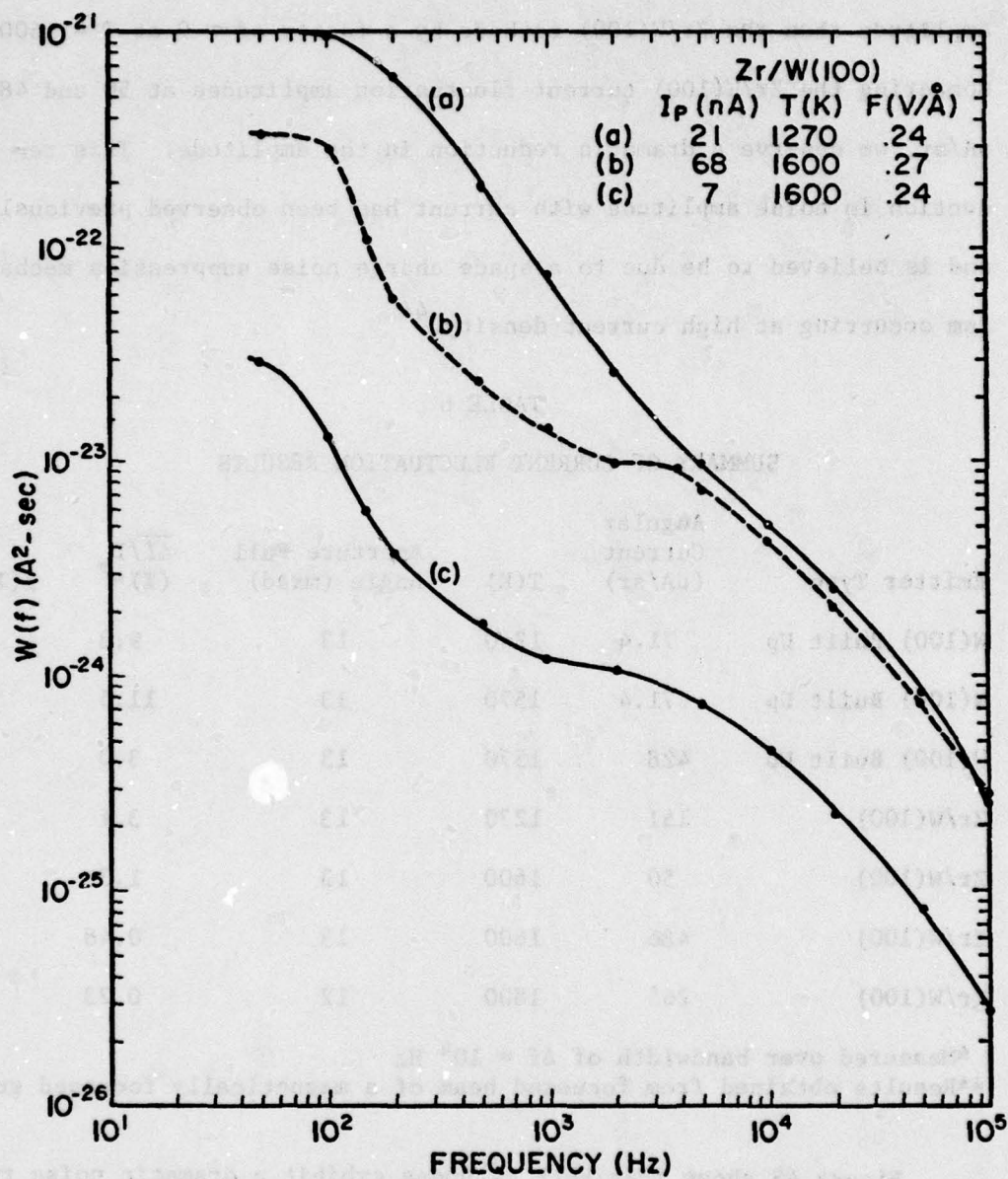


Figure 47. Plot of the spectral density function  $W(f)$  vs  $f$  for a Zr/W field cathode. Measurements obtained from current through a 13 mrad. aperture,  $P = 5 \times 10^{-10}$  torr.



amplitude than the Zr/W(100) cathode by a factor of  $\sim 9$  at  $T = 1600$  K. Comparing the Zr/W(100) current fluctuation amplitudes at 50 and 486  $\mu\text{A}/\text{sr}$ , we observe a dramatic reduction in the amplitude. This reduction in noise amplitude with current has been observed previously<sup>14</sup> and is believed to be due to a space charge noise suppression mechanism occurring at high current density.<sup>44</sup>

TABLE 6  
SUMMARY OF CURRENT FLUCTUATION RESULTS

Emitter Type	Angular Current ( $\mu\text{A}/\text{sr}$ )	T(K)	Aperture Full Angle (mrad)	$\overline{\Delta I}/I$ (%) *P	$\beta (10^4 \text{ cm}^{-1})$
W(100) Built Up	71.4	1240	13	9.3	2.0
W(100) Built Up	71.4	1570	13	11.5	2.0
W(100) Built Up	428	1570	13	3.0	2.0
Zr/W(100)	151	1270	13	3.1	1.23
Zr/W(100)	50	1600	13	1.3	1.23
Zr/W(100)	486	1600	13	0.48	1.23
Zr/W(100)	265	1800	12	0.23	0.1**

\*Measured over bandwidth of  $\Delta f = 10^4$  Hz

\*\*Results obtained from focussed beam of a magnetically focussed gun

Figure 48 shows that both cathodes exhibit a dramatic noise reduction at high beam currents. Normally, at lower currents we found that  $W(f) \propto I_p^2$ ,<sup>7,14</sup> which means that  $\overline{\Delta I}/I_p$  is nearly constant with increasing  $I_p$ . However, as shown in Fig. 48, when  $I_p/\Omega > 0.1 \text{ mA}/\text{sr}$ ,  $W(f)$ , instead of being quadratically dependent on  $I_p/\Omega$ , becomes almost independent of

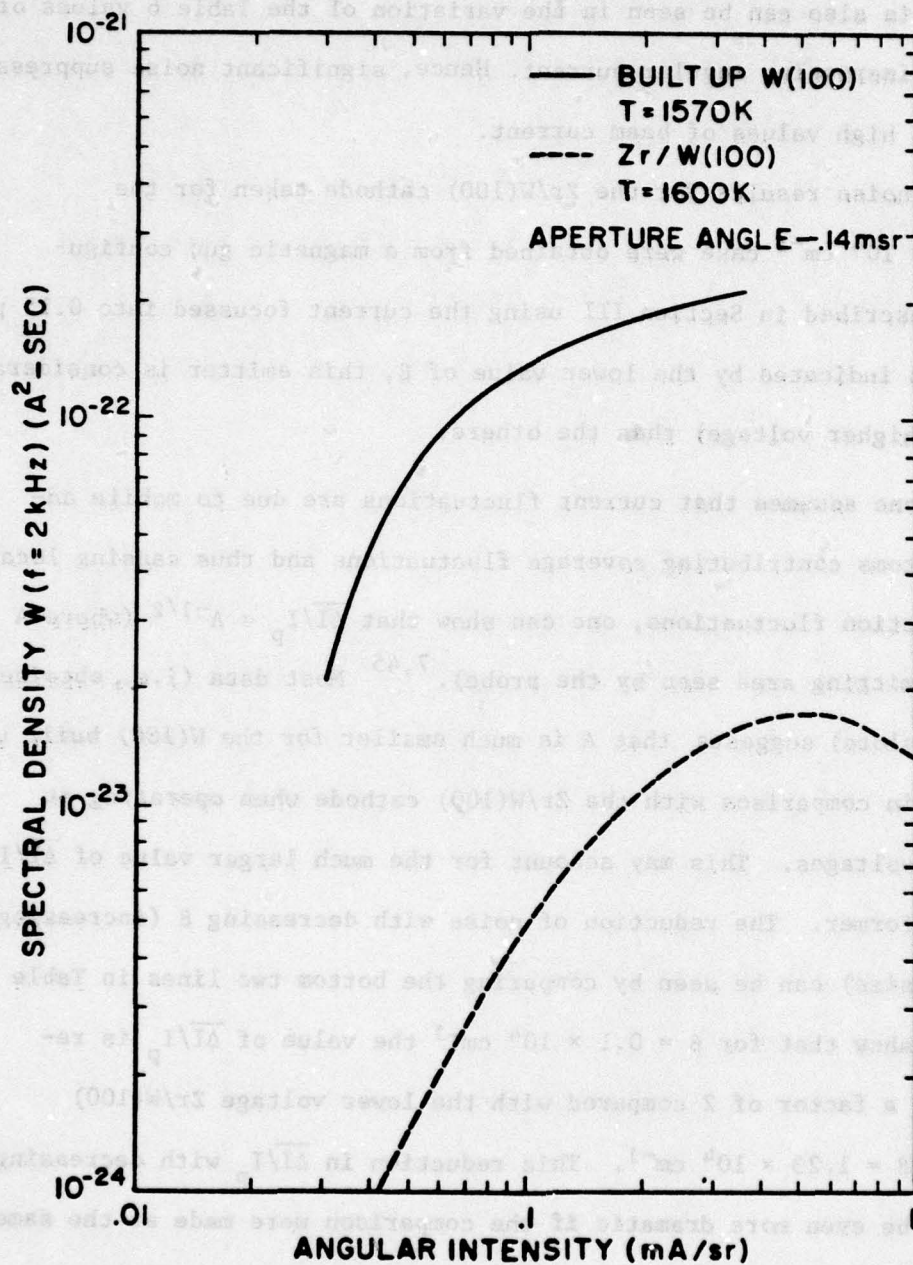


Figure 48. The variation of the spectral density function  $W(f)$  with probe current  $I_p$  is given for the built up and zirconium coated W(100) emitters at  $f = 2000$  Hz and  $\Delta f \approx 300$  Hz. The  $\beta$  values for these emitters were  $2.0$  and  $1.23 \times 10^4 \text{ cm}^{-1}$  for the built-up and zirconium coated emitters respectively.



$I_p/\Omega$ . This also can be seen in the variation of the Table 6 values of  $\overline{\Delta I}/I$  for increasing angular current. Hence, significant noise suppression occurs at high values of beam current.

The noise results for the Zr/W(100) cathode taken for the  $\beta = 0.1 \times 10^4 \text{ cm}^{-1}$  case were obtained from a magnetic gun configuration described in Section III using the current focussed into 0.15  $\mu\text{m}$  spot. As indicated by the lower value of  $\beta$ , this emitter is considerably duller (higher voltage) than the others.

If one assumes that current fluctuations are due to mobile adsorbed atoms contributing coverage fluctuations and thus causing local work function fluctuations, one can show that  $\overline{\Delta I}/I_p \propto A^{-1/2}$  (where  $A$  is the emitting area seen by the probe).<sup>7,45</sup> Most data (i.e., obtained from FN plots) suggests that  $A$  is much smaller for the W(100) built up cathode in comparison with the Zr/W(100) cathode when operating at similar voltages. This may account for the much larger value of  $\overline{\Delta I}/I_p$  for the former. The reduction of noise with decreasing  $\beta$  (increasing emitter size) can be seen by comparing the bottom two lines in Table 6 which show that for  $\beta = 0.1 \times 10^4 \text{ cm}^{-1}$  the value of  $\overline{\Delta I}/I_p$  is reduced by a factor of 2 compared with the lower voltage Zr/W(100) emitter  $\beta = 1.23 \times 10^4 \text{ cm}^{-1}$ . This reduction in  $\overline{\Delta I}/I_p$  with decreasing  $\beta$  would be even more dramatic if the comparison were made at the same value of angular intensity. It should also be pointed out that the low value of  $\overline{\Delta I}/I_p$  in Table 6 for the low  $\beta$  value Zr/W(100) emitter is not due to the space charge effect since in this case  $W(f) \propto I_p^2$

in the angular intensity range investigated. Apparently, due to the larger radius of the low  $\beta$  emitter the cathode current density for a specific angular intensity is considerably reduced. Thus, space charge suppression occurs at considerably larger values of angular intensity than the 0.1 mA/sr value observed in Fig. 48.

Figure 49 gives the spectral density function  $W(f)$  for the Zr/W(100)  $\beta = 0.1 \times 10^4 \text{ cm}^{-1}$  emitter. Recall that this emitter was in an electron beam column and the noise taken from the submicron focussed beam. For these results the Quan-Tech spectrum analyzer was used which allowed the lower frequency limit to be extended to 1 Hz. It can be observed that  $W(f)$  shows a rapid decrease with increasing  $f$  in the frequency interval 1 to 10 Hz. However, as indicated in Table 6 the mean noise to signal ratio obtained from integration of Eq.(24) in interval 0 to  $10^4$  Hz was only 0.23%.

Another comparison of practical interest is the values of transmitted to total current ratios  $I_p/I_T$  given in Figs. 42 and 43. At 1600 K this ratio is  $\sim 300$  times greater for the W(100) built up cathode due to the negligible thermionic emission contributing to  $I_T$  for the higher work function W(100) built-up cathode.

In conclusion these results show that at similar values of  $\beta$  and angular intensity the Zr/W(100) emitter exhibits an almost 10 times reduction in  $\overline{\Delta I}/I$ . This seems to be due to the inherently smaller emitting area of the built up emitter when viewed through a specified beam aperture angle. This conclusion is corroborated by the reduction in noise for the Zr/W(100) emitter with decreasing  $\beta$ .



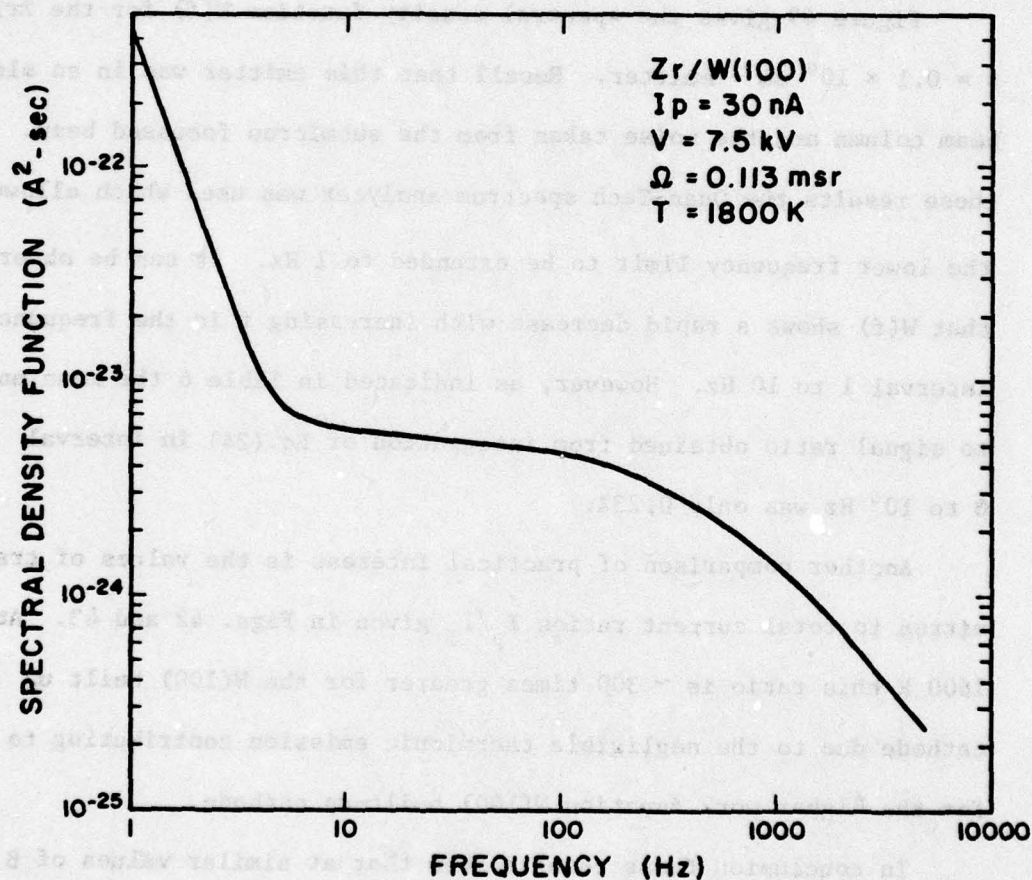


Figure 49. The variation of the spectral density function  $W(f)$  for the Zr/W(100) with  $\beta = 0.1 \times 10^4 \text{ cm}^{-1}$ . Data taken from a focussed beam in an electron gun column.

For emitters with values of  $\beta$  between 1 and  $2 \times 10^4 \text{ cm}^{-1}$  a further reduction in  $\overline{\Delta I}/I$  is observed at angular intensities ( $> 0.1 \text{ mA/sr}$ ) and is most likely due to a space charge noise suppression occurring at the emitter surface.

#### G. Thermal-Field Cathode Life Studies

Several life tests have been carried out for the TF emitters discussed in this report. These tests were carried out in a vacuum pumped chamber which could be baked to  $\sim 150 \text{ C}$ . The base pressure after bake out was between  $5 \times 10^{-9}$  and  $1 \times 10^{-8}$  torr. Most of the life tests were carried out in a background pressure of  $8 \times 10^{-9}$  torr. During the course of the life testing the vacuum system was frequently cycled to atmosphere to exchange emitters; this led to substantial current variations that would not have occurred if constant vacuum were maintained.

Life tests carried out previously<sup>14</sup> on the Zr/W(100) and W(100) built-up cathode have shown that emitter life in excess of 2000 and 1000 hrs respectively can be realized. The main feature of the present life test results is the use of higher voltage emitters and the inclusion of a Ta(111) built-up emitter in our study.

Table 7 gives the emitter temperature and operating voltage adjustments during the course of each run. The Zr/W(100) cathodes were configured in a glass gun structure depicted in Fig. 50. The measured current for emitters #1 and #6 was transmitted through an aperture of 1.2 rad full angle subtended at the emitter. For emitter #5 the aperture full angle was decreased to 15 mrad. The W(100) and Ta(111)



TABLE 7

## LIFE TEST DATA SUMMARY; NOMINAL PRESSURE DURING TESTS:

~  $8 \times 10^{-9}$  TORR; VOLTAGE CHANGES OCCURRED AT THE INDICATED TIMES

<u>Emitter</u>	<u>Temp (K)</u>	<u>Time (hrs)</u>	<u>Voltage (volts)</u>	<u>Total Operating Time (hrs)</u>
#1 Zr/W	1850	0	3660	4898
		968	5810	(Emission died)*
		1568	4310	
		3472	3980	
		3936	5590	
#6 Zr/W	1850	0	3230	4828
		500	4940	(Emission died)*
		952	5910	
		1264	5700	
		3136	6340	
		3928	6980	
#5 Zr/W	1850	0	5160	3300
		672	7090	(Still operating)
#8 W(100) Built-up	1850	0	3770	3372
		368	4200	(Emission died)
		1000	4090	
		1320	3980	
#9 W(100) Built-up	1850	0	5380	4928
		508	5590	(Terminated by operator error)
		1660	5480	
		1948	5910	
		2356	5810	
		3500	5700	
		4000	5590	
#4 Ta(111) Built-up	1770	0	2800	3108
		1755	2910	(Still operating)
		1755	3440	
		1735	3550	
		1800	3340	
		1775	3340	
		1800	3550	
		1710	2910	
	1755	2968	3340	

\*post-mortem showed zirconium exhausted

# MAGNETICALLY FOCUSED THERMAL FIELD ELECTRON GUN

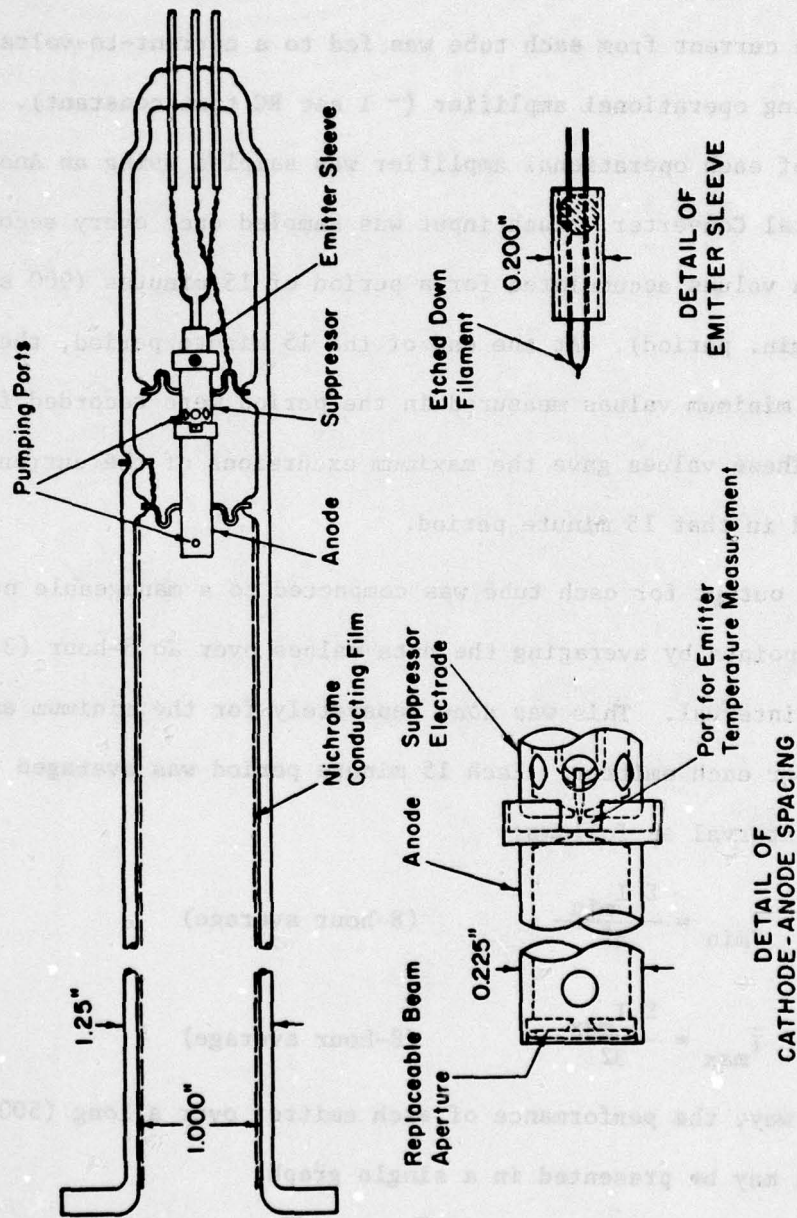


Figure 50. Detailed drawing of an electron gun using the Zr/W(100) TFE cathode.



emitters were placed in simple FEM diode structures and the total emission current was monitored.

The current from each tube was fed to a current-to-voltage converting operational amplifier ( $\sim 1$  sec RC time constant). The output of each operational amplifier was sampled using an Analog-to-Digital Converter. Each input was sampled once every second and data values accumulated for a period of 15 minutes (900 samples per 15 min. period). At the end of the 15 minute period, the maximum and minimum values measured in the period were recorded for each tube. These values gave the maximum excursions of the currents measured in that 15 minute period.

The output for each tube was compacted to a manageable number of data points by averaging the data values over an 8-hour (32-period) interval. This was done separately for the minimum and maximum values for each emitter. Each 15 minute period was averaged over an 8-hour interval as follows:

$$\bar{I}_{\min} = \frac{\sum I_{\min}}{32} \quad (8\text{-hour average})$$

$$\bar{I}_{\max} = \frac{\sum I_{\max}}{32} \quad (8\text{-hour average})$$

In this way, the performance of each emitter over a long (5000 hour) interval may be presented in a single graph.

The difference between the  $\bar{I}_{\min}$  and  $\bar{I}_{\max}$  values for a given period were quite small, and we present in Figs. 51 to 56 only the  $\bar{I}_{\max}$  values. Also presented in Figs. 51 to 56 is the average percent

variation  $\overline{\Delta I}/\overline{I}$  in each 8 hr interval determined according to

$$\frac{\overline{\Delta I}}{\overline{I}} (\%) = \frac{\overline{I}_{\max} - \overline{I}_{\min}}{\frac{\overline{I}_{\max} + \overline{I}_{\min}}{2}} \times 100$$

The current variation calculated in this fashion gives the magnitude of the maximum and minimum current fluctuation during each 8 hour period.

In general the magnitude of the fluctuations for the Zr/W(100) emitters are lower than the built-up emitters. This agrees with the more detailed current fluctuation study described in Sec. IIF. The magnitude of the long term current variations in this study are much larger than normally encountered because of the many voltage changes (see Table 7) and recycles to atmospheric pressure (several times for each emitter). A typical characteristic for an emitter operated without recycling to atmospheric pressure and without voltage changes is given in Fig. 57 for a Zr/W(100) emitter. This was a much lower voltage emitter which terminated at a much shorter life, i.e. 880 hrs.

The primary purpose of the Figs. 51 to 56 results is to show that high voltage TF emitters can operate under practical conditions typically found in instrument applications with very long life in comparison with the lower voltage life studies carried out earlier.<sup>13</sup>

The unusual cyclic current variations observed in Fig. 53 were not understood and not observed with other Zr/W(100) emitters. The long term current increase for the W(100) built-up emitter in Fig. 54



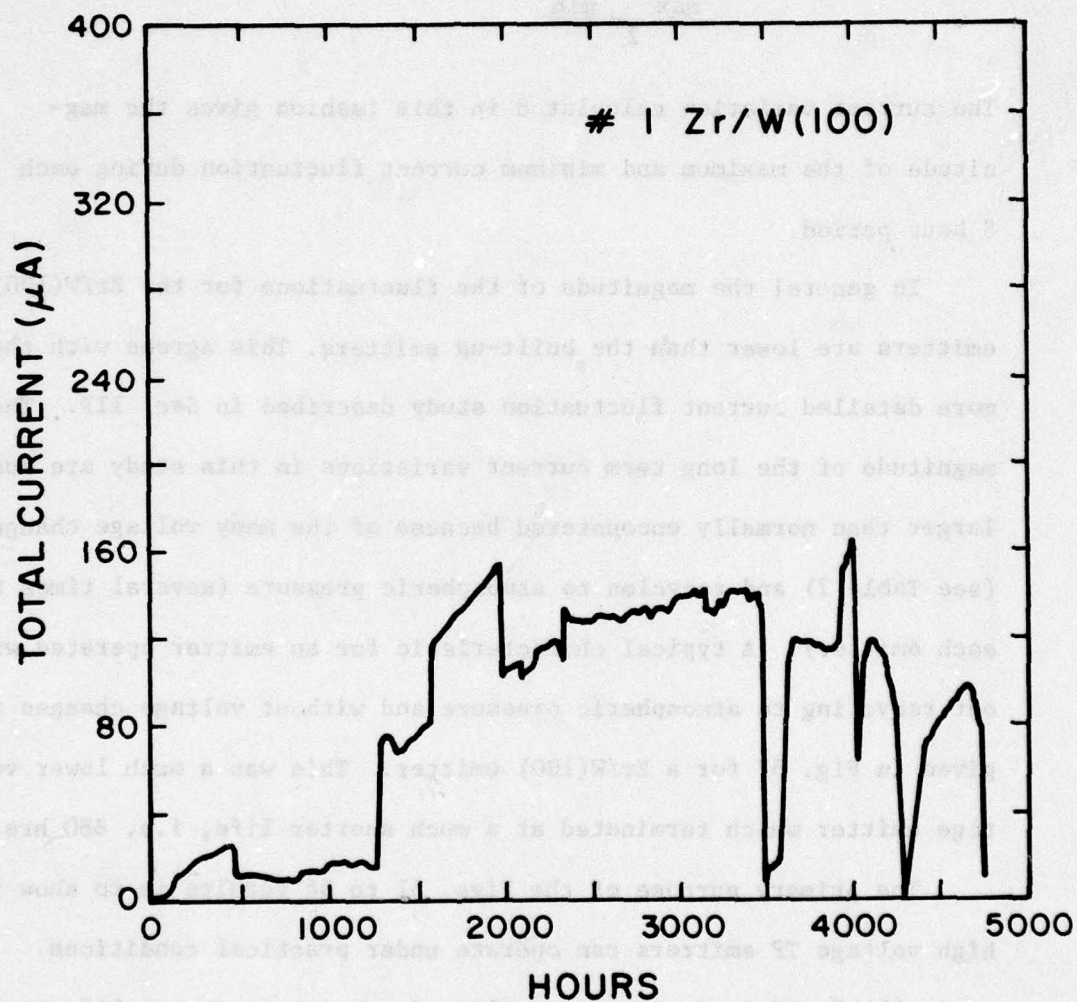


Figure 51(a). Total current vs. time data; operating conditions given in Table 7.

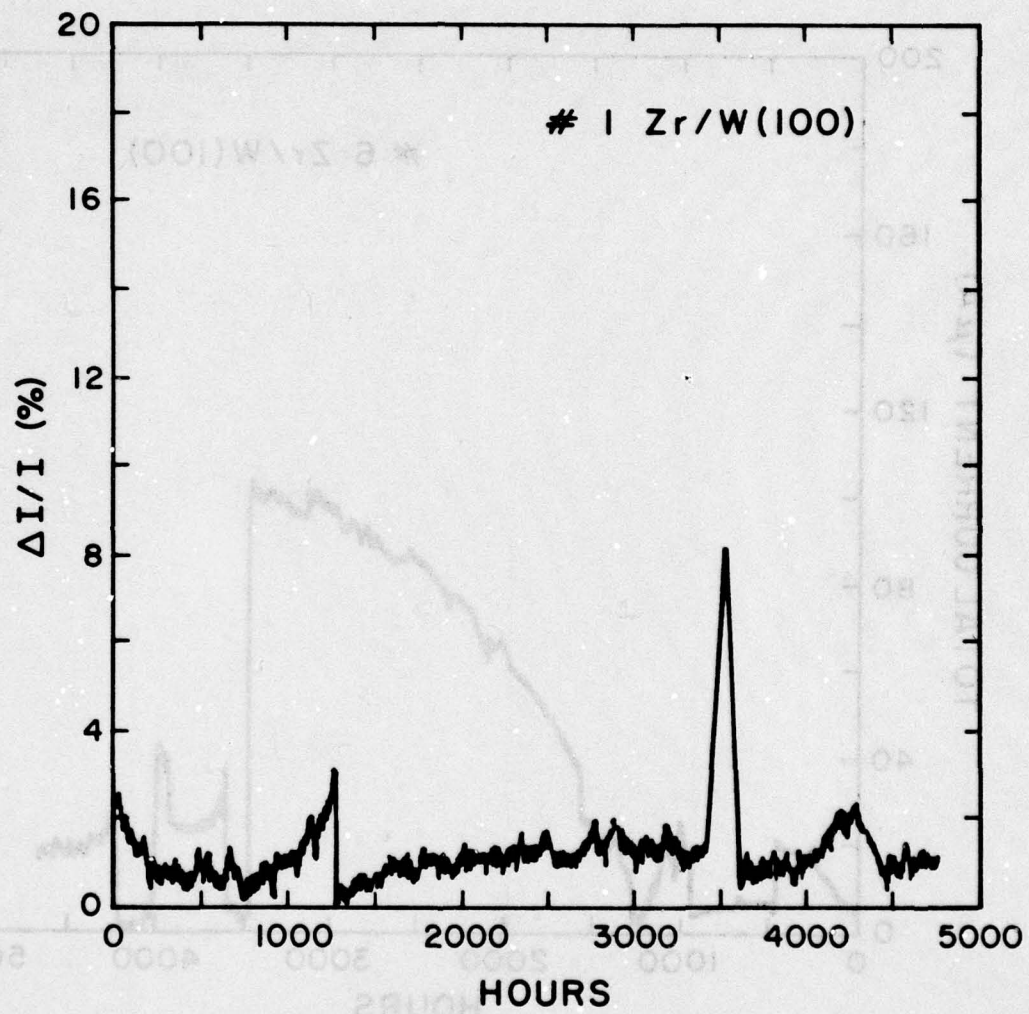


Figure 51(b). Percent current fluctuation averaged over 8 hour time intervals for data in (a).



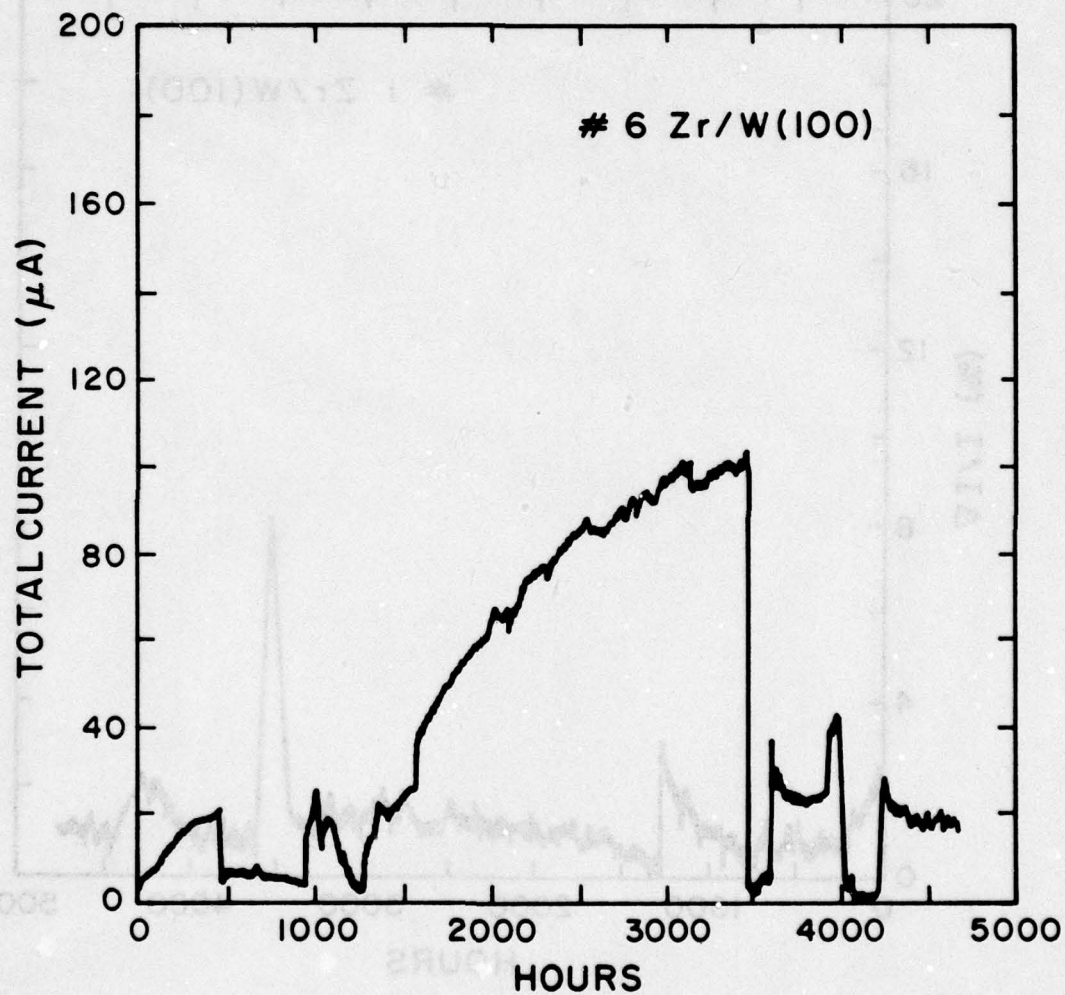


Figure 52(a). Total current vs. time data; operating conditions given in Table 7.

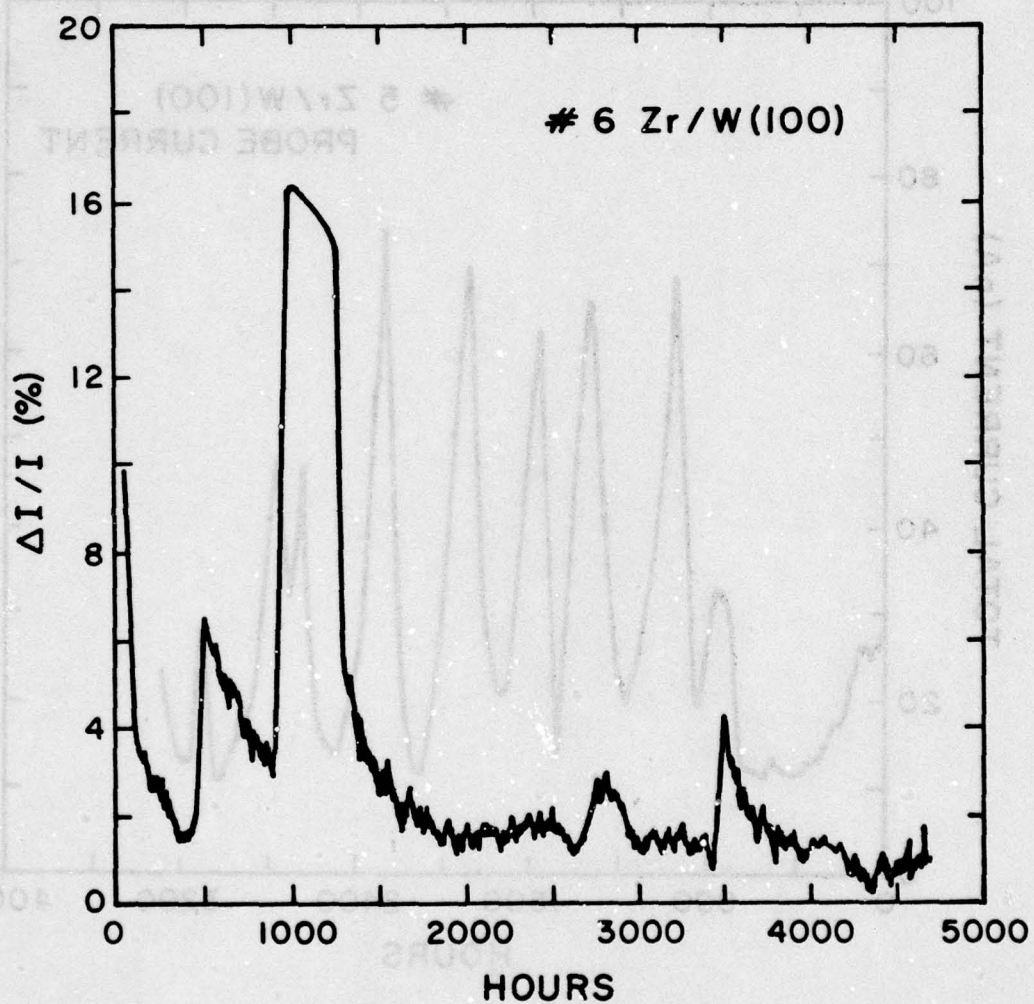


Figure 52(b). Percent current fluctuation averaged over 8 hour time intervals for data in (a).



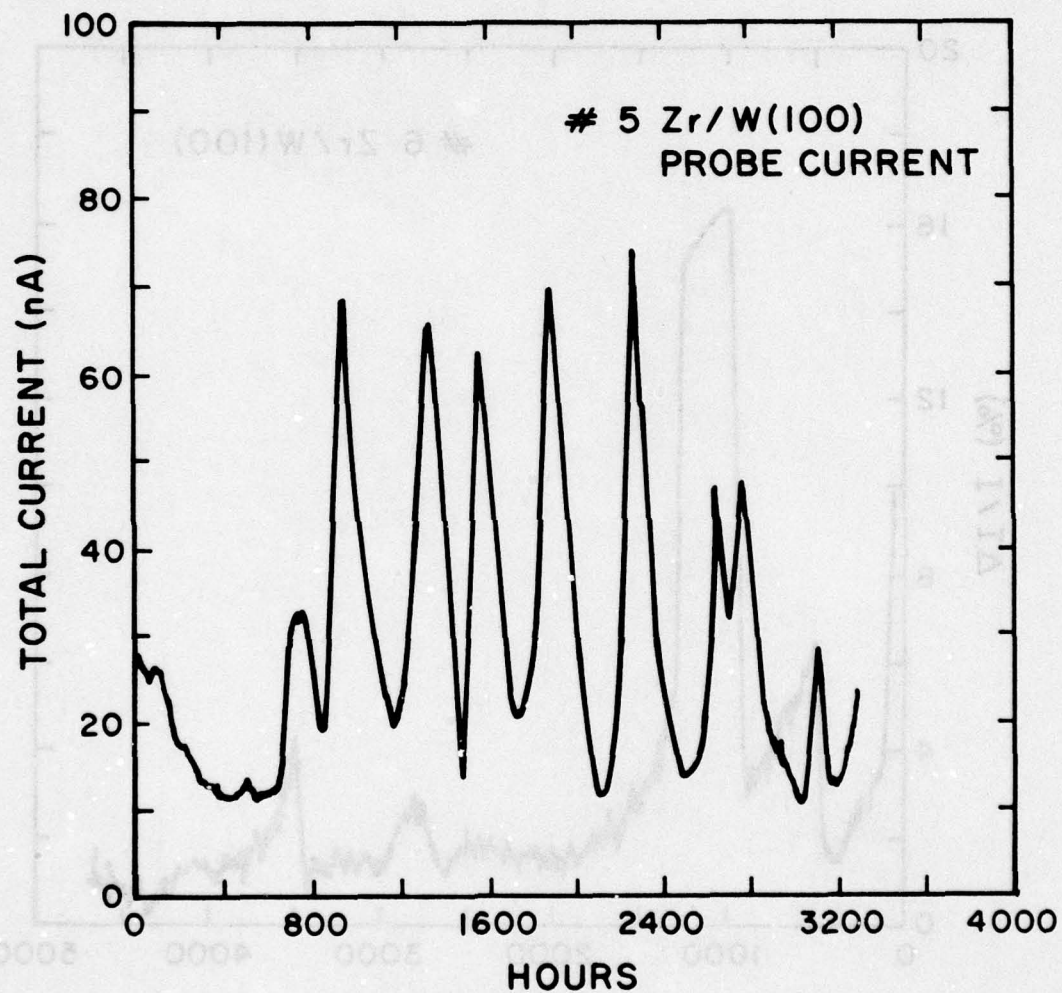


Figure 53(a). Probe current vs. time data; operating conditions given in Table 7.

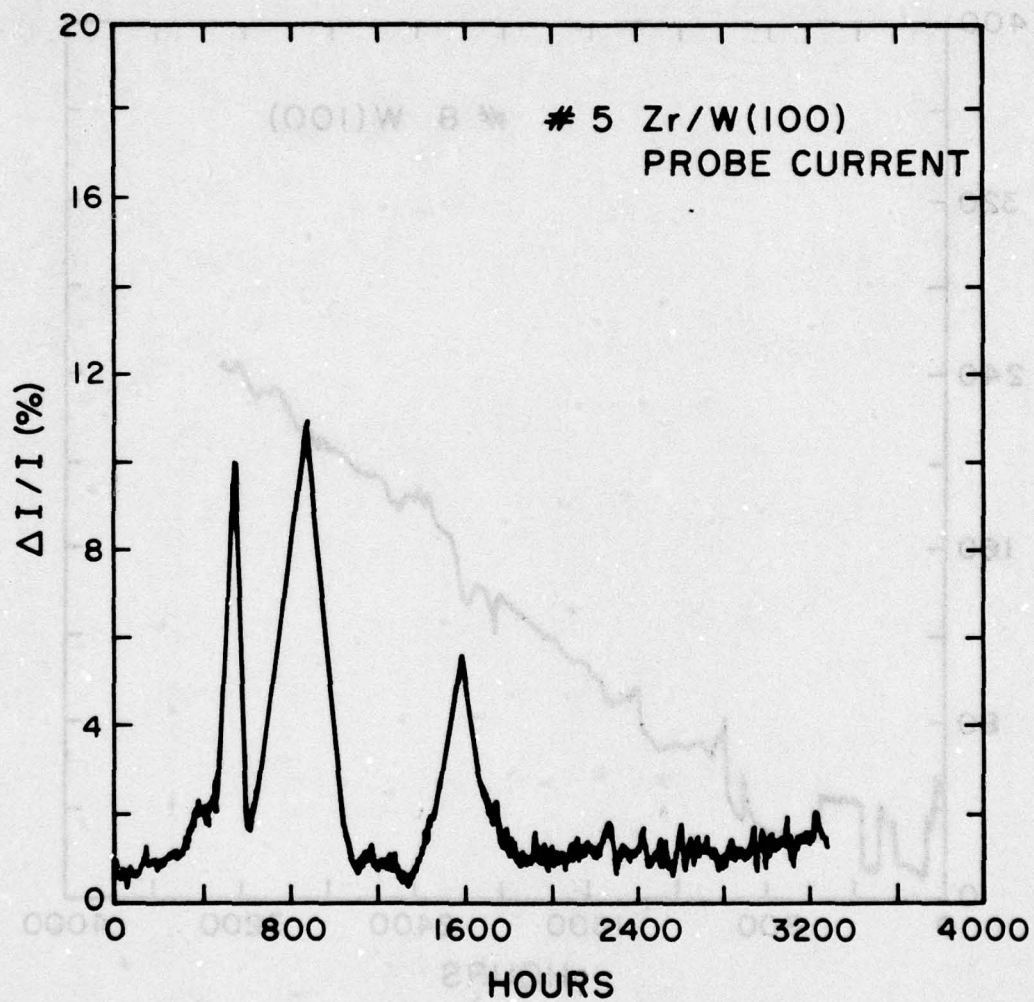


Figure 53(b). Percent current fluctuation averaged over 8 hour time intervals for data in (a).



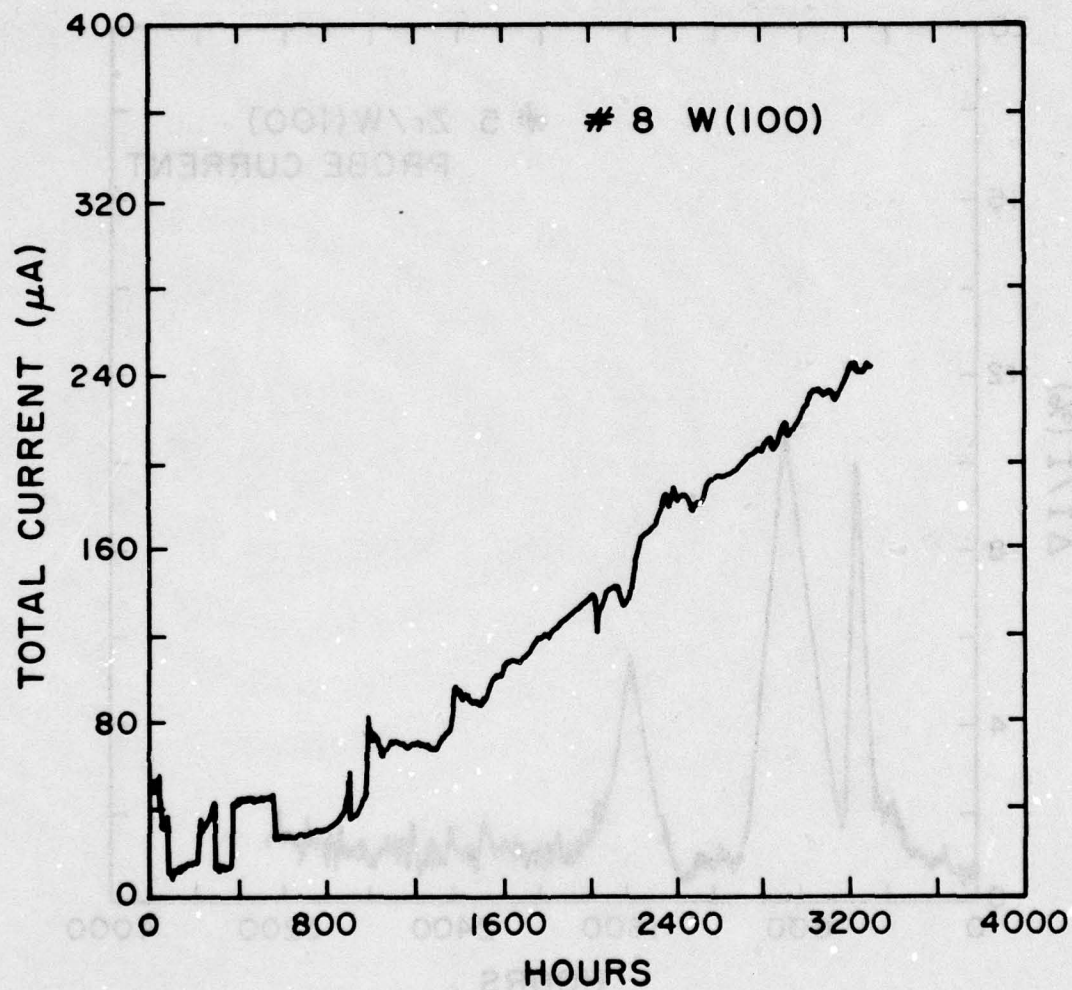


Figure 54(a). Total current vs. time data; operating conditions given in Table 7.

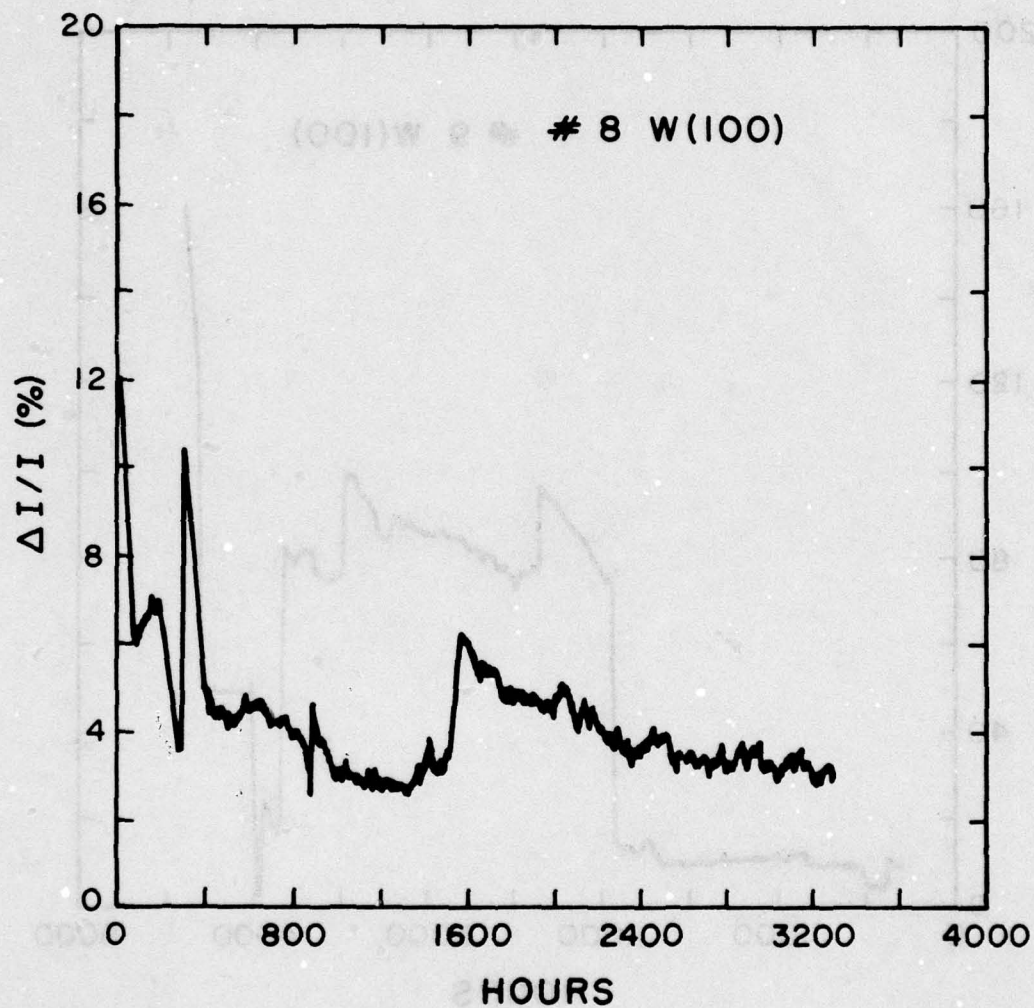


Figure 54(b). Percent current fluctuation averaged over 8 hour time intervals for data in (a).



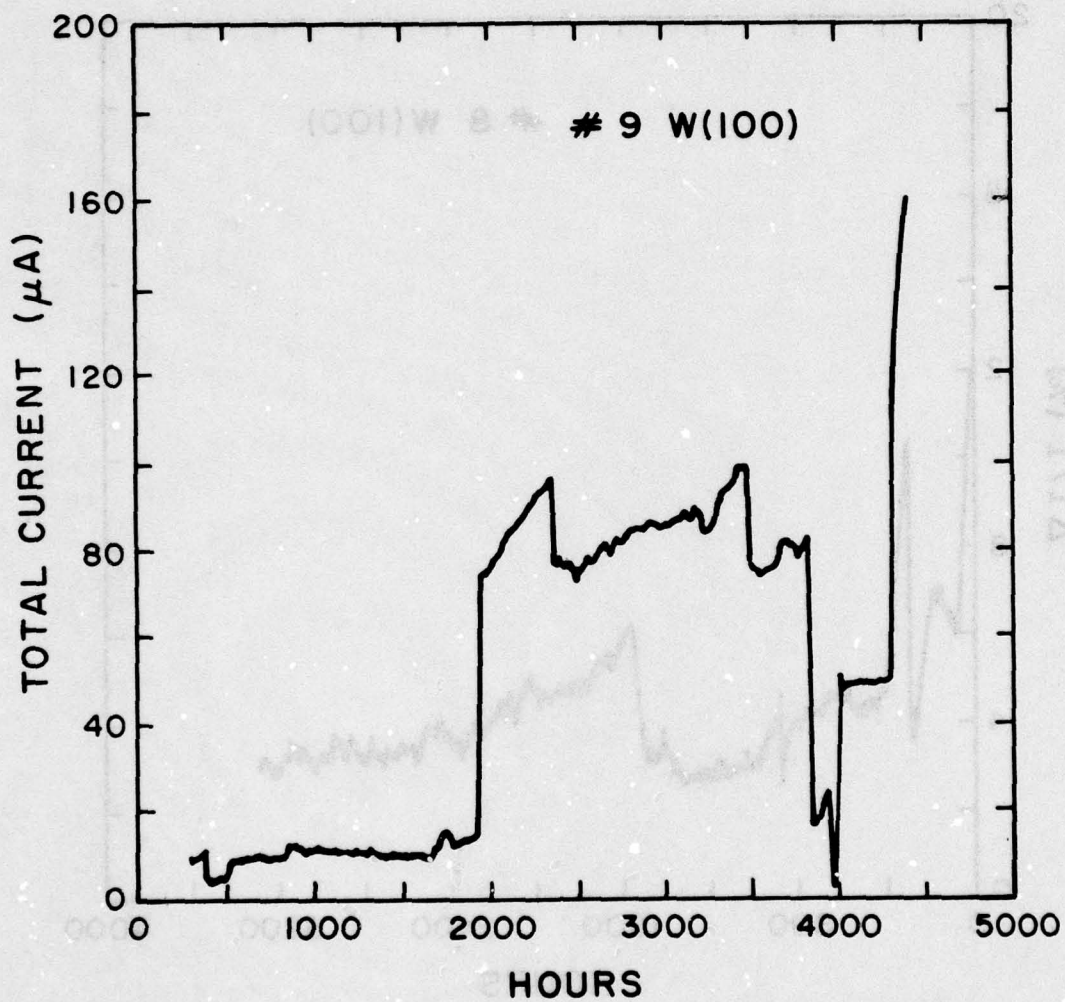


Figure 55(a). Total current vs. time data; operating conditions given in Table 7.

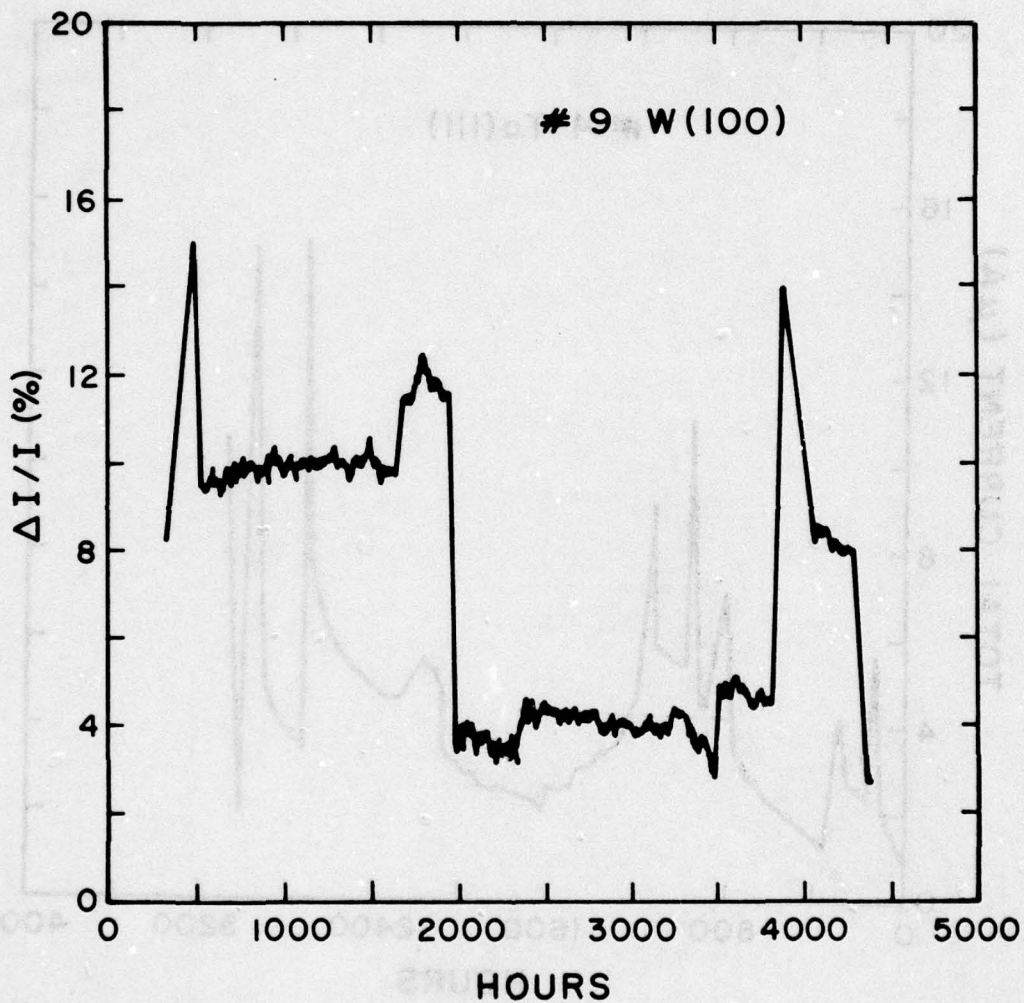


Figure 55(b). Percent current fluctuation averaged over 8 hour time intervals for data in (a).



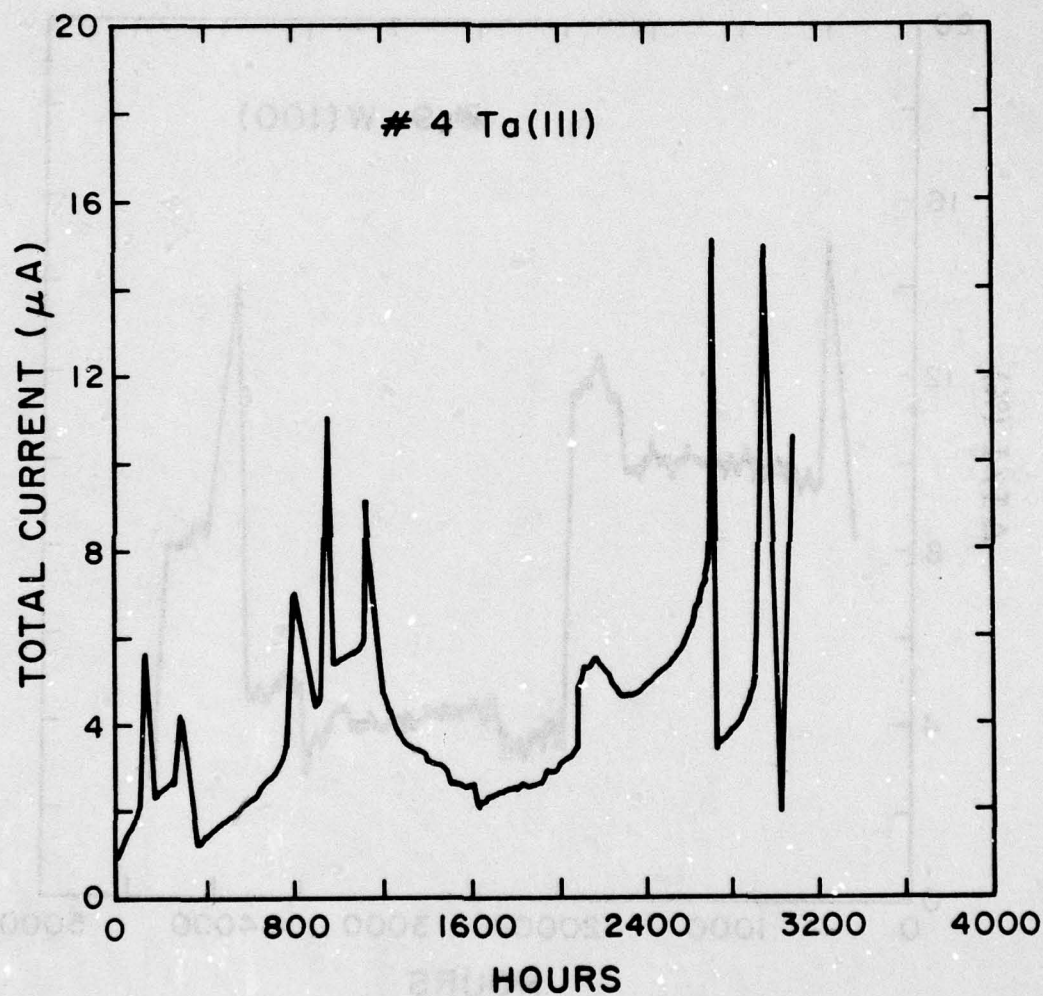


Figure 56(a). Total current vs. time data; operating conditions given in Table 7.

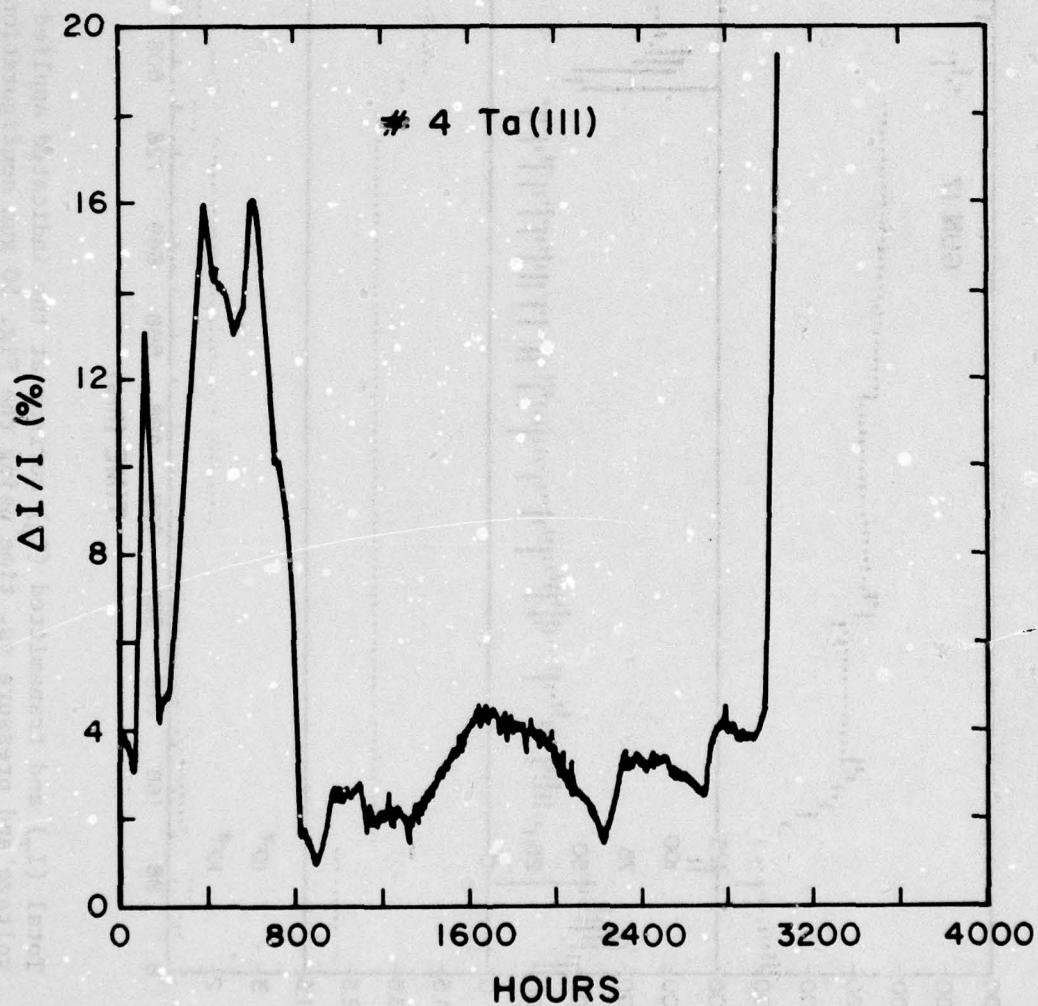


Figure 56(b). Percent current fluctuation averaged over 8 hour time intervals for data in (a).



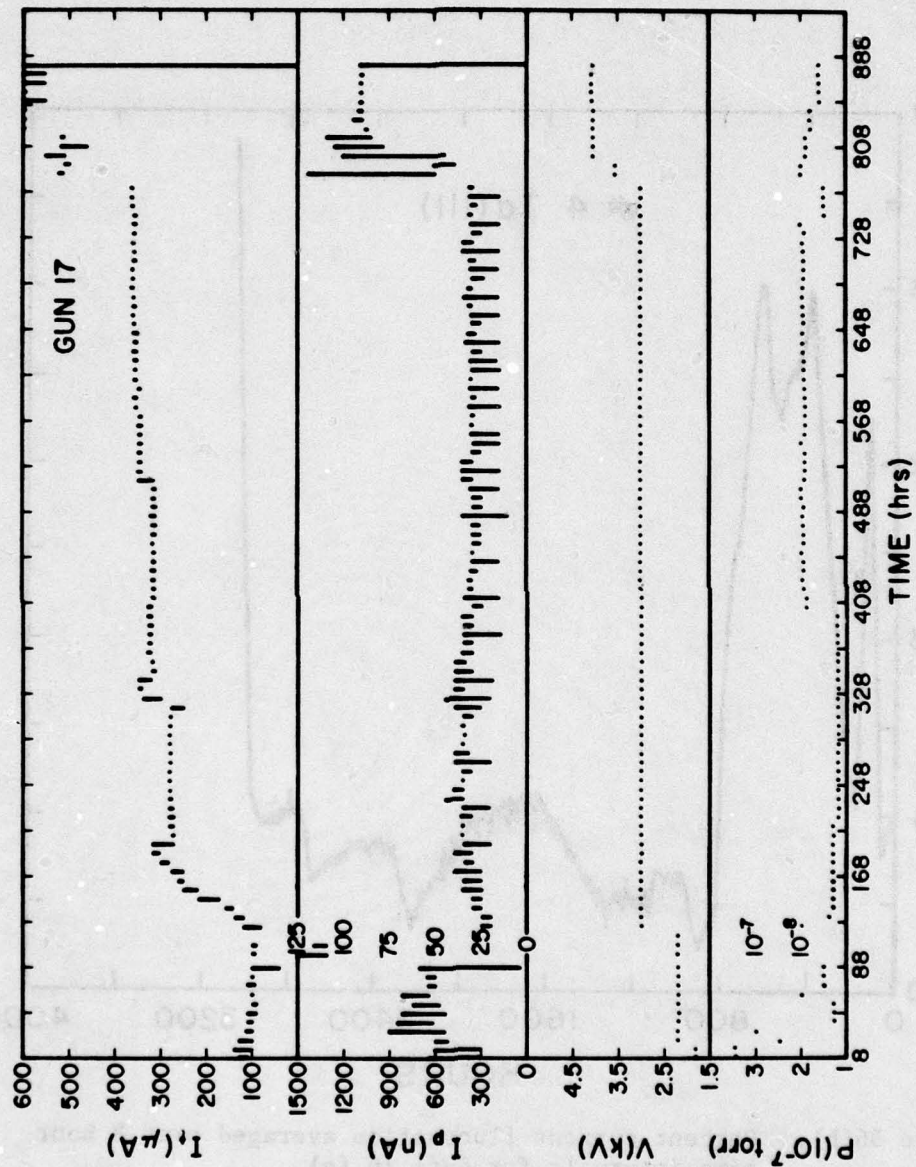


Figure 57. Total ( $I_T$ ) and transmitted ( $I_p$ ) current at the indicated applied emitter voltage and pressure vs. time using the Fig. 50 gun configuration. At 90 hrs the half angle of the beam aperture was decreased from 86 to 5 mrad.

was frequently observed for the lower voltage built-up emitters and appears to be due to a long term geometric change in the emitter size. Even though it was a low voltage emitter, the Ta(111) built-up emitter appeared to be very durable. An undesirable feature, however, was the frequent change in the built-up end form and concomitant increase in current. This required stopping the life test and reforming the proper built-up end form.

In conclusion, these studies have shown that larger radii emitters of both the W(100) built-up and Zr/W(100) type operating at  $\sim 1850$  K can last several thousand hours in practical vacuum environments. Our experience shows that emitter failure is usually due to operator error or stray voltage pulses due to electrical breakdown in the high voltage circuit. These problems can be reduced, if not eliminated, by careful gun construction and protection circuitry.



### SECTION III

#### FOCUSSED ELECTRON BEAM MEASUREMENTS

In this section a preliminary investigation of a magnetically focussed electron gun using the Zr/W(100) TFE emitter is reported. The design objective of the TF gun was the attainment of  $\sim 100$  nA of current into a  $\sim 0.1$   $\mu\text{m}$  focussed beam. Careful measurement of the lens aberration coefficients enabled us to compare the predicted and experimental gun performance data. The results showed that the design objective was largely met with a low noise (i.e.  $\sim 0.22\%$  noise to signal ratio) beam current.

##### A. Gun and System Configuration

An overall diagram of the field emission (FE) SAM system is shown in Fig. 58. The upper lens (Celco PF-648-380) collimates the emission transmitted through the anode aperture and the lower lens (Celco NF-434-366) forms a focussed image on the sample plane. For this optical system the overall gun magnification  $M$  is given the ratio of lower lens focal length  $f_2$  to upper lens focal length  $f_1$

$$M = f_2/f_1 \quad (25)$$

The focussed spot diameter  $d_1$  formed by the upper lens is then obtained by adding in quadrature the gaussian  $d_g$ , diffraction  $d_d$ , spherical  $d_s$  and chromatic aberration disks, that is

$$d_1^2 = M_1^2 \left( d_g^2 + d_{d_1}^2 + d_{s_1}^2 + d_{c_1}^2 \right) \quad (26)$$

where

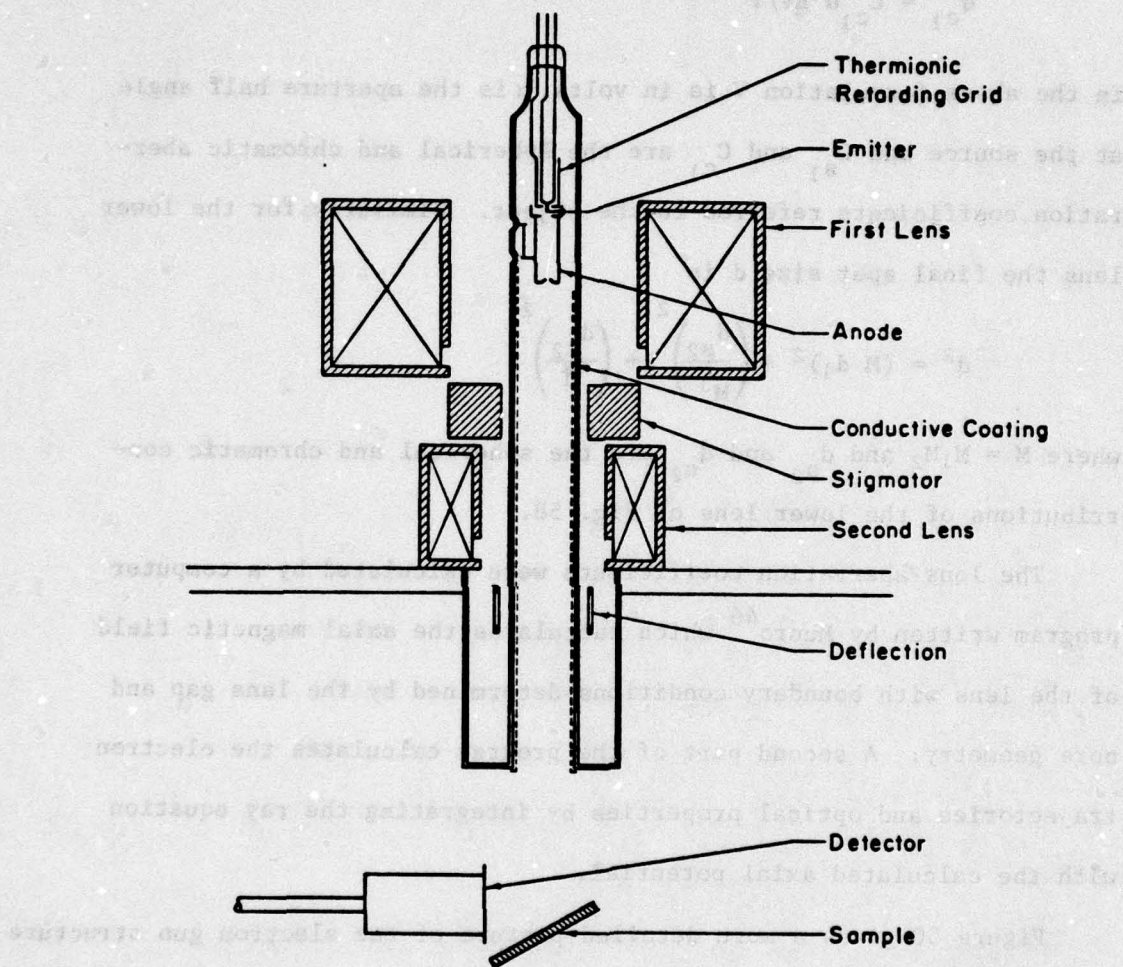


Figure 58. Diagram of the magnetically focussed TFE gun and detector configuration.



$$d_{d_1} = 15.1/V^{1/2}\alpha \text{ (Å)}$$

$$d_{s_1} = (1/2)C_{s_1}\alpha^3$$

$$d_{c_1} = C_{c_1}\alpha \Delta V/V$$

In the above formulation  $V$  is in volts,  $\alpha$  is the aperture half angle at the source and  $C_{s_1}$  and  $C_{c_1}$  are the spherical and chromatic aberration coefficients referred to the object. Similarly for the lower lens the final spot size  $d$  is

$$d^2 = (M d_1)^2 + \left(\frac{d_{s_2}}{M^3}\right)^2 + \left(\frac{d_{c_2}}{M}\right)^2$$

where  $M = M_1M_2$  and  $d_{s_2}$  and  $d_{c_2}$  are the spherical and chromatic contributions of the lower lens of Fig. 58.

The lens aberration coefficients were calculated by a computer program written by Munro<sup>46</sup> which calculates the axial magnetic field of the lens with boundary conditions determined by the lens gap and bore geometry. A second part of the program calculates the electron trajectories and optical properties by integrating the ray equation with the calculated axial potential.

Figure 50 gives a more detailed picture of the electron gun structure which consisted of a cathode (precision mounted in a molybdenum sleeve), a suppressor electrode and an anode. The suppressor electrode operated at -200 to -400 V with respect to the cathode and served to reduce the thermionic emission from the shank of the low work function TFE Zr/W(100) emitter. The anode contained a replaceable beam defining aperture located 2.55 cm from the emitter. The inside of the glass envelope

which housed the gun was coated with a nichrome film so that no insulating surfaces were exposed to the beam.

The beam spot size and gun performance characteristics were determined by configuring the gun into an SEM system. A Galileo Electro-Optics Corp. CDEM 4700 electron multiplier was used for SEM imaging. The SEM video signal was fed to a Tektronix 606 display monitor.

A metal bell jar containing the TFE gun, CMA, ion sputtering gun, SEM electron detector and Physical Electronics specimen stage was mounted on a standard 200  $\ell$ /s, bakeable UHV system capable of  $5 \times 10^{-10}$  torr pressure. The FE gun can be routinely operated in a  $1 \times 10^{-8}$  torr environment but, for these studies, was operated in the pressure range 0.5 to  $1 \times 10^{-9}$  torr.

#### B.80 Gun Performance Data

Because of geometric constraints of the bell jar system the overall beam throw from the lower lens of Fig. 58 to the specimen was 13 cm. Table 8 gives the relevant lens parameters of the upper and lower magnetic lens. The effective beam aperture seen by the Zr/W(100) emitter was a .006 rad half angle. In Table 9 the experimental and calculated beam diameters at various beam current levels are given. An assumed gaussian source diameter of 150 Å was included in the calculations. Contributions of the spherical ( $d_s$ ) and chromatic ( $d_c$ ) aberration disks of both the upper (subscript 1) and lower (subscript 2) lenses are also indicated. The value of the energy spread  $\Delta V$  is known to increase with source angular intensity ( $I_p/\Omega$ ) as described



TABLE 8

## MAGNETIC LENS PARAMETERS

	f (mm)	C <sub>s</sub> (mm)	C <sub>c</sub> (mm)
Upper	63	139.2	53.7
Lower	139.2	3001.2	132.9

Overall magnification  $M = 2.2$

Beam half angle  $\alpha = .006$  rad

Beam solid angle  $\Omega = 0.113$  msr

TABLE 9

EXPERIMENTAL AND PREDICTED GUN OPERATING PARAMETERS; VALUES OF d IN  $\mu\text{m}$ 

$I_p$ (na)	d(exp)	T(K)	V(kV)	$\Delta V(\text{eV})^*$	$I_p/\Omega$ (mA/sr)	$d_{c1}$	$d_{s1}$	$d_{c2}$	$d_{s2}$	d(calc)
40	.108	1800	8.5	1.08	0.35	.091	.033	.046	.030	.116
60	.095	1800	9.5	1.32	0.53	.099	.033	.050	.030	.125
66	.100	1850	10.0	1.40	0.58	.100	.033	.051	.030	.125
98	.105	1850	11.5	1.79	0.87	.110	.033	.056	.030	.136
110	.104	1850	12.0	1.93	0.97	.114	.033	.058	.030	.140

\*Experimental values based on a  $\beta = 1.2 \times 10^4 \text{ cm}^{-1}$  emitter

in Sec. IIE; thus, experimental values for  $\Delta V$  obtained in Sec. IIE from a lower voltage emitter were used. We believe that the assumed values of  $\Delta V$  used here are probably pessimistic since the Fig. 39 results indicate that for a higher voltage (i.e. larger radius) emitter the values of  $\Delta V$  decrease. In this study an emitter with a value of  $\beta = 0.1 \times 10^4 \text{ cm}^{-1}$  was used.

The beam spot size values in Table 9 were measured three different ways. Two of the methods involved scanning the beam over the sharp edge of an 8  $\mu\text{m}$  grid wire and measuring the reflected and transmitted beam currents. The other method consisted of measuring the reflected current as the beam was scanned across a deposited MgO particle that was small compared to the beam size. All three methods agreed within  $\pm .02 \mu\text{m}$ .

We are gratified with these results which show that the experimental values of  $d$  achieved between 40 and 110 nA with  $M = 2.2$  are all of the order of 0.10  $\mu\text{m}$ . The dominance of the chromatic aberration disk means we have not underestimated (apparently we have overestimated) the value of  $\Delta V$  as expected. Beam currents were varied by changing the beam voltage from 8.5 to 12.0 kV. Because of the large value of  $dI/dT$  for the low work function Zr/W(100) TFE source, the beam current can also be varied by changing the emitter temperature while keeping the beam voltage constant. Figures 59 and 60 show typical experimental variation of beam current with beam voltage and temperature. To some extent the grid voltage can also be used to vary both the beam and total currents at constant beam voltage as shown in Fig. 61.

Upon achieving the 0.1  $\mu\text{m}$  beam size a study was made of the spatial stability of the emitter using the Fig. 58 system. The gun was left operating on several occasions for 16 hr periods and the movement of the pattern on the display was noted. The results showed an average drift of 0.11  $\mu\text{m/hr}$ . If we attribute the drift totally to the emitter, which we believe not to be the case since the stage drift appears to



be the major contributor, the average drift rate of the emitter is .05  $\mu\text{m/hr}$ .

A careful analysis of the beam noise in the specimen current was made using a spectrum analyzer. The spectral density function  $W(f)$  was measured over the frequency range 1 to 5 kHz and is shown in Fig. 49. Over the frequency range indicated (1 to  $5 \times 10^3$  Hz) the mean noise to signal ratio  $(\overline{\Delta I^2})^{1/2}/I_p$  was 0.0023 or a signal to noise ratio of 434. This unusually low noise factor is due in part to the large emitting area (i.e. large radius emitter) contributing to the solid angle of emission. A more detailed account of the noise measurements is given in Sec. IIF.

Typical SEM photographs taken of various objects are shown in Fig. 62. The high quality of the SEM images are indicative of the low noise-to-signal ratio characteristic of the Zr/W(100) TFE cathode. The large beam current available at a resolution of 0.1  $\mu\text{m}$  allows the image to be scanned at video rates. A resolution of  $\sim 0.05$   $\mu\text{m}$  without greatly limiting the beam current can be achieved by simply reducing the beam throw from 13 to 5 cm.

### C. Conclusions

The high voltage Zr/W(100) TFE emitter not only exhibits long life ( $\sim 5000$  hrs on several tests), but sufficiently low noise (e.g. 0.22%) to be used for most applications without the need for sophisticated beam current stabilization schemes. Very high specimen current densities can be obtained at 0.1  $\mu\text{m}$  or less beam size with relatively simple gun optics. At present a current density of 1295 A/cm<sup>2</sup> or power

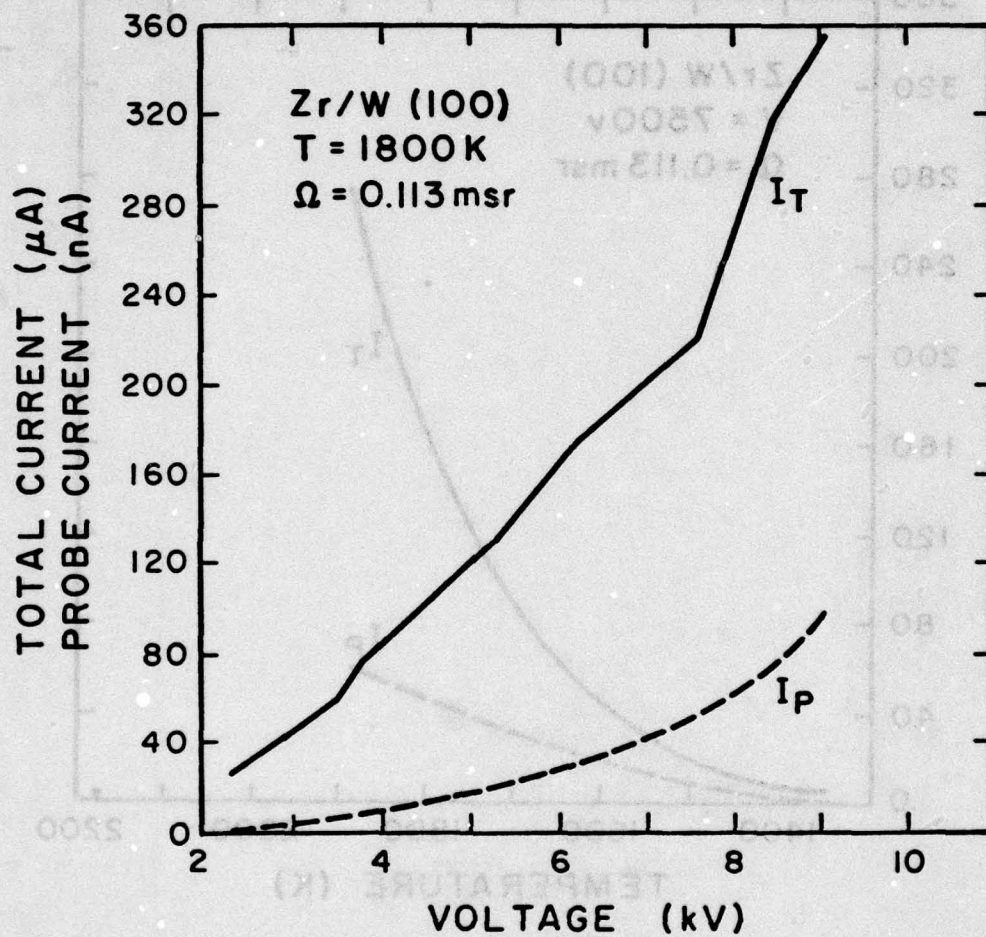


Figure 59. Total ( $I_T$ ) and beam ( $I_P$ ) current vs voltage characteristics for a high voltage Zr/W(100) TFE emitter in the Fig. 50 gun configuration.



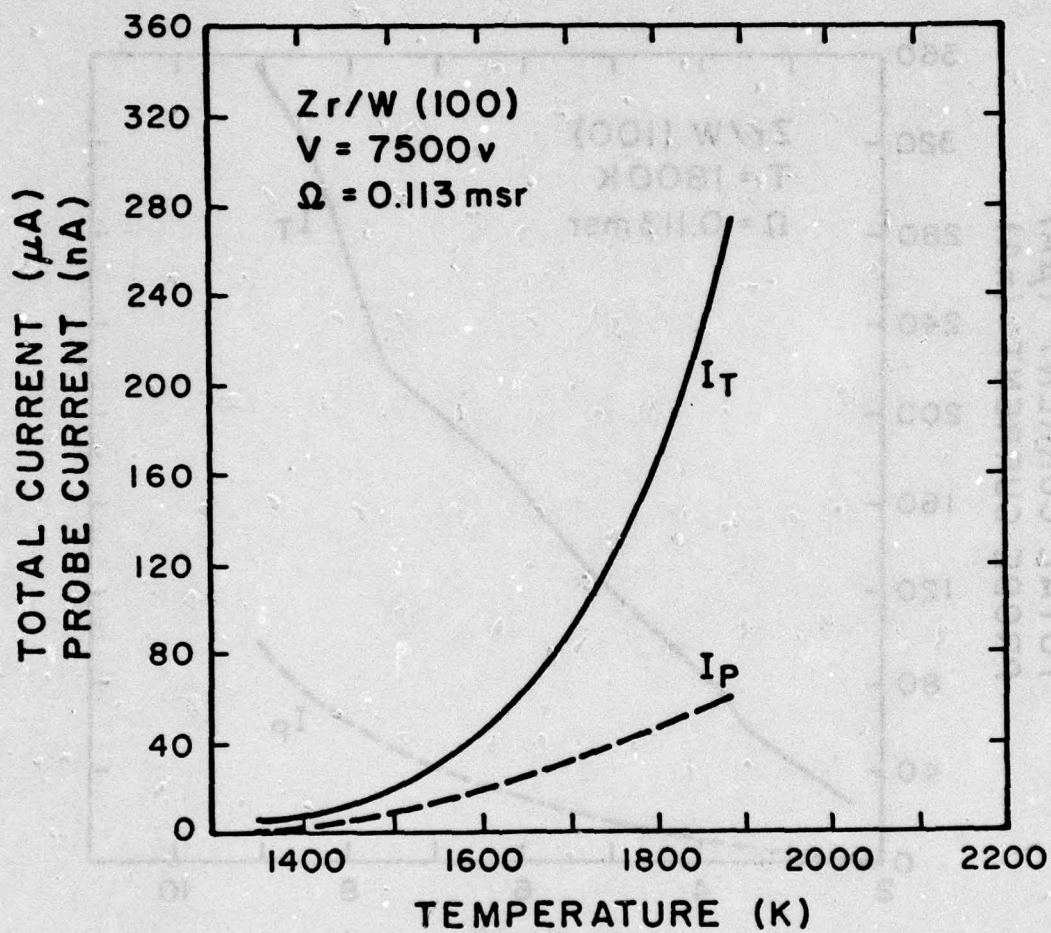


Figure 60. Total ( $I_T$ ) and beam ( $I_P$ ) current vs emitter temperature characteristics for a high voltage Zr/W(100) TFE emitter in the Fig. 50 gun configuration.

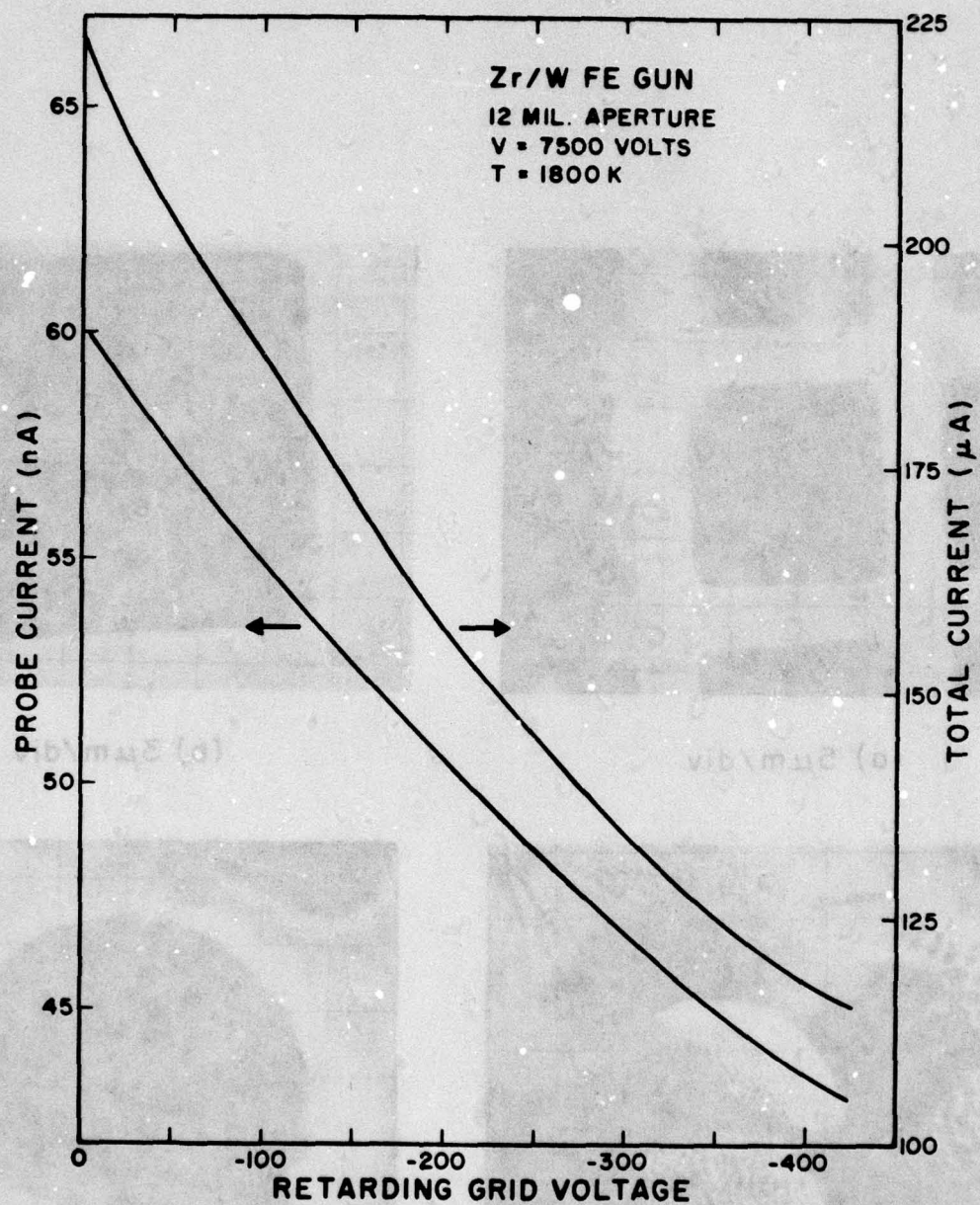
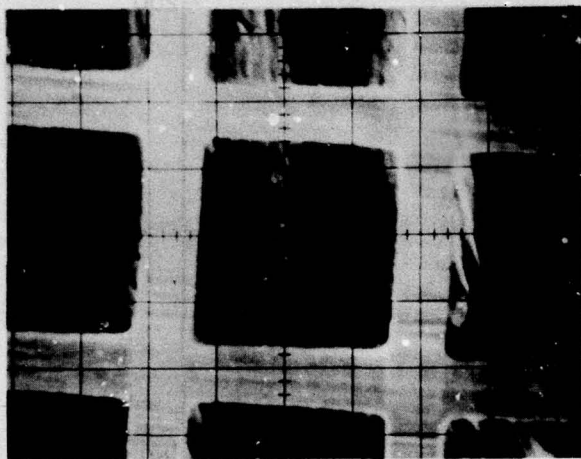
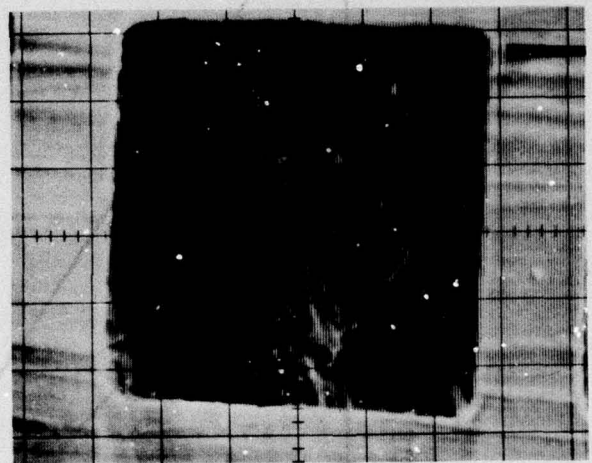


Figure 61. Total and beam current vs suppressor electrode voltage for the Fig. 50 gun configuration.

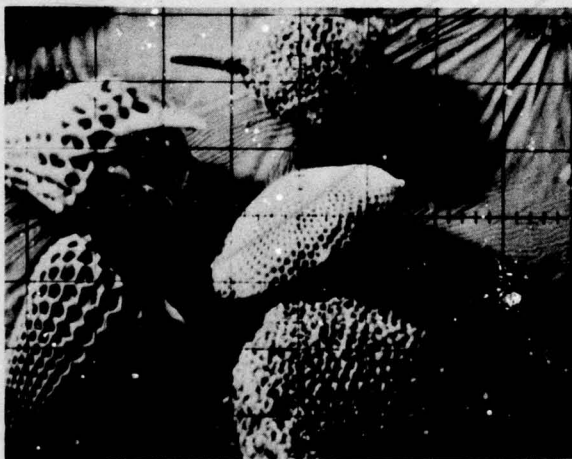




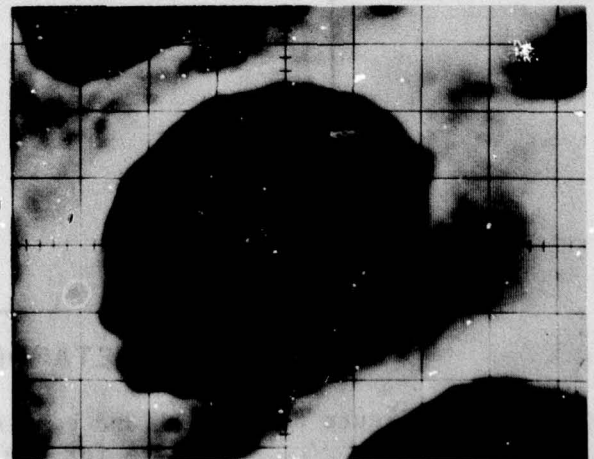
(a)  $5\mu\text{m}/\text{div}$



(b)  $3\mu\text{m}/\text{div}$



(c)  $90\mu\text{m}/\text{div}$



(d)  $1\mu\text{m}/\text{div}$

Figure 62. Typical SEM photographs at the indicated magnifications of a mesh with  $5\mu\text{m}$  wide wires (a) and (b) and radiolarian (c) and (d).

density of  $1.55 \times 10^7$  watts/cm<sup>2</sup> has been achieved in a 0.1  $\mu$ m beam spot. This corresponds to an image plane brightness of  $5.5 \times 10^7$  A/cm<sup>2</sup>-sr at 12 kV. An operating range of beam voltage, e.g. 8 to 15 kV, can be realized while maintaining a constant beam current by making compensating variations in emitter temperature. Different operating ranges of beam voltage can be achieved by controlling the emitter radius during fabrication.

Finally, the geometric stability of the emitter structure once the system achieves an equilibrium temperature is excellent. Measurements show the emitter drift when measured over 16 hr periods to be  $< .05 \mu\text{m/hr}$  for a TF emitter operating at 1800 K.



## SECTION IV

### ION SOURCE DEVELOPMENT AND CHARACTERIZATION

We have completed an investigation of a number of source materials and modes of operation suitable for high brightness field ionization beam formation. In this section a report of progress on the gas phase field ionization (FI) and liquid metal ion (LMI) sources will be given. For a complete history of work on this subject the reader is referred to a previous report describing earlier work carried out on both of these sources.<sup>6</sup> For the gas phase FI source studies have been primarily carried out using hydrogen and argon gases, however other volatile, nonreactive gases can be used with equal ease.

The advent of the LMI source extends high brightness field emission source prospects to a variety of nonvolatile materials, e.g. gallium, indium, bismuth, gold, aluminum, silicon and germanium, to name a few. The thrust of the LMI work reported here has been to gain an understanding of the basic mechanism of ion formation and source characteristics using principally gallium as the source material.

#### A. Gas Phase Field Ionization Source Characterization

##### 1. Source Materials and Emission Characteristics

Further studies of the angular intensity of hydrogen ions from an iridium field ion emitter have been carried out. As discussed previously<sup>6</sup>, because of its insensitivity to field induced chemical attack, iridium has proven to be an exceptionally durable emitter for field ionization.

## SECTION IV

### ION SOURCE DEVELOPMENT AND CHARACTERIZATION

We have completed an investigation of a number of source materials and modes of operation suitable for high brightness field ionization beam formation. In this section a report of progress on the gas phase field ionization (FI) and liquid metal ion (LMI) sources will be given. For a complete history of work on this subject the reader is referred to a previous report describing earlier work carried out on both of these sources.<sup>6</sup> For the gas phase FI source studies have been primarily carried out using hydrogen and argon gases, however other volatile, nonreactive gases can be used with equal ease.

The advent of the LMI source extends high brightness field emission source prospects to a variety of nonvolatile materials, e.g. gallium, indium, bismuth, gold, aluminum, silicon and germanium, to name a few. The thrust of the LMI work reported here has been to gain an understanding of the basic mechanism of ion formation and source characteristics using principally gallium as the source material.

#### A. Gas Phase Field Ionization Source Characterization

##### 1. Source Materials and Emission Characteristics

Further studies of the angular intensity of hydrogen ions from an iridium field ion emitter have been carried out. As discussed previously<sup>6</sup>, because of its insensitivity to field induced chemical attack, iridium has proven to be an exceptionally durable emitter for field ionization.



Because the natural orientation of polycrystalline iridium exposes either a (100) or (111) plane perpendicular to the emitter axis and because both of these planes form relatively large facets, the field strength is less than on the neighboring planes. As a result the emission along the emitter axis is relatively small. Ion emission from an iridium emitter can be concentrated along the axis if the emitter is fabricated from wire re-oriented along the  $\langle 110 \rangle$  direction. Figure 63(a) shows the emission distribution of hydrogen ions from a thermally annealed  $\langle 110 \rangle$  oriented iridium emitter. The emission distribution along the emitter axis can be further enhanced by field evaporation or field build up as discussed in Section IIC and illustrated in Fig. 63(b). Although the ion emission along the  $\langle 110 \rangle$  direction is greatly enhanced after build-up, experience has shown that sufficient emission distribution reproducibility could be obtained from the easier field evaporation procedure. Field evaporation of iridium was normally carried out at room temperature and an applied voltage of approximately twice the hydrogen best image voltage.

Figure 64 shows an argon ion image taken with the Ir(110) built-up emitter and again illustrates the angular confinement of the beam. The photographs in Figs. 63 and 64 were taken with a microchannel plate image intensifier inserted in the FIM; this allowed images to be taken at relatively low gas pressures.

Angular confinement of the ion beam emission from a tungsten emitter can be realized by allowing a  $\langle 100 \rangle$  oriented emitter



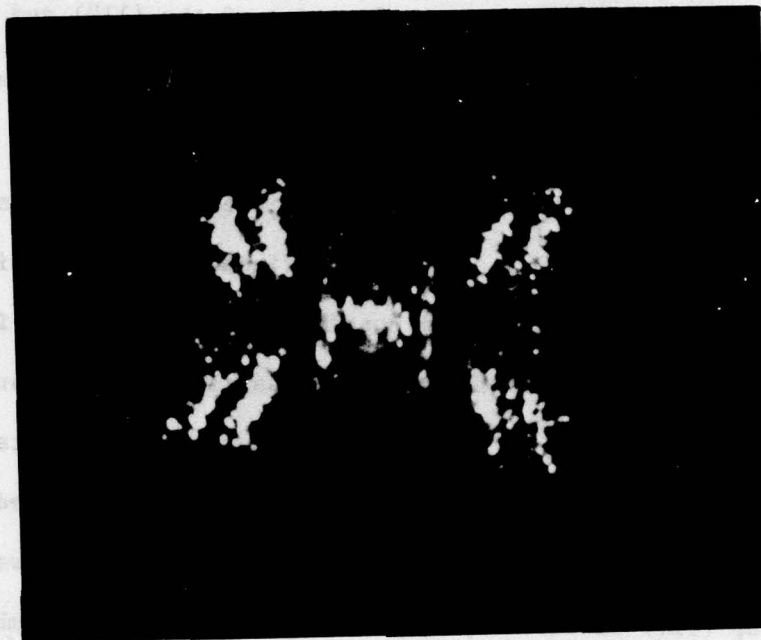
(a)



(b)

Figure 63. Field ion microscope patterns of a  $\langle 110 \rangle$  oriented iridium emitter taken at  $3 \times 10^{-3}$  torr of hydrogen and 77 K. (a) After field build-up,  $V = 20$  kV. (b) After thermal annealing at  $\sim 2000$  K,  $V = 28$  kV.





$$V = 20 \text{ kV}$$

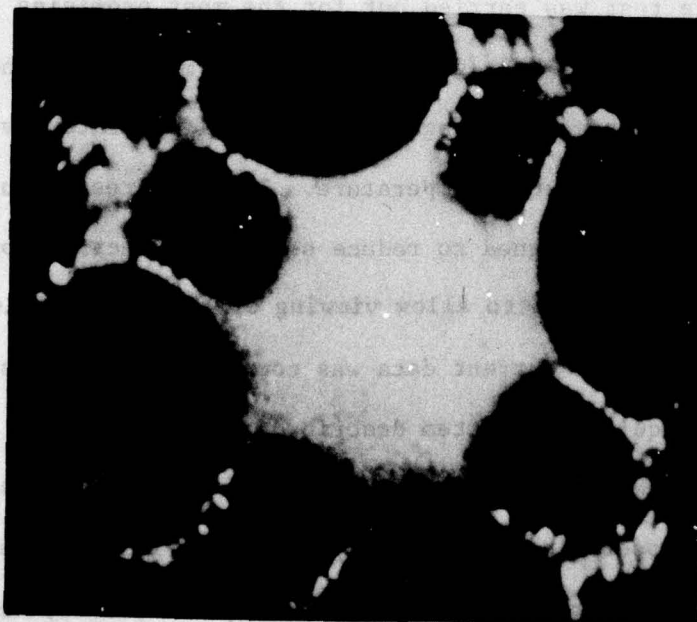
**Figure 64.** Same emitter as in Figure 63(b) taken at  $1 \times 10^{-6}$  torr argon pressure, 77 K and  $V = 20$  kV.

to undergo (100) build-up as described in Sec. IIC. This is illustrated in Fig. 65 where the hydrogen ion emission patterns of built-up and thermally annealed end forms are compared. Examination of the Fig. 65 patterns shows clearly the faceting of the (110) and (112) planes of the built-up emitter and concentration of the ion emission along the  $\langle 100 \rangle$  direction.

A similar angular confinement of the ion beam emission was obtained from (111) build-up of a  $\langle 111 \rangle$  oriented tantalum emitter. However, unless ultra-high vacuum conditions exist prior to inlet of the ionizing gas and unless the ionizing gas is free of impurities (particularly water vapor), the built-up end forms of both tantalum and tungsten will be quickly eroded away by the field induced chemical etch. A quantitative assessment of the field etch problem was obtained for built-up (111) tantalum by operating it in a vacuum chamber at 77 K and  $5 \times 10^{-6}$  torr of air admitted through a leak valve. After operation for one hour at 10 kV the hydrogen ion pattern (BIV was 13 kV) showed that the built up structure was completely eroded away by the field etch. The same experiment carried out at  $6 \times 10^{-9}$  torr showed no effect on the built-up pattern. In contrast, the same experiment carried out with (110) built-up iridium at a  $5 \times 10^{-6}$  torr air leak showed no effect on the built-up end form. This demonstrates again the superior resistance of iridium to the field induced chemical etch which was discussed previously.<sup>6,47</sup>

In addition to FI emitter materials fabricated from single component refractory metals, preliminary studies of FI emission from





(a)

$V = 10.5 \text{ kV}$



(b)

$V = 16.5 \text{ kV}$

Figure 65. Hydrogen field ion patterns of a  $\langle 100 \rangle$  oriented tungsten emitter,  $P_{H_2} = 1.3 \times 10^{-3}$  torr. (a) After (100) build-up,  $I_{TOTAL} = 1 \times 10^{-9} \text{ A}$ ; (b) after thermal annealing,  $I_{TOTAL} = 3.6 \times 10^{-9} \text{ A}$ .

a LaB<sub>6</sub> emitter was performed. After fabrication according to procedures outlined in Sec. IIB, the LaB<sub>6</sub> emitter was placed in a FI microscope including a microchannel plate for image intensification. The emitter was easily cleaned and a symmetric emission pattern obtained by field evaporation in a low pressure of hydrogen ( $P_{H_2} \approx 1 \times 10^{-4}$  torr). The typical ion emission pattern obtained after field evaporation is shown in Fig. 7(a) where high emission density is obtained from both the (110) and (100) planes. The LaB<sub>6</sub> emitter processed as described appears to be a potentially practical emitter material if the applied field does not exceed the BIV. If the applied field appreciably exceeds the BIV a hydrogen promoted field induced etch of the emitter occurs, probably via removal of material as LaH<sup>+</sup> or BH<sup>+</sup>.

## 2. Field Ionization Emitter Life Study

A life test was carried out for the most promising emitter material, iridium, using hydrogen as the ion forming gas. The life test assembly was a simple arrangement that could operate several emitters in parallel at room temperature. The life test structure shown in Fig. 66 was designed to reduce secondary electron contribution to the total current and also to allow viewing of the ion emission patterns.

The life test current data was compiled and processed by the life test data acquisition system described in Sec. IIG. At this juncture two extended life test runs have been carried out using iridium emitters operating at room temperature. Field induced chemical etch is more rapid at room temperature than at 77 K, thus, these life



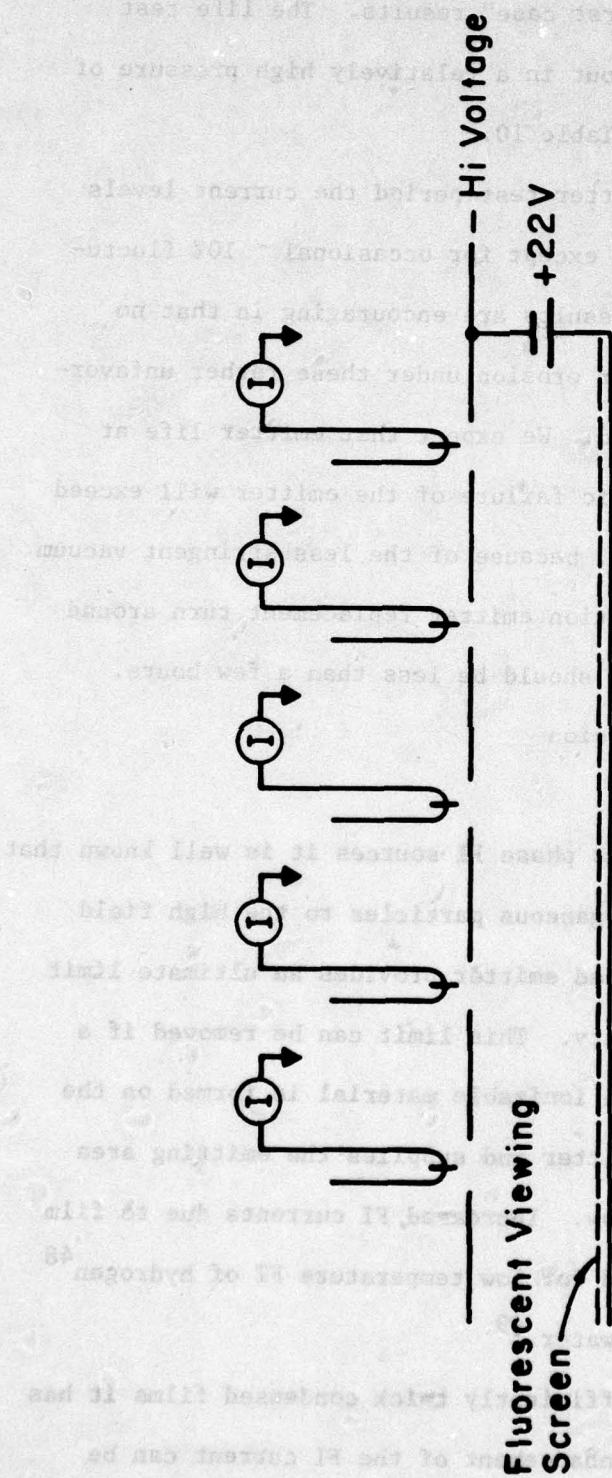


Figure 66. Schematic diagram of multiemitter field ionization life test device.

tests probably represent "worst case" results. The life test results, which were carried out in a relatively high pressure of hydrogen, are summarized in Table 10.

Throughout the emitter test period the current levels remained virtually unchanged except for occasional  $\sim 10\%$  fluctuations. These preliminary results are encouraging in that no evidence of long term emitter erosion under these rather unfavorable conditions was observed. We expect that emitter life at 77 K with respect to intrinsic failure of the emitter will exceed several hundred hours. Also, because of the less stringent vacuum requirements of field ionization emitter replacement turn around time in typical applications should be less than a few hours.

#### B. Liquid Gallium Ion Emission

##### 1. Introduction

With respect to gas phase FI sources it is well known that kinetic supply of ionizable gaseous particles to the high field region of the conically shaped emitter provides an ultimate limit to the emitted current density. This limit can be removed if a liquid film reservoir of the ionizable material is formed on the high field region of the emitter and supplies the emitting area via diffusion or viscous flow. Increased FI currents due to film formation have been reported for low temperature FI of hydrogen<sup>48</sup> and room temperature FI of water.<sup>49</sup>

In the case of sufficiently thick condensed films it has been shown that a further enhancement of the FI current can be



TABLE 10

## IRIDIUM LIFE TEST SUMMARY

<u>Emitter</u>	<u>Gas</u>	<u>Pressure</u>	<u>Average Emission</u>	<u>Voltage</u>	<u>Hours Run</u>	<u>Comments</u>
#5	H <sub>2</sub>	15 m Torr	$3.8 \times 10^{-9}$ A	10 kV	220	Tip Failed Unknown Reason
#7	H <sub>2</sub>	15 m Torr	$1.4 \times 10^{-9}$ A	10 kV	385	Test Terminated

realized through the formation of a field stabilized cone of the liquid film supported on an underlying solid emitter structure. It was shown by G. Taylor<sup>50</sup> that a balance between surface tension and electrostatic stress leads to the formation of a liquid cone of half angle  $49.3^\circ$  where the onset of cone formation occurs at a critical voltage  $V_c$  (typically 5-10 kV) which depends on the surface tension and electrode geometry. As the cone forms, the apex radius decreases sufficiently to enable field emission to occur. If a negative field is applied to the emitter, field electron emission occurs when the local apex field reaches typical field emission values ( $0.1-0.5 \text{ V/\AA}$ ),<sup>6,51</sup> while field desorption or field ionization occurs when the polarity is reversed and the local apex field reaches values  $\geq 1 \text{ V/\AA}$ .

Stable and exceedingly bright ion sources of long life ( $> 100$  hours) have been developed using this technique. Ion emission has been obtained for Ga,<sup>52</sup> Au,<sup>53</sup> Hg,<sup>53</sup> Woods metal,<sup>54</sup> alkali metals,<sup>52,55,56</sup> and others.<sup>53</sup> Typically for Ga, ion currents of 1-100  $\mu\text{A}$  may be obtained, corresponding to source angular intensities of up to  $10^{-4} \text{ A/sr}$  which is approximately 100 times greater than the gas phase FI sources.

The purpose of the present investigation was to provide a more detailed characterization of the gallium liquid metal ion (LMI) source with respect to parameters of interest to microprobe applications. Relevant source parameters such as current-voltage



relationship, angular intensity, energy distribution, noise spectrum and the effects of source temperature and current on these parameters will be presented. Previous investigators<sup>54</sup> have shown that singly charged monatomic ions are the dominant mass species in the beam of a gallium LMI source. In addition, an energy spread of 10 eV for currents of 10  $\mu$ A was reported<sup>52</sup> for a gallium LMI source. Based on focussed beam results using a gallium LMI source Krohn and Ringo<sup>52</sup> and others<sup>57</sup> have measured a source brightness of  $> 1.4 \times 10^6$  A cm<sup>-2</sup> sr<sup>-1</sup> and effective source diameter of  $\sim 100$  Å.

## 2. Mechanism

The mechanism of LMI source operations falls into three categories: (1) cone formation; (2) ionization; (3) mass transport. For a liquid film to exhibit a stable geometry in the presence of an electric field, it is necessary for the electrostatic stress normal to the surface to be exactly balanced by the surface-tension force. Taylor<sup>50</sup> has treated this problem in some detail and showed that for stable "Taylor cone" formation the cone half-angle  $\alpha$  for which the electrostatic and surface tension forces balance is  $\alpha = 49.3^\circ$ , in which case

$$F(\text{cone}) = 0.93 (8\pi\gamma/R)^{1/2} = 1399 (\gamma/R)^{1/2} \text{ (volts/cm)} \quad (25)$$

where  $F$  is the applied electrostatic field,  $\gamma$  is the surface tension in dyne/cm and  $R$  is the distance along the cone axis from the apex in cm. From these considerations Taylor<sup>50</sup> was able to derive a critical voltage  $V_c$  for cone formation given by

$$V_c = 1.432 \times 10^3 (\gamma R_0)^{1/2} \text{ (volts)} \quad (26)$$

where  $R_0$  is a form factor dependent on electrode geometry and the order of the electrode spacing in cm.

An important consideration is the apex radius  $r_a$  of the liquid cone which ultimately relates directly to the virtual size of the ion source. From considerations of a sphere on orthogonal cone conductor used by Dyke, et al.<sup>58</sup> to generate equipotential shapes describing a field emitter structure, it can be shown that the proportionality constant  $\beta = F/V$  relating electric field and applied voltage at the apex of a Taylor cone is<sup>59</sup>

$$\beta(\text{apex}) \approx 2.32 (R_0 r_a)^{-1/2} \text{ (cm}^{-1}\text{)} \quad (27)$$

Thus, by combining Eqs.(26) and (27) it can be shown that the apex field given by

$$F(\text{apex}) = 3322 (\gamma/r_a)^{1/2} \text{ (volts/cm)}. \quad (28)$$

A comparison of Eqs.(25) and (28) shows that at  $R = r_a$ ,

$F(\text{apex}) > F(\text{cone})$ . Since the end of the cone most likely terminates in a hemisphere we note that for field stabilization of a liquid sphere of radius  $r_a$  we have

$$F(\text{sphere}) = 4(\pi\gamma/r_a)^{1/2} = 2127(\gamma/r_a)^{1/2} \text{ (volts/cm)} \quad (29)$$

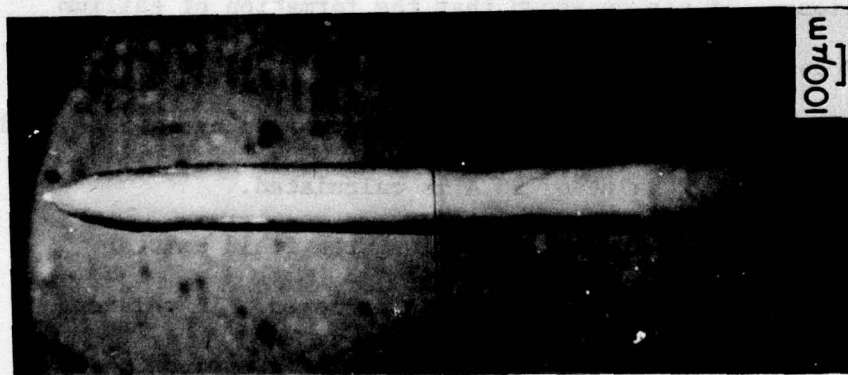
thus, it also follows that  $F(\text{apex}) > F(\text{sphere})$ . Hence, when  $V > V_c$  the formation of the Taylor cone occurs with an excess field stress at its apex. Thus, the apex radius will be unstable with respect to further elongation unless it is limited by the emission process or a compensating change in  $\gamma$  with decreasing  $r_a$ .



Gomer<sup>59</sup> has recently investigated the mechanism of ion formation and concludes that at the onset of formation of the Taylor cone, ions are generated by field desorption while at higher voltages, considerable heating takes place resulting in vaporization of the liquid metal and concomitant field ionization of thermally evaporated atoms. An interesting feature of Gomer's analysis<sup>59</sup> is the appearance of space charge effects even at onset currents which are the order of  $1 \mu\text{A}$ . The space charge is responsible for stabilizing the cone apex radius which, in the absence of space charge, would decrease without obvious limit during cone formation.

The magnitude of the value of  $r_a$  which can be formed on the liquid metal field ion source may be calculated from the following considerations. It can be shown that the formation of gallium ions via field desorption requires a field of  $1.6 \times 10^8 \text{ volt/cm}$ .<sup>60</sup> If the latter value for  $F(\text{apex})$  and  $\gamma_{\text{Ga}} = 700 \text{ dynes/cm}$  are substituted into Eq.(28) a maximum  $r_a$  value of  $30 \text{ \AA}$  is calculated.

For the present study a simple tungsten field emitter coated with gallium as shown in Fig. 67 was employed. In this case supply of ionizable material to the tungsten emitter apex on which the Taylor cone forms occurs through capillary flow along the  $\sim 1 \mu\text{m}$  grooves of the drawn tungsten emitter shaft and field induced viscous flow along the smooth conical section of the tungsten emitter. By use of the Poiseuille equation, which assumes laminar flow in the



(a)



(b)

**Figure 67.** (a) SEM photographs (backscattered mode) of a tungsten emitter wetted with a thick coating of gallium; (b) a similar photograph of a poorly or nearly exhausted emitter. The light and dark areas correspond to bare tungsten and gallium respectively.



liquid film, one can show that flow rates along the emitter shaft is sufficient to supply the equivalent of several mA of ion current provided a well wetted and continuous film coats both the emitter shaft and shank. Figure 67 gives a comparison of a well and poorly wetted emitter support.

### 3. Experimental Procedure

The source configuration consisted of a tungsten field emitter fabricated from 127  $\mu\text{m}$  drawn tungsten wire and spot welded to a 177  $\mu\text{m}$  tungsten loop which could be used to resistively heat the emitter. The conically shaped point whose cone half angle and radius were  $23 \pm 2^\circ$  and  $5 \pm 2 \mu\text{m}$  respectively was formed electrochemically. Temperature measurement was accomplished in the usual fashion by spot welding 76  $\mu\text{m}$  tungsten leads on a section of the filament loop containing the emitter and thereby measuring the filament resistance which could be converted to temperature.

A film of gallium several  $\mu\text{m}$  thick was coated onto the tungsten emitter by dipping a previously vacuum fired ( $T > 1800 \text{ K}$ ) emitter into a pool of oxide free liquid gallium. The entire process was carried out in  $\sim 10^{-6}$  torr vacuum. Proper wetting requires care in obtaining clean surface conditions for both the emitter support and liquid gallium pool. After proper wetting, emitters could be stored in inert gas environments or for short (several day) periods in air without adverse effects on subsequent performance.

For a  $\sim 10 \mu\text{m}$  thick film on a 2 mm length of emitter, one can calculate an 18 hr life at 1  $\mu\text{A}$ . By wetting emitters so that a

larger thickness of the gallium was contained at the region of the spot weld of the tungsten emitter, source life at 5 to 10  $\mu\text{A}$  current level exceeded 100 hrs.

Two tube embodiments were used to investigate the emission properties of the aforementioned LMI source. In each case the emitter tip was mounted a few mm behind and concentric with an extractor ring electrode consisting of a wire loop 10 mm in diameter. First, a standard field ion microscope with a microchannel plate amplifier was used. This allowed the gallium ions to be converted to electrons and multiplied prior to impingement on a fluorescent screen on which the ion beam pattern could be directly viewed in real time. A second embodiment was a tube in which the negative planar electrode contained a 127  $\mu\text{m}$  aperture through which a small solid angle of the beam was transmitted. The latter aperture was followed by a retarding energy analyzer employing an intermediate image filter lens arrangement of the type described by Simpson and Morton.<sup>61,62</sup> The ion current that was transmitted through the filter lens was collected in a Faraday cup. Electronic differentiation of the collected current was accomplished by capacitively coupling a 0.3 to 1.0 V ac signal to the dc ramp voltage applied to the central retarding electrode of the filter lens and detecting it with a Lock-in amplifier. The high voltage was applied positively to the emitter and retarding electrode. Emitter heating was accomplished by a dc current supply which floated at emitter potential.



The emitter and extractor electrode were mounted as a unit on an xyz manipulator which allowed the effective beam acceptance aperture half angle to be varied from 1 to 5 mr by moving the emitter in the z direction. Experiments showed that no change in the energy analyzer performance occurred with z variation, although all total energy distribution (TED) measurements were performed at maximum emitter to aperture distance ( $z \approx 4.6$  cm) in order to minimize secondary electrons returned to the emitter.

Performance of the LMI source was unaffected by background residual gas pressure up to  $10^{-4}$  torr; in all measurements reported here  $P \leq 1 \times 10^{-7}$  torr.

#### 4. Results and Discussion

The dominant emission mode of the Fig. 67 gallium LFI source configuration was dc with an occasional pulse mode observed near the threshold voltage  $V_c$ . In most cases the pulse mode frequency increased with extractor voltage and in a few cases could not be made to operate in a dc mode. Based on the fact that well coated emitters did not exhibit pulse mode emission, we concluded that it results from insufficient mass flow to the Taylor cone which leads to oscillations of the Taylor cone. When insufficient mass flow to the Taylor cone occurred it was necessary to increase the voltage such that  $V > V_c$  to promote flow along the smooth conical section of the emitter. The resultant Taylor cone is rapidly depleted due to the excess apex field and a cyclic process occurs. Even in the case of dc mode emission a higher

threshold voltage was frequently required to initiate emission than to quench emission. For example emission may turn on at several  $\mu\text{A}$  and turn off at  $\sim 1 \mu\text{A}$ .

A typical total current  $I_T$  vs voltage characteristic for a well coated gallium LMI source is given in Fig. 68 along with the current transmitted through a  $6 \mu\text{sr}$  solid angle centered on beam axis. Although the  $I(V)$  curves shift horizontally as much as 1 kV during operation and sometimes with a change in slope, the general features of the  $I \propto (V - V_c)^{1/2}$  functional relationship and decrease in beam transmission with voltage was observed for all well coated emitters. Tungsten emitters made from larger diameter wire, and usually with larger cone angle ( $\sim 30^\circ$  half angle), operated at higher voltage (i.e. 9-10 kV). It was interesting to note that as the LFI source approached exhaustion of the gallium coating the operating voltage increased significantly and  $dI/dV$  usually decreased. From these results we conclude that in the case of improperly wetted emitters or nearly exhausted coatings (e.g. Fig. 67(b)), the variation in mass flow rate alters the  $I(V)$  characteristics.

Another common observation was the decreasing value of transmission with  $V$  for the on axis probe current as shown in Fig. 68. The cause of this can be observed in the Fig. 69 photos which show the beam pattern size significantly increases with total beam current. A more quantitative presentation of this effect can be seen in the Fig. 70 plot of the beam angular distribution at 3 values of  $I_T$ . These results show that the angular intensity is strongly



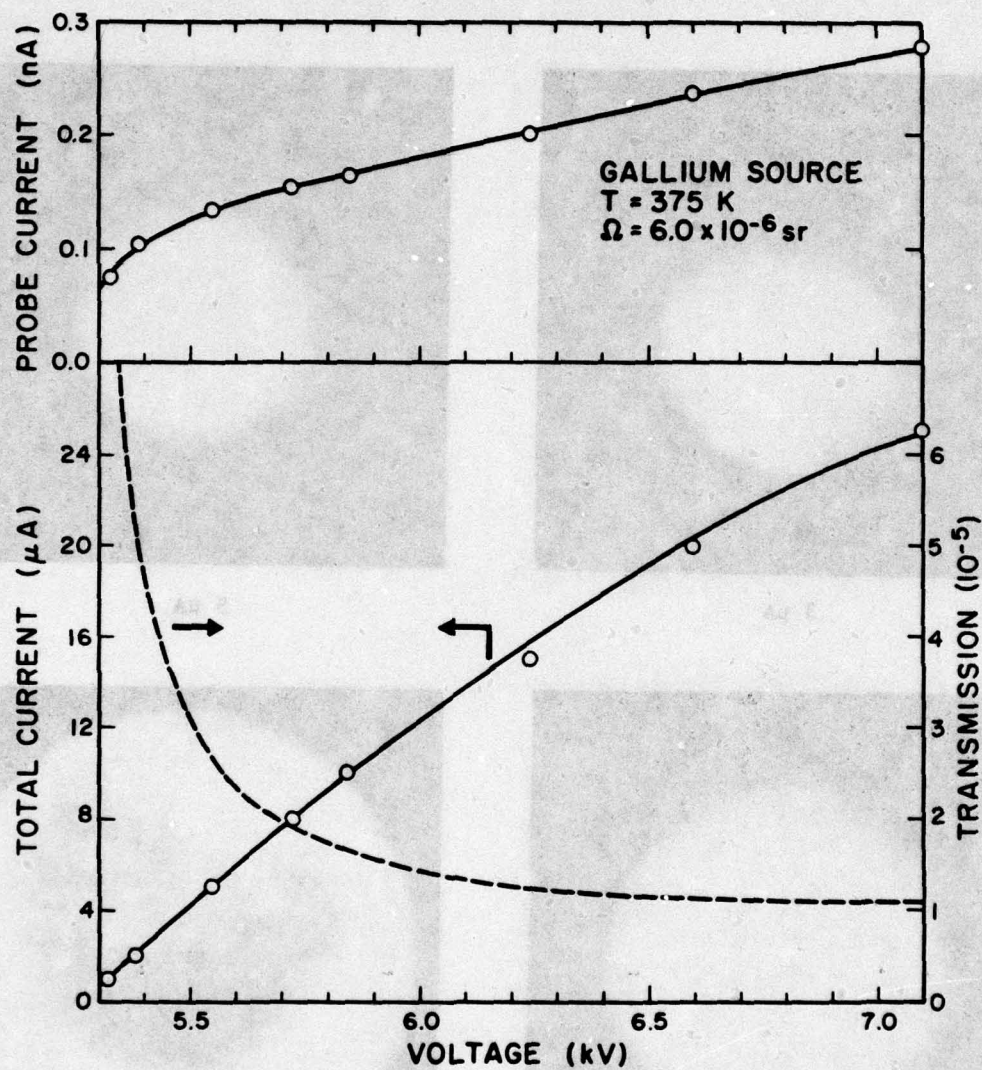
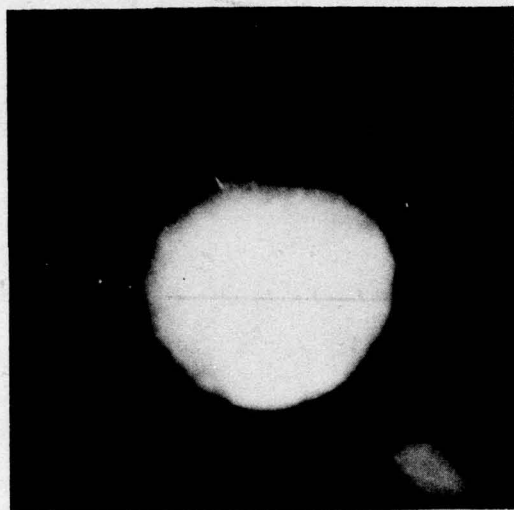
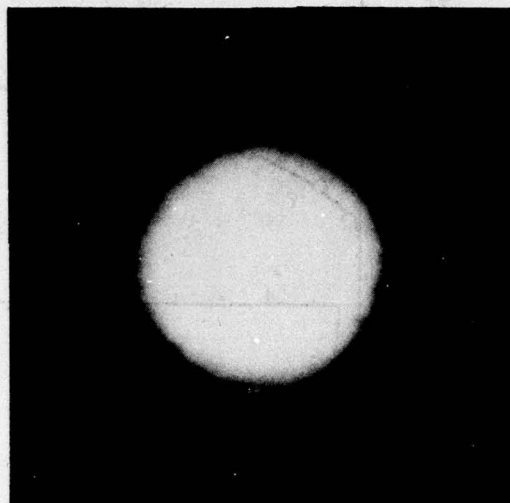


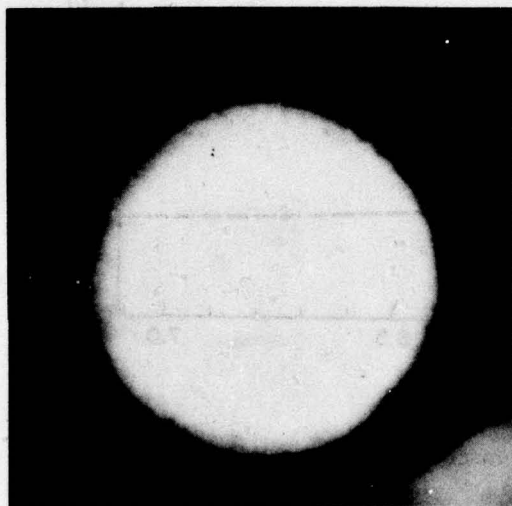
Figure 68. Typical total and probe current-voltage characteristics for a gallium LMI source.



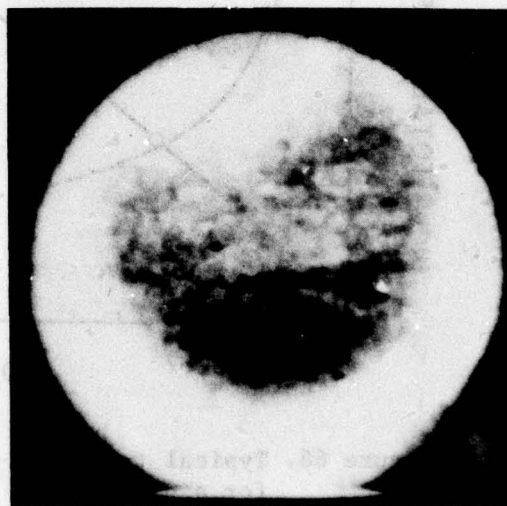
3  $\mu\text{A}$



5  $\mu\text{A}$



10  $\mu\text{A}$



20  $\mu\text{A}$

Figure 69. Ion patterns of an operational gallium LMI source at various total current levels. The dark region in the central portion of the 20  $\mu\text{A}$  photo is due to ion beam damage.



peaked along the emitter axis and nearly doubles its angular divergence as  $I$  increases from 4 to 25  $\mu A$ . In view of the anticipated small

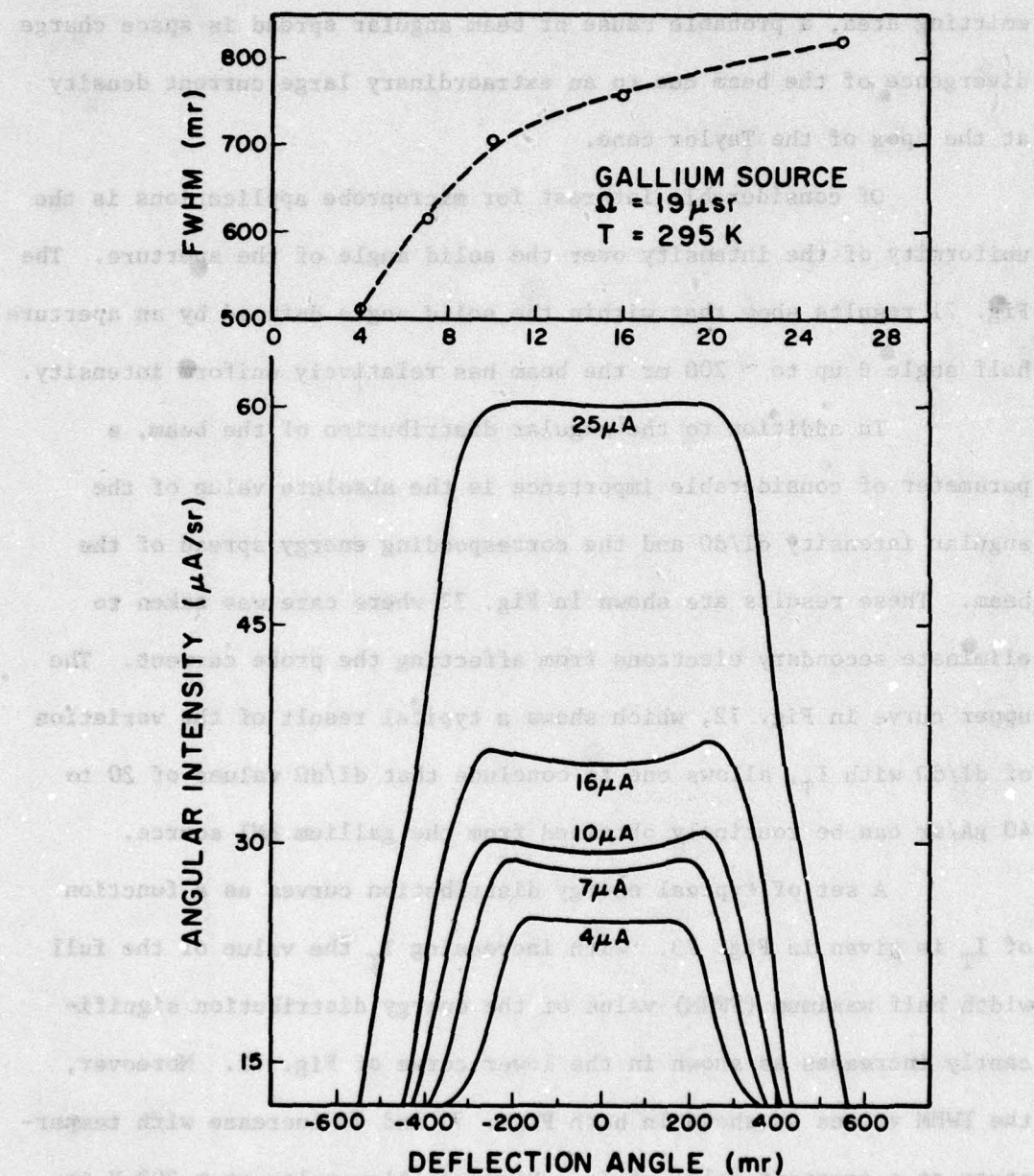


Figure 70. Angular intensity distribution for a gallium LMI source at various values of total current using a probe with the indicated solid angle  $\Omega$ . Upper curve gives the FWHM of the lower curves vs total current.

peaked along the emitter axis and nearly doubles its angular divergence as  $I_T$  increases from 4 to 25  $\mu\text{A}$ . In view of the anticipated small emitting area, a probable cause of beam angular spread is space charge divergence of the beam due to an extraordinary large current density at the apex of the Taylor cone.

Of considerable interest for microprobe applications is the uniformity of the intensity over the solid angle of the aperture. The Fig. 71 results show that within the solid angle defined by an aperture half angle  $\theta$  up to  $\sim 200$  mr the beam has relatively uniform intensity.

In addition to the angular distribution of the beam, a parameter of considerable importance is the absolute value of the angular intensity  $dI/d\Omega$  and the corresponding energy spread of the beam. These results are shown in Fig. 72 where care was taken to eliminate secondary electrons from affecting the probe current. The upper curve in Fig. 72, which shows a typical result of the variation of  $dI/d\Omega$  with  $I_T$ , allows one to conclude that  $dI/d\Omega$  values of 20 to 40  $\mu\text{A}/\text{sr}$  can be routinely obtained from the gallium LMI source.

A set of typical energy distribution curves as a function of  $I_T$  is given in Fig. 73. With increasing  $I_T$  the value of the full width half maximum (FWHM) value of the energy distribution significantly increases as shown in the lower curve of Fig. 72. Moreover, the FWHM values as shown in both Figs. 71 and 73 increase with temperature at a constant value of  $I_T$ . Since gallium melts at  $\sim 302$  K it is impossible to operate at lower temperature; even so, the FWHM



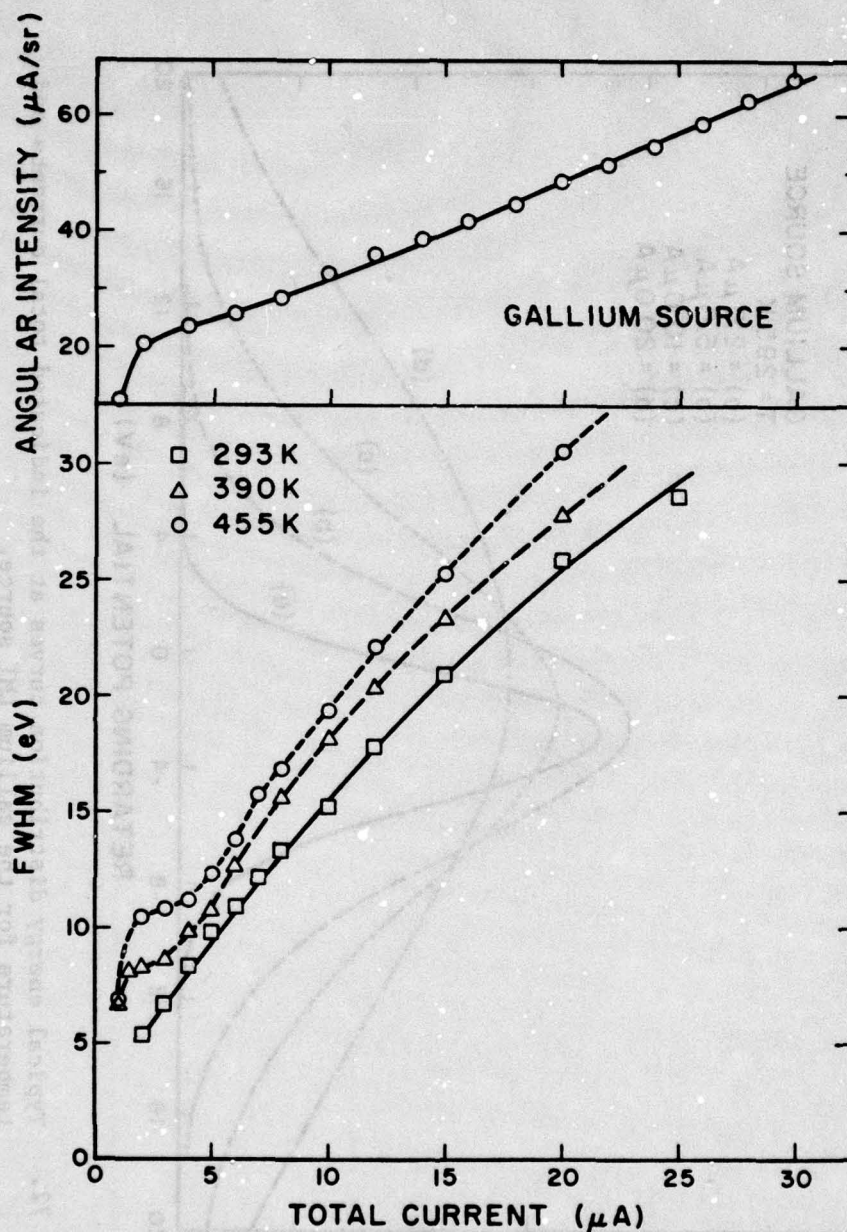


Figure 71. Values of FWHM for the total energy distribution of a gallium LMI source vs total current at the indicated temperatures. Upper curve shows a typical relationship between source angular intensity and total current.

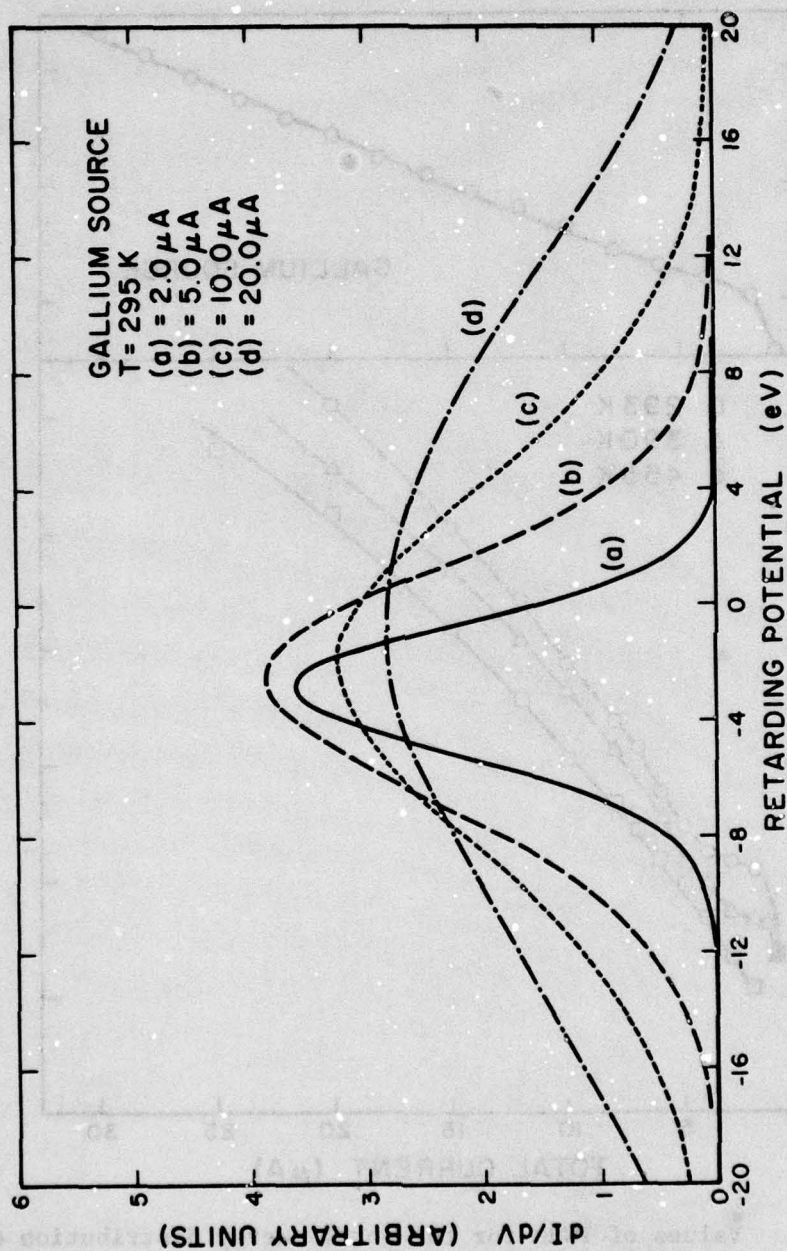


Figure 72. Typical energy distribution curves at the indicated total currents and temperature for the gallium LMI source.



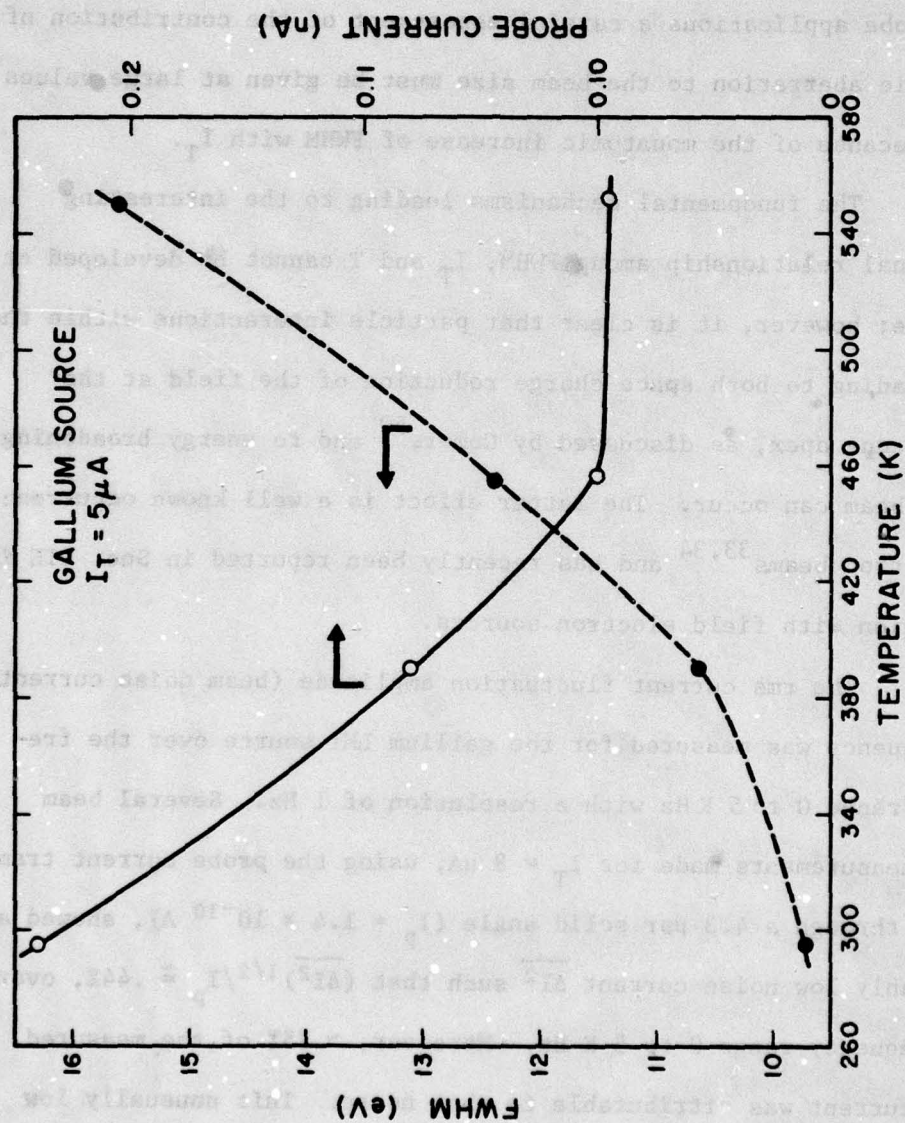


Figure 73. Curves show the variation of the total energy distribution FWHM and corresponding probe current with emitter temperature at the indicated total current for a gallium LMI source.

value at the lowest operating temperature attains a value of  $\sim 4.5$  eV which is only  $\sim 2.5$  eV larger than values reported for gas phase FI sources<sup>63</sup> with  $dI/d\Omega$  values some 50 times smaller. For use in microprobe applications a careful assessment of the contribution of chromatic aberration to the beam size must be given at large values of  $I_T$  because of the monotonic increase of FWHM with  $I_T$ .

The fundamental mechanisms leading to the interesting functional relationship among FWHM,  $I_T$  and  $T$  cannot be developed at this juncture; however, it is clear that particle interactions within the beam leading to both space charge reduction of the field at the Taylor cone apex, as discussed by Gomer,<sup>59</sup> and to energy broadening of the beam can occur. The latter effect is a well known occurrence in electron beams<sup>33,34</sup> and has recently been reported in Sec. IIE in connection with field electron sources.

The rms current fluctuation amplitude (beam noise current) vs frequency was measured for the gallium LMI source over the frequency range 0 to 5 KHz with a resolution of 1 Hz. Several beam noise measurements made for  $I_T = 8 \mu\text{A}$ , using the probe current transmitted through a  $4.3 \mu\text{sr}$  solid angle ( $I_p = 1.4 \times 10^{-10}$  A), showed a remarkably low noise current  $\overline{\Delta I^2}$  such that  $(\overline{\Delta I^2})^{1/2}/I_p \cong .44\%$ , over the frequency range 0 to 5 KHz. Moreover,  $\sim 75\%$  of the measured noise current was attributable to shot noise. This unusually low noise figure could be due to a space charge noise suppression mechanism proposed elsewhere<sup>44</sup> for high current density field emission sources. Thus, further support of the notion of a space charge



dominated operation of the LMI source put forth by Gomer<sup>59</sup> is provided by the beam noise results.

## 5. Conclusions

This investigation shows that the gallium LMI source has excellent properties as a source for microprobe applications provided care is taken to operate the source at low temperature and low total current in order to minimize the beam energy spread. The source angular intensity does not increase linearly with  $I_T$ , and exhibits a value of  $dI/d\Omega \approx 20 \mu\text{A}/\text{sr}$  at threshold which is approximately 20 times the value observed for a gas phase hydrogen FI source.

This impressive performance of the gallium LMI source coupled with its low noise characteristic underscores the remarkable nature of the gallium LMI source. Similar investigations of other LMI source materials, such as bismuth, must be carried out in order to determine whether higher melting metals will show similar characteristics and modes of operation.

## SECTION V

### FOCUSSED ION BEAM MEASUREMENTS

The objective of this task has been to show the possibility of producing focussed ion beams with  $< 0.1 \mu\text{m}$  size and 10 to 1000 pA current. A scanning ion microscope (SIM) has been built and tested with hydrogen and argon as the field ion sources. The use of the SIM has enabled us to easily measure properties such as resolution, beam current, and noise. Resolution is limited by chromatic aberration to  $\sim 6500 \text{ \AA}$  with hydrogen when the SIM is operated at 10-15 kV, as  $\Delta E \approx 4 \text{ eV}$  for the two component beam  $\text{H}^+ + \text{H}_2^+$  at a field of  $\sim 2 \text{ V/\AA}$  at the emitter tip. Higher resolution is achieved with monoatomic gases such as Ar where  $\Delta E \approx 1 \text{ eV}$ . Although results of the SIM have been reported elsewhere<sup>6,47,64</sup> a few additional results along with plans for a greatly improved electrostatic lens are presented here.

#### A. Gun and System Configuration

The SIM consists of a differentially pumped FI source<sup>6</sup> coupled to an electrostatic electron optical column which consists of two einzel lenses arranged as a doublet, a stigmator, and a post-lens deflection system (see Fig. 74).

Since the beam is collimated by the objective lens and objective aperture the axial placement of the remaining optical components is not critical. In this case the aperture is located approximately 4 cm below the objective lens, the stigmator is approximately 10 cm below the aperture and the projector lens is approximately 5 cm



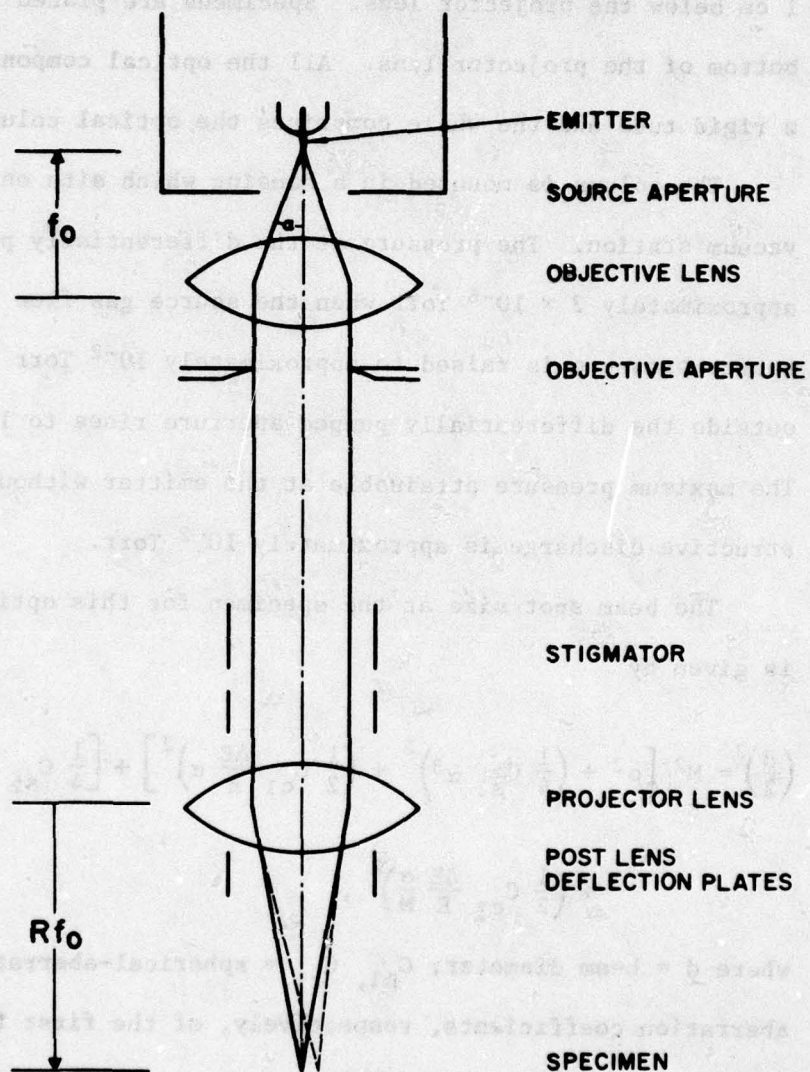


Figure 74. Schematic diagram of the SIM optical system, with FI source at the top. Typical values for  $f_0$  are 5-9 mm and  $R = 5-9$ .

below the stigmator. The deflection plates are located approximately 1 cm below the projector lens. Specimens are placed 3-5 cm from the bottom of the projector lens. All the optical components are held in a rigid tube and the whole comprises the optical column.

The column is mounted in a housing which sits on a commercial vacuum station. The pressure at the differentially pumped source is approximately  $2 \times 10^{-6}$  Torr when the source gas flow is off. When the source pressure is raised to approximately  $10^{-2}$  Torr the pressure just outside the differentially pumped aperture rises to  $1-3 \times 10^{-5}$  Torr. The maximum pressure attainable at the emitter without incurring destructive discharge is approximately  $10^{-2}$  Torr.

The beam spot size at the specimen for this optical arrangement is given by

$$\left(\frac{d}{2}\right)^2 = M^2 \left[ \rho^2 + \left(\frac{1}{4} C_{s1} \alpha^3\right)^2 + \left(\frac{1}{2} C_{c1} \frac{\Delta E}{E} \alpha\right)^2 \right] + \left[\frac{1}{4} C_{s2} \left(\frac{\alpha}{M}\right)^3\right]^2 + \left(\frac{1}{2} C_{c2} \frac{\Delta E}{E} \frac{\alpha}{M}\right)^2,$$

where  $d$  = beam diameter;  $C_{s1}$ ,  $C_{c1}$  = spherical-aberration and chromatic-aberration coefficients, respectively, of the first (objective) lens;  $C_{s2}$ ,  $C_{c2}$  = spherical aberration and chromatic aberration coefficients, respectively, of the second (projector) lens;  $M$  = overall magnification of the system;  $\rho$  = virtual source radius,  $\alpha$  = half-angle defined by the beam limiting aperture;  $\Delta E$  = beam energy spread;  $E$  = beam energy.  $M$  is equal to the ratio of the focal length of the second lens to that of



the first,  $M = R \equiv f/f_0$ . The values of our components were  $f_0 = 5.5$  mm;  $C_{s1} = 88$  mm;  $C_{c1} = 18$  mm;  $C_{s2} \approx 4000$  mm;  $C_{c2} = 150$  mm;  $f \approx 35$  mm;  $\alpha = 0.012$  radians;  $\rho \approx 10$  Å,  $M = R \approx 6$ .

When the SIM is operated in the secondary electron mode the electron signal, amplified with a channeltron electron multiplier, modulates the intensity of a CRT driven synchronously with the beam deflection plates. With this arrangement photographic exposure times of approximately 100 s are required for 100-1000  $\times$  magnification.

In situations typical of ion damage writing, where high currents are desired in focussed beam spots of approximately 1000-2000 Å, the virtual source size  $\rho$  has a relatively small effect on the final beam diameter. This is because the large acceptance angles into the optical system necessary for high current, result in discs of confusion at the virtual source due to the chromatic and spherical aberrations of the optical system which are large compared to the virtual source. In many cases, the contribution to the beam diameter of the virtual source can be ignored and the current and beam spot size are determined by the optics alone. This means that the optical system does not have to demagnify, indeed a practical system may have an overall magnification greater than unity, especially if a large working distance is required. This in turn implies the quality of the optics of the source become very important, rather than the quality of the final lens as with a conventional electron or ion source. The most important characteristics of the field emission source are now the angular intensity  $\frac{dI}{d\Omega}$ , and the energy spread of the beam ( $\Delta E$ ).

Routine operation of the TFE sources with  $\frac{dI}{d\Omega} \approx 10^{-3} \text{ A sr}^{-1}$ , gas phase FI sources with  $\frac{dI}{d\Omega} \approx 5 \times 10^{-7} \text{ A sr}^{-1}$ , and LFI sources with  $\frac{dI}{d\Omega}$  of from  $10^{-5}$  to  $10^{-4} \text{ A sr}^{-1}$  have been obtained. In each case the beam energy spread increases with  $\frac{dI}{d\Omega}$ . The large values of  $\frac{dI}{d\Omega}$ , coupled with small virtual source size allow new dimensions of experiments and applications; however, because of the larger beam energy spreads than either conventional thermionic or cold field emission systems, the optics must be chosen with some care. For example, the energy spread of a gas phase FI source can range from 0.5 eV to 4 eV at normal operating voltage,<sup>65</sup> depending on the nature of the gas. The energy spread of the gallium LFI source has been measured to range from 5 eV to 30 eV and is strongly current dependent. It is clear that the chromatic aberration of the source optics, or gun lens, will play an important role in the performance of any field emission system utilizing FI, TFE or LFI.

Under other support we have calculated the properties of a physically and voltage asymmetric three-element electrostatic lens which is suitable for use with a field emission source at modest acceleration ratios  $0.2 \leq V_f/V_i \leq 6$ , where  $V_f/V_i = V_{\text{final}}/V_{\text{initial}}$ . A brief report of this lens will be given here. We have chosen the range of  $V_f/V_i$  so that a field emission source operated in the usual voltage range of 3-8 kV (TFE, LFI) or 10-20 kV (FI) could be used to produce a beam with energy in the 1-30 keV range. The lens is based on one analyzed by Riddle<sup>66</sup> as an asymmetric einzel lens.



Conventional two-element immersion lenses such as the Crewe lens<sup>67,68</sup> or the design by Munro<sup>69</sup> are generally not suitable in the range of interest.

Previous investigations of physically symmetric, voltage asymmetric lenses by Read,<sup>70,71</sup> Imhof and Read<sup>72</sup> and Kuroda et al.<sup>73,74,75</sup> turned up some interesting features, such as the "zoom" property which allows the object and image distances to remain fixed while the beam energy is varied. We were led to investigate a lens which was also physically asymmetric in the hope that superior aberration coefficients could be found as well.

Lens properties were calculated by means of the finite element method, using computer programs of Munro.<sup>69,76,77</sup> We consider here the following results: a comparison with the two-element Munro lens;<sup>69</sup> use of the asymmetric lens to produce a crossover; use of the asymmetric lens to produce a collimated beam brought to a focus by a second lens (see Fig. 74).

The lens geometry is shown in Fig. 75. A number of working voltage ratios  $\frac{V_3}{V_1} = \frac{V_f}{V_1}$  were examined and results for  $\frac{V_3}{V_1} = 2$  are shown in Fig. 76.  $C_{s\infty}$  refer to the spherical and chromatic aberration coefficients for the infinite magnification case (object at focal point).  $F$  is the focal position measured to the left of the first electrode, i.e., measured to the left of 0.0 mm in Fig. 75, and  $f$  is the focal length. Note the favorable ratio of  $\frac{C_{s\infty}}{f}$ , which is less than 0.5 when  $\frac{V_2}{V_1} = 7$ . The focussed beam diameter  $d$  in Å is calculated from

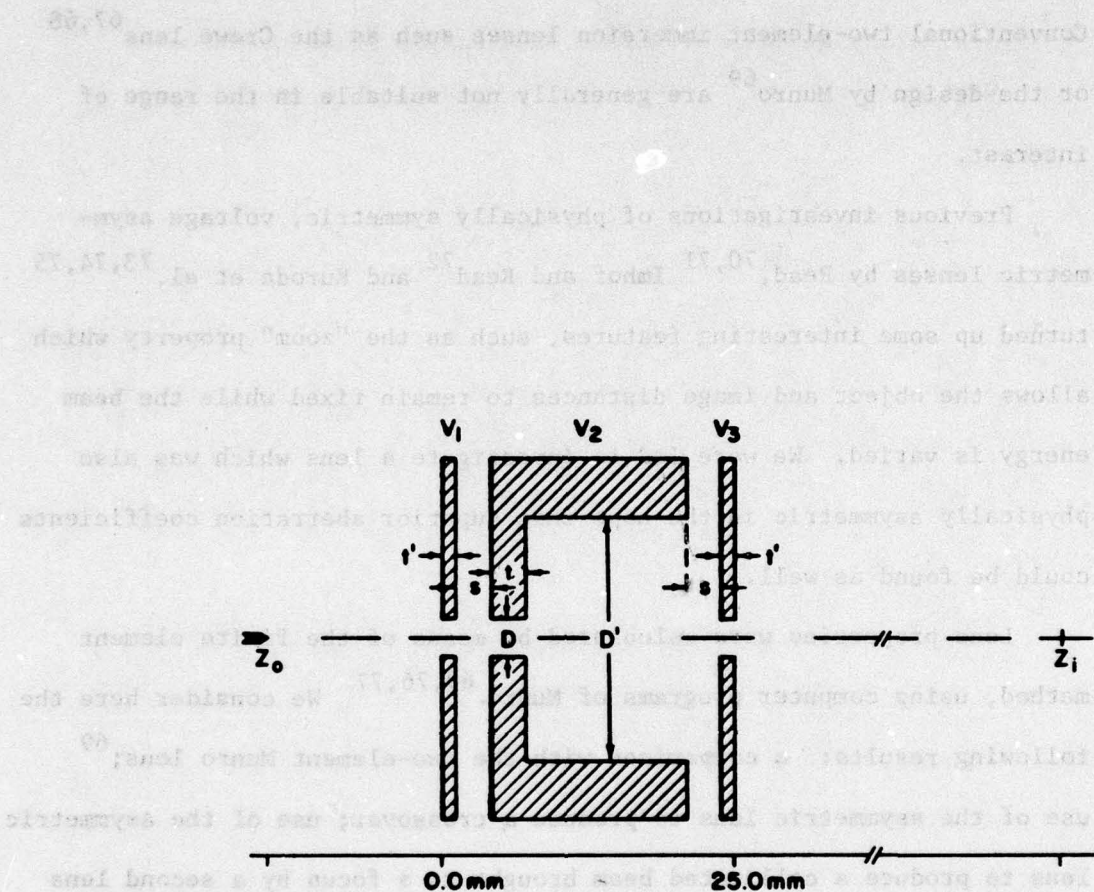


Figure 75. Scale drawing of the asymmetric, three-element lens.  
 $D = S = t = 3$  mm,  $t' = 1$  mm,  $D' = 18$  mm.  $V_1 = V_{\text{initial}}$ ,  
 $V_3 = V_{\text{final}}$ ,  $V_2$  is the control voltage.



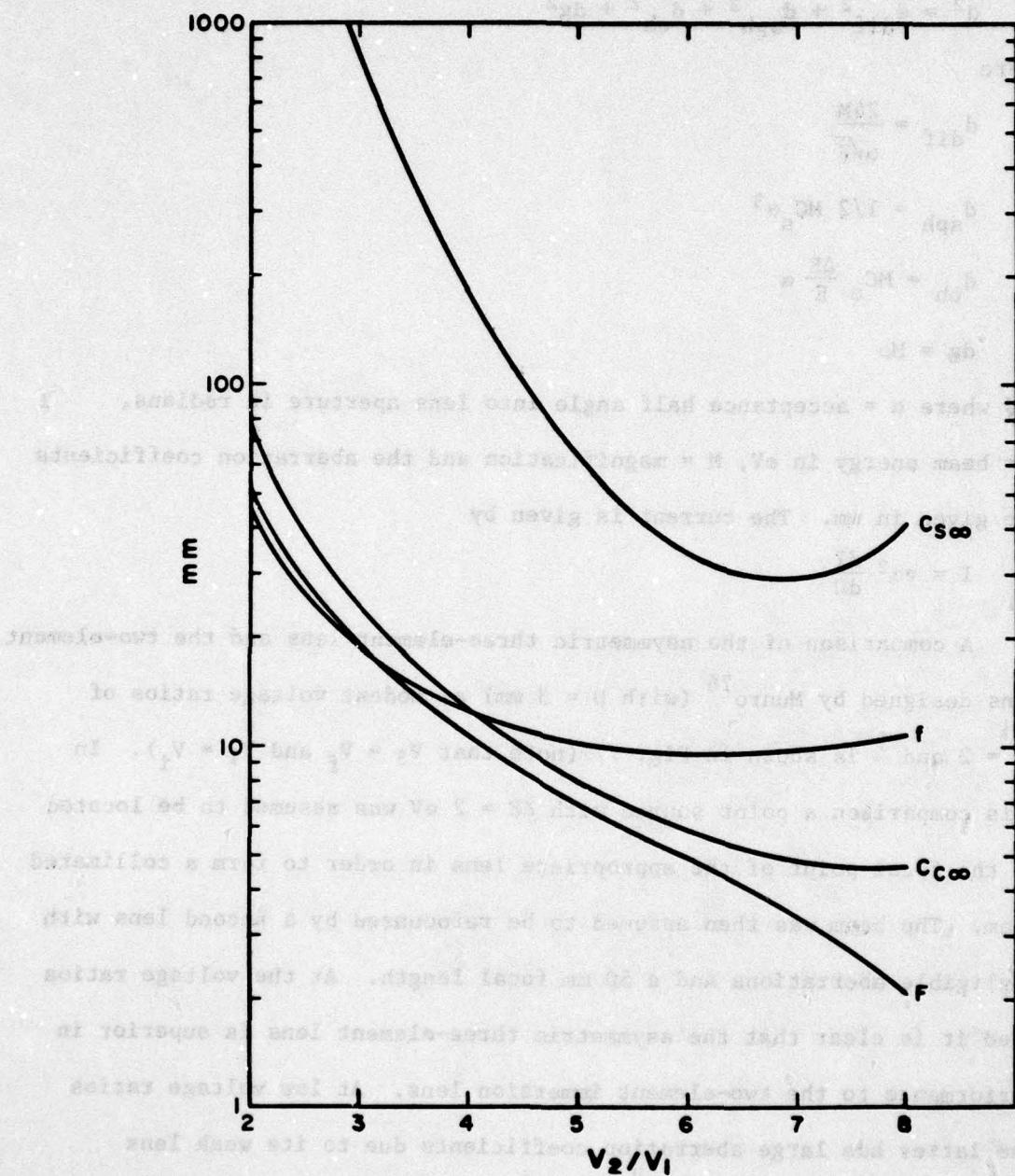


Figure 76. The properties of the three-element lens in the infinite magnification mode as a function of the control voltage when  $V_3/V_1 = 2$ .  $F$  is the position of the focal point to the left of the first electrode.

$$d^2 = d_{\text{dif}}^2 + d_{\text{sph}}^2 + d_{\text{ch}}^2 + dg^2$$

where

$$d_{\text{dif}} = \frac{24M}{\alpha\sqrt{E}}$$

$$d_{\text{sph}} = 1/2 MC_s \alpha^3$$

$$d_{\text{ch}} = MC_c \frac{\Delta E}{E} \alpha$$

$$dg = M\rho$$

and where  $\alpha$  = acceptance half angle into lens aperture in radians,

$E$  = beam energy in eV,  $M$  = magnification and the aberration coefficients are given in mm. The current is given by

$$I = \pi\alpha^2 \frac{dI}{d\Omega}$$

A comparison of the asymmetric three-element lens and the two-element lens designed by Munro<sup>76</sup> (with  $D = 3$  mm) at modest voltage ratios of  $\frac{V_f}{V_1} = 2$  and 4 is shown in Fig. 77 (note that  $V_3 = V_f$  and  $V_1 = V_i$ ). In this comparison a point source with  $\Delta E = 2$  eV was assumed to be located at the focal point of the appropriate lens in order to form a collimated beam. The beam was then assumed to be refocussed by a second lens with negligible aberrations and a 50 mm focal length. At the voltage ratios used it is clear that the asymmetric three-element lens is superior in performance to the two-element immersion lens. At low voltage ratios the latter has large aberration coefficients due to its weak lens action ( $f/D = 55$  and 12 for  $\frac{V_f}{V_1} = 2$  and 4, respectively). The three-element lens with a high center electrode potential ( $\frac{V_2}{V_1} = 7$  and 11 for



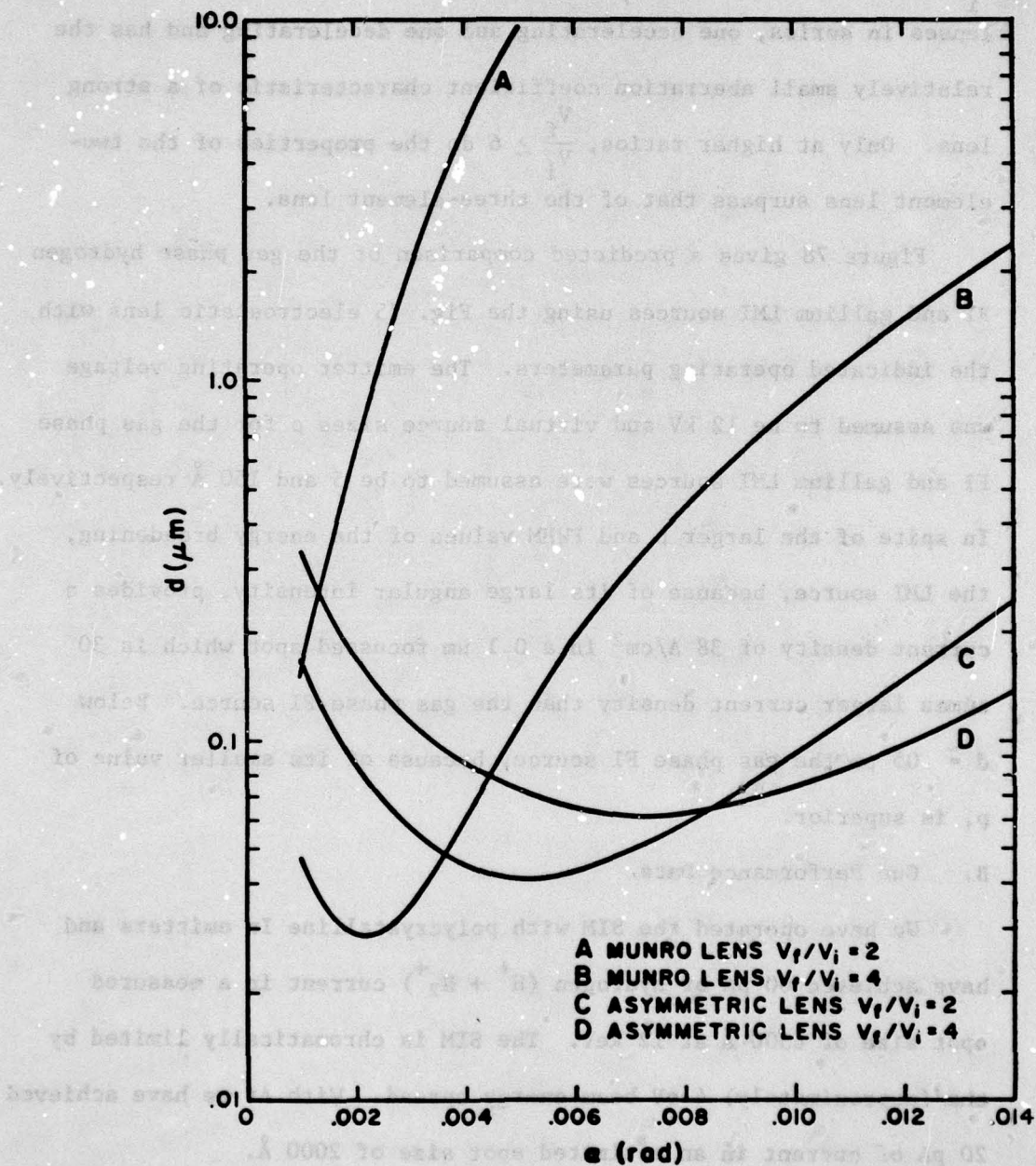


Figure 77. A comparison of the three-element lens with the two-element Munro lens at low voltage ratios and for  $\Delta E = 2$  eV as a function of lens entrance aperture half angle,  $\alpha$ . In cases C and D,  $V_2/V_1 = 6.5$  and 11, respectively. Field emission voltage  $E = 5$  kV.

$\frac{V_f}{V_i} = 2$  and 4, respectively) behaves somewhat like two strong immersion lenses in series, one accelerating and one decelerating and has the relatively small aberration coefficient characteristic of a strong lens. Only at higher ratios,  $\frac{V_f}{V_i} \gtrsim 6$  do the properties of the two-element lens surpass that of the three-element lens.

Figure 78 gives a predicted comparison of the gas phase hydrogen FI and gallium LMI sources using the Fig. 75 electrostatic lens with the indicated operating parameters. The emitter operating voltage was assumed to be 12 kV and virtual source sizes  $\rho$  for the gas phase FI and gallium LMI sources were assumed to be 5 and 150 Å respectively. In spite of the larger  $\rho$  and FWHM values of the energy broadening, the LMI source, because of its large angular intensity, provides a current density of 38 A/cm<sup>2</sup> in a 0.1 μm focussed spot which is 30 times larger current density than the gas phase FI source. Below  $d \approx .05$  μm the gas phase FI source, because of its smaller value of  $p$ , is superior.

#### B. Gun Performance Data

We have operated the SIM with polycrystalline Ir emitters and have achieved 60 pA of hydrogen ( $H^+ + H_2^+$ ) current in a measured spot size of 6500 Å at 12 keV. The SIM is chromatically limited by the (approximately) 4 eV beam energy spread. With Ar we have achieved 20 pA of current in an estimated spot size of 2000 Å.

Images in the secondary-electron mode are similar to those of an SEM. The main contrast mechanism is the variation of the secondary electron yield  $\gamma$  with angle of incidence of the beam as it strikes



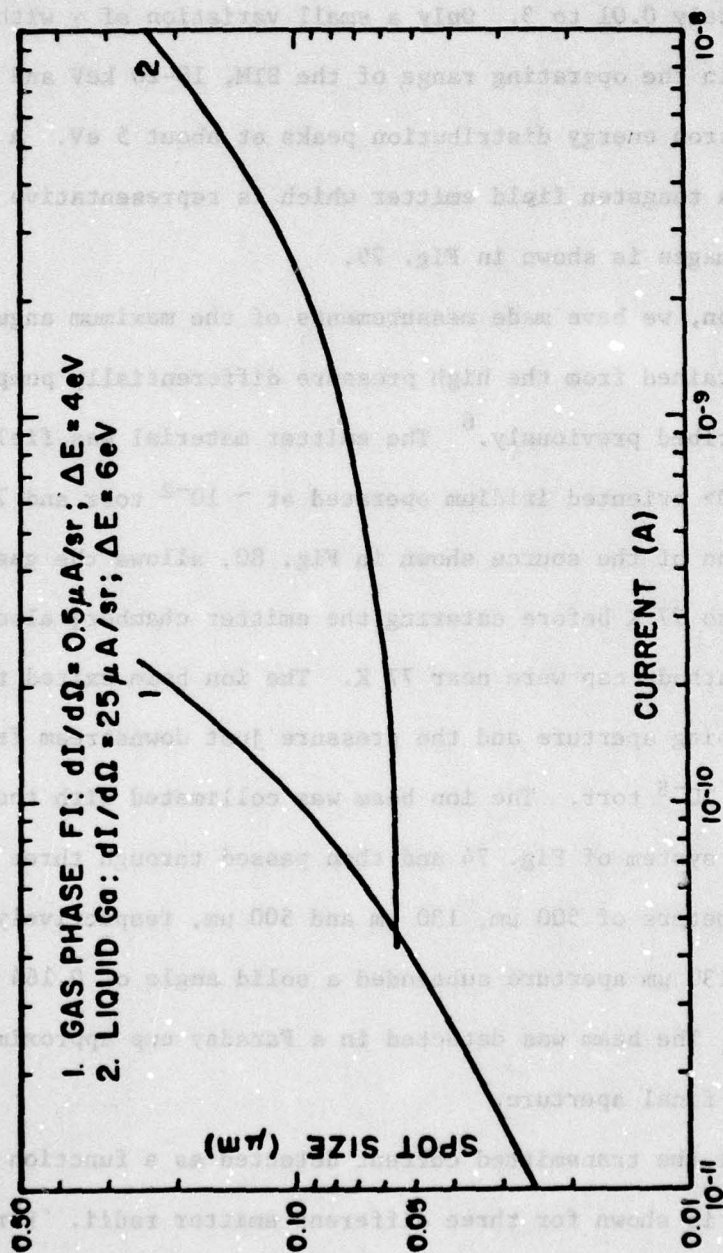


Figure 78. Curves show the predicted variation of beam current in the focussed spot for hydrogen gas phase FI and gallium LMI sources. The three-element electrostatic lens, has a beam voltage of 36 kV, a central lens voltage of 55 kV, a magnification of 3.65,  $C_s = 68.2 \text{ mm}$ ,  $C_c = 7.9 \text{ mm}$  and working distance of 25 mm.

AD-A078 520

OREGON GRADUATE CENTER BEAVERTON DEPT OF APPLIED PHY--ETC F/G 20/12  
FIELD ELECTRON AND ION SOURCE RESEARCH FOR HIGH DENSITY INFORMA--ETC(U)  
MAY 79 L W SWANSON , J ORLOFF , A E BELL F33615-76-C-1327

UNCLASSIFIED

AFAL-TR-79-1133

NL

3 OF 3  
ADA  
078520

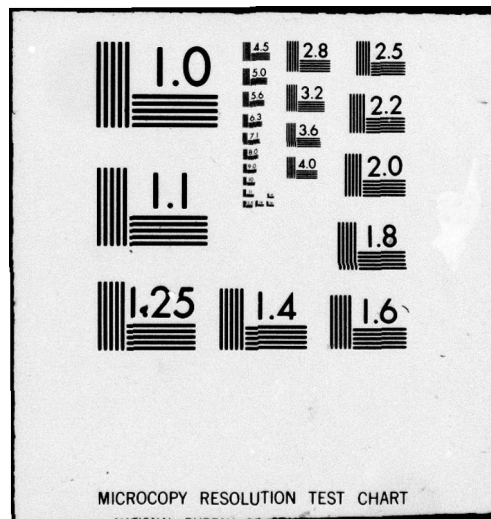


END  
DATE  
FILMED

1-80

DDC





different portions of the specimen.  $\gamma$  depends on the particular ion-specimen-energy combination in a complicated fashion and varies from approximately 0.01 to 3. Only a small variation of  $\gamma$  with energy occurs in the operating range of the SIM, 10-20 keV and the secondary-electron energy distribution peaks at about 5 eV. A micrograph of a tungsten field emitter which is representative of hydrogen-ion images is shown in Fig. 79.

In addition, we have made measurements of the maximum angular intensities obtained from the high pressure differentially pumped FI source described previously.<sup>6</sup> The emitter material was field evaporated <110> oriented iridium operated at  $\sim 10^{-2}$  torr and 77 K. The construction of the source shown in Fig. 80, allows the gas to be pre-cooled to 77 K before entering the emitter chamber; also the walls of the cathode cap were near 77 K. The ion beam exited through the 0.5 mm pumping aperture and the pressure just downstream from the source was  $5 \times 10^{-5}$  torr. The ion beam was collimated with the electrostatic lens system of Fig. 74 and then passed through three apertures with diameters of 500  $\mu\text{m}$ , 130  $\mu\text{m}$  and 500  $\mu\text{m}$ , respectively. The beam defining 130  $\mu\text{m}$  aperture subtended a solid angle of 0.164 msr at the source. The beam was detected in a Faraday cup approximately 6 cm below the final aperture.

In Fig. 81 the transmitted current detected as a function of source voltage is shown for three different emitter radii. For each voltage the electrostatic lens was adjusted to maintain a collimated beam. The source pressure was kept constant for each measurement.



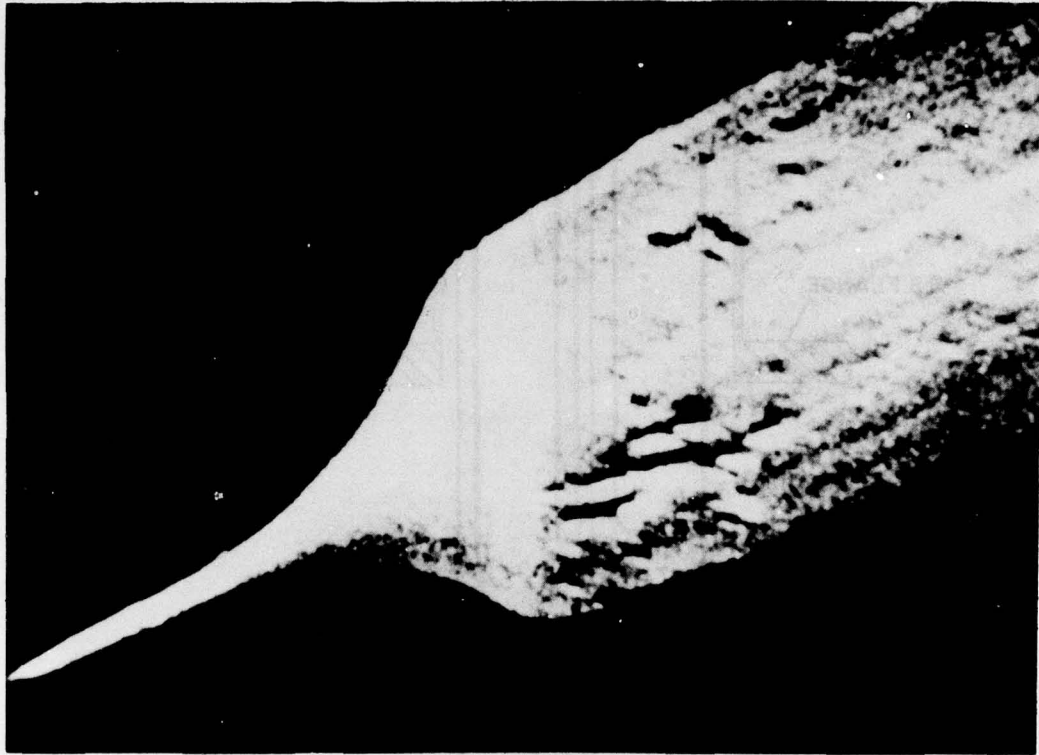


Figure 79. Micrograph of a dc dropoff W field emitter. Diameter at widest point is 130  $\mu\text{m}$ . Imaged with hydrogen ions at 15 kV.

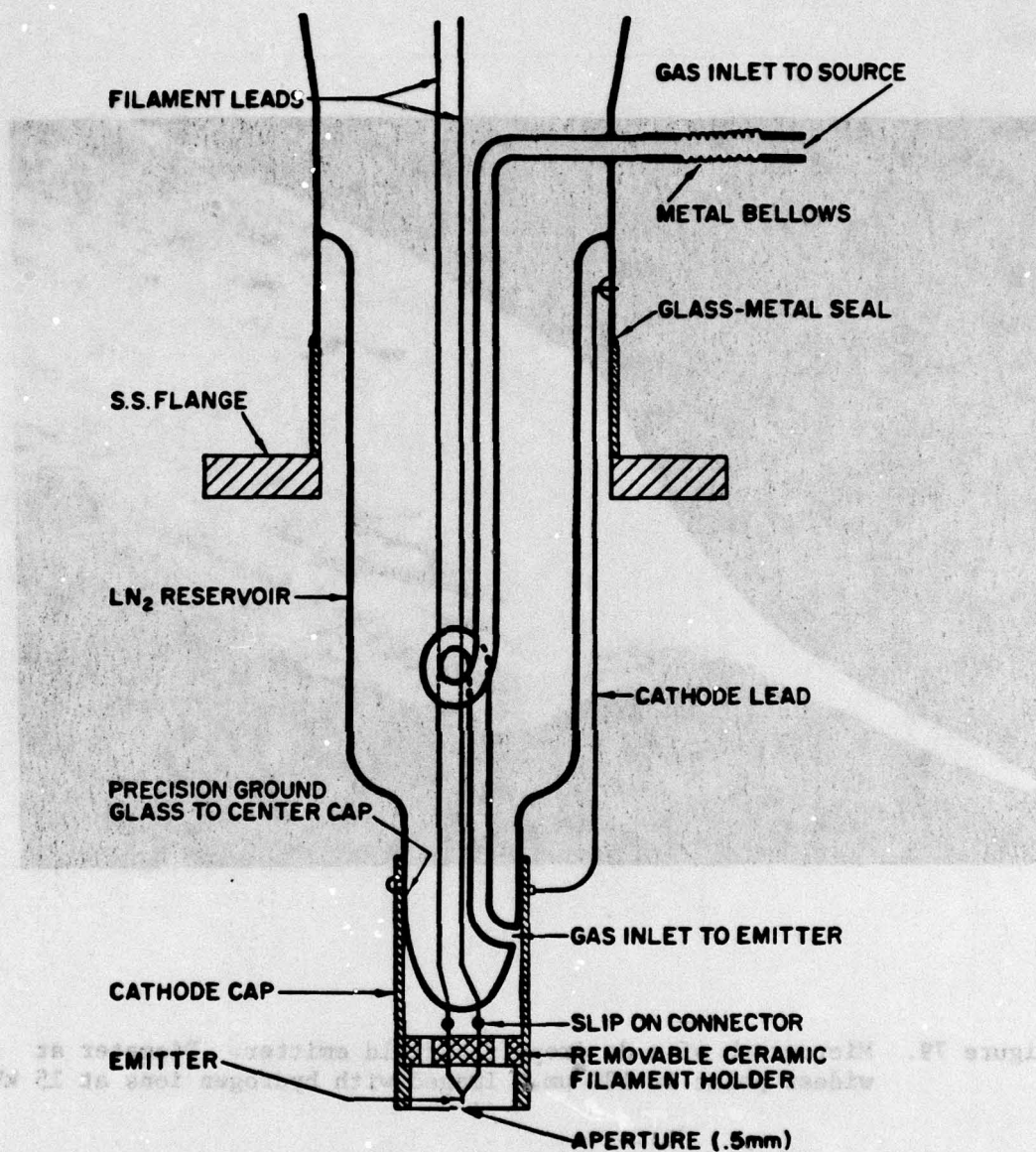


Figure 80. Schematic diagram of the FI source used in this experiment.



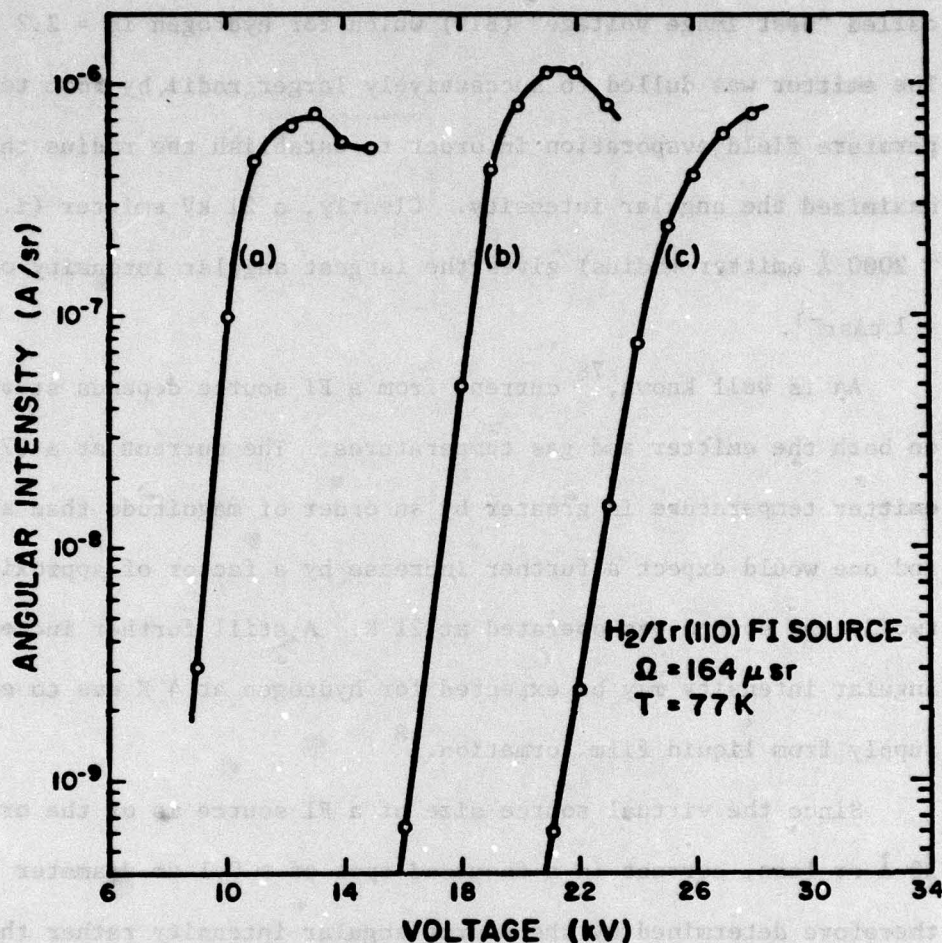


Figure 81. A plot of the experimental angular intensity vs. voltage for an iridium (110) oriented hydrogen field ionization source. Curve (a) was a source which had no prior processing; (b) a source that was field evaporated at room temperature; (c) the same as (b) but with further field evaporation. The hydrogen pressure at the emitter was approximately  $1 \times 10^{-2}$  torr. Data was taken in an ion beam optical column with the indicated beam aperture solid angle  $\Omega$  subtended at the emitter.

As can be seen the ion current goes through a maximum near the so-called "best image voltage" (BIV) which for hydrogen is  $\approx 2.2 \text{ V/\AA}$ . The emitter was dulled to successively larger radii by room temperature field evaporation in order to establish the radius that maximized the angular intensity. Clearly, a 21 kV emitter (i.e.  $\sim 2000 \text{ \AA}$  emitter radius) gives the largest angular intensity of  $\approx 1 \mu\text{Asr}^{-1}$ .

As is well known,<sup>78</sup> current from a FI source depends strongly on both the emitter and gas temperatures. The current at a 77 K emitter temperature is greater by an order of magnitude than at 300 K, and one would expect a further increase by a factor of approximately two if the source was operated at 21 K. A still further increase in angular intensity may be expected for hydrogen at 4 K due to enhanced supply from liquid film formation.<sup>48</sup>

Since the virtual source size of a FI source is of the order of  $10 \text{ \AA}$  or less, current in a focussed spot of  $\sim 0.1 \mu\text{m}$  diameter is therefore determined by the source angular intensity rather than brightness. With the results reported here and using the three element asymmetric lens described in Sec. IIA it should be feasible to focus 0.1 nA of ion current into a  $0.1 \mu\text{m}$  beam spot or 0.05 nA into a  $0.05 \mu\text{m}$  spot.



## REFERENCES

1. Oppenheimer, J. R., "Three Notes on the Quantum Theory of Aperiodic Effects," Phys. Rev., Vol. 31, pp 66-81 (1928).
2. Fowler, R. H., and Nordheim, L. W., "Electron Emission in Intense Electric Fields," Proc. Roy. Soc., Vol. A119, p 173 (1928).
3. Müller, E. W., "Electron-microscopic Observations upon Field Cathodes," Z. Physik, Vol. 106, p 541 (1937); "The Field-ion Microscope," Z. Physik, Vol. 131, p 136 (1951).
4. Swanson, L. W., and Crouser, L. C., "Angular Confinement of Field Electron and Ion Emission," J. Appl. Phys., Vol. 40, p 4741 (1969).
5. Swanson, L. W., "Comparative Study of the Zirconioted Built-up W Thermal-field Cathode," J. Vac. Sci. and Technol., Vol. 12, p 1228 (1975).
6. Swanson, L. W., Interim Tech. Report No. 4, "Field Electron and Ion Source Research for High Density Information Storage System," AFAL TR-78-174 (1978).
7. Swanson, L. W., and Martin, N. A., "Field Emission Cathode Stability Studies: Zirconium/Tungsten Thermal Field Cathode," J. Appl. Phys., Vol. 46, p 2029 (1975).
8. Martin, E., Trolan, J., and Dyke, W., "Stable, High Density Field Emission Cold Cathode," J. Appl. Phys., Vol. 31, p 782 (1960).
9. Dyke, W., Charbonnier, F., Strayer, R., Floyd, R., Barbour, J., and Trolan, J., "Electrical Stability and Life of the Heated Field Emission Cathode," J. Appl. Phys., Vol. 31, p 790 (1960).
10. Verhoeven, J. D., Gibson, E. D., Noack, M. A., Conzemius, R. J., "An Arc Floating Zone Technique for Preparing Single Crystal Lanthanum Hexaboride," J. Cryst. Growth, Vol. 36, p 115 (1976).
11. Futamoto, M., Hosoki, S., and Kawabe, U., "Field-emission and Field-ion Microscopy of Lanthanum Hexaboride," J. Appl. Phys., Vol. 48, p 3541 (1977).
12. Eckstein, B., and Forman, R., "Preparation and Some Properties of Tantalum Carbide," J. Appl. Phys., Vol. 33, p 82 (1962).
13. Bettler, P. C., Charbonnier, F. M., "Activation Energy for the Surface Migration of Tungsten in the Presence of a High-Electric Field," Phys. Rev., Vol. 119, p 85 (1960).

14. Swanson, L. W., "Comparative Study of the Zirconiated and Built-up Thermal Field Cathode," J. Vac. Sci. Technol., Vol. 12, p 1228 (1975).
15. Swanson, L., Crouser, L., and Charbonnier, F., "Energy Exchanges Attending Field Electron Emission," Phys. Rev., Vol. 151, p 327 (1966).
16. Pickard, M., and Drechsler, M., "A Field Emission Measurement of the Influence of Adsorption on Surface Self-Diffusion," Surface Sci., Vol. 32, p 341 (1972).
17. Danielson, L., and Swanson, L., "High Temperature Study of Zirconium and Oxygen on the W(100) Crystal Face," Surface Sci. (in press).
18. Swanson, L. W., and Crouser, L. C., "Total-Energy Distribution of Field-Emitted Electrons and Single-Plane Work Functions for Tungsten," Phys. Rev., Vol. 163, pp 622 (1967).
19. Gadzuk, J. W., and Plummer, E. W., "Field Emission Energy Distribution (FEED)," Rev. Mod. Phys., Vol. 45, p 487 (1973).
20. Czyzeivski, J. J., "The Field Emission Energy Distribution (FEED) Study of Electron Interactions in Tungsten," Surface Sci., Vol. 39, p 1 (1973).
21. Plummer, E. W., and Gadzuk, J. W., "Surface States on Tungsten," Phys. Rev. Letters, Vol. 25, p 1493 (1970).
22. Dionne, N. J., and Rhodin, T. N., "Field Emission Energy Spectroscopy of the Platinum Group Metals," Phys. Rev., Vol. B14, p 322 (1976).
23. Good, R. H., and Müller, E. W., "Field Emissions," Handbuch der Physik, Vol. 21, p 176 (1956).
24. Penn, D. R., and Plummer, E. W., "Field Emission as a Probe of the Surface Density of States," Phys. Rev., Vol. B9, p 1216 (1974).
25. Nicolaou, N. and Modinos, A., "Band Structure Effects in Field Emission Energy Distribution in Tungsten," Phys. Rev., Vol. B11, p 3687 (1975).
26. Plummer, E. W., and Young, R. D., "Field-Emission Studies of Electronic Energy Levels of Adsorbed Atoms," Phys. Rev., Vol. B1, p 2088 (1970).
27. Gadzuk, J. W., "Resonance-Tunneling Spectroscopy of Atoms Adsorbed on Metal Surfaces: Theory," Phys. Rev., Vol. B1, p 2110 (1970).



28. Lea, C., and Gomer, R., "Evidence of Electron-Electron Scattering from Field Emission," Phys. Rev. Letters, Vol. 25, p 804 (1970).
29. Gadzuk, J. W., and Plummer, E. W., "Hot-Hole Electron Cascades in Field Emission from Metals," Phys. Rev. Letters, Vol. 26, p 92 (1971).
30. Gadzuk, J. W., and Lucas, A. A., "Field Emission Energy Tails and Tunneling Lifetimes," Phys. Rev., Vol. B7, p 4770 (1973).
31. Barbour, J. P., Dolan, W. W., Martin, E. E., Dyke, W. P., "Space-Charge Effects in Field Emission," Phys. Rev., Vol. 92, p 45 (1953).
32. Veneklasen, L. H., and Siegel, M., "Oxygen-Processed Field Emission Source," J. Appl. Phys., Vol. 43, p 1600 (1972).
33. Loeffler, K. H., "Energy-Spread Generation in Electron-Optical Instruments," Z. Angew. Phys., Vol. 27, p 145 (1969).
34. Zimmerman, B., "Broadened Energy Distribution in Electron Beams," Adv. Electronics and Electron Phys., Vol. 29, p 257 (1970).
35. Ditchfield, R. W., and Whelan, M. J., "Energy Broadening of the Electron Beam in the Electron Microscope," Optik, Vol. 48, p 163 (1977).
36. Boersch, H., "Experimental Determination of Energy Distribution of Thermally Released Electron Rays," Z. Physik, Vol. 136, p 115 (1954).
37. Murphy, E. L., and Good, R. H., Jr., "Thermionic Emission, Field Emission, and the Transition Region," Phys. Rev., Vol. 102, p 1464 (1956).
38. El-Kareh, A. B., Wolfe, J. C., and Wolfe, J. E., "Contribution to the General Analysis of Field Emission," J. Appl. Phys., Vol. 48, p 4749 (1977).
39. Dolan, W. W., and Dyke, W. P., "Temperature-and-Field Emission of Electrons from Metals," Phys. Rev., Vol. 95, p 327 (1954).
40. Gadzuk, J. W., and Plummer, E. W., "Energy Distribution for Thermal Field Emission," Phys. Rev., Vol. B3, p 2125 (1971).
41. Modinos, A., and Nicolaou, N., "Surface Density of States and Field Emission," Phys. Rev., Vol. B13, p 1536 (1976).

42. Simpson, J. A., and Kuyatt, C. E., "Anomalous Energy Spreads in Electron Beams," J. Appl. Phys., Vol. 37, p 3805 (1966).
43. Seliger, R. L. (Hughes Research Laboratories, Malibu, California, private communication).
44. Pushpavati, J., and Van der Ziel, A., "Noise in Space Charge Limited Field Emission Devices," IEEE Trans-Electron Devices, Vol. ED-12, p 395 (1965).
45. Swanson, L. W., "Current Fluctuations from Various Crystal Faces of a Clean Tungsten Field Emitter," Surface Sci., Vol. 70, p 165 (1978).
46. Munro, E., Ph.D. dissertation, University of Cambridge, Cambridge, England (1972).
47. Orloff, J., and Swanson, L. "Study of Field-Ionization Source for Microprobe Applications," J. Vac. Sci. and Technol., Vol. 12, p 1209 (1975).
48. Jason, A., Halpern, B., Inghram, M. G., and Gomer, R., "Field Ionization from  $H_2$  Layers," J. Chem. Phys., Vol. 52, p 2227-2234 (1970).
49. Anway, A. R., "Field Ionization of Water," J. Chem. Phys., Vol. 50, p 2012-2021 (1969).
50. Taylor, G. I., "Disintegration of Water Drops in an Electric Field," Proc. R. Soc. (London), Vol. A280, p 383-397 (1964).
51. Swanson, L. W., Schwind, G. A., "Electron Emission from a Liquid Metal," J. Appl. Phys., Vol. 49, p 5655-5662 (1978).
52. Krohn, V. E., Ringo, G. R., "Ion Source of High Brightness Using Liquid Metal," Appl. Phys. Letters, Vol. 27, p 479-481 (1975).
53. Clampitt, R., Jefferies, D. K., "Miniature Ion Sources for Analytical Instruments," Nucl. Inst. and Methods, Vol. 149, p 739-742 (1978).
54. Colby, B. W., Evans, C. A., Jr., "Electrohydrodynamic Ionization Mass Spectrometer," Anal. Chem., Vol. 45, p 1884-1889 (1973).
55. Mahoney, J. F., Yahiku, A. T., Daley, H. L., Moore, R. D., Perel, J., "Electrohydrodynamic Ion Source," J. Appl. Phys., Vol. 40, p 5101-5106 (1969).



56. Clampitt, R., Aitken, K. L., Jefferies, D. K., "Intense Field Emission Ion Source of Liquid Metals," J. Vac. Sci. Technol., Vol. 12, p 1208 (1975).
57. Seliger, R. L., Ward, J. W., Wang, V., Kubena, R. L., "A High Intensity Scanning Ion Probe with Submicrometer Spot Size," J. Appl. Phys. (in press).
58. Dyke, W. P., Trolan, J. K., Dolan, W. W., Barnes, G., "The Field Emitter: Fabrication, Electron Microscopy and Electric Field Calculations," J. Appl. Phys., Vol. 24, p 570-576 (1953).
59. Gomer, R., "On the Mechanism of Liquid Metal Electron and Ion Sources," Appl. Phys. (in press).
60. Brandon, D. G., Field Ion Microscopy, J. H. Hren and S. Ranganathan, eds., Plenum Press, New York (1968) p. 28.
61. Simpson, J. A., Morton, L., "Improved Filter Lens," Rev. Sci. Inst. Vol. 32, p 802-803 (1961).
62. Simpson, J., "Design of Retarding Field Analyzers," Rev. Sci. Inst., Vol. 32, p 1283-1293 (1961).
63. Tsong, T. T., and Müller, E. W., "Measurement of the Energy Distribution in Field Ionization," J. Chem. Phys., Vol. 41, p 3279-3284 (1964).
64. Orloff, J., Swanson, L., "Fine-Focus Ion Beams with Field Ionization," J. Vac. Sci. and Technol., Vol. 15, p 845 (1978).
65. Tsong, T. T., Müller, E. W., "Measurement of the Energy Distribution in Field Ionization," J. Chem. Phys., Vol. 41, p 3279-3284 (1964).
66. Riddle, G. H. N., "Electrostatic Einzel Lenses With Reduced Spherical Aberration For Use In Field Emission Guns," J. Vac. Sci. Tech., Vol. 15, p 857-860 (1978).
67. Crewe, A. V., Wall, J., Welter, L. M., "A High-Resolution Scanning Transmission Electron Microscope," J. App. Phys., Vol. 39, p 5861-5868 (1968).
68. Swanson, L. W., "Comparative Study of the Zirconiased and Built-Up W Thermal Field Cathode," J. Vac. Sci. Tech., Vol. 12, p 1228-1233 (1975).

69. Munro, E., "Design of Electrostatic Lenses For Field-Emission Electron Guns," Proc. Fifth Congress on Electron Microscopy, University of Manchester, Institute of Physics Conf. Series No. 14 (1972) p 22-23.
70. Read, F. H., "Calculated Properties of Electrostatic Einzel Lenses of Three Apertures," J. Sci. Inst., Vol. 2, p 679-684 (1969).
71. Read, F. H., "Asymmetric Electrostatic Lenses Of Three Apertures," J. Sci. Inst., Vol. 3, p 127-131 (1970).
72. Imhof, R. E., Read, F. H., "A Three-Aperture Electron Optical Lens For Producing An Image of Variable Energy But Fixed Position," J. Sci. Inst., Vol. 1, p 859-860 (1969).
73. Kuroda, K., Suzuki, T., "Analysis of Accelerating Lens System in Field Emission Scanning Electron Microscope," J. App. Phys., Vol. 45, p 1436-1441 (1974).
74. Kuroda, K., Ebisui, H., Suzuki, T., "Three Anode Accelerating Lens System For The Field Emission Scanning Electron Microscope," J. App. Phys., Vol. 45, p 2336-2342 (1974).
75. Kuroda, K., Suzuki, T., "Three Anode Accelerating Lens System for Field Emission Scanning Electron Microscopy (11)," App. Phys. Lett., Vol. 25, p 23-24 (1974).
76. Munro, E., "Computer-Aided Design of Electron Lenses by the Finite Element Method," Image Processing and Computer Aided Design In Electron Optics, P. Hawkes, Ed., Acad. Press, London (1973) p 284-323.
77. Munro, E., Ph.D. Dissertation, University of Cambridge Dept. of Engineering, Cambridge, England (1972).
78. Tsong, T. T., Muller, E. W., "Current-Voltage Characteristics by Image Photometry in a Field Ion Microscope," J. App. Phys., Vol. 37, p 3065 (1966).